# CONSTRAINING NUCLEAR STRUCTURE: USING PHYSICAL MODELS OF HEAVY-ION COLLISIONS TO INFER FLUCTUATIONS IN THE SHAPES OF ATOMIC NUCLEI

NICOLAS MIRÓ FORTIER

Supervisor: Sangyong Jeon

Department of Physics

McGill University

Montreal, Québec

October 2024

A thesis submitted to McGill University in partial fulfillment of the requirements for the degree of Doctor of Philosophy

# ABSTRACT

Heavy-ion collisions performed at facilities such as the Large Hadron Collider (LHC) and the Relativistic Heavy Ion Collider (RHIC) produce the hottest matter in the universe at $\sim 10^{12}$ K. This generates an energetic state of matter in which quarks and gluons become deconfined, known as the Quark Gluon Plasma. This material only survives for approximately $10^{-23}$ s, presenting many challenges for precise study. However, its fleeting nature can, at times, be used as a powerful tool.

Atomic nuclei, as natural phenomena described by quantum field theory, are defined by their reliance on the wavefunction and its internal and external fluctuations. As prescribed by quantum mechanics, these fluctuations are guided by underlying states encoded in the wavefunction of a specific nucleus. Ascribing a physical feature to an atomic nucleus demands that its overall wavefunction - the superposition of its intrinsic quantum states - prescribe this feature. This means that, when trying to determine the overall structural 'shape' of a nucleus, the wavefunction generally appears as spherically symmetric, even though it may be composed of a superposition of quantum states which individually have well-defined shapes due to their angular momentum structures. For a given nucleus, the typical time scale of fluctuations in angular (or rotational) degrees of freedom is $\sim 10^{-21}$ s. Typical spectroscopic imaging methods offer resolutions on much longer timescales, probing a superposition of a large number of these underlying states, and therefore complicating the task of understanding the underlying states. More energetic and targeted methods, such as electron-ion collisions, do provide sufficiently short resolution scales, but the nature of these probes only allows for highly-localized 'images': building a composite out of a collection of these images over many events simply leads to the same problem as with spectroscopic methods.

Heavy-ion collisions provide us with the tools to solve the nuclear imaging problem. Indeed, the nucleus-nucleus interaction happens fast enough as to resolve only a single state fluctuation, and the high-energy nucleons participating in a collision give us access to the superposition of the many-body nucleon distributions of the collision system. In essence, they act as a camera with an exposure rapid enough to capture a single constituent state of the nuclear wavefunction, essentially peering into the shape of these fluctuations; these fluctuations then create anisotropic geometric configurations in the initial state, which are detectable in experimental observables. That is, experimental results gathered during collisions of deformed systems would be irreconcilable with a theoretical picture excluding the shapes of these fluctuations.

In this study, we use a fully state-of-the-art hybrid model of heavy-ion collisions consisting of the IP-Glasma initial state and pre-equilibrium evolution, 2+1 and 3+1D MUSIC viscous hydrodynamics, iSS particlization and SMASH hadronic cascade. Our end-to-end physical model allows us to generate nucleon configurations consistent with low-energy estimates of nuclear structure, collide them at a given energy, evolve the thermalized QGP and produce observables which are directly comparable to results produced in experiments. This one-to-one comparison to experiment allows us to put strong constraints on the shape of the fluctuations of the wavefunction and therefore on the nuclear wavefunction itself, in turn informing low-energy physicists as to what the most likely geometric properties of the wavefunction are.

We share results for 3 different systems, namely $^{238}$U, $^{197}$Au and $^{129}$Xe at RHIC and LHC energies, which show that our cutting-edge, QCD-based framework can select appropriate nuclear configurations based on direct comparisons to experimental results.

# RÉSUMÉ

Les collisions d'ions lourds réalisées dans des installations telles que le Grand collisionneur de hadrons (LHC) et le collisionneur d'ions lourds relativistes (RHIC) produisent la matière la plus chaude de notre univers, donc la température s'approche de $10^{12}$ K. Ces collisions génèrent un état extrêmement énergétique et éphémère dans lequel les quarks et les gluons deviennent déconfinés, le Plasma de Quarks et de Gluons (QGP). Cet état de déconfinement ne dure qu'environ $10^{-23}$ s, ce qui complique son analyse précise. Sa brève nature peut toutefois aussi être utilisée comme puissant outil.

Les noyaux atomiques, en tant que phénomènes naturels décrits par la théorie quantique des champs, sont définis par leur dépendance à l'égard de la fonction d'onde et de ses fluctuations internes et externes. Comme le prescrit la mécanique quantique, ces fluctuations sont guidées par des états sous-jacents encodés dans la fonction d'onde d'un noyau donné. L'attribution d'une caractéristique physique à un noyau atomique exige que sa fonction d'onde globale, c'est-à-dire la superposition de ses états quantiques intrinsèques, prescrive cette caractéristique. Cela signifie que, lorsqu'on essaie de déterminer la « forme » globale d'un noyau, la fonction d'onde apparaît généralement comme étant à sphérique, même si elle peut être composée d'une superposition d'états quantiques qui, individuellement, ont des formes bien définies en raison de leurs structures de moment angulaire. Pour un noyau donné, l'échelle de temps typique sur laquelle les fluctuations des degrés de liberté angulaires (ou rotationnels) se produisent est de $\sim 10^{-21}$ s. Les méthodes d'imagerie spectroscopique typiques offrent des résolutions sur des échelles de temps beaucoup plus longues que celle-ci, sondant une superposition d'un grand nombre d'états sous-jacents, ce qui complique la tâche de compréhension desdits états. Des méthodes plus énergétiques et plus ciblées, telles que les collisions électron-ion, permettent d'obtenir des échelles de résolution suffisam-

ment courtes, mais la nature de ces sondes ne permet d'obtenir que des « images » très localisées : la construction d'un composite à partir d'une collection de ces images sur de nombreux événements conduit simplement au même problème qu'avec les méthodes spectroscopiques.

Les collisions d'ions lourds nous fournissent les outils nécessaires pour résoudre le problème de l'imagerie nucléaire. En effet, l'interaction entre les noyaux est suffisamment rapide pour ne résoudre qu'une seule fluctuation d'état, et les nucléons participant à une collision à haute énergie nous donnent accès à une superposition des distributions de nucléons du système de collision. Ils agissent essentiellement comme une caméra dont le temps d'exposition est suffisamment rapide pour capturer un seul état constitutif de la fonction d'onde nucléaire, produisant une image de la forme d'une de ces fluctuations. Ces fluctuations créent alors des configurations géométriques anisotropes dans l'état initial, qui sont détectables dans les données expérimentales. Les résultats expérimentaux recueillis lors de collisions de systèmes déformés seraient inconciliables avec une image théorique excluant les formes de ces fluctuations.

Dans cette étude, nous utilisons un modèle hybride de collisions d'ions lourds composé d'IP-Glasma comme état initial évolutif, de MUSIC pour la phase d'hydrodynamique visqueuse en 2+1 et 3+1D, de la particulation d'iSS et de la cascade hadronique de SMASH. Notre modèle physique nous permet de générer des configurations de nucléons compatibles avec les estimations de la structure nucléaire à basse énergie, de les faire entrer en collision à une énergie donnée, d'évoluer le QGP thermalisé et de produire des données directement comparables aux résultats expérimentaux. Cette comparaison directe aux résultats expérimentaux nous permet d'imposer des contraintes strictes sur la forme des fluctuations de la fonction d'onde et donc sur la fonction d'onde nucléaire en soi. Ces contraintes permettent ensuite aux physiciens des basses énergies de connaître les propriétés géométriques les plus probables de la fonction d'onde.

Nous partageons les résultats obtenus pour trois systèmes différents, soit $^{238}$U, $^{197}$Au et $^{129}$Xe aux énergies du RHIC et du LHC, qui montrent que nos méthodes de pointe,

basé sur la chromodynamique quantique, peut sélectionner des configurations nucléaires appropriées sur la base de comparaisons directes avec les résultats expérimentaux.

# ACKNOWLEDGEMENTS

First and foremost, I would like to thank my advisor, Prof. Sangyong Jeon, for his never-ending patience and guidance as I made small strides towards accomplishing the work collected in this thesis. His patience and dedication to making sure I understood things on a fundamental level have been invaluable to my development as a physicist. His character as a person has made me feel extremely lucky to have been allowed to join his group as his student, and I will forever be grateful our paths crossed. I would also like to sincerely thank Prof. Charles Gale for his timely guidance, his invaluable insights and his anecdotes!

Special thanks are due to Scott McDonald for innumerable useful discussions and insights as well as his constant willingness to lend a hand where it was needed. Without Scott to develop McGill's version of IP-Glasma and explain it to me, this work would have been much more tiring. Scott deserves much of the credit for this thesis' work. I am unbelievably grateful to have been able to join this research group at a time when he was still a member.

Special thanks are also due to Matthew Heffernan and Rouzbeh Yazdi, who became close friends during my PhD. Their camaraderie, encouragement, and help, along with their good mood and joy, have made this challenging path a less scary one. More importantly, their help and guidance across both my MSc and PhD were of the greatest quality, allowing me to find a path that was truly my own and ensuring that it was well-motivated.

To Xiang-Yu Wu, Lipei Du and Shuzhe Zhi, I extend my heartfelt appreciation for their guidance, intelligence and vision, and for their unwavering commitment to providing support to graduate students in our group.

I would obviously also like to thank my parents, Michael and Marisol, as well as Sophie, Guillaume, Émilie, Anne, Adam and Charles, my brothers and sisters. You have all been an integral part in making me who I am, and I would not be writing these lines without your being in my life. There is also my partner Gabrielle and our dog Huggy, who have both supported me more than anyone in this endeavor, and whom I love deeply. And, finally, thank you to all my loving friends outside of physics; you have all heard me talk (and tolerated me talking) about my passion so often, and without your love and support through the years, I would not be here.

Importantly, I would also like to thank the support staff as well as administrators at the Digital Research Alliance of Canada for the computing clusters which were crucial to my research projects.

# CONTENTS

# LIST OF FIGURES

# LIST OF TABLES

# ACRONYMS

QGP Quark-Gluon Plasma

QCD Quantum ChromoDynamics

WLOG Without Loss of Generality

ALICE A Large Ion Collider Experiment

ATLAS A Toroidal LHC ApparatuS

HICs Heavy-Ion Collisions

MUSIC MUScl for Ion Collisions

SMASH Simulating Many Accelerated Strongly-interacting Hadrons

iSS iSpectra Sampler

CMS Compact Muon Solenoid, experiment located in Switzerland

DGLAP Dokshitzer-Gribov-Lipatov-Altarelli-Parisi

PHENIX Pioneering High Energy Nuclear Interaction eXperiment, experiment located in the USA

RHIC Relativistic Heavy Ion Collider, collider located in the USA

STAR Solenoidal Tracker at RHIC, experiment located in the USA

LHC Large Hadron Collider

IP-Sat Impact Parameter dipoler Saturation model

CYM Classical Yang-Mills

WS Woods-Saxon

# CONTRIBUTION TO ORIGINAL KNOWLEDGE

---

*Chapters 1-4* — These chapters provide, in order, a general introduction to nuclear physics, theoretical and experimental advancements in nuclear structure studies and emulation, a complete review of the pre-equilibrium and hydrodynamics evolution phases of heavy-ion collisions, and a thorough description of experimental observables which are relevant to the current study. I have contributed significantly to our nucleon sampling procedure [1] and to the ensuring stability in the pre-equilibrium evolution. Furthermore, I have made significant advancements in automation procedures for running our codes on high performance computing infrastructure.

*Chapter 5* — Introduces first-of-their-kind results stemming from fully physically-motivated simulations of heavy-ion collisions across two beam energies and systems ($^{197}$Au and $^{238}$U), and four total nuclear parametrizations [1]. My results establish the efficacy and sensitivity of our framework to fairly small changes to the nuclear parametrizations and, therefore, initial state geometry. Through a single calibration step, our framework reproduces all provided baseline observables, confirming our approach's reliability. In a first, I then use our appropriately calibrated model to discriminate between potential nuclear parametrizations, providing physics-backed insights as to which parametrizations are better matches for the entirety of the experimental data. This thorough reproduction and combined matching of experimental data are novel to the field, and have been published in Ref. [1]. The calculations producing our results were conducted on high performance computing infrastructure and totalized approximately 450 core-years of compute time.

*Chapter 6* — We extend the boost-invariant framework to 3+1 dimension, providing

theoretical motivation and some numerical details. Once again, similar advancements to the computing procedures have been made in the 3+1D framework, allowing for a more streamlined process, quicker computations and, therefore, better statistics.

*Chapter 7* — Building on the novel work from Chapter 5, I conduct the first complete analysis and synthesis of the nuclear structure of $^{129}$Xe using the entirety of available experimental data simultaneously, seeking a parametrization which best reproduces all the data. Furthermore, I provide the first thorough analysis of the sensitivity of longitudinal observables to geometric fluctuations in the initial state, allowing for further studies to build on our acquired knowledge. Finally, I use novel techniques to provide a most-likely parametrization fit for $^{129}$Xe, constraining the wide collection of 'accepted' $^{129}$Xe parametrizations down to a much narrower range of parametrization parameters. These calculations were made using our physics-based model, and which required the use of 700 core-years of compute time.

# 1

# INTRODUCTION TO NUCLEAR PHYSICS

When Ernest Rutherford arrived at McGill in 1898, he was already a renowned physicist with years of contributions to the nascent field of radioactivity. His discovery and subsequent naming of alpha and beta rays provided him with a view of the microscopic world that few of his time had been able to formalize; a view which, through years of experimental process and progress, would lead to his landmark 'gold foil experiment,' proving once and for all that atoms, the building blocks of all known matter at the time, were made up predominantly of vacuum, harboring an extremely dense nucleus of positive charge at their cores. His discovery of the true nature of atoms spurred the golden age of nuclear physics, from the discovery of neutrons by James Chadwick [2] to the initial description and characterization of nuclear fusion as stars' secret to longevity and energy by Eddington [3]. The contemporaneous discovery and description of quantum mechanics finally led to an event which is directly linked to the writing of this thesis today: the initial positing by Hideki Yukawa [4] of the fundamental force required for binding neutrons and protons inside an atomic nucleus. This new force, mediated by a yet-to-be-discovered particle he named *pi mesons*, would come to be known as the strong nuclear force.

Over the next 90 years, our understanding and definitions of the strong nuclear force have evolved and complexified. Following the successful characterization of electromagnetism via quantum field theory, a similar program was introduced to attempt to describe the strong force as a fundamental interaction fully. While, at first, the strong force could not be fully described by quantum field theory given quarks, the theorized fundamental building blocks of hadrons, had never been detected alone, deep inelastic

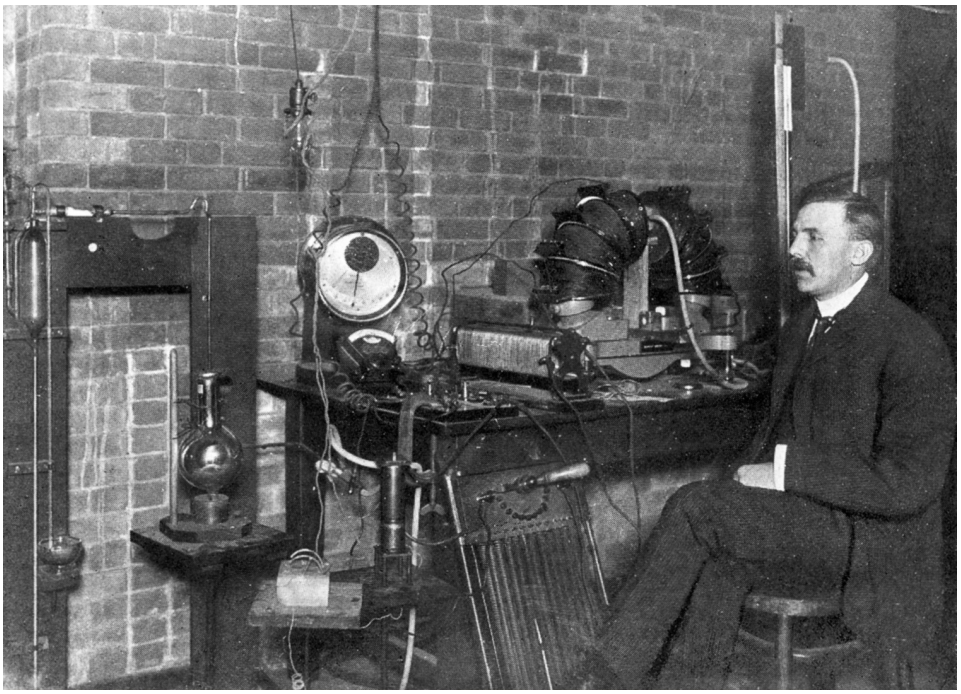

Figure 1: Ernest Rutherford, the 'father of nuclear physics', shown in his laboratory at McGill. His contributions to the field, most notably his descriptions of radiative processes and atomic nuclei, spurred the contemporary era of nuclear physics.

scattering experiments led by James Bjorken [5] showed that quarks really did exist. The subsequent proposal of a new quantum number - color - to explain how the existence of $\Delta^{++}$ did not violate Pauli's exclusion principle sealed the deal: the field of Quantum Chromodynamics (QCD) was born.

## 1.1 QCD CRASH COURSE

QCD is a Yang-Mills theory, a non-abelian group theory. Its non-abelian nature means that its mediators - gluons - are themselves affected by the interaction, and can therefore radiate more gluons. It also means that its coupling strength increases with distance,

making QCD a theory characterized by asymptotic freedom. The QCD Lagrangian is given by

$$\mathcal{L}_{\text{QCD}} = \sum_f \bar{\psi}_f \left(i\not{D} - m_f\right) \psi_f - \frac{1}{4} F^a_{\mu\nu} F^{\mu\nu a} \tag{1.1}$$

with $a$ being the quark color index, which runs from 1 to 8, $f$ being the index that runs over the quark flavor space and $\psi_f$ being the Dirac spinor of the quark field. Here, Dirac slash notation - $\not{D} = \gamma^\mu D_\mu$ - was used for succinctness, where $\gamma^\mu$ are the Dirac matrices and $D_\mu$ is the covariant derivative, defined as

$$D_\mu = \partial_\mu + igA^a_\mu t_a, \tag{1.2}$$

where we have introduced the SU(3) generators $t_a$, commonly referred to as Gell-Mann matrices [6], which are the source of the non-abelian nature of QCD since they do not commute. Indeed,

$$[t_a, t_b] = if^{abc} t_c, \tag{1.3}$$

with $f^{abc}$, the SU(3) structure constant. These generators combined to the color gauge field components $A^a_\mu$ form the color gauge fields (sometimes referred to as gluon fields),

$$A_\mu = A^a_\mu t_a. \tag{1.4}$$

Equation (1.1) also sees the introduction of the QCD field strength tensor $F^a_{\mu\nu}$, which can be understood as being very similar in form to its Quantum Electrodynamics counterpart, with the addition of a non-vanishing commutator between the color gauge fields due to QCD being a non-abelian theory, i.e.,

$$\begin{aligned} & F_{\mu\nu} = \partial_\mu A_\nu - \partial_\nu A_\mu + ig\left[A_\mu, A_\nu\right] \\ \rightarrow & F^a_{\mu\nu} t_a = \partial_\mu A^a_\nu t_a - \partial_\nu A^a_\mu t_a + igA^a_\mu A^b_\nu \left[t_a, t_b\right] \\ \Rightarrow & F^a_{\mu\nu} t_a = \left(\partial_\mu A^a_\nu t_a - \partial_\nu A^a_\mu t_a - g f_{abc} A^b_\mu A^c_\nu\right) t_a. \end{aligned} \tag{1.5}$$

As in other theories, the strong coupling $g$ marks the strength of the interaction between colored particles (quarks or gluons). As mentioned above, its value decreases

with increasing energy, starkly contrasting to the electromagnetic coupling. This means that particles which interact via the strong interaction can not, unless provided tremendous amounts of energy, extirpate themselves from the grasp of its coupling, leading to a phenomenon, hinted at earlier, called *color confinement*. We can understand this behavior theoretically by looking at the $\beta$-functions of both theories, a function which quantifies changes in a theory's coupling strength at different energy scales. In QED, we have

$$\beta(e) = \frac{\partial e}{\partial \log Q} = \frac{e^3}{12\pi^2}, \tag{1.6}$$

where $Q$ designates the energy scale and $e$ is the QED coupling. We see that the QED $\beta$-function is constant and positive, meaning that, with increasing energy, the QED coupling increases. In QCD, on the other hand, we have

$$\beta(g) = -\left(\frac{11}{3}N_c - \frac{2}{3}n_f\right)\frac{g^3}{16\pi^2}, \tag{1.7}$$

where $N_c$ is the number of colors and $n_f$ is the number of quark flavors. Therefore, for $n_f < \frac{11}{2}N_c$, the $\beta$-function is negative. There are 3 colors ($N_c = 3$) and, in perturbative calculations, the number of allowed quark flavors depends on the energy scale $Q$. Theoretically, 6 quark flavors are included in the Standard model; taking this value, $\beta(g)$ remains negative. Therefore, QCD is an *asymptotically free* gauge theory.

Asymptotic freedom makes QCD a particularly hard theory to study. The usual prescription of perturbation theory, which analyzes theories at low energies (and, therefore, at small couplings), does not work for QCD, given that its coupling increases as energy is decreased. Indeed, looking at Fig. 2, we find that the strong coupling $\alpha_s = \frac{g^2}{4\pi}$ increases exponentially as we move towards low energies. As a result, non-perturbative numerical techniques (such as lattice QCD) do great at high temperatures where the degrees of freedom are quarks and gluons (i.e. in a state of deconfinement) [8]. Moving our attention to Fig. 3, current lattice QCD calculations probe the region at and above the crossover temperature (which newer estimates set to 155 MeV, rather than 170 MeV [9]). However, they do not connect smoothly to the hadronic phase below the

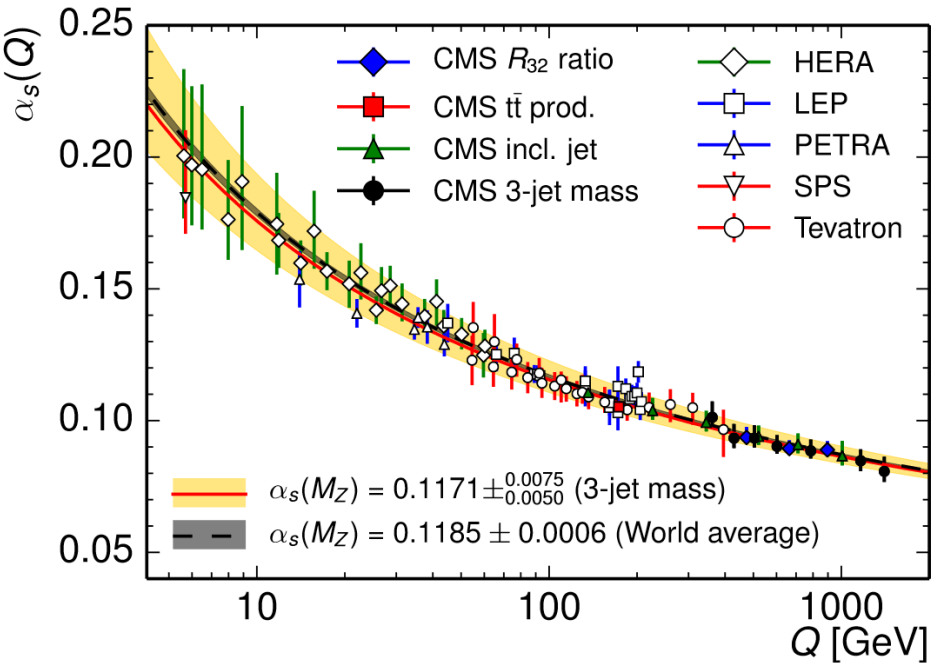


Figure 2: The running coupling $\alpha_s$ as a function of energy $Q$. Figure taken from Ref. [7].

crossover temperature, let alone to highly complex states of many hadrons combining to form nuclear matter.

This is where a good question emerges: All of our descriptions in this section seem to be more applicable to high-energy studies and particle physics; we have given the QCD Lagrangian, but it (obviously) only contained quarks (as opposed to entire nucleons); we have described at length how matter interacting via QCD is asymptotically free, meaning that studying free quarks inherently relies on us moving to a high-energy regime. High-energy nuclear physics, the topic of this thesis, may therefore seem like somewhat of a contradiction since nuclear physics has, for more than a century, been concerned with descriptions of larger-scale systems at energies many orders of magnitude below those at which the strong coupling allows us to peer into QCD's structure. However, since the inception of the first particle colliders, a new paradigm of nuclear physics research is born. Indeed, while nuclear physics is interested in the mass, energy levels, geometry and other general features of atomic nuclei, it has also become interested in understanding how these complex features emerge from elementary descriptions of quarks and gluons interacting via the strong force. As such, while nuclear physics is

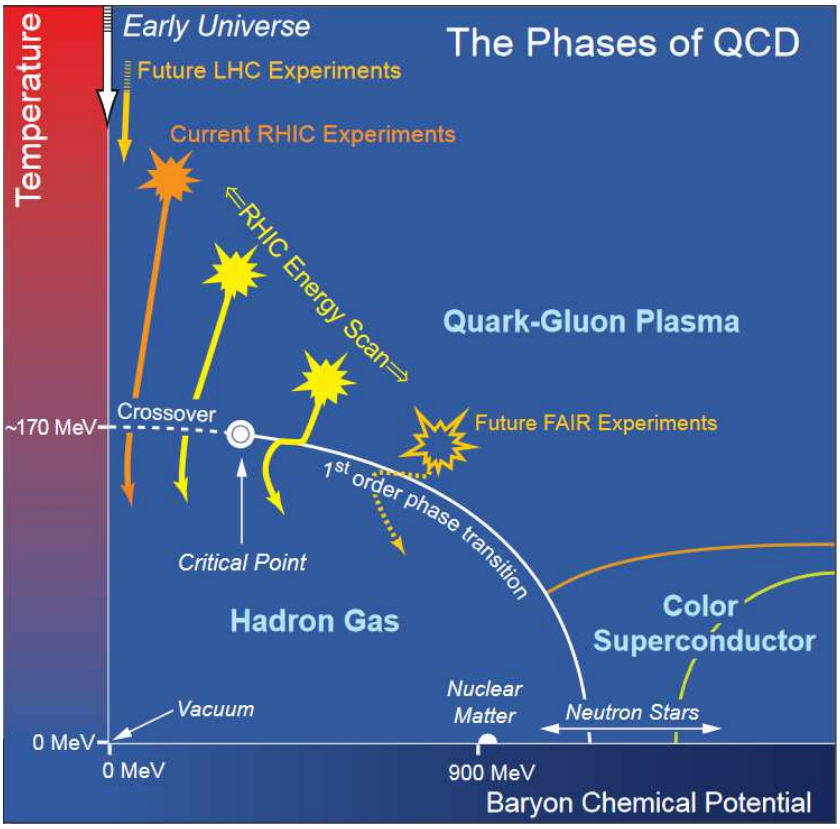


Figure 3: A schematic representation of the QCD phase diagram and where different experimental probes sit. Figure taken from Ref. [10].

still very much interested in descriptions of pure nuclear matter (as found along the Baryon Chemical Potential axis of Fig. 3, at 900 MeV), it is now also concerned with reconciling the entirety of the QCD phase diagram with the properties of atomic nuclei as we know and understand them in nature. Therefore, while particle accelerators are often associated with particle physics, their use of heavy ions (i.e. medium- to large-sized atomic nuclei) as collision systems display their use and relevance for nuclear physics, helping tie the two fields in their quest for a deeper understanding of QCD.

## 1.2 HEAVY-ION COLLISIONS AND THE QUARK-GLUON PLASMA

In Fig. 3 are inscribed the names of famous experiments conducted over the past few decades. Those include the Large Hadron Collider (LHC) and the Relativistic Heavy-Ion

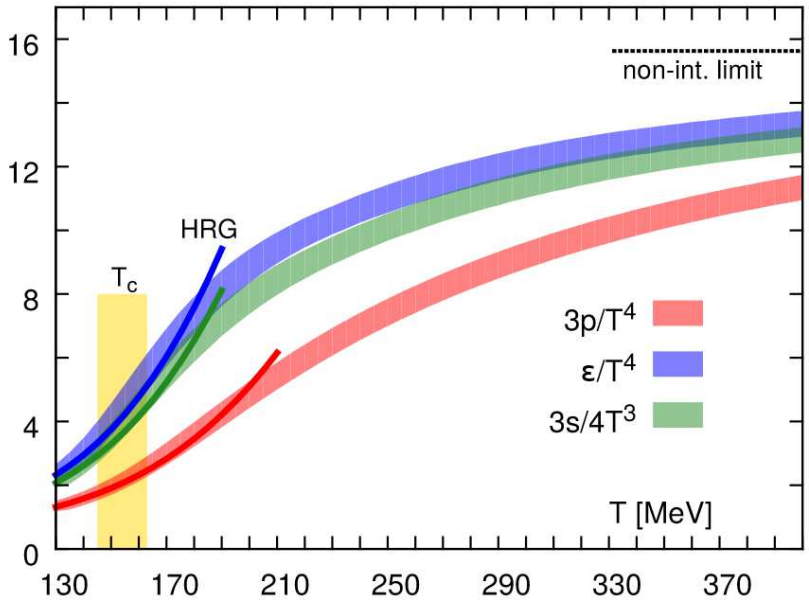


Figure 4: Blue curves show the ratio $\epsilon/T^4$. The solid line shows low-temperature Hadron Resonance Gas (HRG) estimates, while the fuller curve shows the HotQCD prediction. Figure taken from Ref. [11]

Collider (RHIC), the only two operating heavy-ion colliders, with the former providing the largest beam energies of the two (as is evident from Fig. 3). These experiments cover a relatively wide area of the QCD phase diagram, and they all originate from the same general region, that of the Quark-Gluon Plasma, or QGP. The QGP designates a high-temperature state of deconfined quarks and gluons, an exotic state of matter without nucleonic degrees of freedom. Heavy-ion collisions provide the perfect conditions for creating QGP, as they create states where large amounts of quark matter are packed into extremely small spaces, i.e. extremely large densities and temperatures. The first particle accelerators were concerned with smashing single protons into one another. However, following initial results, it was understood that QGP, which was only hypothesized at the time, could only be generated in yet more extreme and dense environments; the need for atomic nuclei collisions became apparent, so heavy-ion collision programs were undertaken. To understand where the idea of the QGP originates, one must turn to lattice QCD.

In statistical mechanics, the Stefan-Boltzmann law predicts that the ratio of the energy density $\epsilon$ to the fourth power of the temperature $T$ - $\epsilon/T^4$ - should be proportional to the number of degrees of freedom in the system when $T \gg m$ (or we are considering massless degrees of freedom). Understanding that these two quantities are related to one another through the system's equation of state, this quantity has a non-trivial dependence on one's precise and accurate understanding of the system's evolution. When moving from a system of hadrons - be they mesons or baryons - to a system made up of deconfined quarks and gluons, one expects the release of a large number of degrees of freedom. Indeed, while a gas of pions may only have 3 degrees of freedom in its phase space, a gas made of the quarks and gluons composing these pions would quickly gain more than 30 degrees of freedom, accounting for the spins of the quarks and gluons (2 each), the colors of both particles (3 and 8), the allowed quark flavors (2 for a gas of pions) and a whether a given quark is itself or its antiquark.

This liberation of degrees of freedom shows itself in Fig. 4. There, we see that the ratio steadily increases from $\sim$ 2 at temperatures below 155 MeV to $\sim$ 14 beyond 370 MeV - a considerable jump. This indicates that degrees of freedom are being liberated continuously, leading us to conclude that the transition between a gas of hadrons and a deconfined state of quark matter is smooth. This fact is represented in Fig. 3; indeed, we see that at 0 baryon chemical potential, moving up the temperature axis leads us to a crossover line which is not a first-order phase transition. The smoothness exhibited by the $\epsilon/T^4$ curve in Fig. 4 across the temperature range allows us to infer that no discontinuity exists in its first derivative, confirming that this transition is smooth and not a first-order phase transition. Therefore, in heavy-ion collisions, one should expect to create a state of deconfined quarks and gluons - the QGP - which, as it cools and expands, smoothly transitions into a shower of hadrons - a hadron gas.

QGP, born out of conditions thought to have first occurred naturally at the onset of our universe [13], is extremely short-lived. Indeed, because the conditions needed for its existence are so extreme, heavy-ion collisions can only generate QGP for $\sim 10^{-23}$ s [14]. With its lifetime being so small, direct evidence of its existence can not be gathered

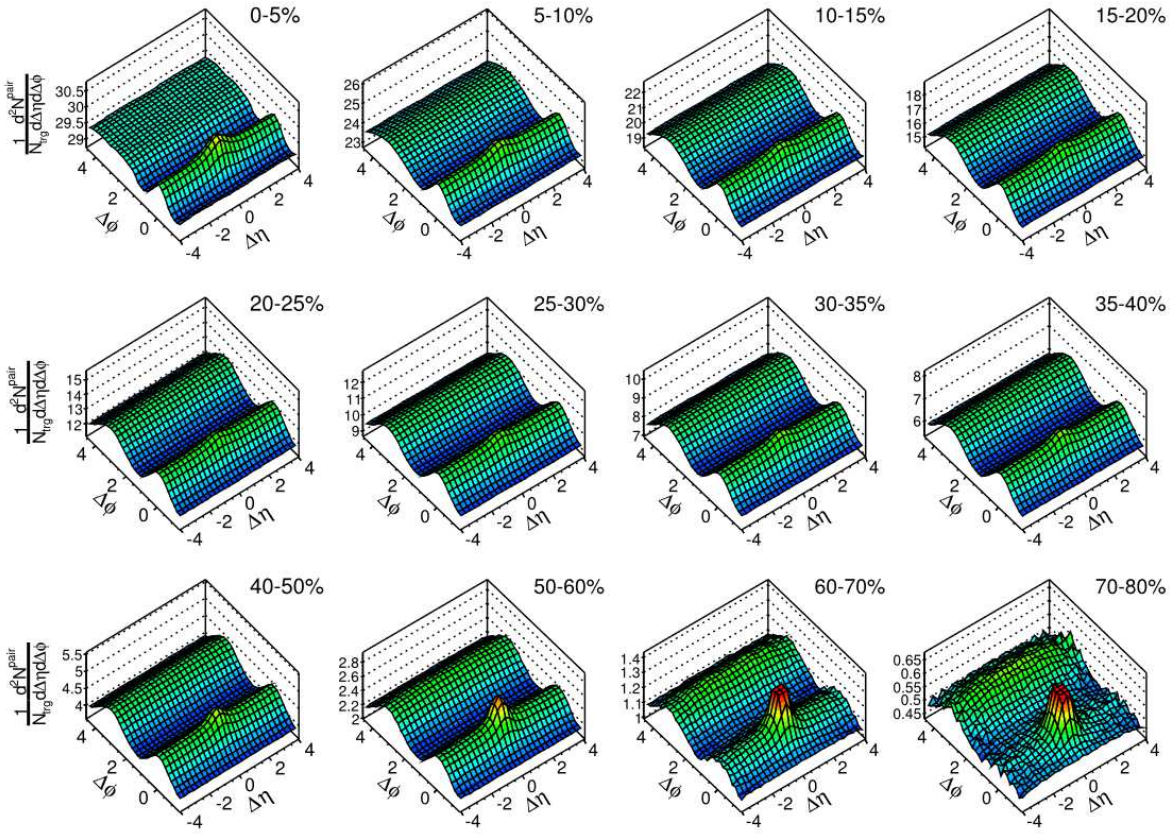


Figure 5: Particle pair production as a function of $\Delta\phi$, the azimuthal angle separation between the particles, and $\Delta\eta$, the separation in rapidity space. As we move to more and more peripheral collisions, the 'ridge' phenomenon becomes more apparent. Figure taken from Ref. [12]

in the lab; one must infer that the products of a given collision event - the hadron gas produced by the cooling QGP - have collective properties which are consistent with their constituent quarks and gluons having existed in a fluid-like state moments prior to their formation.

Figure 5 shows how particle pair production is correlated across centrality, azimuthal angle spread and rapidity space spread; we will provide precise and complete definitions of all of these quantities in due time, but for now, one must only understand the following:

- **Centrality** measures how much two colliding nuclei overlap, with 100% being a collision where both nuclei just missed one another, and 0% (conversely) representing collisions of two perfectly-aligned nuclei (refer to Section 2.3).

- **Azimuthal angle** $\phi$ is the emission angle of a given particle in the transverse plane ($x - y$ plane, perpendicular to the beam axis).

- **Rapidity** $\eta$ is the longitudinal variable of choice in heavy-ion collisions because it expands with time, allowing us to describe the QGP in its entirety, whether it is close to static in the longitudinal direction or moving close to the speed of light.

What Fig. 5 shows, then, is how correlated pairs of particles are across space. Starting with the upper-left-most panel (marked 0-5%) - the most central collisions analyzed in this experiment - we find a peak at $\Delta\eta \sim \Delta\phi \sim 0$. This peak is explained by quantum field theory, which dictates that the probability of particle emission be enhanced when two particles are collinear; one finds this same peak, with more or less definition, in all subsequent panels. Beyond this peak, the critical takeaway from this central panel is the flatness of the $\Delta\eta$ distribution, which implies that particles detected at the two opposite ends of the experimental apparatus have the same relative azimuthal angle as particles detected within a much narrower rapidity spread. This entails that particle emission follows global rules, exhibiting collectivity. This is a tell-tale sign that an intermediary phase guided by hydrodynamics exists. It also means that the momentum of each produced hadron is 'chosen' independently and at random.

Moving to different panels of Fig. 5, we find the same general features as the 0-5% panel, with one striking difference emerging as we progress to more peripheral collisions. While the 0-5% panel plateaus in the $\Delta\phi$ direction beyond $\Delta\phi = 2$, the other panels exhibit progressively clearer $\cos(2\Delta\phi)$ modulation; why should such a modulation appears as we move to more and more peripheral collisions. As explained briefly above, peripheral collisions are defined by the two nuclei not overlapping perfectly. This leads to an almond-shaped - or elliptical - overlap region in which the QGP will be generated. This anisotropic overlap region breaks azimuthal symmetry at initial time, which leads to differences in pressure gradients along the two major axes of the elliptic region. Pressure gradients in turn lead to tangible differences in the momentum distribution

of particles generated in the collision. This momentum anisotropy is measured by extracting the Fourier coefficients of the azimuthal angle of the particle distribution, i.e.

$$\frac{dN}{p_T dp_T dy d\phi} = \frac{dN}{2\pi p_T dp_T dy}\left(1 + \sum_{n=1}^{\infty} 2v_n \cos\left[n\left\{\phi - \Psi_R\right\}\right]\right). \tag{1.8}$$

Looking at the $n = 2$ coefficient - called the elliptic flow coefficient - we find $\cos\left(2\left(\phi - \Psi_R\right)\right)$, which, ignoring the event-plane angle $\Psi_R$, reminds us of the $\cos(2\Delta\phi)$ modulation we found in Fig. 5. As we will see in Chapter 4, Eq. (1.8) is not well-suited to extract actual flow coefficients, mostly because $\Psi_R$, the event plane angle, can not be determined experimentally. Nevertheless, Eq. (1.8) provides us with a basic intuition for why a modulation is observed in Fig. 5: an elliptical anisotropy in the overlap between the colliding nuclei will lead to measurable momentum anisotropies in the final state thanks to an intermediary phase of collective motion, referred to as hydrodynamics.

## 1.3 NUCLEAR STRUCTURE AND ANISOTROPY

In relating proofs of the existence of QGP, we introduced the idea of initial state overlap regions and the anisotropies they may exhibit. However, this discussion implicitly assumed that we were colliding nuclei described by spherical density distributions. Indeed, the idea that central collisions could not create elliptic flow implies that the overlap shape generated in these collisions is circular. Since central collisions occur when nuclei are perfectly overlapping, we are forced to conclude that the nuclei themselves are spherical, leading to a circular cross-section in the transverse plane.

However, as we will show in detail in Chapter 2, this picture of atomic nuclei is inaccurate for most species. The complex inner workings of nuclei are described by low-energy QCD interactions between their constituent quarks, interactions which are, as we have established previously, extremely hard to study experimentally and describe analytically. Nevertheless, the century-long quest to properly characterize and model atomic nuclei is still very much active. Our current understanding of the nuclear wavefunction and of the nucleons that constitute it is that, as a whole, they exhibit

rotational invariance, implying that their wavefunction should be spherically symmetric. However, this wavefunction is but a collection of underlying nucleonic states which, on their own, can break rotational invariance, but collectively form a rotationally invariant state. In other words, the Hamiltonian and its associated wavefunction *are* invariant, but the physical underlying states *are not*; nucleon-nucleon correlations, which are now known to be key parts of nuclear structure descriptions, inevitably lead to clustering and complex, asymmetric physical states, steering the field away from the simplistic view of spherical symmetry [15]. It should, therefore, be understood, as mentioned above, that *most* nuclei feature some deformed states, with their total wavefunction being comprised of fluctuations between all underlying states.

As we will explore in Chapter 2, low-energy experiments may have difficulty probing the underlying state instead of the total wavefunction. This complicates the task of characterizing the actual shape of a given nucleus, as low-energy experiments may only be capable of resolving the total wavefunction. Conversely, heavy-ion collisions, with their high energies, large longitudinal velocities, and, consequently, near-instantaneous interaction timescales, provide the perfect setting to probe these states, which spontaneously break rotational symmetry. Indeed, it is understood that the dominant fluctuations in nuclei exhibiting large deformation occur once every $10^{-21}$ s - timescales which are so small that one may be excused for calling them instantaneous. Low-energy probes are not suited for resolving rapidly shifting states; instead, they capture a coherent superposition of physical states. As established previously, a collision between two nuclei moving at relativistic speeds is comprised of different stages which, in all, last around $10^{-23}$ s, making them 100× shorter-lived than the typical nuclear fluctuation scales. This means that the colliding nuclei in heavy-ion collisions are not represented by the superposition of their underlying states, but rather by a single one of the physical states comprising their total wavefunction. This fact has considerable ramifications on the modelling of heavy-ion collisions, but also regarding what insights heavy-ion collisions provide: while we have described collider programs as being concerned with

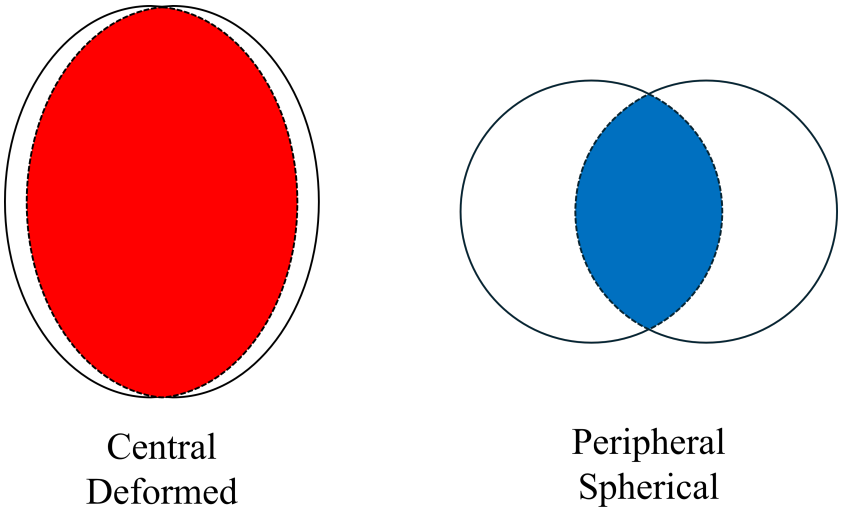


Figure 6: Schematic representation of a central collision between two deformed nuclei and a peripheral collision of spherically symmetric nuclei.

fundamental QCD, it turns out they can also serve as probes, helping us sharpen our understanding of low-energy nuclear matter!

To understand why this is, recall Fig. 5 - where we described elliptic flow as caused by spherically symmetric nuclei colliding off-center. Looking at Fig. 6, we find two schematic representations of collision events. On the left, we have a central collision of deformed nuclei, while, on the right, we have a peripheral collision of central nuclei. Recall that the latter's elliptic overlap region is the source of the $\cos(2\Delta\phi)$ modulation found in Fig. 5's panels showing results from more peripheral ($> 15\%$) collisions; the fact that this modulation was not found in the more central panels was explained by a conversely circular overlap shape between the two colliding nuclei. Figure 6 tells us that, in collisions of nuclei which present considerably deformed physical state fluctuations, one should expect to find signals of elliptic flow - caused by an elliptic overlap region - across *all* centralities. Furthermore, the scale of the elliptic flow in collisions involving fully overlapping deformed nuclei informs us on the effective shape of the underlying fluctuations, allowing us to infer the nuclear distributions that caused the specific geometrical conditions needed to produce such flow. Therefore, heavy-ion collisions and their extreme environments somewhat paradoxically provide unique tools

to resolve nuclear structure at a fundamental level, a problem which had, for a long time, been seen as belonging exclusively to low-energy nuclear physics.

## 1.4 THESIS PURPOSE AND ORGANIZATION

While studies of nuclear structure through the lens of heavy-ion collision modelling have been undertaken before, they were exclusively concerned with analyzing one or two 'observables' - experimentally detectable particle distribution properties - at a time. Without reproducing groups of observables simultaneously, these analyses open themselves up to questions regarding their calibration and specific tuning and whether or not their findings should be considered final. Furthermore, the use of models incorporating non-physically-motivated phases, especially before the hydrodynamic description of the QGP, suggests that these inquiries are more focused on feasibility than on fundamental physics at different scales.

This thesis, on the other hand, will show results produced using an end-to-end, state-of-the-art, physically-motivated hybrid model. This model is composed of, in order, IP-Glasma [16, 17], a model motivated by deep inelastic scattering experiments and their constraints on gluon saturation, which evolves pure color gauge fields using the Classical Yang-Mills (CYM) equations; MUSIC [18], a relativistic viscous hydrodynamics code developed at McGill, which has become the standard in our field; and, iSS [19, 20] and SMASH [21], Cooper-Frye sampling code and particle cascading codes respectively, which produce the observables which may then be compared to experimental results.

This comprehensive, physics-based approach will allow us to confidently infer which nuclear parametrizations appropriately reflect experimental results and, therefore, are accurate representations of the physical states fluctuating within the overall nuclear wavefunction. We will use our framework to analyze different systems at different energies. We will start by analyzing $^{238}$U and $^{197}$Au collisions at 193 GeV and 200 GeV respectively, comparing to experimental results gathered at RHIC. These results will provide a basis for the reliability and resilience of our model across many observables,

along with insights as to its sensitivity to initial state fluctuations caused by changes in nuclear structure parametrizations. We will then apply our findings to a new system and energy, namely $^{129}$Xe at 5.44 TeV, with the specific inclusion of longitudinal observables in our analysis. The inclusion of these new observables, along with the use of our physics-based model, will mark a new shift in the field's attempts to properly characterize stable nuclear matter at low- and high-energies. Furthermore, $^{129}$Xe is defined by the uncertainty surrounding its appropriate nuclear parametrization, allowing us to conduct an in-depth and wide-reaching study, which will fill a gap in the literature and allow for more precise analyses using better-informed parametrizations shortly, further pushing our knowledge and understanding of the various features of nuclear structure across atomic species. By using our unique model, we will provide reliable insights which may be used in future analyses.

This thesis is organized as follows: Chapter 2 introduces the theoretical underpinnings of nuclear structure studies and of high-energy nuclear parametrizations, along with a detailed description of the expected effects of structure features on specific observables. Chapters 3 and 4 detail our model's theoretical and numerical features in 2 dimensions, going from the initial state to the final state observables. Throughout, thorough investigations and explanations of the different features are provided. A detailed description of relevant observables is provided at the end of Chapter 4. Chapter 5 provides the combined results of $^{238}$U and $^{197}$Au and details how and what conclusions may be extracted from a wide and comprehensive collection of results. Chapter 6 explains how our model can be extended to include longitudinal dynamics in a way that preserves the critically consistent physical features that define our 2D model. It also contributes definitions of longitudinal observables which will be used in our $^{129}$Xe analyses. Chapter 7 shows the results from our first-of-its-kind detailed analysis of $^{129}$Xe results, sharing our insights and new constraints on the nuclear parametrization of this nucleus. The final chapter will synthesize and discuss the findings of our two studies, conclude, and give an outlook perspective for future work.

## 1.5 CONVENTIONS

Throughout this thesis, natural units, where $\hbar = c = k_B = 1$ are assumed unless explicitly noted otherwise. In SI units, these constants are the speed of light $c = 299\,792\,458\,\mathrm{m\,s^{-1}}$, the reduced Planck constant $\hbar = 1.054\,571\,817 \times 10^{-34}\,\mathrm{J\,s}$ and the Boltzmann constant $k_B = 1.380\,649 \times 10^{-23}\,\mathrm{J\,K^{-1}}$. In practice, one uses multiples of $\hbar c = 0.1973\,\mathrm{GeV\,fm} = 1$ to convert between distances and energies. This constant also allows for the reinstatement of SI units in given results. The mostly negative Minkowski metric $g^{\mu\nu} = (+, -, -, -)$ will be used throughout.

# 2

# NUCLEAR CONFIGURATIONS

Our description of heavy-ion collisions must begin with the components of nuclei: nucleons. While in experiments nucleons are part of a larger nuclear wavefunction and therefore have intricate properties, most simulations of heavy-ion collisions sample nucleons according to simple rules. The 'extent' of the nucleon is determined by the collision energy $\sqrt{s_{\mathrm{NN}}}$ which dictates the inelastic cross-section $\sigma_{\mathrm{NN}}$. Their positions, on the other hand, are sampled according to some density distribution $\rho(r)$. This process entails that the nuclei sampled in most simulated events are collections of independent nucleons. This idea, of course, is a simplification of the true nature of atomic nuclei and their wavefunctions, where correlations between nucleons play an important role in determining their shapes [22–24]. However, this simple picture has proven remarkably robust and fruitful, providing a simple and malleable framework that can incorporate and emulate features as needed.

## 2.1 SIMPLE WOODS-SAXON DISTRIBUTION

The density distribution $\rho(r)$ of choice is the Woods-Saxon distribution, which itself is taken from the two-parameter Fermi distribution,

$$\rho(r) = \frac{\rho_0}{1 + \exp\left(\frac{r - R_0}{a}\right)}. \tag{2.1}$$

It was first employed in electron-nucleus scattering experiments, characterizing multiple nuclear species across a wide range of atomic and mass numbers [25]. Because this is a nuclear density distribution, it must integrate to $A$, the atomic number of the nucleus

we are considering. Therefore, $\rho_0$ is a normalization factor - the normal nuclear density, and is $\approx 0.16\,\mathrm{fm}^{-3}$. $R_0$ and $a$ are the nuclear radius and the diffusiveness, respectively. The radius is, by construction, the distance from the center of the nucleus at which the density $\rho(r) = \rho_0/2$. The diffusiveness, on the other hand, controls the rate at which the density falls once one approaches and passes $r = R_0$. One of the shortcomings of this type of distribution comes with the fact that nuclei usually have a neutron skin, i.e. a neutron-rich outer layer [26, 27]. This fact therefore demands that neutrons and protons be sampled according to different distributions (mostly differing in diffusiveness $a$), and its omission from the basic Woods-Saxon picture can lead to tangible differences in certain observables, especially if experimental centrality classes rely on counting undeflected neutrons, like Zero Degree Calorimeters (ZDC) do [28].

Figure 7 shows 3 distinct but related Woods-Saxon distributions and their associated 2-dimensional projections which illustrate the impact of change $a$ and $R_0$. Because the Woods-Saxon distribution as presented in Eq. (2.1) is spherically symmetric, the 2D projections have trivial (i.e. no) dependence on the polar angle $\theta$. The distributions shown in Fig. 7 illustrate the effects of modifications to the two defining parameters, $R_0$ and $a$. The initial unmodified parameters are $R_0 = 6.37\,\mathrm{fm}$ and $a = 0.535\,\mathrm{fm}$, taken from Ref. [25], and are plotted in green. The blue distributions exhibit the effect of doubling the diffusiveness ($a = 1.07\,\mathrm{fm}$), while the red ones show that of increasing the nuclear radius by 40%, to $R_0 = 8.92\,\mathrm{fm}$. The latter's effects are noticeable, while those of the former appear more subtle; the increase in diffusiveness increases the likelihood of nucleons being sampled further from the center, even if the nuclear radius itself is unmodified. Indeed, the likelihood of finding a nucleon beyond $R_0$ essentially doubles, from 6% to 12%. On the other hand, the increase of $R_0$ creates a considerably larger sampling area which, at constant mass number $A$, entails a much less dense (or more diffuse) nucleus. However, it is essential to note that $R_0 \sim A^{\frac{1}{3}}$ and so, at fixed $A$, the nuclear radius should not be increased by as large a margin as was used here. Therefore, if one wants to decrease nucleon density (for a neutron-specific distribution), one usually only modifies the diffusiveness $a$. $R_0$ and $a$ being the only two modifiable parameters

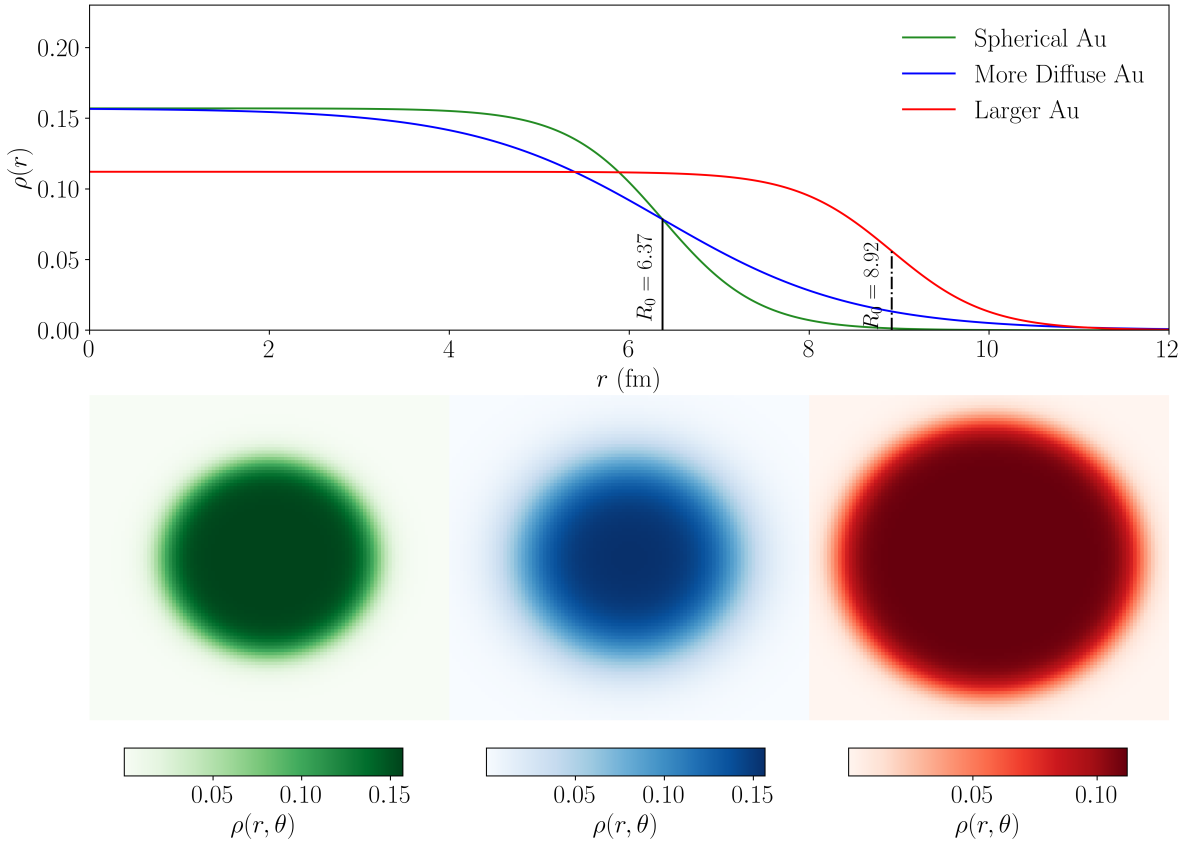


Figure 7: The Woods-Saxon distribution of spherically symmetric $^{197}$Au shown in **(top)** one- and **(bottom)** two-dimensions. The parameters for $^{197}$Au are taken from Ref. [25], with modifications made sequentially to $R_0$ and $a$ to show the impact of the nuclear radius and diffusiveness.

of the simple Woods-Saxon distribution, along with the physical limits imposed by the mass number on the nuclear radius, reveal its fundamentally limited nature.

## 2.2 NUCLEAR DEFORMATION

We now move on to the subject which is at the core of this thesis, nuclear deformity. We will first discuss direct experimental evidence of deformity, followed by the modifications to the Woods-Saxon distribution brought on by this deformity.

### 2.2.1 *Low-Energy Evidence of Deformation*

While today it is understood that most (if not all) nuclei are not perfectly spherically symmetric, determining the geometric shape of a nucleus experimentally remains impossible [29]. Indeed, nuclear deformation can only, at best, be deduced indirectly using models. What does one mean, then, when one says that a nucleus is deformed? Following discussions presented in Ref. [30, 31], deformity will mainly imply quadrupole deformation, which occurs when

$$\beta_2 \sim \left\langle Y_2^0(\theta,\phi) r^2 \right\rangle \propto \left\langle \left(3\cos^2(\theta) - 1\right) r^2 \right\rangle \neq 0, \tag{2.2}$$

i.e., when the nucleus' quadrupole moment $\beta_2$ does not vanish. This expression should be understood in terms of the nuclear wavefunction, with the brackets denoting its expectation value. Given this relationship to the wavefunction, we should be conscientious that descriptions of deformed nuclei as football- or rugby-shaped do not reflect the true nature of nuclei at low-energies. Indeed, many nuclei present evidence of a non-vanishing quadrupole moment alongside null total angular momentum $J$, the latter being indicative of rotational invariance. The rotational invariance measured in low-energy experiments is consistent with the fact that typical spectroscopic measurements are made on timescales which are much longer than the typical scale for fluctuations in the rotational degree of freedoms of the wavefunction [32]. Therefore, measurements made in such experiments capture a coherent superposition of wavefunctions in *all* orientations. By comparing data obtained in spectroscopic experiments to model calculations, we can extract information about the underlying geometrical properties of the nuclear wavefunction and, therefore, of the shape of nuclei themselves. With that in mind, model calculations replace nuclear wavefunctions, which may look spherically symmetric on timescales longer than those of typical rotational fluctuations, by rotational models. These models describe nuclei as ellipsoidal density distributions randomly oriented in space. Averaging over all directions preserves the rotational invariance of the system.

This approach necessitates the assumption that once the *actual* nuclear wavefunction collapses it follows the shape of one of these randomly oriented oblong configurations.

The quadrupole moment for even-even nuclei, introduced in Eq. (2.2), is related to the transition probability from the ground state to $2^+$, referred to as $B(E2)$, by [33]

$$\beta_2 = \frac{4\pi}{5ZeR^2}\sqrt{B(E2)}, \tag{2.3}$$

which comes from the general multipole moment $\beta_l$ definition, given below in Eq. (2.4), based on ground state electric transition rates $B(El)$,

$$\beta_l = \frac{4\pi}{(2l+1)ZeR^l}\sqrt{B(El)}. \tag{2.4}$$

Here, $R$ is the empirical nuclear radius ($= 1.2A^{\frac{1}{3}}$), $Z$ is the atomic number and $e$ is the fundamental electric charge. Equations (2.3) and (2.4) are only applicable under strict assumptions [34]. Furthermore, at first glance, this idea of $\beta_2$ as a parameter for oblong deformation may not seem obvious. However, it is well-defined geometrically. Indeed, taking a uniform ellipsoidal density $\rho(\vec{r})$ having the same quadrupole moment $\beta_2$ and same volume as a given nucleus, then [33–35]

$$\beta_2 = \frac{4\pi \int_{\vec{r}} r^2 \rho(\vec{r}) Y_2^0(\theta,\phi)\sin(\theta) dr d\theta d\phi}{3R^2 A}, \tag{2.5}$$

which itself is generalized for all $l$ as [36]

$$\beta_l = \frac{4\pi \int_{\vec{r}} r^l \rho(\vec{r}) Y_l^0(\theta,\phi) d^3r}{3R^l A}, \tag{2.6}$$

where $A$ is the mass number. Equation (2.6) is a strict geometric definition based on the nuclear density function $\rho(\vec{r})$. The relationship between Eqs. (2.4) and (2.6) is not immediately apparent. However, referring back to Eq. (2.2), we find that the moments are defined as expectation values of a multipole operator [33]. This multipole operator's matrix elements themselves are related to the transition rates $B(El)$, completing the link between the two seemingly unrelated formulas.

In any case, $\beta_2$ is both related to the shape of the density distribution of the nucleus *and* to transition probabilities. The geometric nature of Eq. (2.6) is a much more general definition which itself applies to any nucleus, contrary to Eq. (2.4) [34]. A spherical nucleus has $\beta_l = 0 \,\forall\, l$, while a deformed one takes $\beta_l \neq 0$ for some $l$. We have given general expressions for $\beta_l$, which may puzzle the reader given our focus on the quadrupole moment $\beta_2$. This focus is driven by the model we will introduce in Section 2.2.2, but does not mean that $\beta_l$ for $l > 2$ are irrelevant: their analysis in improving our understanding of nuclear structure is important. However, measurements of $B(El)$ for $l > 2$ are mostly inexistent, even for considerably deformed nuclei. Therefore, the modelling focus is generally set on $\beta_2$.

One must keep in mind the previous discussions regarding the *true* nature of nuclei as wavefunctions; imposing a definite value of $\beta_2$ to a specific nucleus is only justified within the confines of rotational models, and that certain species with more minor ($\beta_2 < 0.1$) deformation may be subject to considerable fluctuations in their shape [37]. Nevertheless, these are the foundations on which non-trivial nuclear structure is analyzed.

### 2.2.2 *Determining the Quadrupole Moment $\beta_2$*

Without precise measurements of the electric transition rate $B(E2)$, any modern theoretical calculation that wishes to shed light on fundamental nuclear structure will have to start with the nuclear wavefunction. However, large numbers of nucleons make the most fundamental version (i.e., solving the Schrödinger equation for the entire nuclear wavefunction) of this problem practically insoluble. Since independent particles and their wavefunctions have been studied in much detail, building a model where the foundational assumption is that nucleons are independent particles has proven to be a reasonable solution [38],

$$H|\Psi\rangle = E|\Psi\rangle \quad \rightarrow \quad \sum_i h_i|\Psi_i\rangle = \sum_i E_i|\Psi_i\rangle. \tag{2.7}$$

This is called the mean-field method, attributed to Hartree-Fock, and it may at first seem like an oversimplification of the problem at hand, given that it averages nucleon-nucleon interactions over all nucleons. However, nucleons are fermions, which means that the Pauli exclusion principle naturally keeps them apart. Furthermore, nucleons are fairly spread out at low energies within the nuclear volume [38]. Therefore, converting nucleon-nucleon interactions into a mean-field is a fair first approximation at low energies. These methods are now generally designated as Energy Density Functional (EDF) theories and have been used at length to provide insights on nuclear wavefunctions of all elements.

We will note here that this specific method cannot be used to extract $\beta_l$ for $l > 2$, given the specific assumptions of the model [15]. In the context of constraining the quadrupole moment $\beta_2$, EDF is generally used as follows:

1. Pick a value of $\beta_2$ that is sensible.
2. Find the ground state of the system $|\Psi_0\rangle$ at given value of $\beta_2$ using variational methods (i.e. minimize $\delta\left(\langle\Psi_0|(H-\mu\beta_2)|\Psi_0\rangle\right) = 0$ where $\mu$ is a Lagrange multiplier which forces the returned ground state to have quadrupole moment $\beta_2$).
3. Repeat for values of $\beta_2$ within a given range.
4. Build a curve of ground state energies E as functions of $\beta_2$.
5. Find where the minimum ground state energy lies.

The value of $\beta_2$ providing the smallest ground state energy is attributed to that nucleus. Luckily, given the persistent relevance of nuclear structure research, these types of calculations have already been made for practically all nuclei in Ref. [39], with the added specificity that their mean-field wavefunctions were expanded in the

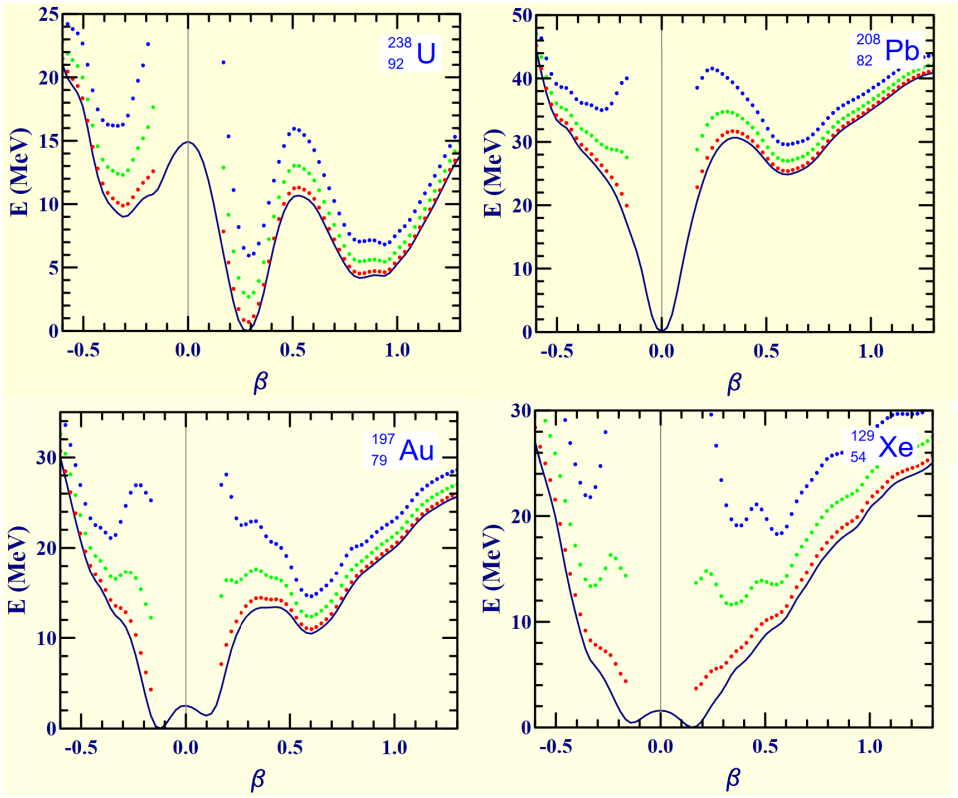


Figure 8: Potential energy surfaces as a function of $\beta_2$ (shown as $\beta$), calculated using Hartree-Fock-Bogoliubov framework, taken from Ref. [15]. The solid lines are the ground state energies, while the dashed lines present rotational energy corrections for spins $I = 8, 16 \,\&\, 24$.

quantum harmonic oscillator basis, which allows their solutions to break spherical symmetry while preserving axial symmetry, i.e. providing exclusively oblong shapes.

Fig. 8 shows the mean-field method applied in the context of determining the quadrupole moment of four isotopes, some of which will be important parts of this thesis' main results, namely $^{238}$U, $^{197}$Au and $^{129}$Xe. This collection of isotopes spans all geometric subtypes of nuclear distributions allowed by the mean-field calculation as undertaken in Ref. [15]: $^{208}$Pb is undeformed, and $^{238}$U is heavily deformed and prolate. We will note the great concordance between this relatively simple model and experimental data. Indeed, $^{238}$U is an isotope that subscribes to the strict assumptions guiding Eqs. (2.3) and (2.4) [40]; using $B(E2) = (12.19 \pm 0.62)\ \mathrm{e}^2\mathrm{fm}^4$ [41], one obtains

$\beta_{2,U} = (0.287 \pm 0.007)$, which is consistent with the minimum found in the upper left panel of Fig. 8.

$^{129}$Xe and $^{197}$Au, on the other hand, provide an unclear picture. They have neighboring minima on both sides of $\beta_2 = 0$, which indicates that these nuclei do not, according to the mean-field method, have a well-defined shape. These two isotopes embody the fundamental limitations of the EDF approach and of trying to attribute a definite shape to wavefunctions. While both $^{129}$Xe and $^{197}$Au present the same level of uncertainty concerning their true minima, the qualitative features of their respective potential curves provide discerning information: the broadness of the $^{129}$Xe curve implies that the shape of its distribution is subject to even more fluctuations than that of $^{197}$Au.

This uncertainty (or 'fuzziness') regarding the shape of these nuclei is precisely why using results from heavy-ion collisions to extract signals of deformity is important to the future of nuclear structure research. As mentioned at the onset of this section, low-energy experiments' temporal resolution are much longer than that of the usual rotational fluctuations of a nuclear wavefunction, leading to 'images' of nuclei actually representing rotational averages. Heavy-ion collisions, on the other hand, provide much shorter 'exposure times' than low-energy scatterings. Indeed, the initial impact lasts $\sim$ 10000 times less than the rotational fluctuation time scales of nuclear wavefunctions [32]. In the right conditions, as we will show in Section 2.3.2, we gain access to an overlap region whose shape directly mirrors those of the colliding nuclei. Therefore, tensions in nuclear structure theories, if they exist, may only be resolved through combining low- and high-energy data into a coherent picture of atomic geometry. The most general and permissive of approximations are, however, clear: nuclear deformation exists and is a defining characteristic of some (if not most) nuclei.

### 2.2.3 *Deformed Woods-Saxon*

Now that we have reviewed evidence of nuclear deformity, we can modify Eq. (2.1) to produce deformed nuclei that break spherical symmetry in different ways. To do so, we add angular dependencies to the nuclear radius $R_0$,

$$R_0 \rightarrow R(\theta,\phi) = R_0\left(1+\sum_{l=2}^{l_{max}}\sum_{m=-l}^{l}\tilde{\beta}_l^m Y_l^m(\theta,\phi)\right). \tag{2.8}$$

Here, the $\tilde{\beta}_l^m$ are real-valued coefficients of deformation which, if non-zero, induce dependency upon the polar and azimuthal angles via the spherical harmonics $Y_l^m$. By definition, the spherical harmonic $Y_l^m$ is dependent on the Legendre Polynomial $P_l^m(\cos(\theta))$,

$$Y_l^m(\theta,\phi) = \sqrt{\frac{(2l+1)}{4\pi}\frac{(l-m)!}{(l+m)!}}P_l^m(\cos(\theta))e^{im\phi}, \tag{2.9}$$

which itself has the following property relating $P_l^m$ to $P_l^{-m}$,

$$P_l^{-m}(x) = (-1)^m\frac{(l-m)!}{(l+m)!}P_l^m(x). \tag{2.10}$$

Therefore, Eqs. (2.9) and (2.10) imply that

$$Y_l^{-m}(\theta,\phi) = (-1)^m(Y_l^m(\theta,\phi))^*, \tag{2.11}$$

which in turn leads to the conclusion that $Y_l^m + Y_l^{-m}$ is real for even-$m$ and imaginary for odd-$m$. $R(\theta,\phi)$ being, by definition, a real-valued function, means that odd-valued $m$ are not permitted and that coefficients obey $\tilde{\beta}_l^m = \tilde{\beta}_l^{-m}$.

Before going any further, it is important to underline that the deformation parameter $\beta_l$ defined in Eqs. (2.4) and (2.6) is related, but not equal to any of the $\tilde{\beta}_l^m$ defined above. Indeed, the former are related to expectation values of operators over the entire nuclear

volume, while the latter describe the deformation of the nuclear surface [36]. Definite expressions linking the two quantities exist, but are tedious to extract [42]. Here is one such expression, generated by taking a combined power series of $\tilde{\beta}_l^m$ and $\frac{a}{R_0}$, in the limit of a sharp nuclear profile (i.e. $a \to 0$) [36]:

$$\beta_2 = \frac{R_0^2}{R^2}\left(\tilde{\beta}_2^0 + \sqrt{\frac{20}{49\pi}}(\tilde{\beta}_2^0)^2 + \frac{12}{7\sqrt{\pi}}\tilde{\beta}_2^0\tilde{\beta}_4^0\right), \tag{2.12}$$

where $R_0$ is the nuclear radius of the Woods-Saxon distribution and $R$ is the empirical nuclear radius. This small contrast between the two groups of quantities heightens the tension (and, at times, confusion) between low- and high-energy conceptions of deformity. Equation (2.12) indeed shows that in the presence of a small hexadecapole Woods-Saxon parameter $\tilde{\beta}_4^0$, the gap between the nuclear quadrupole moment and the Woods-Saxon quadrupole deformation parameter can become relatively large. Other non-zero Woods-Saxon deformation parameters $\tilde{\beta}_l^m$ can contribute to furthering this difference between the two quantities.

The radius function described in Eq. (2.8) is inserted in lieu of $R_0$ in the unmodified Woods-Saxon distribution Eq. (2.1),

$$\rho(r,\theta,\phi) = \frac{\rho_0}{1+\exp\left(\frac{r-R(\theta,\phi)}{a}\right)} \tag{2.13}$$

This is the distribution that is used to sample nucleons within deformed nuclei. Figure 9 shows the effects of inserting $R(\theta,\phi)$ into the unmodified Woods-Saxon distribution. When deformed Woods-Saxon parametrizations only have $m = 0$ non-zero components, they do not depend on the azimuthal angle $\phi$. Therefore, building their 3-dimensional surfaces from the 2D cross-sections (like those shown in the bottom of Fig. 9) simply requires revolving the cross-sections through $\phi$. However, when parametrizations involve non-zero $\tilde{\beta}_l^m$ with $m \neq 0$, Eq. (2.9) dictates that the resulting radius function depends on $\phi$. Therefore, the cross-section of $^{197}$Au shown in the bottom-middle panel of Fig. 9 is evaluated at $\phi = \frac{\pi}{2}$. Changing the value of $\phi$, as is

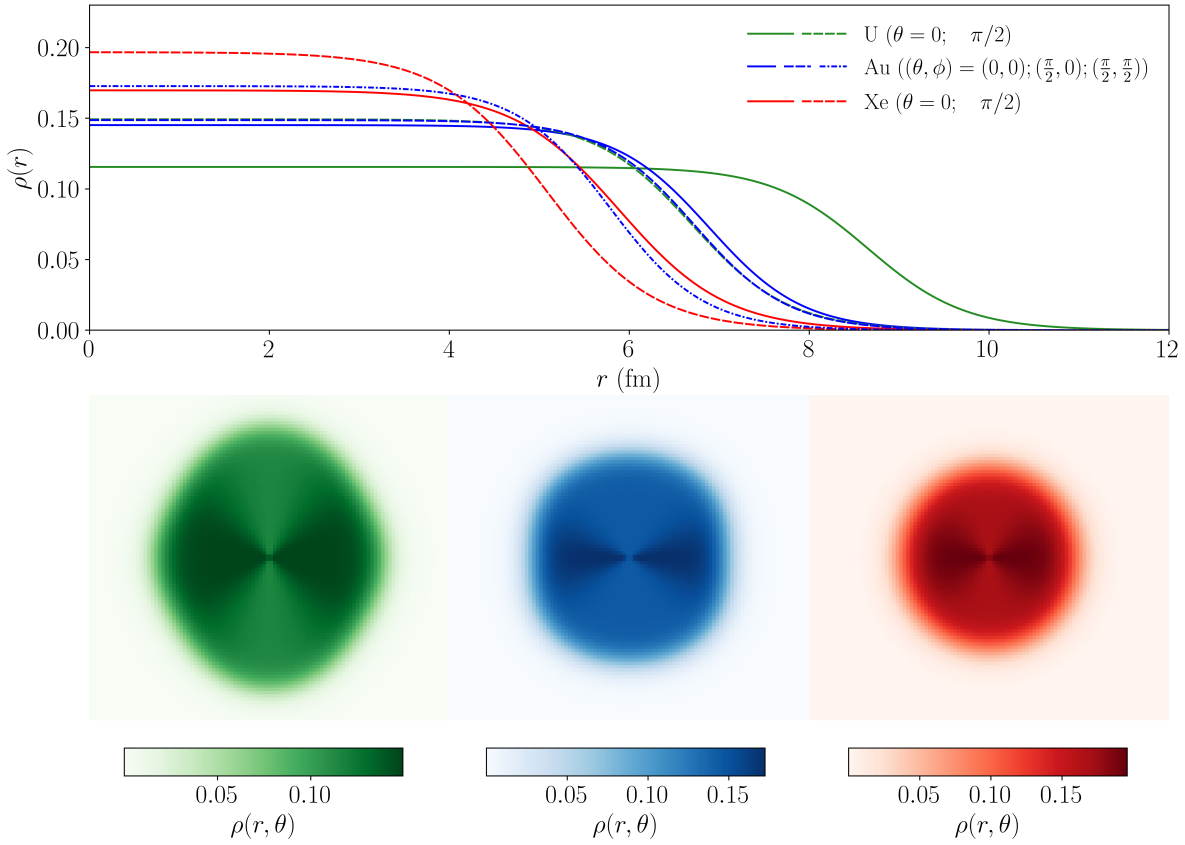


Figure 9: The Woods-Saxon distribution of deformed $^{238}$U, $^{197}$Au and $^{129}$Xe shown in **(top)** one- and **(bottom)** two-dimensions. The parameters for $^{238}$U and $^{197}$Au are taken from Ref. [36], while $^{129}$Xe parameters are taken from Ref. [43]. $^{238}$U and $^{129}$Xe are represented by 2 curves each, one taken at $\theta = 0$ and the other at $\theta = \frac{\pi}{2}$. $^{197}$Au, on the other hand, requires 3 curves, as it also depends on the azimuthal angle $\phi$ thanks to its non-zero $\beta_2^2, \beta_4^2$ and $\beta_4^4$ parameters. The details of the parametrizations can be found in Table 1.

apparent in the collection of blue curves in the top panel of Fig. 9, changes the density function appreciably; at $\phi = 0$, the deformity of the nucleus is barely apparent, with the radius function only varying by approximately 2% across $0 \leq \theta \leq \frac{\pi}{2}$. Comparatively, at $\phi = \frac{\pi}{2}$, the radius varies by 20% within the same $\theta$ range.

Beyond these secondary parameters, the hexadecapole parameter $\tilde{\beta}_4^0$'s sign has a significant effect on the qualitative shape of the cross-sections. Indeed, referring to Table 1, one notices that both $^{197}$Au and $^{129}$Xe have negative $\tilde{\beta}_4^0$, while $^{238}$U's is positive.

| | $R_0$ (fm) | $a$ (fm) | $\tilde{\beta}_2^0$ | $\tilde{\beta}_2^2$ | $\tilde{\beta}_4^0$ | $\tilde{\beta}_4^2$ | $\tilde{\beta}_4^4$ |
|---|---|---|---|---|---|---|---|
| $^{238}$U | 7.068 | 0.538 | 0.247 | 0 | 0.081 | 0 | 0 |
| $^{197}$Au | 6.62 | 0.519 | 0.098 | 0.076 | −0.025 | −0.018 | −0.018 |
| $^{129}$Xe | 5.36 | 0.559 | 0.161 | 0 | −0.003 | 0 | 0 |

Table 1: Woods-Saxon parameters used for $^{238}$U, $^{197}$Au and $^{129}$Xe nuclei in Fig. 9. The parameters are from Ref. [36] for $^{238}$U and$^{197}$Au and Ref. [43] for $^{129}$Xe.

Referring back to Fig. 9, one can see that $^{238}$U's cross-section is more 'diamond-shaped', while the two others are more 'pill-shaped'. While these are interesting qualitative features, results presented in later parts of this thesis will show that discerning between the two shapes through heavy-ion collision observables is, at least for now, difficult to achieve.

It is also interesting to recall the discussion regarding $^{197}$Au and $^{129}$Xe's ambiguous status with regards to mean-field calculations. Indeed, in Section 2.2.2, we showed that these isotopes have subtle deformations which probably manifest themselves as fluctuations in their shapes. While their respective Woods-Saxon distributions are static in nature, their relatively faint deformations allow for fluctuations to play a major role in their final 'perceived' shape, especially in the context of heavy-ion collisions. Indeed, looking at $^{197}$Au, the dependency of its Woods-Saxon distribution $\rho$ on $\phi$ brings about unique fluctuations in its cross-sectional shapes. Then, looking at $^{129}$Xe, its more subtle quadrupole deformation along with its relatively small number of nucleons means that the nuclei generated through sampling its Woods-Saxon distribution will exhibit greater fluctuations on a nucleus-to-nucleus basis. Indeed, statistical fluctuations in nucleon samplings are proportional to $\frac{1}{\sqrt{A}}$, where $A$ is the atomic mass number.

Up to this point, our discussions have focused solely on single-nucleus distributions. However, heavy-ion collisions involve collisions of *two* nuclei. How, then, can single-nucleus density distributions be extracted from collision events between two nuclei?

## 2.3 OVERLAP SHAPES

When two nuclei's paths intersect in a collider experiment, their alignment has a major impact on the results of a given collision event. By alignment, one usually thinks of how off-center the projectile nucleus 'appears' to the target nucleus. However, in experiments, it is impossible to determine the geometric alignment of two colliding nuclei. Therefore, experimentalists must resort to looking at the amount of particles generated in a given event (called that event's 'charged particle multiplicity', $N_{\mathrm{CH}}$) to determine which collisions were 'head-on' (or central) and what others were more peripheral. Other methods are available to experimentalists, but are more limited in scope. Zero Degree Calorimeters (ZDC), mentioned previously, constitute one such method. However, its scope can be quite limited and can lead to erroneous conclusions about a given event. Indeed, given ZDCs only detect neutrons, and that neutrons have a tendency of being found further away from the nuclear core than protons, ZDCs can have a difficult time differentiating between types of peripheral events. Therefore, most experiments determine centrality via multiplicity. The centrality $c$ of an event with charged particle multiplicity $N_{\mathrm{CH}}$ is given by

$$c = 1 - \int_0^{N_{\mathrm{CH}}} P(N)dN \tag{2.14}$$

i.e. the cumulative distribution of $N_{\mathrm{CH}}$. Figure 10 shows $P(N_{\mathrm{CH}})$, the multiplicity probability density function. It also provides schematic representations of the general collision types represented on the different regions of the curve. We find that moving from central $(0-5\%)$ to more peripheral $(30+\%)$ centralities implies looking at collisions where the overlap between the colliding nuclei gets smaller. This overlap is controlled by the impact parameter. As theorists and modelers, we have access to and control over information about the pre-collision phase that experimentalists do not. For instance, nucleon distribution of a colliding nucleus, obtained through sampling the Woods-Saxon distribution. For another, the exact impact parameter used in a given collisions.

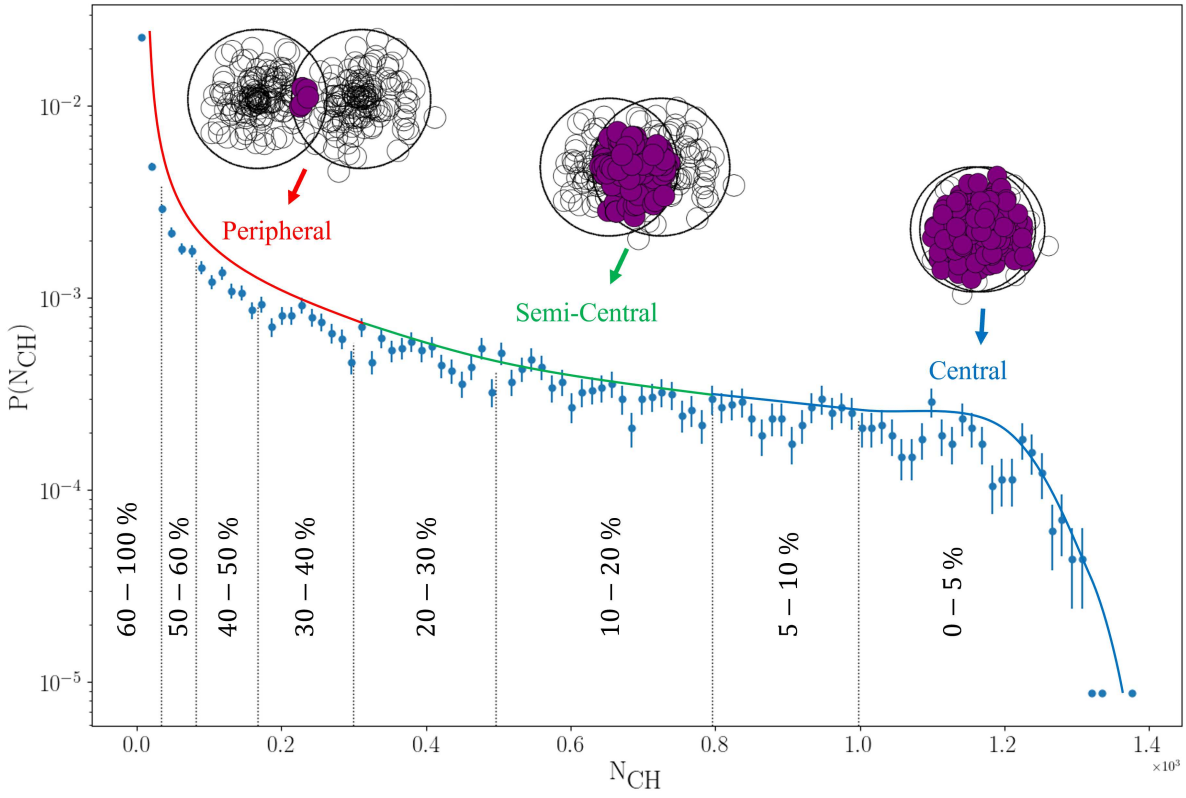


Figure 10: Relative frequency histogram of charged particle multiplicities $N_{\mathrm{CH}}$ recorded in simulations of minimum-bias collisions of $^{129}$Xe. Schematic representations of collisions of $^{129}$Xe associated to each region of the histogram are provided.

### 2.3.1 *Impact Parameter*

The impact parameter $b$ is the distance separating the centers of the colliding nuclei. The larger the $b$, the more peripheral the event; $b = 0$ fm is a head-on collision. In our simulations, $b$ is sampled at initialization according to

$$\frac{2bdb}{b_{\mathrm{max}}^2 - b_{\mathrm{min}}^2} \tag{2.15}$$

where $b_{\mathrm{min/max}}$ designate the minimal and maximal desired impact parameter; $b_{\mathrm{min}}$ is usually 0 fm, while $b_{\mathrm{max}}$ must be determined based on needs and on system size. For our $^{238}$U and $^{197}$Au runs presented in Chapter 5, $b_{\mathrm{max}}$ was set at 8 fm since our interest in those cases was directed towards ultra-central collisions, while for our $^{129}$Xe

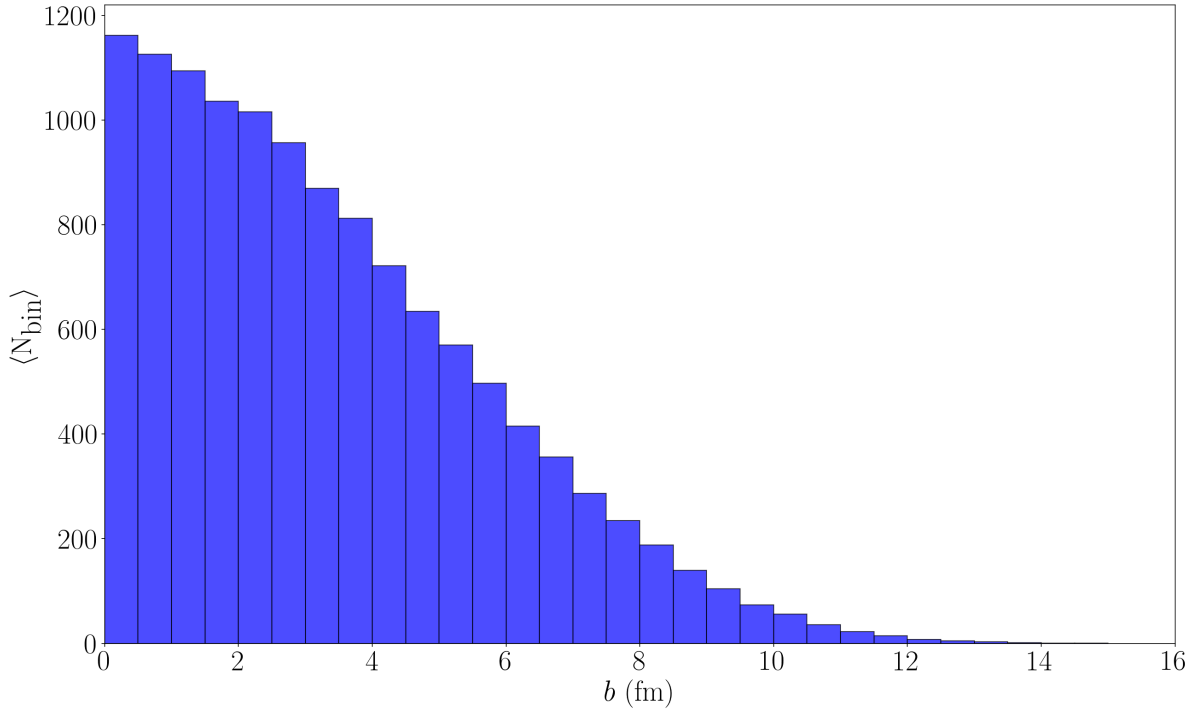


Figure 11: Average number of binary collision per event $\langle N_{bin} \rangle$ as a function of impact parameter $b$, for $^{129}$Xe collisions. As we progress towards larger $b$, we find fewer binary collisions, until practically no binary collisions are found beyond $b = 15$ fm.

runs, it was set to 15 fm. The larger impact parameters were chosen to produce so-called 'minimum-bias' sets of events: a set of events comprised of every possible general overlap configuration, from fully head-on collisions ($b = 0$ fm) to full misses ($b \sim 15$ fm for $^{129}$Xe). This allows for direct reproduction of the entire multiplicity spectrum, which leads to a more accurate and complete reproduction of reality, at the cost of more computation. To determine the upper limit for our $^{129}$Xe runs, we generated 10000 sample nuclei pairs along with randomly sampled $b$ and calculated the number of binary collisions for each sampling, using $\sigma_{NN} = 79$ mb $= 7.9$ fm$^2$, which is consistent with a beam-energy of 5.44 TeV. Figure 11 shows the results of our impact parameter range analysis, which led us to select $b_{max} = 15$ fm.

Beyond being an excellent measure of collision centrality, the impact parameter is directly related to the shape of the overlap between the two colliding nuclei, or what we usually call 'initial state anisotropies'.

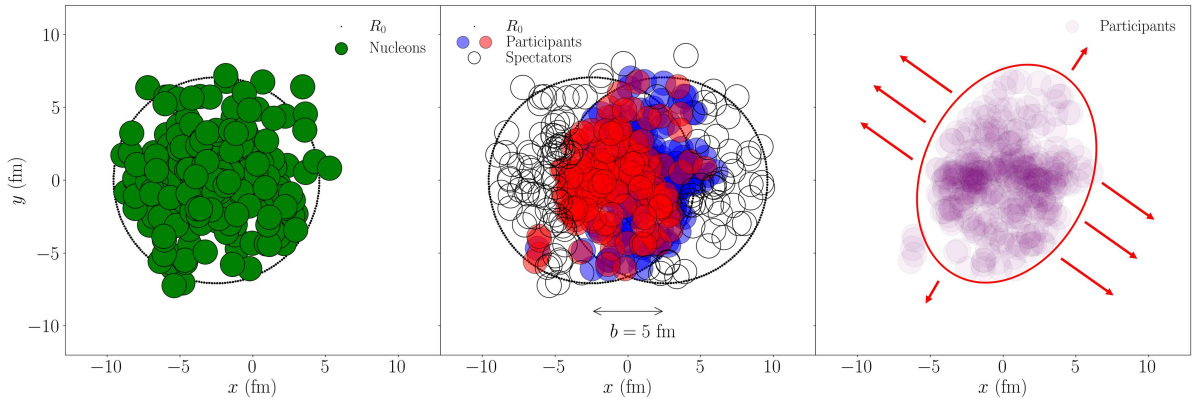


Figure 12: Transverse plane view of (**left**) a single undeformed nucleus via its sampled nucleons; (**middle**) the resulting collision between two undeformed nuclei sampled from the same distribution; and (**right**) the interaction region produced by participating nucleons. In the **left** and **middle** panels, the Woods-Saxon $R_0$ is represented by a black line. In the **right** panel, the interaction region is surrounded by an ellipse to represent the general shape of the interaction region, with arrows schematically representing the resulting flow. The impact parameter $b$ was set to 5 fm.

### 2.3.2 *Initial State Anisotropies*

When two spherically symmetric nuclei collide with one another, their overlap produces a shape which has a substantial effect on the subsequent evolution of the interaction region (to be discussed in more detail in Chapter 4. As we will see, isotropic interaction regions in the initial stage expand symmetrically in the hydrodynamics stage. Anisotropic (usually elliptically-so) overlaps, on the other hand, tend to have build-ups of momentum which are roughly proportional to $1/R$, with $R$ being the transverse size of the interaction region [44]. Therefore, elliptical interaction regions will lead to larger flow buildups along their short axes when compared to flow along their long axes. This anisotropy in the flow velocitiy is directly translated into anisotropies in final-state particle momentum distributions. Indeed, anisotropic initial states and their resulting momentum anisotropies mean that the energy of the medium is distributed asymmetrically, leading to particles hadronizing more in certain directions than others, leading in turn to measurable anisotropies in the distributions of their azimuthal angles $\phi$ in the

transverse plane. This fact and its corresponding observables will be discussed in detail in Section 4.3.

Figure 12 shows a semi-peripheral collision of two spherically-symmetric versions of $^{238}$U (i.e. setting all $\tilde{\beta}_l^m = 0$). As we can see, an elliptic overlap region is formed and would lead, following our previous explanations, to more flow along the ellipse's short axis. Figure 12's right panel also provides a further qualitative assessment of the density of nucleons along the beam axis. Indeed, given the transparency of the nucleon markers, darker pockets of participants are meant to convey a relatively large nucleonic density in said pocket. This will be an important idea which we will revisit in section Chapter 3. As should be clear by now, spherically symmetric nuclei are predictable when it comes to the overlap shapes they produce. Figure 13 clarifies this idea further. Indeed, we find 3 collision events stemming from identical nucleon samplings simply shifted along the $x$ direction by various values of the impact parameter $b$. We see that, in central collisions ($b = 0$ fm), the overlap region is more or less circular: very small amounts of anisotropy in the initial state means we do not expect any meaningful anisotropy in the final state. In mid-central collisions ($b = 3$ fm), we find a small but noticeable anisotropy. This would lead to a detectable (even if slight) signal in the produced particles. Finally, in peripheral collisions ($b = 10$ fm), we find a small interaction region presenting clear ellipsoidal anisotropy, which would lead to an unmistakable signal in the produced particles.

At this point, it is important to keep in mind that while anisotropy increases with impact parameter $b$, multiplicity progresses the opposite way: less overlap (and, therefore, binary collisions) usually means smaller numbers of generated particles in the final state. This means that types of collisions are fairly well-defined for spherical systems: one has high multiplicity, low anisotropy collisions at one end of the spectrum, and low multiplicity and high anisotropy at the other. This also means that these high initial anisotropy events are subject to higher levels of event-to-event fluctuations than events at the other end of the spectrum. Indeed, given the reduced size of the interaction region

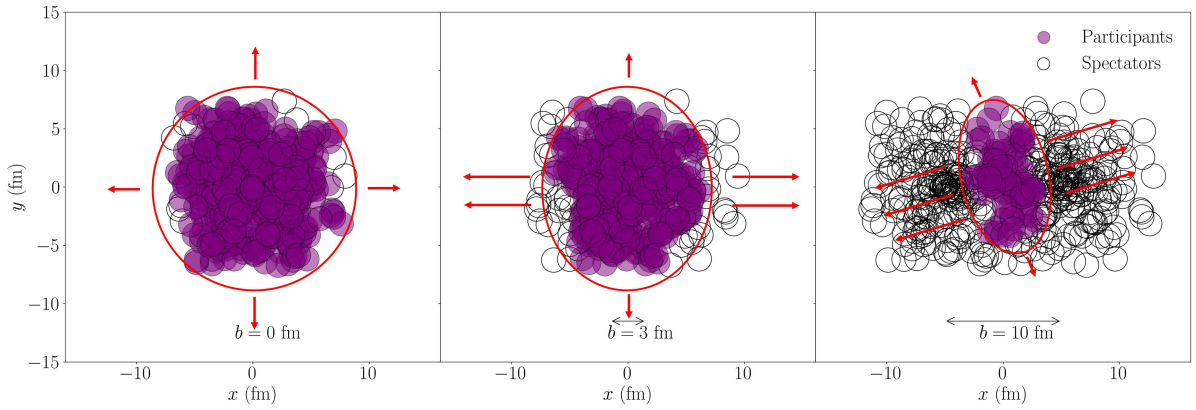


Figure 13: Transverse plane view of 2 nuclei colliding at (**left**) $b = 0$ fm; (**middle**) ; $b = 3$ fm; and (**right**) $b = 10$ fm. As we move to larger impact parameters, collisions produce more and more elliptic overlap regions.

and the reduced number of interacting nucleons, each nucleon and its position has a greater effect on the final state than interacting nucleons in central collisions do.

What makes deformed nuclei such interesting systems in heavy-ion collisions is the simple fact that non-trivial anisotropies can be generated at practically *all* impact parameters $b$. Indeed, deformed nuclei can overlap in eccentric shapes at even the smallest $b$. Figure 14 makes this strikingly clear. The top panels of Fig. 14 show a collision event where the long axes of both nuclei are aligned with the beam axis. These events are usually designated 'tip-tip'. The bottom panels, on the other hand, show a 'body-body' event: both nuclei's short axes are aligned with the beam axis, and their long axes are aligned with one another. The differences in their resulting anisotropies (or lack thereof) is marked. Indeed, body-body collisions present large amounts of elliptic anisotropies, while tip-tip collisions are isotropic in the transverse plane. However, given they result from setting $b = 0$ fm, both collisions will produce large enough amounts of particles in their final states to belong to the upper few percents of collisions in terms of centrality. There will, however, be noticeable differences between the two events given the orientations of the colliding nuclei.

As we had done for Fig. 12, the participating nucleon markers of the right panels of Fig. 14 are purposefully transparent to provide a qualitative idea of nucleon density. We

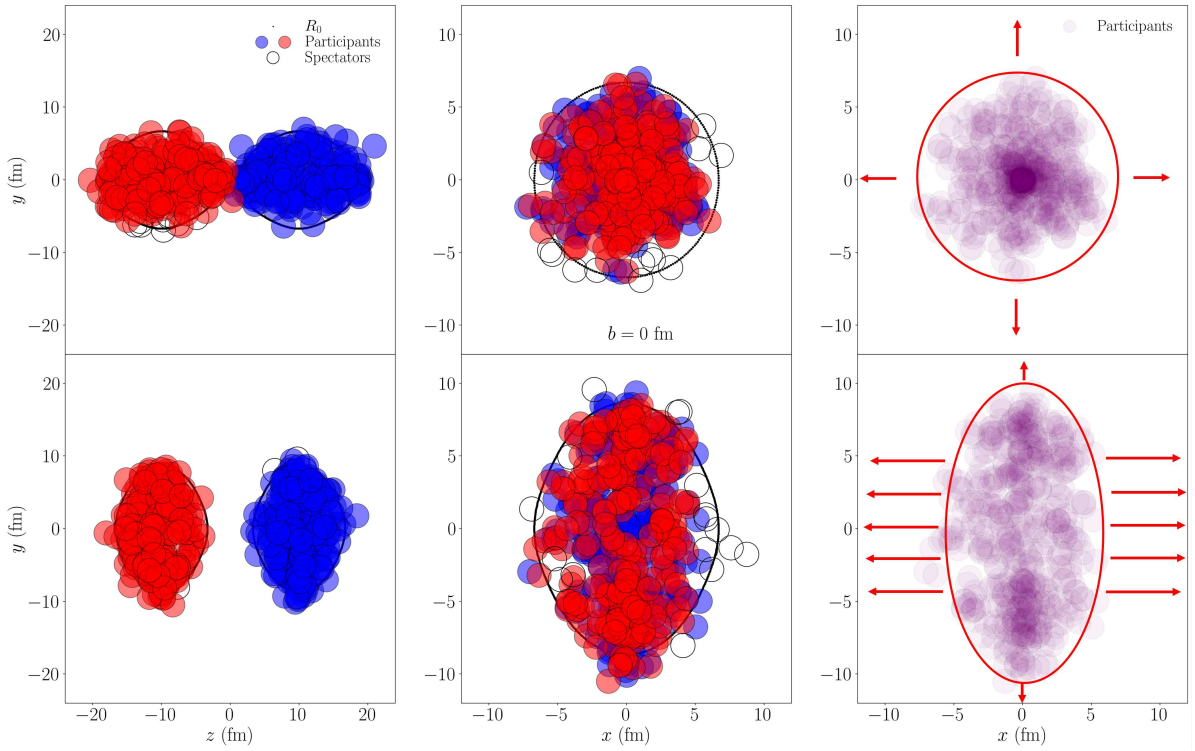


Figure 14: Commonly named (**top**) Tip-Tip and (**bottom**) Body-Body collision events of deformed $^{238}$U presented 3 ways. (**left**) 'Overhead' view of the pre-collision configuration, with the beam axis ($z$) replacing the usual $x$-axis; (**middle**) tranverse plane view of the collision event; and (**right**) the interaction region produced by participating nucleons. In the **left** and **middle** panels, the Woods-Saxon $R_0$ is represented by a black line. In the **right** panel, the interaction region is surrounded by an ellipse to represent the general shape of the interaction region, with arrows schematically representing the resulting flow.

find that tip-tip collisions have extremely dense interaction regions, especially at their cores. Body-body collisions, comparatively, do not present any pockets which are as dense as the central pocket of the tip-tip collision. Therefore, when colliding 2 largely deformed nuclei (like $^{238}$U), there will be clear signals of their deformity in the most central centrality classes. However, with more subtle deformities (such as those of $^{197}$Au and $^{129}$Xe), those signals themselves become more subtle. The point remains, however, that non-spherically symmetric collisions present increased variance in overlap shapes

in central and mid-central collisions, as their asymmetric distribution of geometries provides extra degrees of freedom from which anisotropies can originate.

A final important observation to make here is that of the specific size and shape of the interaction region of fully-aligned (i.e. body-body and tip-tip) collisions of spherical and deformed nuclei. Figures 13 and 14 show that in collisions at $b = 0$ fm, the overlap region clearly reflects the value of $R_0$ (for spherical nuclei) or $R(\theta, \phi)$ (for deformed nuclei) in the transverse plane. Therefore, linking the exact shape of the nuclear density distributions from initial to final state is actually possible, with final-state observable effects in central collisions being directly proportional to the Woods-Saxon radius.

# 3

# PRE-EQUILIBRIUM EVOLUTION

As mentioned before, QGP is a nearly perfect fluid, allowing us to model it using relativistic viscous hydrodynamics. However, for hydrodynamics to apply, the system in question must be at (or close to) thermal equilibrium. In heavy-ion collisions, directly after the collision event, the interaction region is highly excited and far from equilibrium. Therefore, one must include some form of a *thermalization* phase to bridge the gap between the collision event and the time where hydrodynamics becomes applicable, which is $\sim O(1\,\text{fm})$. Historically, some purely phenomenological pre-equilibrium models, such as MC-Glauber [45] and TRENTo [46], have been used to produce surfaces which were in thermal equilibrium and ready to be evolved hydrodynamically. MC-Glauber is a wounded nucleon model, meaning that the initial energy deposit is directly proportional to some combination of the number of participants and the number of binary collisions. TRENTo is in some ways a generalization of MC-Glauber; it provides means through which the initial energy deposit can be modulated so that it isn't just a linear combination of the number of participants and the number of binary collisions, and so the energy deposit function's form is itself a parameter of the model. TRENTo , contrarily to MC-Glauber, includes some simple pre-equilibrium flow [16]. However, while both models have been successful in their own rights, neither is fully grounded in first-principles thinking. Furthermore, avoiding treating this phase with a firm QCD-based model somewhat undermines the stated goal of studying heavy-ion collisions theoretically, i.e. to build a physically representative model of QCD which can explain the different phases of hadronic matter in extreme conditions. While simple initial conditions models like MC-Glauber have found success in describing event-averaged

quantities like integrated elliptic flow $v_2$, they are unable to produce differential distributions of these quantities that are consistent with experimental data [47]; these models are generally exclusively geometric in nature and lack, as stated above, any realistic approach to pre-equilibrium dynamics and evolution. That is why IP-Glasma [16, 17], a physically-motivated initial state model, has had success in describing a wide range of differential observables [47, 48] and of observables involving higher order correlations [1, 17]. While IP-Glasma integrates the simple geometrical features that made MC-Glauber successful in some respects, it goes far beyond counting binary collisions.

In the following sections, we will introduce the theoretical underpinnings of the boost-invariant (or 2D) formulation of IP-Glasma. We will first discuss Color Glass Condensate (CGC) theory, and how it applies to heavy-ion collisions. We will then use the theoretical prescription of the CGC to introduce the concept of gluon saturation at low momentum fraction and how it relates to the initial color charge distributions. These distribution, which will need to be sampled according to a specific fluctuation scale, will act as sources for the color gauge fields $A_\mu$, which happen to be the intrinsic degrees of freedom of the pre-equilibrium phase. We will then show how the Classical Yang-Mills equations apply to the color gauge fields, and we will provide detailed evolution equations for all degrees of freedom. Throughout, we will relate these continuum theories and properties to their equivalents on a discrete lattice: because we are ultimately running simulations, numerical methods are as important to IP-Glasma as its underlying theories in the continuum limit. For now, let us introduce the fundamental concept from which all of IP-Glasma is sourced: the Color Glass Condensate.

## 3.1 COLOR GLASS CONDENSATE

The Color Glass Condensate (CGC) provides an *effective* description of a single, fast-moving nucleus composed of valence and sea quarks, as well as gluons. CGC, as we will show, maintains that at low momentum fraction, or 'small-$x$', hadronic matter is almost entirely gluonic. This fact births an *effective field theory*, which allows us to

only take into account the degrees of freedom - here, gluons - which are relevant to our system. This discussion will be condensed and to the point; for a more detailed treatment of the assumptions, results and consequences of using the CGC theory, one should consult Refs. [49–53].

CGC separates partons based on their momentum fraction $x$,

$$x = \frac{p_{\text{part}}}{P_{\text{N}}}, \tag{3.1}$$

i.e., the fraction of the nucleonic momentum $P_{\text{N}}$ that they carry. A priori, these partons can be quarks or gluons. To separate between hard (large-$x$) and soft (small-$x$) partons, one must first introduce light-cone coordinates,

$$x^{\pm} = \frac{t \pm z}{\sqrt{2}} \tag{3.2}$$

$$p^{\pm} = \frac{E \pm p^z}{\sqrt{2}}. \tag{3.3}$$

We see that both $x^+$ and $x^-$ involve longitudinal and temporal degrees of freedom. The two transverse coordinates, $x$ and $y$, are left unchanged in this coordinate system. The light-cone coordinate metric is

$$g_{\mu\nu} = \begin{pmatrix} 0 & 1 & 0 & 0 \\ 1 & 0 & 0 & 0 \\ 0 & 0 & -1 & 0 \\ 0 & 0 & 0 & -1 \end{pmatrix} \tag{3.4}$$

which allows us to define the four-vectors and their invariant dot product as [54, 55]

$$x^{\mu} = \left(x^+, x^-, x, y\right) \tag{3.5}$$

$$p^{\mu} = \left(p^+, p^-, p^x, p^y\right) \tag{3.6}$$

$$p \cdot x = p^- x^+ + p^+ x^- - p^x x - p^y y. \tag{3.7}$$

If we define $x^+$ as our light-cone 'time' variable and $x^-$ as our 'longitudinal coordinate', then, looking at Eq. (3.7), we find that $p^+$, the conjugate to $x^-$, will be our longitudinal

momentum variable, while $p^-$, the conjugate to $x^+$, will be our energy. The parton momentum fraction $x$ in terms of our new coordinate system is given by

$$x = \frac{p^+}{P^+}, \tag{3.8}$$

where $p^+$ is the longitudinal momentum of the parton we are interested in and $P^+$ is the total momentum of the hadron it is a part of.

Let us now consider a hadron moving with a very large longitudinal momentum and how different partons may 'perceive' others based on their momentum fraction $x$. Recalling that the position-momentum uncertainty principle provides insights as to how localized certain partons can be, we find that

$$\Delta x^- \approx \frac{1}{\Delta p^+} = \frac{1}{x\Delta P^+} \sim \frac{1}{xP^+}, \tag{3.9}$$

where $x^-$ and $p^+$ are used here, given that they form a conjugate pair. Equation (3.9) provides a powerful basis for comparing the localization of different partons. Being quantum fields, all partons are delocalized according to the uncertainty principle. However, if we consider a large-$x$ parton ($x > 0.1$) and compare it to a small-$x$ parton ($x < 10^{-3}$), we will find that the large-$x$ parton is much more localized than the small-$x$ parton. Therefore, the small-$x$ parton will 'perceive' the large-$x$ parton as being highly localized on the light cone. We can do the same exercise for the $x^+$ and $p^-$ pair, which yields

$$\Delta x^+ \approx \frac{1}{\Delta p^-}. \tag{3.10}$$

However, since $x$ was defined in terms of $p^+$, we cannot make the same substitution as we did in Eq. (3.9).

Therefore, at first glance, Eq. (3.10) may provide little added insight. However, multiplying $p^+$ by $p^-$, we find

$$p^+p^- = \left(\frac{E + p_z}{\sqrt{2}}\right)\left(\frac{E - p_z}{\sqrt{2}}\right) = \frac{E^2 - p_z^2}{2}. \tag{3.11}$$

Recalling that $E^2 = p_x^2 + p_y^2 + p_z^2 + m^2$, we obtain

$$p^+p^- = \frac{p_x^2 + p_y^2 + m^2}{2} = \frac{p_\perp^2 + m^2}{2}. \tag{3.12}$$

Inserting Eq. (3.12) into Eq. (3.10), we have

$$\Delta x^+ \approx \frac{2p^+}{p_\perp^2} \approx \frac{2xP^+}{p_\perp^2}, \tag{3.13}$$

where we have utilized the fact that we are in the high-energy limit which allows us to neglect mass, i.e. $p_\perp \gg m$.

Following the same logic as we laid out for the localization of the partonic quantum fields, Eq. (3.13) provides further grounds for discriminating between different partons. Indeed, since $x^+$ serves as our time variable for a hadron propagating along the positive $z$ direction, Eq. (3.13) tells us that large-$x$ partons will suffer from large amounts of time dilation relative to small-$x$ partons, making them appear frozen. Therefore, within the time scales relevant to heavy-ion collisions, partons that carry most of the nucleonic momentum are essentially static. This fact allows for the use of the following *effective* action for CGC,

$$S_{CGC} = \int d^4x \left( -\frac{1}{4} F^a_{\mu\nu} F^{\mu\nu a} + J^{\mu a} A^a_\mu \right), \tag{3.14}$$

where $F^a_{\mu\nu}$ is defined in Eq. (1.5) and the second term $J^{\mu a} A^a_\mu$ is a source term. This source term is directly related to the ideas developed in this section. Indeed, according to this action, $J^{\mu a}$ is a current that sources color gauge fields $A^a_\mu$, i.e. gluons. $J^{\mu a}$ is therefore constructed using the large-$x$ partons which are static throughout the relevant interaction. In principle, the color current $J^{\mu a}$ could generate quark-antiquark pairs. However, as we will argue below, these contributions are subdominant.

Figure 15 shows the parton distribution function (PDF) of a proton probed at $Q^2 = 10\,\text{GeV}$; it shows $xf$, for $f = u_v$ (valence up quarks), $d_v$ (valence down quarks), $g$ (gluons) and $S = u + d$ (sea quarks). Since this is for a single proton, integrating all of the components of the PDF over momentum fraction $x$ and summing all of their contributions must equal one. We find that, at very small $x$, the PDF is dominated by gluons. Therefore, at small momentum fractions, it is clear that an *effective* field theory may ignore other contributions and focus solely on gluons. However, in heavy-ion collisions, how can we be sure what momentum fraction $x$ we are probing? Let

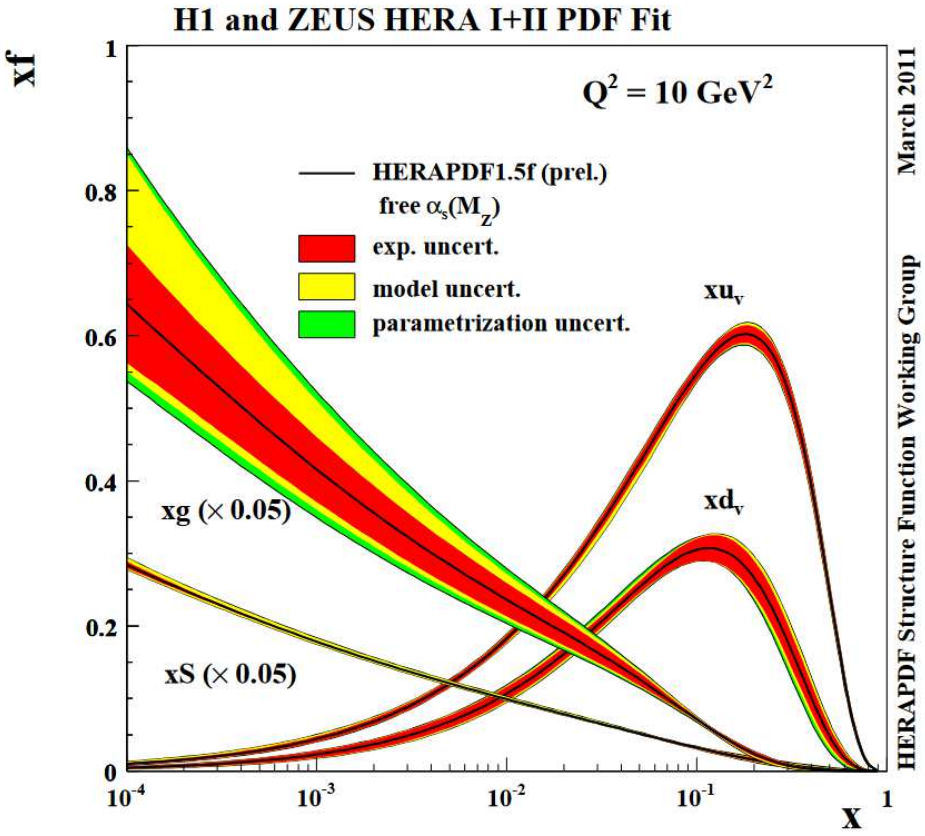


Figure 15: Parton distribution function (PDF) for $Q^2 = 10\,\text{GeV}$, from Ref. [56]. Note that for clarity's sake, the gluon and sea quark distributions $xg$ and $xS$ were divided by 20.

us consider a parton at very small momentum fraction, such that $p^+ = \sqrt{p_\perp^2 + m^2}/\sqrt{2}$. Inserting this into our definition for the momentum fraction $x$, we find

$$x = \frac{\sqrt{p_\perp^2 + m^2}}{\sqrt{2}P^+}. \tag{3.15}$$

In a collision, one right-moving ($P_R$) and one left-moving ($P_L$) hadron collide. They both have a longitudinal momentum of magnitude $|p_z|$. The right-moving hadron's four-momentum is

$$P_R^\mu = \left(P_R^+, P_R^-, P_R^x, P_R^y\right) \approx \left(\sqrt{2}p_z, \frac{M^2}{2P_R^+}, 0, 0\right), \tag{3.16}$$

where we have assumed the momentum in the $z$-direction is very large, such that $p_z \gg M$, the hadron's mass. The left-moving hadron's four-momentum is

$$P_L^\mu = \left(P_L^+, P_L^-, P_L^x, P_L^y\right) \approx \left(\frac{M^2}{2P_R^+}, \sqrt{2}p_z, 0, 0\right). \tag{3.17}$$

The invariant energy is then

$$s = (P_R + P_L)^2 = 2P_R \cdot P_L \approx 2P_R^+ P_L^- \approx 4p_z^2$$
$$\Rightarrow \sqrt{s} = 2p_z = \sqrt{2}P_R^+. \tag{3.18}$$

Inserting Eq. (3.18) into Eq. (3.15), and substituting $P_R^+$ by $P^+$, we obtain

$$x = \frac{\sqrt{p_\perp^2 + m^2}}{\sqrt{s}}. \tag{3.19}$$

Therefore, using Eq. (3.19) with estimates of $\langle p_T \rangle$, the mean transverse momentum, at $\sqrt{s} = 5.44\,\text{TeV}$ obtained through experimental fits [57], as well as the proton mass in lieu of $m$, we find

$$x \sim \frac{1\,\text{GeV}}{5440\,\text{GeV}} \approx 10^{-4}. \tag{3.20}$$

Equation (3.20) makes it clear that the momentum fraction we are probing at beam energies we are concerned with is mostly gluonic.

The CGC effective field theory is therefore an appropriate approximation for the the interaction region of heavy-ion collisions, and provides a physical framework under which the pre-equilibrium phase can be developed and evolved.

## 3.2 GLUON SATURATION

Figure 15 supplied clear evidence that the small-$x$ partons are almost exclusively gluons. It did not, however, provide us with an explanation for why that is. Through perturbative QCD, we know that high-energy partons evolve and radiate through bremsstrahlung, which favors the emission of soft gluons. Indeed, the differential probability for emitting gluons with $x \ll 1$ is [50]

$$dP_{\text{brem}} \propto \frac{dx}{x} \tag{3.21}$$

i.e., when $x \to 0$, the probability of bremsstrahlung emission diverges. This fact, taken on its own, entails that gluons should be all-encompassing at small-$x$ beyond simply

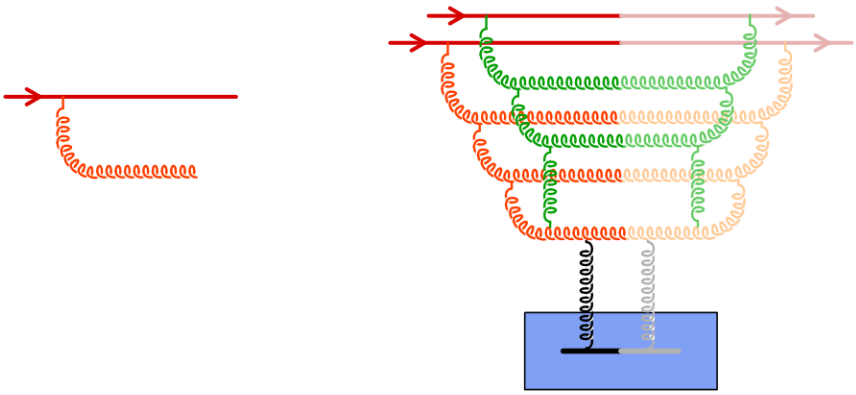

Figure 16: (**Left**) Elementary radiation and (**right**) high-energy scattering, evolution and recombination of gluons via bremsstrahlung. Figure taken from Ref. [50].

dominating. However, gluons can not only radiate other gluons, but can also recombine (i.e. $gg \rightarrow g$), a fact which we illustrate in Fig. 16. Therefore, as more and more gluons are radiated via bremsstrahlung, both the phase space and the physical space become more and more densely packed with gluons, leading to more and more recombination. Eventually, when the number of gluons radiated rivals the amount of recombination that occurs in a given time lapse, the system is said to have reached *saturation*.

The typical gluon recombination cross-section $\sigma_{gg}$ at a given energy scale $Q^2$ is equal to $\alpha_s/Q^2$ [58], where $\alpha_s$ is the strong coupling. We can then define the packing factor $\kappa$,

$$\kappa = \rho \cdot \sigma_{gg}, \tag{3.22}$$

which relies on the transverse gluon density $\rho$ and the cross-section $\sigma_{gg}$ we just defined. Defining $xg(x, Q^2)$, the number of gluons with momentum fraction $x$ and scale $Q$, and considering the transverse projection of a given hadron to be a circle of radius $R$, we can rewrite the packing factor $\kappa$,

$$\kappa \approx \frac{xg(x, Q^2)}{\pi R^2} \cdot \frac{\alpha_s}{Q^2}. \tag{3.23}$$

The energy scale at which the packing factor becomes $O(1)$ is the saturation scale $Q_s$, i.e.,

$$\kappa \approx 1 \iff Q_s^2 \approx \frac{xg(x, Q_s^2)\alpha_s}{\pi R^2}. \tag{3.24}$$

$Q_s$ is of great importance to the initialization of the color gauge fields $A_\mu$, as it controls the scale of color charge fluctuations in the source partons contained in the current term $J^{\mu a}$ introduced earlier. These fluctuations will, in turn, control how and how much energy is deposited in the transverse plane at the time of the collision, $\tau = 0^+$.

### 3.2.1 *Determining $Q_s$*

At first glance, Eq. (3.24) seems to suggest that the saturation scale $Q_s$ is fairly constant across relatively large portions of hadronic matter. However, given its dependence on $xg(x, Q^2)$, it can actually vary considerably depending on local fluctuations in gluon densities. The definition provided in Eq. (3.24) can help provide general estimates of the saturation scale in large systems. For example, at the LHC, estimates of the saturation scale generally hover around 2 – 3 GeV [59]. However, in IP-Glasma, local fluctuations in the saturation scale $Q_s$ are taken into account, and it is made to vary from one lattice site to another. Using the Impact Parameter Dipole Saturation Model, or IP-SAT [60], $Q_s$ is calculated at each point in the transverse lattice based on a multitude of local physical properties, including the local nuclear density.

We begin by determining the nuclear thickness function $T_A(\vec{x}_\perp)$,

$$T(\vec{x}_\perp) = \frac{e^{-\vec{x}^2/2B_G}}{2\pi B_G}, \tag{3.25}$$

$$T_A(\vec{x}_\perp) = \sum_{i=1}^{A} T(\vec{x}_\perp - \vec{x}_{\perp_i}), \tag{3.26}$$

where the $\vec{x}_{\perp_i}$ represent the positions of the nucleons (sampled via Woods-Saxon distribution), $A$ is the mass number of the nucleus we are considering (we do this for both nuclei individually), and $B_G$, which controls the 'extent' of nucleons, is set to $B_G = 4.0\,\text{GeV}^{-2}$ based on fits to DIS data [61]. If we are evaluating $T_A(\vec{x}_\perp)$ close to the boundaries of the transverse plane, most (if not all) nucleons will be far away and $T(\vec{x}_\perp - \vec{x}_{\perp_i}) \sim 0\,\forall\, i$, meaning that $T_A(\vec{x}_\perp) \to 0$ as $|\vec{x}_\perp| \to \infty$. Alternatively, when we

are in a region of the transverse plane where many nucleons intersect, $T_A(\vec{x}_\perp) \propto \frac{1}{2\pi B_G}$, i.e., we have denser hadronic matter.

The thickness function is then inserted into the Glauber-Mueller dipole cross-section [62],

$$\frac{d\sigma_{q\bar{q}}}{d^2b} = 2\left(1 - \exp\left(-\frac{\pi^2}{2}N_c T_A(\vec{x}_\perp) r^2 x g(x, \mu^2(r^2))\alpha_s(\mu^2(r^2))\right)\right), \tag{3.27}$$

where $b$ is the impact parameter of the interaction, $xg(x, \mu^2(r^2))$ is the local gluon density (not to be confused with $xG$ defined previously, which is the integrated gluon distribution function), $r^2$ is the dipole size and $N_c = 3$ is the number of colors; $\sigma_{q\bar{q}}$ is the total cross section for a small $q\bar{q}$ dipole to pass through a gluon cloud [63]. It provides a simple measure of the probability of interaction between a quark-antiquark dipole and a dense target. If the gluon density $xg$ and thickness function $T_A$ are large, so is the cross-section and, therefore, the interaction probability. However, it is clear from Eq. (3.27) that the differential cross-section does not grow indefinitely; as the argument of the exponential grows, the exponential itself (because of the minus sign preceding its argument) goes to 0.

How does this relate to the saturation scale $Q_s$? The form of Eq. (3.27) suggests that the control over whether or not the dipole interacts lies with the exponential term. Therefore, we define the saturation radius $r_s$ as the dipole size at which the proton consists of one interaction length, where the interaction probability is given by the second term squared, i.e.

$$\begin{aligned} e^{-1} &= \exp\left(-\frac{\pi^2}{N_c} T_A(\vec{x}_\perp) r_s^2 x g(x, \mu^2(r_s^2))\alpha_s(\mu^2(r_s^2))\right) \\ \Rightarrow 1 &= \frac{\pi^2}{N_c} T_A(\vec{x}_\perp) r_s^2 x g(x, \mu^2(r_s^2))\alpha_s(\mu^2(r_s^2)) \\ \Rightarrow \frac{2}{r_s^2} &= \frac{2\pi^2}{N_c} T_A(\vec{x}_\perp) x g(x, \mu^2(r_s^2))\alpha_s(\mu^2(r_s^2)), \end{aligned} \tag{3.28}$$

where both sides in Eq. (3.28) have been multiplied by 2 as a matter of convention. The RHS of Eq. (3.28) is called the density profile $D$, and the saturation scale $Q_s$ is the value of $D$ at $r = r_s$. Therefore,

$$Q_s^2 = \frac{2}{r_s^2}. \tag{3.29}$$

Now that we have an implicit equation to solve, we must define its various components precisely. The gluon density $xg(x, \mu^2)$ is initialized as

$$xg(x, \mu_0^2) = A_g x^{\lambda_g} (1 - x)^{5.6}, \tag{3.30}$$

with $A_g = 2.308$, $\lambda_g = 0.058$ and $\mu_0^2 = 1.51\,\text{GeV}^2$ [61]. This gluon density is then evolved to all other values of $\mu^2$ relevant to our analysis through the leading-order DGLAP equation [50, 64–66], assuming a purely gluonic state. The energy scale $\mu$ itself is related to the saturation dipole size $r_s$ (and, therefore, saturation scale $Q_s$) through

$$\mu^2 = \frac{4}{r_s^2} + \mu_0^2 = 2Q_s^2 + \mu_0^2. \tag{3.31}$$

The leading-order QCD running coupling constant, which relies on the inherent energy scale $\mu^2$, is given by

$$\alpha_s(\mu^2) = \frac{12\pi}{(33 - 2N_f) \ln\left(\frac{\mu^2}{\Lambda_{\text{QCD}}^2}\right)}, \tag{3.32}$$

with $N_f$, the number of allowed quark flavors, set to 4 and $\Lambda_{\text{QCD}} = 156\,\text{MeV}$.

The interdependence of Eqs. (3.28) and (3.30) to (3.32) and, more fundamentally, of the variables $(x, r_s, \mu)$ means that solving for the saturation length $r_s$ must be done iteratively. Concretely, a table with values of $x$ and $\mu^2$, as well as the value of $xg(x, \mu^2)$, the gluon density, associated with the $x$ and $\mu^2$ pair is generated. Given the relationships between all variables, we can progress through this value table until we approach the correct set of values. We can then interpolate between neighboring parameter sets to find an appropriate and unique value for $r_s$. As mentioned above, this is done at every point in the transverse plane.

Once the saturation scale has been determined everywhere, it can be used to generate a random color charge distribution in the transverse plane, which, as mentioned previously, will source the color gauge fields $A_\mu$. Indeed, assuming the following relationship between the saturation scale and the scale of color charge fluctuations $\mu_A$,

$$Cg^2\mu_A = Q_s, \tag{3.33}$$

where $C \approx 0.5 - 0.75$ in 2D and $\approx 1.2 - 1.5$ in 3D is a proportionality constant that must be calibrated using charged particle yields (since it controls the energy normalization of the system), we have

$$\langle \rho_A^a(\vec{x}_\perp)\rho_A^b(\vec{y}_\perp)\rangle = g^2\mu_A^2(\vec{x}_\perp)\delta^{ab}\delta^2(\vec{x}_\perp - \vec{y}_\perp). \tag{3.34}$$

It is important to note here that $\mu_A \neq \mu$; $\mu$ is the intrinsic energy scale considered in our calculation of $r_s$, while $\mu_A$ is a measure of the color charge fluctuations and is defined entirely in terms of the saturation scale $Q_s$. Once the color charge distributions of both colliding nuclei are sampled via Eq. (3.34), they can be used as sources for the color gauge fields $A_\mu^a$, and the pre-equilibrium evolution can commence.

## 3.3 EVOLUTION

In the following sections, we will describe the pre-collision conditions and the post-collision evolution of the color gauge fields $A_\mu^a$. Because IP-Glasma is a numerical program, we will introduce relevant lattice quantities alongside the fundamental mathematical and physical theories underpinning them. As we will show, moving to a discrete lattice presents both advantages and challenges to solving the various equations that describe pre-equilibrium QGP, or glasma.

### 3.3.1 *Sampling $\rho^a$ and Generating Pre-Collision Fields*

Equation (3.34) describes the properties of the color charge distribution and how it relates to the saturation scale $Q_s$. Numerically, we sample from the following distribution,

$$\langle \rho_k^a(\vec{x}_\perp)\rho_l^b(\vec{y}_\perp)\rangle = \delta^{ab}\delta^{kl}\delta^2(\vec{x}_\perp - \vec{y}_\perp)\frac{g^2\mu_A^2(\vec{x}_\perp)}{N_y}, \tag{3.35}$$

where the indices $k, l$ label the discretized and sub-divided longitudinal coordinate, and $N_y$ is the number of discrete points in the longitudinal direction. Our color charge distribution therefore has 'depth', a feature which we will now motivate.

Suppose we have the color charge distribution $\rho_A$ of the nucleus moving with velocity $\sim$ c in the positive $z$ direction. Referring back to Eq. (3.14), we know that the Classical Yang-Mills equation related to such an action is [67, 68]

$$\left[D_\mu, F^{\mu\nu}\right] = J^\nu, \tag{3.36}$$

where

$$D_\mu = \partial_\mu + igA_\mu \tag{3.37}$$

$$F_{\mu\nu} = \partial_\mu A_\nu - \partial_\nu A_\mu + ig\left[A_\mu, A_\nu\right] \tag{3.38}$$

$$J^\nu = \rho_A(x^-, \vec{x}_\perp)\delta^{\nu+}. \tag{3.39}$$

The $\delta$ function in Eq. (3.39) signals that we are considering a right-moving source on the light cone, and the dependency of $\rho_A$ upon $x^-$ signals that the color charge distribution is delocalized, in line with the light-cone coordinate work we did in Section 3.1.

The fundamental degrees of freedom of these equations, the color gauge fields $A_\mu$, must be translated to lattice quantities for our simulations. On the lattice, the gauge fields become gauge links[1],

$$U_i(\vec{x}_\perp) = \exp(iga_i A_i(\vec{x}_\perp)) \tag{3.40}$$

where $\vec{x}_\perp$ is the position of a given link, $i = \{x, y, \eta\}$ indicates its direction, $a_i$ is the size of the lattice spacing and $g$ is the strong coupling constant. One can reverse a link by taking $U_i^\dagger$; 'normal' links go clockwise, while reversed links move counter-clockwise. Therefore, the gauge fields in our simulations are defined strictly on the edges of our discrete lattice, as Fig. 17 makes clear. The direction of a link will be a crucial feature for building emergent quantities such as chromo-electric and -magnetic fields later on.

Moving back to the continuum limit, the covariant continuity equation in the axial gauge ($A^- = A_+ = 0$) yields

$$\begin{aligned} &\left[D_\mu, J^\mu\right] = 0 \\ &\iff \partial_+\rho = 0, \end{aligned} \tag{3.41}$$

[1] See Appendix A for further explanation of the motivation behind the use of this representation of the gauge fields.

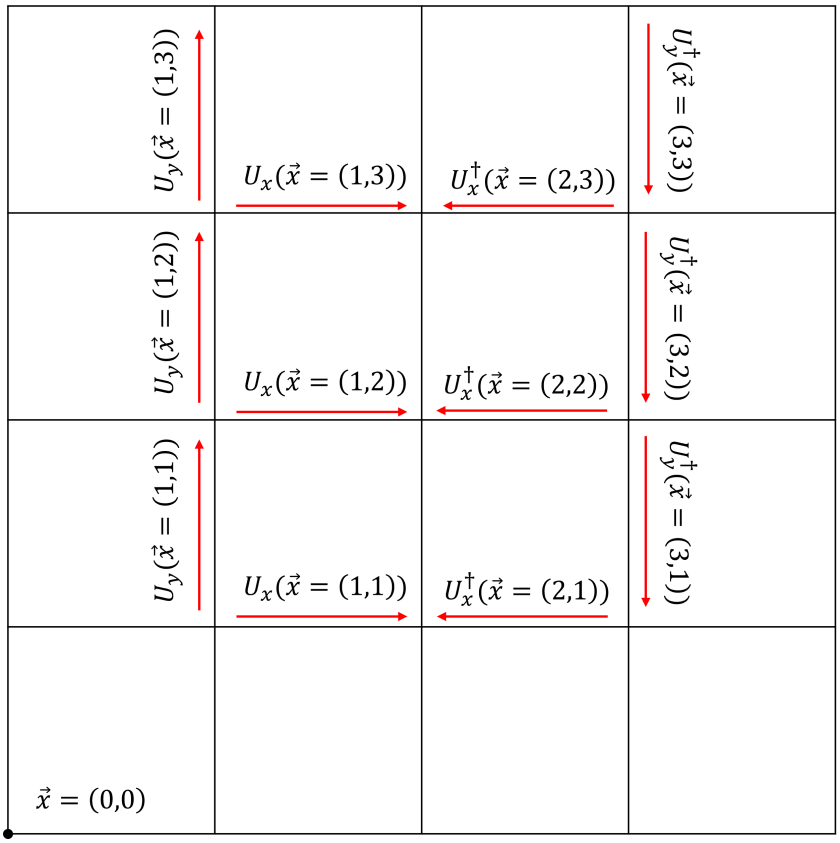


Figure 17: Schematic representation of gauge links and their relation to the lattice. The position of a given link is determined by the starting point of the toe of the arrow of the regular link $U_i$.

which entails that the charge distribution, in this gauge, is static (independent of $x^+$). Assuming a static solution $A^\mu$ yields trivial solutions for most field-strength tensor components $F_{\mu\nu}$: $F^{\mu+} = 0$ because $A_+ = 0$ by gauge choice and $F^{ij} = 0$ because of the transverse equations

$$\left[D_i, F^{ij}\right] = 0, \tag{3.42}$$

with the corollary that the transverse gauge fields are *pure gauge* (i.e. do not generate chromo-electric or -magnetic fields). The only non-trivial (and non-vanishing) components are therefore $F_{i-} = -F^{i+}$, which yield

$$\begin{aligned} &\left[D_i, F^{i+}\right] = -\nabla_\perp^2 A^+ = \rho(x^-, \vec{x}_\perp) \\ &\Rightarrow \nabla_\perp^2 A^{+a} = \nabla_\perp^2 A_-^a = -\rho^a(x^-, \vec{x}_\perp). \end{aligned} \tag{3.43}$$

Equation (3.43) represents 2D Poisson equations for each color index, which are solved to determine the gauge fields $A^+$ in the axial gauge where, again, $A^- = 0$. This gauge is also called the covariant gauge because $\partial_\mu A^\mu = \partial_+ A^+ = 0$. We then transform to light-cone gauge $A^+ = A_- = 0$ through the usual gauge transformation, i.e.,

$$A_\mu = -\frac{i}{g} V \partial_\mu V^\dagger + V \mathcal{A}_\mu V^\dagger, \tag{3.44}$$

where $\mathcal{A}_\mu$ represents the desired field in the gauge we are transforming from. In our case, then, $\mathcal{A}_-$ is the solution to Eq. (3.43) with all other components vanishing. The new gauge condition $A_- = 0$ leads to

$$\begin{aligned} 0 &= -\frac{i}{g} V \partial_- V^\dagger + V \mathcal{A}_- V^\dagger \iff \\ V^\dagger(x^-, \vec{x}_\perp) &= \mathcal{P} \exp\left( ig \int_{-\infty}^{x^-} dy^- \mathcal{A}_-(y^-, \vec{x}_\perp) \right) \iff \\ V^\dagger(x^-, \vec{x}_\perp) &= \mathcal{P} \exp\left( -ig \int_{-\infty}^{x^-} dy^- \frac{\rho(y^-, \vec{x}_\perp)}{\nabla_\perp^2} \right), \end{aligned} \tag{3.45}$$

where in the last line we have used the fact that $\mathcal{A}_-$ is the gauge field in the axial gauge which we know, thanks to Eq. (3.43), is entirely defined by the static color charge distribution $\rho$. Equation (3.45) entails that the pre-collision gauge fields in the light-cone gauge are strictly transverse, since

$$A_+ = -\frac{i}{g} V \partial_+ V^\dagger + V \mathcal{A}_+ V^\dagger = 0 \tag{3.46}$$

in the axial gauge. Equation (3.45) therefore dictates that $V^\dagger$ is independent of $x^+$.

We can now refer back to Eq. (3.35) to make sense of its discrepancies concerning Eq. (3.34). When implemented numerically, Eq. (3.45) becomes [69]

$$V(\vec{x}_\perp) = \prod_{k=1}^{N_y} \exp\left( -ig \frac{\rho_k^a(\vec{x}_\perp) t^a}{\nabla^2 - m^2} \right), \tag{3.47}$$

where $t^a$ are the Gell-Mann matrices [6] and $m^2$ acts as a regulating mass, set to 200 MeV, and we have absorbed the differential element $dy$ of the integral into $\rho_k^a$. In the $N_y \to \infty$ limit, Eq. (3.47) recovers Eq. (3.45), the path-ordered Wilson line. Therefore, our stochastic charge density $\rho$ requires some longitudinal extent, or 'thickness', to generate the pre-collision gauge fields; multiple samplings of the color charge

distribution are undertaken and 'stitched' together, allowing for the construction of the numerical Wilson line. The longitudinal dependence of the continuous color charge distribution $\rho_A(x^-, x_\perp)$ is also recovered through these consecutive samplings. That is precisely why, in Eq. (3.35), the indices $k$ and $l$ were added: they mark the fact that a specific sampling belongs to a specific slice in the longitudinal direction, slice which is then used to construct Eq. (3.47). These slices are normalized so that

$$\sum_{k,l} \langle \rho_k^a(\vec{x}_\perp) \rho_l^b(\vec{y}_\perp) \rangle = g^2 \mu_A^2(\vec{x}_\perp) \delta^{ab} \delta^2(\vec{x}_\perp - \vec{y}_\perp). \tag{3.48}$$

In other words, the sum of the fluctuations of all of the sampled color charge distributions must be equal to the fluctuations dictated initially by the saturation scale determined by IP-SAT.

Once the Wilson line is constructed numerically, it must be put on the lattice through the gauge links defined in Eq. (3.40). To do so is simple: since the pre-collision gauge fields are strictly transverse, we know that

$$A_i = -\frac{i}{g} V \partial_i V^\dagger \tag{3.49}$$

given the fact that the transverse gauge fields in the axial gauge were all evenly 0. Inserting Eq. (3.49) into Eq. (3.40), we find

$$\begin{aligned}
U_i(\vec{x}_\perp) &= \exp\left( iga \left( -\frac{i}{g} V(\vec{x}_\perp) \partial_i V(\vec{x}_\perp)^\dagger \right) \right) \\
U_i(\vec{x}_\perp) &\sim 1 + a_i V(\vec{x}_\perp) \partial_i V^\dagger(\vec{x}_\perp) \\
U_i(\vec{x}_\perp) &\sim 1 + a_i V(\vec{x}_\perp) \left( \frac{V^\dagger(\vec{x}_\perp + \vec{a}_i) - V^\dagger(\vec{x})}{a_i} \right) \\
U_i(\vec{x}_\perp) &\sim 1 + V(\vec{x}_\perp) V^\dagger(\vec{x}_\perp + \vec{a}_i) - V(\vec{x}_\perp) V^\dagger(\vec{x}_\perp) \\
U_i(\vec{x}_\perp) &\sim V(\vec{x}_\perp) V^\dagger(\vec{x}_\perp + \vec{a}_i),
\end{aligned} \tag{3.50}$$

where we have used the fact that $V(\vec{x}_\perp) V^\dagger(\vec{x}_\perp) = 1$ and where $\vec{a}_i$ represents a vector the size of the lattice spacing $a$ pointing in the direction $i$. The pre-collision gauge fields are therefore constructed at all lattice edges through the sampling of the color charge distribution and construction of the discretized path-ordered Wilson lines.

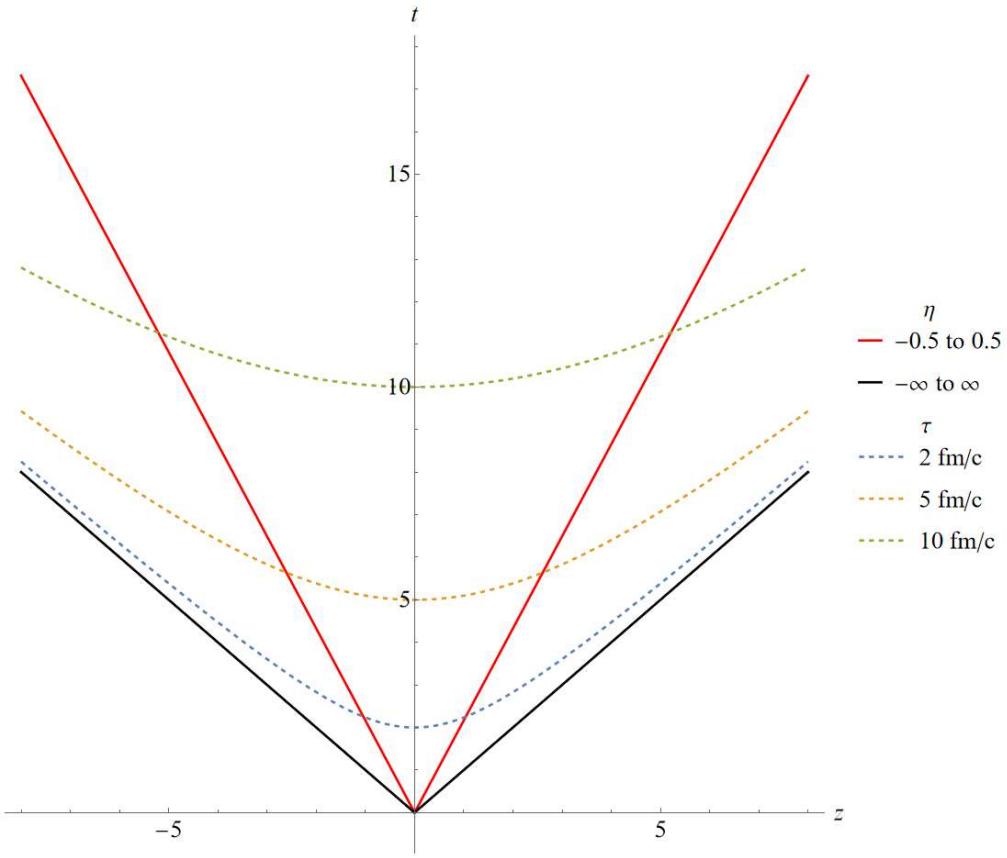


Figure 18: $\tau - \eta$ coordinates plotted in Minkowski space. Lines at equal proper time $\tau$ span regions of spacetime delimited by a given $\eta$ range, in this case $-0.5 \leq \eta \leq 0.5$ (mid-rapidity).

### 3.3.2 *Post-Collision Gauge Fields*

At the onset of this section, it is important to remind the reader that the evolution equations which will be described in this section apply to the boost-invariant (or 2D) formulation of IP-Glasma. Later in this thesis, we will generalize these evolution equations to a 3D description of the initial conditions, but only after showing results stemming from boost-invariant simulations.

Before combining pre-collision gauge fields to build post-collision gauge fields, we introduce Milne, or $\tau - \eta$, coordinates. Their definitions are as follow

$$\tau = \sqrt{t^2 - z^2} \tag{3.51}$$

$$\eta = \frac{1}{2} \ln \left( \frac{t+z}{t-z} \right) = \tanh^{-1} \left( \frac{z}{t} \right), \tag{3.52}$$

and their metric is $g_{\mu\nu} = \text{diag}(1, -1, -1, -\tau^2)$. This coordinate system is the best suited for the conditions of heavy-ion collisions for a multitude of reasons:

1. The forward light-cone is delimited by the $\tau = 0$ line.

2. Spacetime rapidity $\eta$ is $\pm\infty$ on the light-cone axes and does not have a meaningful definition beyond them.

3. $\tau$, the 'proper' time, is the time as measured in the local rest frame of any cell or particle that was located at $z = 0$ at $t = 0$ and moved with constant longitudinal velocity $v_z$. For any cell with properties which do not align with this condition, it holds as an approximation of its proper time.

4. The length element is $\tau d\eta$.

The first two items of the list point out that $\tau - \eta$ coordinates are only defined in the relevant space when analyzing heavy-ion collisions, i.e., the forward light cone. On the other hand, the final two points are crucial qualities of this coordinate system. Indeed, given the highly relativistic nature of the partons involved in heavy-ion collisions, time dilation effects must be taken into consideration when analyzing their evolution. If we were to take the lab-frame time $t$ as our time variable, partons with different longitudinal velocities would evolve at different rhythms, making it difficult to analyze their temporal evolution. Instead, taking the 'proper' time $\tau$, we track almost every cell in their respective rest frames, relative to the time of collision. The fact that the longitudinal length element is $\tau d\eta$ leads to an expansion of the coordinate system with time, reconciling rapidly expanding QGP with a stable coordinate system. Figure 18 illustrates this idea: as proper time increases, the longitudinal extent of the region encompassed by a static $\eta$ range also increases.

Finally, given our use of light-cone coordinates in the previous sections, converting between the two coordinate systems will prove important. To go from light-cone coordinates to Milne coordinates, we do

$$\tau = \sqrt{2x^+x^-}, \tag{3.53}$$

$$\eta = \frac{1}{2}\ln\left(\frac{x^+}{x^-}.\right) \tag{3.54}$$

Now that we have properly defined the coordinate system used in the glasma evolution equations, we can construct them. The initial conditions described in Section 3.3.1 were concerned with a single nucleus. We will now be interested in the fields immediately *after* the collision when the color gauge fields of the *two* colliding nuclei are combined. As a visual aid, we will refer to Fig. 19 as our convention for naming different spacetime regions. The pure, pre-collision gauge fields exist in 2 regions: the fields sourced by the nucleus propagating on $x^+$ exist in regions 1 and 4, while those generated by the nucleus propagating along $x^-$ exist in regions 1 and 2.

In the continuum limit, the transverse gauge fields at light-cone axes (intersections between regions 1, 2 and 4) are given by [70–72]

$$A^i = A^i_{(A)} + A^i_{(B)}, \tag{3.55}$$

where the $(A, B)$ subscripts represent the 2 nuclei. The color charge currents are confined to the light-cone. Therefore, in region 1, the sourceless CYM equations are used,

$$\left[D_\mu, F^{\mu\nu}\right] = 0. \tag{3.56}$$

In the proper-time gauge $x^-A^+ + x^+A^- = 0$, the components of the gauge fields, in light-cone coordinates, look like

$$\begin{aligned} A^+ &= x^+\alpha(x^+, x^-, \vec{x}_\perp), \\ A^- &= -x^-\alpha(x^+, x^-, \vec{x}_\perp), \\ A^i &= \alpha^i_1(x^+, x^-, \vec{x}_\perp), \end{aligned} \tag{3.57}$$

where the $\alpha$ are ansatz that are taken to be independent of spacetime rapidity $\eta$ and the subscript 1 refers to the field in region 1. Using these ansatz to find the field strength

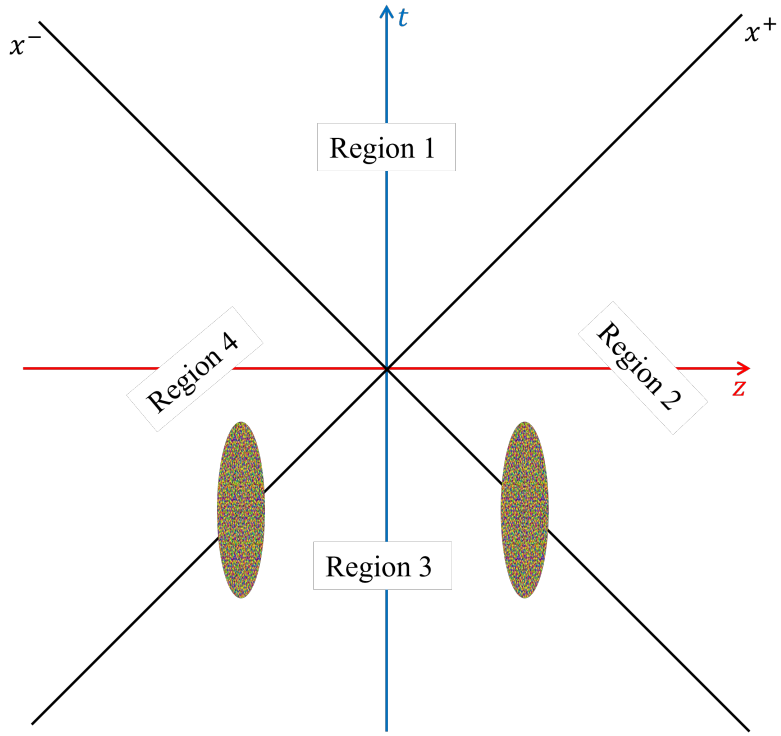


Figure 19: Visual representation and identification of the different spacetime regions. The collision occurs at the origin, and the post-collision fields evolve in region 1.

tensor components, converting them to $\tau - \eta$ coordinates and inserting said components into Eq. (3.56), we obtain [70]

$$\begin{aligned}
&\frac{1}{\tau}\left[D^i, \partial_\tau \alpha_1^i\right] + ig\tau\left[\alpha, \partial_\tau \alpha\right] = 0, \\
&\frac{1}{\tau}\partial_\tau\tau\partial_\tau\alpha_1^i - ig\tau^2\left[\alpha, \left[D^i, \alpha\right]\right] - \left[D^j, F^{ji}\right] = 0, \\
&\frac{1}{\tau^3}\partial_\tau\tau^3\partial_\tau\alpha - \left[D^i, \left[D^i, \alpha\right]\right] = 0.
\end{aligned} \tag{3.58}$$

These equations are satisfied in all regions of interest and are continuous on the boundaries between these regions. Equation (3.55), however, also requires us to treat the two pre-collision fields distinctly at the time of the collision $\tau = 0^+$, i.e.,

$$\alpha_1^i(\tau = 0^+, \vec{x}_\perp) = \alpha_4^i(\vec{x}_\perp) + \alpha_2^i(\vec{x}_\perp), \tag{3.59}$$

where, again, numerical subscripts refer to the regions the quantities exist in. Naturally, we must redefine our initial ansatz $\alpha$ in terms of these static pre-collision gauge fields $\alpha_{2,4}$ using the same sourced CYM equation as in Section 3.3.1, which yields

$$\alpha(\tau = 0^+, \vec{x}_\perp) = \frac{ig}{2}\left[\alpha_4^i(\vec{x}_\perp), \alpha_2^i(\vec{x}_\perp)\right]. \tag{3.60}$$

Converting our initial ansatz Section 3.3.2 to $\tau - \eta$ coordinates gives

$$\begin{aligned} A^\tau &= \frac{1}{\tau}\left(x^- A^+ + x^+ A^-\right) = 0, \\ A^\eta &= \frac{1}{\tau^2}\left(x^- A^+ - x^+ A^-\right), \end{aligned} \tag{3.61}$$

where $A^\tau = 0$ because of the gauge we have chosen. Using Eq. (3.60) to further define $A^+$ and $A^-$, Eq. (3.61) becomes

$$A^\eta(\tau = 0^+) = \frac{ig}{2}\left[\alpha_4^i, \alpha_2^i\right]. \tag{3.62}$$

However, as seen in the previous section, we are interested in lower-indexed quantities in our Wilson lines, so $A_\eta = -\tau^2 A^\eta = 0$ if $\tau = 0^+$. Therefore, in an expressly boost-invariant ($\eta$ independent) formulation of IP-Glasma, the $\eta$ component of the gauge field is made to vanish at the time of the collision.

The post-collision situation has been entirely defined in the continuum limit. However, as we have established, we work on a discrete lattice. Equation (3.55) on the lattice is [73]

$$\Re\left[\mathrm{Tr}\left(t_a\left(\left(1 + U^\dagger\right)(U_A + U_B)\right)\right)\right] = 0, \tag{3.63}$$

where $U_{A,B}$ represents pre-collision links associated to both nuclei and $U$ is the resulting 'total' gauge link. This corresponds to 8 equations that must be solved numerically, since we have $N_c^2 - 1 = 8$ color indices and $t_a$ specifies the color index of interest. Thankfully, work done in Ref. [74] shows how to resolve this problem numerically. We begin by defining $F_a$, the quantity we want to be equal to 0, as

$$F_a = \Re\left[\mathrm{Tr}\left(t_a\left(\left(1 + U^\dagger\right)(U_A + U_B)\right)\right)\right].$$

We know that the solution to Eq. (3.63) is an element of $SU(3)$, given the nature of QCD. Based on this fact, we can take the following ansatz for the final solution,

$$U = \exp(ix_b t_b) U_0, \tag{3.64}$$

with $U_0$ being an initial guess for the gauge link (which we set to $\exp(-iga(A_{i(A)} + A_{i(B)}))$). With this in hand, we can Taylor expand $F_a$ about $x_b$ for each color index, i.e.,

$$F_a(\delta x_b) = F_a + \sum_{b=1}^{8} \frac{\partial F_a}{\partial x_b} \delta x_b, \tag{3.65}$$

where we have kept only the first two terms of the expansion. Since we want $F_a = 0$, we state that small deviations about $F_a(x_b = 0)$ must also be 0 (i.e. $F_a(\delta x) = 0$). This gives us

$$F_a = -\sum_{b=1}^{8} \frac{\partial F_a}{\partial x_b} \delta x_b. \tag{3.66}$$

Taking the derivative of $F_a$, we find

$$\begin{aligned} &\frac{\partial}{\partial x_b} \Re \left[ \mathrm{Tr} \left( t_a \left( \left( 1 + U^\dagger \right) (U_A + U_B) \right) \right) \right] \delta x_b = \\ &\Re \left[ \mathrm{Tr} \left( t_a \left( \left( -i t_b e^{-i x_b t_b} U_0^\dagger \right) (U_A + U_B) \right) \right) \right] \delta x_b = \\ &\Im \left[ \mathrm{Tr} \left( t_a t_b \left( U_0^\dagger (U_A + U_B) \right) \right) \right] \delta x_b. \end{aligned} \tag{3.67}$$

Combining this result with our initial definition of $F_a$, we find

$$\Re \left[ \mathrm{Tr} \left( t_a \left( \left( 1 + U^\dagger \right) (U_A + U_B) \right) \right) \right] = -\Im \left[ \mathrm{Tr} \left( t_a t_b \left( U_0^\dagger (U_A + U_B) \right) \right) \right] x_b, \tag{3.68}$$

where we have replaced $\delta x_b$ by $x_b$ since we initialize $x_b$ at 0. We update $x_b$ through small incremental steps $x_b^{\text{new}} = x_b^{\text{old}} + \delta x_b$ until Eq. (3.68) converges; moving to the lattice presents its fair share of difficulties.

In previous sections, we have mentioned the chromo-electric field in passing. When we formally introduce the equations of motion in the following section, we will work through the Hamiltonian to deduce the following form for the chromo-electric field,

$$E^\eta = \frac{1}{\tau} \partial_\tau A_\eta. \tag{3.69}$$

For now, it is only important to understand that Eq. (3.69) leads to

$$E^\eta = 2A^\eta = -ig\left[\alpha_4^i, \alpha_2^i\right]. \tag{3.70}$$

We can then use Gauss' law to determine $E^i$, the transverse fields,

$$\begin{aligned}&\left[D_i, E^i\right] + \left[D_\eta, E^\eta\right] = 0, \\ &\Rightarrow E^i = 0\end{aligned} \tag{3.71}$$

where we have used the fact that $E^\eta$ is independent of $\eta$ to simplify Gauss' law to $\left[D_i, E^i\right] = 0$, which in turn is trivially solved by $E^i = 0$. At $\tau = 0^+$, the transverse chromo-electric fields are therefore evenly 0.

The chromo-electric, given its definition in terms of the color gauge fields, also exists on the edges of our lattice. To obtain the $E^\eta$ at a lattice site $\vec{x}_\perp$, one must imagine a single cell on the lattice. This cell is a cube in $x, y$ and $\eta$ coordinates. The value of the chromo-electric field at the position of the center of the cell is taken to be the average of the chromo-electric fields that exist on the edges of the cell which point in the direction of interest, i.e.,

$$\begin{aligned}E^\eta(\vec{x}_\perp) = \frac{1}{4}\Big[&E^\eta(\vec{x}_\perp - \frac{a}{2}(1,1)) + E^\eta(\vec{x}_\perp - \frac{a}{2}(-1,1)) \\ &+E^\eta(\vec{x}_\perp - \frac{a}{2}(1,-1)) + E^\eta(\vec{x}_\perp + \frac{a}{2}(1,1))\Big],\end{aligned} \tag{3.72}$$

where $a$ is the lattice spacing and $\vec{x}_\perp$ is the position of the *center* of the cell of interest. The chromo-electric field on the edges must still be defined in the first place. Following the work done in Ref. [73], we find that at a given edge at time $\tau = 0^+$,

$$\begin{aligned}E^\eta(\vec{x}_\perp) = -\frac{i}{4ga^2}\sum_{i=1}^{2}\Big[&\left(U_i(\vec{x}_\perp) - 1\right)\left(U^\dagger_{i(A)}(\vec{x}_\perp) - U^\dagger_{i(B)}(\vec{x}_\perp)\right) + \\ &\left(U_i^\dagger(\vec{x}_\perp - \vec{a}_i) - 1\right)\left(U_{i(A)}(\vec{x}_\perp - \vec{a}_i) - U_{i(B)}(\vec{x}_\perp - \vec{a}_i)\right) - \text{h.c.}\Big]\end{aligned} \tag{3.73}$$

where h.c. indicates the hermitian conjugate of the two terms explicitly shown. By expanding each term to first order, one can show that this form for $E^\eta$ on the lattice respects Eq. (3.70).

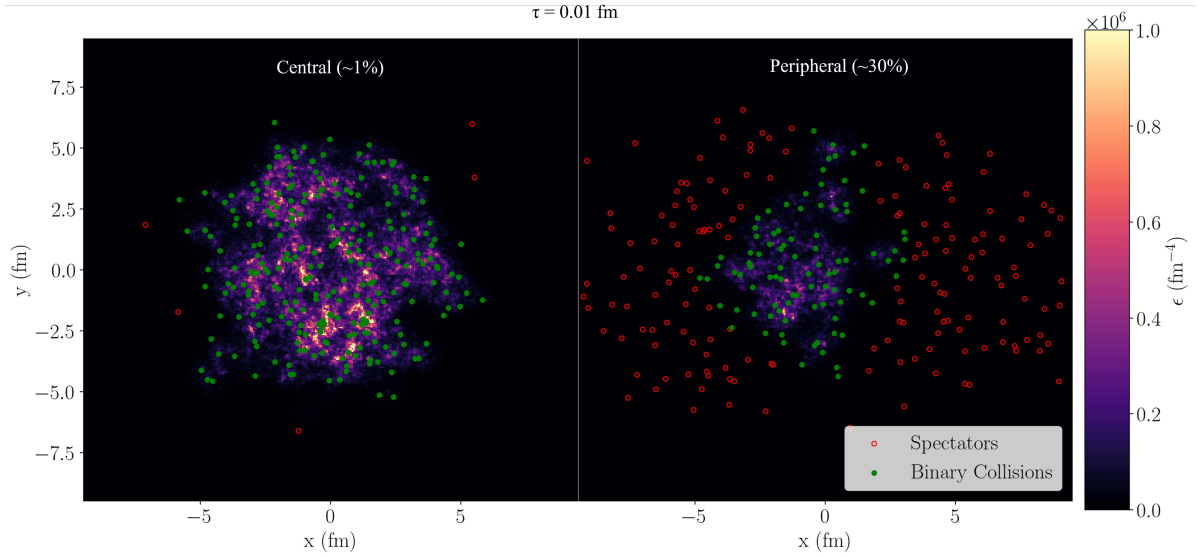


Figure 20: Energy density ($\epsilon$) distributions of a (**left**) central and a (**right**) peripheral event at initial time $\tau = 0.01\,\text{fm}$ for Xe+Xe at 5.44 TeV. An overlay of the locations of spectator nucleons and binary collision sites is also provided for reference.

Figure 20 shows the initial energy density profiles of two $^{129}$Xe events generated using IP-Glasma. The energy density is obtained through the diagonalization of the Yang-Mills stress-energy tensor, which we describe in Section 3.4. In short, the stress-energy is calculated through the field strength tensor $F^{\mu\nu}$ which itself depends on the color gauge fields $A_\mu$. The energy density shown is therefore, in some sense, a composite view of the initial color gauge fields. Figure 20 also provides an overlay of binary collision sites and of spectator nucleon positions. Given the numerical nature of our calculations and the factors of $\frac{1}{\tau}$ brought on by the $\tau - \eta$ metric, the simulations are initialized at $\tau = 0.01\,\text{fm}$ (as opposed to $\tau = 0\,\text{fm}$, which would lead to singularities at initial time). This non-zero initial time is also motivated by the fact that, even though the colliding nuclei are severely Lorentz contracted, they still preserve *some* longitudinal extent. Indeed, for Xe-Xe collisions at $\sqrt{s} = 5.44\,\text{TeV}$, the Lorentz factor $\gamma$ is

$$\gamma = \frac{\sqrt{s}/2}{m_\text{N}} = \frac{2720\,\text{GeV}}{0.940\,\text{GeV}} \approx 2900.$$

Taking the initialization time to be the time at which the two nuclei have completely passed through one another (and are not touching anymore), we have

$$\tau_0 = \frac{2R}{\gamma} \approx \frac{11\,\text{fm}}{2900} \approx 0.004\,\text{fm}, \tag{3.74}$$

which confirms that the initialization time for the color gauge fields should not be $\tau_0 = 0^+$.

Figure 20 makes it clear that the profile fluctuates considerably from lattice site to lattice site, a feature provided by the stochastic sampling of color charges. We can also see that the central collision's profile is more spatially isotropic than the peripheral profile which, as we have established in Section 2.3.2, will lead to tangible differences in the end-state observables we calculate. These extremely energetic profiles must still be evolved temporally before being fed into our hydrodynamics phase, a transition which occurs at $\sim 0.6\,\text{fm}$. The next sections will be concerned with developing and understanding the equations of motion of the color gauge and chromo-electric fields.

Before moving forward, it is important to quickly discuss the inherent link between the 2D and 3D formulations of IP-Glasma. In the previous section, we have gone through the derivation of the initial conditions for the 2D formulation of IP-Glasma specifically. However, we have introduced, towards the end of said section, longitudinal color gauge and chromo-electric fields $A_\eta$ and $E_\eta$. Of course, in the boost-invariant (or 2D) formulation, no longitudinal dependencies are allowed. In the principal derivations of the 2D formulation of IP-Glasma [73], the degrees of freedom found in the Hamiltonian (which we will derive in the next section) are the adjoint representation scalar of $A_\eta$ and its conjugate momentum (which is by definition $E^\eta$). They are usually represented as $\phi$ (for $A_\eta$) and $\pi$ (for $E^\eta$) in order to avoid potential confusion as to the role of longitudinal variables in their expressions. Given the fact that we will be extending the 2D formulation to 3D, we have opted to skip this renaming procedure and have preserved the longitudinal field names so that the adjustments made to them when moving to 3D remain clear.

With this matter dealt with, we shall now explain how to evolve these pre-equilibrium fields temporally until thermal equilibrium is reached. First, let us define further quantities on the lattice.

### 3.3.3 *Using the Lattice Practically*

In Section 3.3.1, we introduced the lattice gauge links $U_i(\vec{x}_\perp)$ in order to allow us to discuss how the initial color charge distributions would be fitted on the lattice. It is now time for us to build more involved lattice quantities for use in the equations of motion. Looking at the definition of our gauge links given in Eq. (3.40), we see that two constant factors stick out: $g$, the strong coupling constant (not running, contrarily to $\alpha_s$ in IP-SAT (Eq. (3.32))) and $a$ is the size of the lattice spacing. To avoid having to keep track of these factors throughout the numerical evolution, we rescale relevant lattice fields so that they contain all constants at the onset. Beginning with the color gauge and chromo-electric fields, we have

$$\begin{aligned}
\mathcal{A}_i &= g a_\perp A_i, \\
\mathcal{A}_\eta &= g A_\eta, \\
\mathcal{E}^i &= g a_\perp E^i, \\
\mathcal{E}^\eta &= g a_\perp^2 E^\eta,
\end{aligned} \tag{3.75}$$

where we have specific $a_\perp$, the transverse lattice spacing as it is a dimensionful quantity (with units of fm) contrarily to the longitudinal lattice spacing $a_\eta$, which does not have units (since $\eta$ itself is dimensionless). Both our time variables and position variables will also have to be rescaled in order to maintain consistency in our evolution equations. We have

$$\mathcal{T} = \frac{\tau}{a_\perp}, \tag{3.76}$$

$$x^i = \frac{x^i}{a_\perp}. \tag{3.77}$$

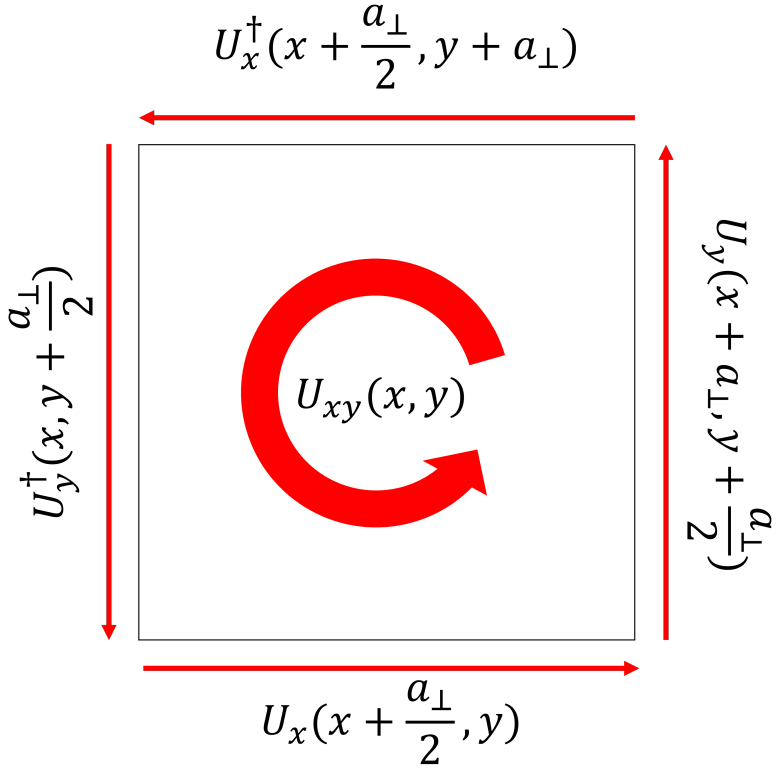


Figure 21: Schematic representation of the construction of a plaquette from gauge links which form a lattice site. By multiplying all of the gauge links shown, we can construct the plaquette $U_{xy}$, a crucial lattice quantity.

As shown in Fig. 17, the gauge links connect neighboring vertices to one another. Explicitly, we will have

$$U_i(\vec{x}_\perp, \eta) = \exp\left(i\mathcal{A}_i(\vec{x}_\perp, \eta)\right), \tag{3.78}$$

where $i = x, y$ and we have kept $\eta$ for specificity of the link in the grid. The longitudinal gauge links will be

$$U_\eta(\vec{x}_\perp, \eta) = \exp\left(ia_\eta \mathcal{A}_\eta(\vec{x}_\perp, \eta)\right). \tag{3.79}$$

In both Eqs. (3.78) and (3.79) we have specified the position in 3D space of the vertex from which the link is sourced through $(\vec{x}_\perp, \eta)$. From here on out, we will only specify the exact 3D positions if absolutely necessary based on context.

The field strength tensor $F_{ij}$ is found in Eq. (3.14), the CGC action, but has yet to be defined on the lattice. Contrarily to the color gauge fields, which exist on the edges

of our lattice, the field strength tensor itself exists within the lattice sites due to its construction. Let us build a 'plaquette', a counter-clockwise loop around one lattice site as shown in Fig. 21. We have

$$\begin{aligned} U_{xy}(x+0.5, y+0.5) = U_x(x+0.5, y) U_y(x+1, y+0.5) \\ U_x^\dagger(x+0.5, y+1) U_y^\dagger(x, y+0.5). \end{aligned} \tag{3.80}$$

Expanding one of these links to quadratic order, we have

$$U_\mu \approx 1 + iga_\perp A_\mu^a t_a - \frac{1}{2} g^2 a_\perp^2 A_\mu^a A_\mu^b t_a t_b, \tag{3.81}$$

where we have reintegrated the color indices $a$, the Gell-Mann matrices and our lattice constants $g$ and $a_\perp$ to remind ourselves of the 'squaring' operation for our color gauge fields. Inserting Eq. (3.81) into Eq. (3.80), we find

$$U_{xy}(x+0.5, y+0.5) \approx 1 + iga_\perp^2 \left(\partial_x A_y - \partial_y A_x\right) - g^2 a_\perp^2 \left[A_x, A_y\right]. \tag{3.82}$$

Reminding ourselves that we have switched to the positive covariant derivative and, therefore, the positive field strength tensor $F_{\mu\nu} = \partial_\mu A_\nu - \partial_\nu A_\mu + ig\left[A_\mu, A_\nu\right]$, we see that

$$U_{xy}(x+0.5, y+0.5) = 1 + iga_\perp^2 F_{xy}^a t^a \sim \exp\left(iga_\perp^2 F_{xy}\right) = \exp\left(i\mathcal{F}_{xy}\right), \tag{3.83}$$

where the last equality implies that the scaled field strength tensor is

$$\mathcal{F}_{ij} = ga_\perp^2 F_{ij}. \tag{3.84}$$

We can therefore obtain the field strength tensor at each lattice site by moving around the target site in a closed loop.

Our last bit of work before diving into the equations of motion themselves is in defining derivatives on the lattice with respect to the color gauge fields. This is fairly simple, but does require us to keep the Gell-Mann matrices in mind explicitly, which we have generally hidden within the definition of the color gauge fields. The transverse derivative is

$$\frac{\partial U_j(\vec{x})}{\partial \mathcal{A}_i^a(\vec{x})} = \frac{\partial}{\partial \mathcal{A}_i^a(\vec{x})} \exp\left(it_a \mathcal{A}_j^a(\vec{x})\right) = it_a \delta_{ij} U_j(\vec{x}), \tag{3.85}$$

while in the $\eta$-direction it reads

$$\frac{\partial U_\eta(\vec{x})}{\partial \mathcal{A}^a_\eta(\vec{x})} = it_a a_\eta U_\eta(\vec{x}), \tag{3.86}$$

where the difference between the two is in the preservation of a factor of the longitudinal spacing $a_\eta$. With this result in hand, we can now develop the equations of motion using the CGC Hamiltonian.

### 3.3.4 *Equations of Motion*

Let us begin by identifying the Lagrangian $\mathcal{L}$ within Eq. (3.14) [75] and move it to $\tau - \eta$ coordinates,

$$\begin{aligned} S &= -\frac{1}{2}\int d\tau d\eta d\vec{x}_\perp \sqrt{-g_{\mu\nu}}\,\mathrm{Tr}\left[F_{\mu\nu}g^{\mu\alpha}g^{\nu\beta}F_{\alpha\beta} + J_\mu g^{\mu\nu}A_\nu\right], \\ S &= \int d\tau d\eta d\vec{x}_\perp \frac{\tau}{2}\mathrm{Tr}\left[\frac{F^2_{\tau\eta}}{\tau^2} + F^2_{\tau i} - \frac{F^2_{\eta i}}{\tau^2} - \frac{F^2_{ij}}{2} + \frac{J_\eta A_\eta}{\tau^2}\right]. \end{aligned} \tag{3.87}$$

The source term $J_\eta A_\eta$ can be dropped here because, as we have established, the color sources are confined to the light-cone itself and exclusively contribute to the evolution through their sourcing of the color gauge fields $A_\mu$ in the initial conditions. Therefore, identifying $\mathcal{L}$ with this in mind, we have

$$\mathcal{L} = \frac{\tau}{2}\mathrm{Tr}\left[\frac{F^2_{\tau\eta}}{\tau^2} + F^2_{\tau i} - \frac{F^2_{\eta i}}{\tau^2} - \frac{F^2_{ij}}{2}\right]. \tag{3.88}$$

As mentioned previously, the conjugate momenta of our fundamental degrees of freedom $A_\mu$ are the chromo-electric fields $E_\mu$ in the proper time gauge $A^\tau = 0$, i.e.

$$\begin{aligned} E^i &= \frac{\partial \mathcal{L}}{\partial\left(\partial_\tau A_i\right)} = \tau\partial_\tau A_i, \\ E^\eta &= \frac{\partial \mathcal{L}}{\partial\left(\partial_\tau A_\eta\right)} = \frac{1}{\tau}\partial_\tau A_\eta, \end{aligned} \tag{3.89}$$

which can be inserted within the Hamiltonian density $\mathcal{H}$,

$$\mathcal{H} = \sum_i \dot{q}_i \frac{\partial \mathcal{L}}{\partial \dot{q}_i} - \mathcal{L}, \tag{3.90}$$

where the $q_i$ are the fundamental degrees of freedom of the Lagrangian. Doing so yields

$$\begin{aligned}\mathcal{H} &= E^i\left(\partial_\tau A_i\right) + E^\eta\left(\partial_\tau A_\eta\right) - \mathcal{L} \\ \mathcal{H} &= \mathrm{Tr}\left[\frac{(E^i)^2}{\tau} + \frac{F_{\eta i}^2}{\tau} + \tau(E^\eta)^2 + \tau F_{xy}^2\right].\end{aligned} \tag{3.91}$$

In the usual boost-invariant formulation discussed at the end of Section 3.3.2, $\mathcal{H}$ would become

$$\mathcal{H} = \mathrm{Tr}\left[\frac{(E^i)^2}{\tau} + \frac{(D_i\Phi)^2}{\tau} + \tau(\pi)^2 + \tau F_{xy}^2\right], \tag{3.92}$$

where the longitudinal direction color gauge and chromo-electric fields have simply been replaced by an adjoint representation scalar $\Phi$ and its conjugate momentum $\pi$.

Moving back to our lattice, we define $DU_i$ and $DU_{ij}$,

$$\begin{aligned}DU_i &= U_i - 1, \\ DU_{ij} &= U_{ij} - 1,\end{aligned} \tag{3.93}$$

which are more convenient for the purpose of numerical implementation. In terms of these 'new' quantities, we have

$$\begin{aligned}&DU_{ij}\left(\exp\left(i\mathcal{F}_{ij}\right)\right) - 1 \approx \left(1 + i\mathcal{F}_{ij}^a t_a - \frac{1}{2}\mathcal{F}_{ij}^a\mathcal{F}_{ij}^b t_a t_b\right) - 1 \\ &\Rightarrow DU_{ij} \approx i\mathcal{F}_{ij}^a t_a - \frac{1}{2}\mathcal{F}_{ij}^a\mathcal{F}_{ij}^b t_a t_b.\end{aligned} \tag{3.94}$$

Using $\mathrm{Tr}(t_a t_b) = \frac{1}{2}\delta_{ab}$, the real part of the trace of $DU_{ij}$ gives

$$\Re\left[\mathrm{Tr}\left(DU_{ij}\right)\right] = -\frac{1}{4}\mathcal{F}_{ij}^2. \tag{3.95}$$

With Eq. (3.95) in hand, we can first rewrite the lattice action $\mathcal{S}$,

$$\mathcal{S} = \frac{1}{2}\sum\left[\left(\mathcal{T}\,\mathrm{Tr}(\mathcal{E}^\eta)^2 + \frac{\mathrm{Tr}(\mathcal{E}^\rangle)^2}{\mathcal{T}} + \frac{4\Re\left[\mathrm{Tr}\left(DU_{i\eta}\right)\right]}{a_\eta^2\mathcal{T}} + 4\mathcal{T}\,\Re\left[\mathrm{Tr}\left(DU_{ij}\right)\right]\right)\right], \tag{3.96}$$

where quantities indexed by $i$ assume a sum over $i = x, y$. The lattice Hamiltonian density is then

$$\tilde{\mathcal{H}} = \frac{1}{2}\left[\frac{\mathrm{Tr}(\mathcal{E}^i)^2}{\mathcal{T}} + \mathcal{T}\,\mathrm{Tr}(\mathcal{E}^\eta)^2 + \frac{4\Re\left[\mathrm{Tr}\left(DU_{i\eta}\right)\right]}{a_\eta^2\mathcal{T}} + 4\mathcal{T}\,\Re\left[\mathrm{Tr}\left(DU_{ij}\right)\right]\right]. \tag{3.97}$$

To find equations of motion through the Hamiltonian (lattice or continuous), we calculate

$$\begin{aligned}\frac{\partial \mathcal{H}}{\partial E^\mu} &= \frac{\partial A_\mu}{\partial \tau} \\ \frac{\partial \mathcal{H}}{\partial A_\mu} &= -\frac{\partial E^\mu}{\partial \tau}.\end{aligned} \tag{3.98}$$

The first two equations are trivial to obtain through, and simply mirror what we found in Eq. (3.89), i.e.

$$\partial_\tau A_i = \frac{1}{\tau} E^i \tag{3.99}$$

$$\partial_\tau A_\eta = \tau E^\eta. \tag{3.100}$$

The other equations of motion are a bit harder to extract. Indeed, taking the typical Hamiltonian formulation, we find

$$\begin{aligned}-\partial_\tau E^i &= \frac{\partial \mathcal{H}}{\partial A_i} \\ -\partial_\tau E^i &= \frac{1}{2}\frac{\partial}{\partial A_i}\left[\frac{F_{i\eta}^2}{\tau} + \tau F_{ij}^2\right]\end{aligned} \tag{3.101}$$

and

$$\begin{aligned}-\partial_\tau E^\eta &= \frac{\partial \mathcal{H}}{\partial A_\eta} \\ -\partial_\tau E^\eta &= \frac{1}{2}\frac{\partial}{\partial A_\eta}\left[\frac{F_{i\eta}^2}{\tau} + \tau F_{ij}^2\right].\end{aligned} \tag{3.102}$$

Equations (3.101) and (3.102) are not easy to parse through. However, we can use the non-Abelian Gauss law to obtain these equations and solve them more efficiently. Indeed, remarking that, in our proper time gauge $A^\tau = 0$, we have

$$\begin{aligned}E^\eta &= \tau F^{\eta\tau} \\ E^i &= \tau F^{i\tau}.\end{aligned} \tag{3.103}$$

We can obtain 4 sets of equations through our Gauss Law. The first, Eq. (3.71), was used previously. Following the general form

$$0 = \left[D_\alpha, \tau F^{\alpha\beta}\right], \tag{3.104}$$

with the first being with $\beta = \tau$, we can create 3 more equations. We start with $\beta = \eta$,

$$\begin{aligned} 0 &= [D_\alpha, \tau F^{\alpha\eta}] \\ 0 &= [D_\tau, \tau F^{\tau\eta}] + \left[D_i, \tau F^{i\eta}\right] \\ 0 &= -\partial_\tau E^\eta + \frac{1}{\tau}\left[D_i, F_{i\eta}\right] \\ \partial_\tau E^\eta &= \frac{1}{\tau}\left[D_i, F_{i\eta}\right], \end{aligned} \tag{3.105}$$

where we have used $g_{ii}g_{\eta\eta} = \frac{1}{\tau^2}$ to lower the indices in the second to last step. The equations for the transverse components $\beta = i$ give

$$\begin{aligned} 0 &= \left[D_\alpha, \tau F^{\alpha i}\right] \\ 0 &= \left[D_\tau, \tau F^{\tau i}\right] + \left[D_j, \tau F^{ji}\right] + \left[D_\eta, \tau F^{\eta i}\right] \\ 0 &= -\partial_\tau E^i + \tau\left[D_j, F^{ji}\right] + \tau\left[D_\eta, F^{\eta i}\right] \\ \partial_\tau E^i &= \tau\left[D_j, F_{ji}\right] + \frac{1}{\tau}\left[D_\eta, F_{\eta i}\right], \end{aligned} \tag{3.106}$$

which completes our set of continuous equations of motion. The fact we have used Gauss' law here entails that the system of equations obtained from the Hamiltonian alone would not have been enough to determine the gauge fields. Therefore, the equations of motion include Gauss' law in the vacuum, such that they read

$$\begin{aligned} \partial_\tau E^i &= \frac{1}{\tau}\left[D_\eta, F_{\eta i}\right] + \tau\left[D_j, F_{ji}\right] \\ \partial_\tau E^\eta &= \frac{1}{\tau}\left[D_i, F_{i\eta}\right] \\ \partial_\tau A_i &= \frac{1}{\tau}E^i \\ \partial_\tau A_\eta &= \tau E^\eta \\ \left[D_i, E^i\right] &+ \left[D_\eta, E^\eta\right] = 0. \end{aligned} \tag{3.107}$$

We can now translate these onto the lattice. Starting from the understanding that Eq. (3.97) constitutes a sum over all lattice sites, and given the fact that we will have to differentiate with respect to the color gauge field $A_\mu$ at a specific edge (i.e., $A_\mu(\vec{x}_\perp)$), the

elements of the Hamiltonian which will 'survive' differentiation by the gauge field will come from two different plaquettes. For a given link in the $x$ direction, we will have

$$\begin{aligned}
&U_{xy}(x+0.5,y+0.5) = \\
&\qquad U_x(x+0.5,y)U_y(x+1,y+0.5)U_x^\dagger(x+0.5,y+1)U_y^\dagger(x,y+0.5), \\
&U_{xy}(x+0.5,y-0.5) = \\
&\qquad U_x(x+0.5,y-1)U_y(x+1,y-0.5)U_x^\dagger(x+0.5,y)U_y^\dagger(x,y-0.5)
\end{aligned} \tag{3.108}$$

where the gauge links $U_x(x+0.5,y)$ and $U_x^\dagger(x+0.5,y)$ both depend on $A_x(x+0.5,y)$. With this in mind, we can take the derivative of our lattice Hamiltonian,

$$\begin{aligned}
\frac{\partial\tilde{\mathcal{H}}}{\partial\mathcal{A}_x^a(\vec{x}_\perp)} &= \frac{\partial}{\partial\mathcal{A}_x^a(\vec{x}_\perp)}\left(-2\mathcal{T}\Re\left[\mathrm{Tr}(U_{xy})\right]-\frac{2}{a_\eta^2\mathcal{T}}\Re\left[\mathrm{Tr}(U_{x\eta})\right]\right) \\
&= -2\Re\left(i\mathrm{Tr}\left[t_a\left(\mathcal{T}\left[U_{xy}(\vec{x}_\perp+\tfrac{a_y}{2})-U_{-yx}(\vec{x}_\perp+\tfrac{a_y}{2})\right]\right.\right.\right. \\
&\quad \left.\left.\left.+\frac{i}{\mathcal{T}a_\perp^2}\left[U_{x\eta}(\vec{x}_\perp+\tfrac{a_\eta}{2})-U_{-\eta x}(\vec{x}_\perp+\tfrac{a_\eta}{2})\right]\right)\right]\right) \\
&= 2\Im\left(\mathrm{Tr}\left[t_a\left(\mathcal{T}\left[U_{xy}(\vec{x}_\perp+\tfrac{a_y}{2})-U_{-yx}(\vec{x}_\perp+\tfrac{a_y}{2})\right]\right.\right.\right. \\
&\quad \left.\left.\left.+\frac{1}{\mathcal{T}a_\perp^2}\left[U_{x\eta}(\vec{x}_\perp+\tfrac{a_\eta}{2})-U_{-\eta x}(\vec{x}_\perp+\tfrac{a_\eta}{2})\right]\right)\right]\right),
\end{aligned} \tag{3.109}$$

where we have used the fact that another two plaquettes, in the $x-\eta$ plane this time, also contain factors of $A_x(x+0.5,y)$, and have used the shorthand $a_y$ to mean the unit lattice vector, in lattice units, in the $y$ direction. Using $\Im(z) = -\frac{i}{2}\left[z-z^*\right]$, we get

$$\begin{aligned}
\frac{\partial\tilde{\mathcal{H}}}{\partial\mathcal{A}_x^a(\vec{x}_\perp)} &= -i\mathrm{Tr}\left[t_a\left(\mathcal{T}\left[U_{xy}(\vec{x}_\perp+\tfrac{a_y}{2})-U_{-yx}(\vec{x}_\perp+\tfrac{a_y}{2})-U_{yx}(\vec{x}_\perp+\tfrac{a_y}{2})\right.\right.\right. \\
&\quad \left.\left.+U_{x-y}(\vec{x}_\perp+\tfrac{a_y}{2})\right]+\frac{1}{\mathcal{T}a_\perp^2}\left[U_{x\eta}(\vec{x}_\perp+\tfrac{a_\eta}{2})-U_{-\eta x}(\vec{x}_\perp+\tfrac{a_\eta}{2})\right. \\
&\quad \left.\left.\left.-U_{\eta x}(\vec{x}_\perp+\tfrac{a_\eta}{2})+U_{x-\eta}(\vec{x}_\perp+\tfrac{a_\eta}{2})\right]\right)\right].
\end{aligned} \tag{3.110}$$

And so, the lattice equation of motion for the chromo-electric field components in the transverse direction is

$$\begin{aligned}
\partial_{\mathcal{T}}\mathcal{E}^i = \frac{i}{2}\left[\left(\mathcal{T}\left[U_{ij}(\vec{x}_\perp)-U_{-ji}(\vec{x}_\perp)-U_{ji}(\vec{x}_\perp)+U_{i-j}(\vec{x}_\perp)\right]\right.\right. \\
\left.\left.+\frac{1}{\mathcal{T}a_\perp^2}\left[U_{i\eta}(\vec{x}_\perp)-U_{-\eta i}(\vec{x}_\perp)-U_{\eta i}(\vec{x}_\perp)+U_{i-\eta}(\vec{x}_\perp)\right]\right)-\mathrm{trace}\right],
\end{aligned} \tag{3.111}$$

where '−trace' subtracts the part that is proportional to the trace taken in Eq. (3.110). In the $\eta$ direction, because of the lattice spacing $a_\eta$, things are a bit different,

$$\begin{aligned}\partial_{\mathcal{T}}\mathcal{E}^{\eta} = \frac{i}{2\mathcal{T}a_{\eta}}\Big[&U_{\eta x}(\vec{x}_{\perp}) - U_{-x\eta}(\vec{x}_{\perp}) - U_{x\eta}(\vec{x}_{\perp}) + U_{\eta -x}(\vec{x}_{\perp}) \\ &+U_{\eta y}(\vec{x}_{\perp}) - U_{-y\eta}(\vec{x}_{\perp}) - U_{y\eta}(\vec{x}_{\perp}) + U_{\eta -y}(\vec{x}_{\perp}) - \text{trace}\Big] .\end{aligned} \tag{3.112}$$

The equations of motion for the transverse gauge fields are simpler to obtain,

$$\begin{aligned}&\partial_{\mathcal{T}}\mathcal{A}_i = \frac{\mathcal{E}^i}{\mathcal{T}} \\ &\partial_{\mathcal{T}}U_i = i\partial_{\mathcal{T}}\mathcal{A}_i U_i \\ &\Rightarrow \partial_{\mathcal{T}}U_i = i\frac{\mathcal{E}^i}{\mathcal{T}}U_i,\end{aligned} \tag{3.113}$$

while in the longitudinal direction, the same logic gives

$$\partial_{\mathcal{T}}U_{\eta} = ia_{\eta}\mathcal{T}\mathcal{E}^{\eta}U_{\eta}. \tag{3.114}$$

We are now able to evolve the color gauge and chromo-electric fields in time. To do so numerically is not trivial, given the coupled nature of the equations of motion. To solve this problem, a leap-frog algorithm is implemented. That is, the two groups of fields $A_\mu$ and $E^\mu$ are evolved sequentially: we evaluate the equations for the chromo-electric fields at time $\tau$, and then evaluate the equations for the color gauge fields at time $\tau + d\tau/2$. We then have a coherent numerical framework from which our degrees of freedom can be evolved. Once our pre-determined thermalization time $\tau_{\text{sw}}$ is reached, IP-Glasma terminates and we move to the hydrodynamic description of the QGP proper. The interface between the out-of-equilibrium glasma and the thermalized QGP is guided by the stress-energy tensor $T^{\mu\nu}$.

## 3.4 SWITCHING TO HYDRODYNAMICS

One of the many advantages of IP-Glasma as an initial state model is its ability to build a coherent and fully physically motivated stress-energy tensor $T^{\mu\nu}$. Indeed, since the hydrodynamics phase will be interested in ensemble averaged quantities such as energy,

pressure, and flow, $T^{\mu\nu}$ is the fundamental quantity that will be evolved. Classical Yang-Mills theory provides an analytical formula for construction of the stress-energy via the field strength tensor $F_{\mu\nu}$ [75],

$$T^{\mu\nu} = -g^{\mu\alpha}g^{\nu\beta}g^{\gamma\delta}F_{\alpha\gamma}F_{\beta\delta} + \frac{1}{4}g^{\mu\nu}g^{\alpha\gamma}g^{\beta\delta}F_{\alpha\beta}F_{\gamma\delta}. \tag{3.115}$$

This tensor is constructed everywhere on the lattice, and is fully symmetric and gauge invariant. It can be diagonalized to obtain its eigenvalues and eigenvector, of which the timelike pair (i.e., the pair with a positive eigenvalue and where the 4-norm of the eigenvector is positive) is kept as the local energy density and glasma flow. Explicitly,

$$T^{\mu}_{\nu}u^{\nu} = \epsilon u^{\mu} \quad \text{where } \epsilon > 0 \ \& \ u_{\mu}u^{\mu} > 0. \tag{3.116}$$

Once this pair is identified, the flow velocity is normalized to 1, i.e., $u_{\mu}u^{\mu} = 1$.

The stress-energy tensor also contains information about the shear-stress tensor $\pi^{\mu\nu}$, which itself is important as it informs us about the viscosity of the system. This viscosity has been shown to be an important feature of QGP [76] which, if ignored, could lead to mismatches between calculations and experimental results. The shear-stress tensor is defined as

$$\pi^{\mu\nu}_{\text{IPG}} = T^{\mu\nu}_{\text{CYM}} - T^{\mu\nu}_{\text{ideal}}, \tag{3.117}$$

where

$$T^{\mu\nu}_{\text{ideal}} = (\epsilon + P)u^{\mu}u^{\nu} - Pg^{\mu\nu}, \tag{3.118}$$

where we are in the Landau frame, which indicates that the flow $u^{\mu}$ is that of the energy density $\epsilon$. Classical Yang-Mills being a massless theory sets the pressure $P$ at each lattice site to be

$$P_{\text{IPG}} = \frac{\epsilon}{3}, \tag{3.119}$$

allowing us to easily evaluate the ideal hydrodynamic stress-energy tensor $T^{\mu\nu}_{\text{ideal}}$ everywhere on the lattice. The construction of $\pi^{\mu\nu}_{\text{IPG}}$ is therefore simple given the theoretical

features of IP-Glasma. The introduction of the conformal pressure in Eq. (3.119) raises an important question: in hydrodynamics, an equation of state will dictate the pressure of the system as a function of its energy density as well as other thermodynamic quantities. This equation of state aims to describe an equilibrated system of quarks and gluons, which is very different from the purely gluonic state described by IP-Glasma. Its form will therefore be much less trivial than that of the conformal pressure. How, then, do we reconcile the system's conformal pressure $P_{\mathrm{IPG}}$ to the hydrodynamic pressure $P_{\mathrm{hydro}}$ at switching time $\tau_{\mathrm{sw}}$? There is no reason for the two values to be equal a priori, so we must find a way to resolve potential tensions between the two pressure values at transition. To do this, we initialize the hydrodynamic phase of the simulation with a bulk pressure $\Pi$ equal to the difference between the conformal pressure and the pressure obtained through the equation of state, i.e.,

$$\Pi = P_{\mathrm{IPG}} - P_{\mathrm{hydro}}. \tag{3.120}$$

We can therefore use all of the information from our initial state to coherently initialize the hydrodynamic phase, a feature unique to IP-Glasma.

We are now ready to look at the remaining phases of heavy-ion collisions, and discuss how they impact the observables which are relevant to our goal of constraining nuclear shape.

# 4

# QGP: EVOLUTION, FREEZE-OUT AND OBSERVABLES

The previous chapters have discussed where and how nuclear deformation occurs, how it manifests itself in the highly energetic and paired (i.e. two ions) setting of heavy-ion collisions, how pre-collision nuclear structure translates directly to color charge fluctuations (and, therefore, fluctuations in the color gauge fields $A_\mu$) and how those purely gluonic fields evolve in the pre-equilibrium phase. We have, consequently, established that this pre-equilibrium phase is essential if we want to capture the entire scope of initial fluctuations in heavy-ion collisions. It is now time to describe the QGP as it only truly becomes a QGP once it is thermalized and offers itself to a hydrodynamical description. We will introduce the ideal hydrodynamic conservation equations which guide the evolution of QGP through its existence. We will then show how deviations from this ideal hydrodynamics formulation, through the inclusion of the viscous components introduced at the end of the last chapter, are integrated into the theory. Including viscosity in the evolution equations will entail the incorporation of specific viscous parameters, which will be appropriately motivated. Since we are interested in simulations, we will introduce the numerical framework through which these equations are implemented and evolved, namely MUSIC [18]. As established in the introduction, as QGP evolves hydrodynamically, it expands and cools until quarks and gluons reconfine into hadrons. We will describe how, through Cooper-Frye freeze-out and sampling [19, 20], a gas of hadrons is generated from a spatiotemporal hypersurface generated by MUSIC throughout its evolution. Once particlized, these hadrons will be evolved as a hadron gas, with relevant scatterings and decays taken into account, until all end-state particles have

reached the 'detectors', represented in our simulations by reaching a pre-determined distance from the position of the beam-pipe in our simulations. This final phase of our framework is performed using SMASH [21]. The final section of this chapter will be dedicated to adequately defining observables (in other words, the properties of collision events belonging to similar centrality classes), their relevance to our stated goal of constraining nuclear deformation, and their relation to the various phases of the entire evolution, from initial state energy deposits to the evolution of the QGP itself.

## 4.1 HYDRODYNAMICS

In our description, we will preserve the natural ordering of the different phases of our simulations by describing them in the order they appear, as was done in the previous two chapters. Let us therefore start by looking at the initialization of the hydrodynamic phase through the final time step of IP-Glasma.

### 4.1.1 *From Glasma to Quark-Gluon Plasma*

At the end of the previous chapter, we introduced the stress-energy and shear-stress tensors $T^{\mu\nu}$ & $\pi^{\mu\nu}$, as well as the bulk pressure $\Pi$. In IP-Glasma, $T^{\mu\nu}$ was calculated using Eq. (3.115), meaning it inherently depended on the degrees of freedom of the theory, the color gauge fields $A^{\mu}$. This dependence upon the color gauge fields means that qualitative features of the fields should, in theory, translate directly to features of the tensor. Figure 20 showed the energy deposit at initial time $\tau = 0.01$ fm; while the goal of Fig. 20 was to link the initialization phase (nucleon sampling, color charge fluctuations) to the initial color gauge fields $A^{\mu}$, it did also provide a small window into the 'spikiness' of initial configurations produced by IP-Glasma. Indeed, one can see that $\epsilon$ varies considerably between neighboring lattice sites (the pixels in the 2D slice). However, the sheer scale of the initial time energy deposits makes this a bit hard

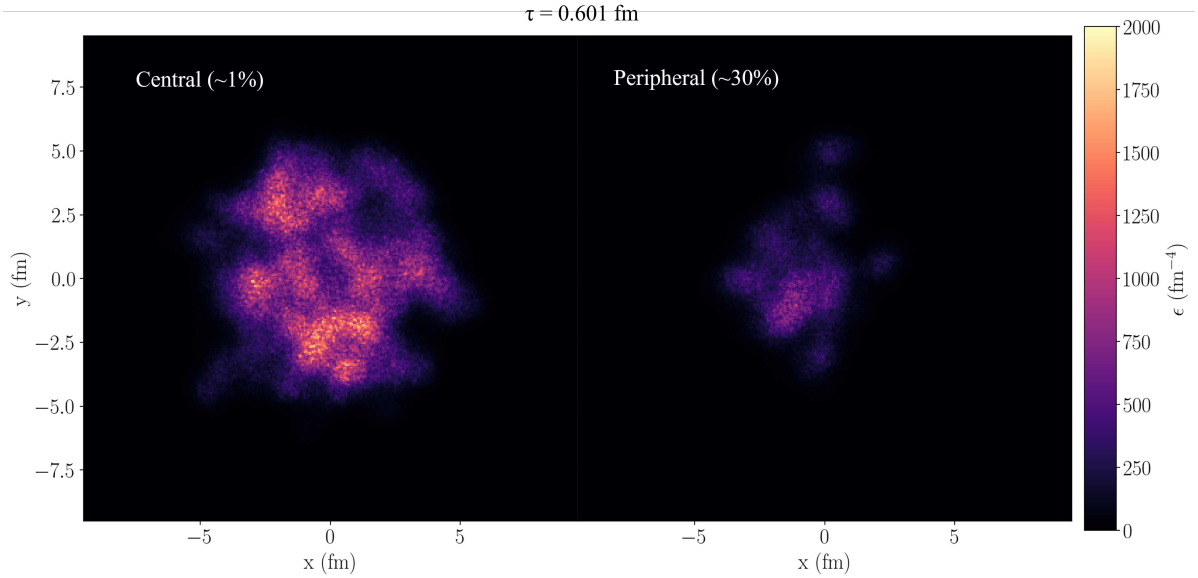


Figure 22: Energy density ($\epsilon$) distributions of a (**left**) central and a (**right**) peripheral event at switching time $\tau = 0.602$ fm for Xe+Xe at 5.44 TeV. The maximum energy of the scale given on the right is 100× smaller than the one provided in Fig. 20.

to appreciate, as most energetic cells are neighbored by other bright cells. Figure 22 provides the energy density configurations of the same two events as Fig. 20 taken at the end of the IP-Glasma evolution, at $\tau = 0.602$ fm[1]. In Fig. 22, the spikiness mentioned above is a lot more apparent, with neighboring cells, at times, having > 50% differences in energy density. As explained previously, this spikiness is due to the color charge fluctuations being dependent on the saturation scale $Q_s$, which is calculated at each lattice site. These large variations in the energy density tell us that the stress-energy tensor $T^{\mu\nu}$ varies greatly from site to site, which makes sense given that the glasma phase is inherently out of equilibrium. Figure 23 shows the same transverse slice rotated in 3D space to provide a better view of the fluctuations exhibited by the IP-Glasma energy deposits. We can see how the surface is far from smooth, and how, while peaks can congregate, most peaks occur close to valleys.

As established in Section 3.4, the energy density is calculated through diagonalizing $T^{\mu\nu}$ and retaining the eigenvalue associated to the timelike eigenvector (i.e. satisfying

[1] This time was chosen phenomenologically and following the Bayesian calibration conducted in Ref. [77].

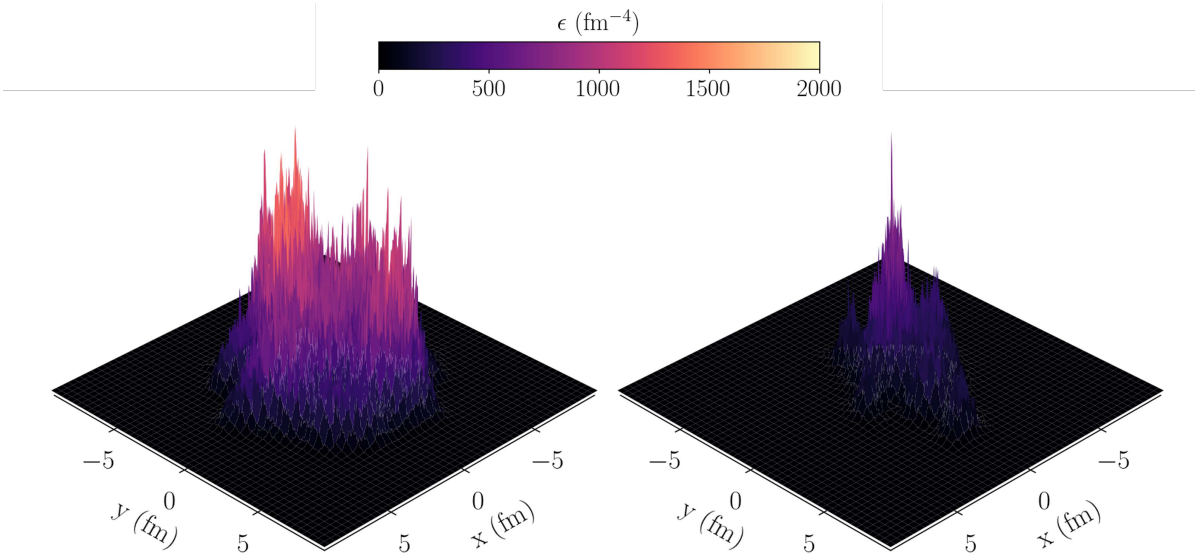


Figure 23: Energy density ($\epsilon$) distributions of a (**left**) central and a (**right**) peripheral event at switching time $\tau = 0.602\,\text{fm}$ for Xe+Xe at 5.44 TeV. Slice is represented in 3 dimensions (with $z$-axis being $\epsilon$) to better show the large variations of energy density.

$u_\mu u^\mu > 0$), which ends up being the glasma flow velocity. Given the significant spatial variations of the energy density and the inherent link between $\epsilon$ and $u^\mu$, it is fair to assume that the flow extracted from the CYM stress-energy tensor is prone to large fluctuations. Figure 24 provides an overlayed view of the flow at switching time for the central event shown in Figs. 20, 22 and 23. It is hard (in the left panel) to make sense of the flow's features when observing the entire interaction region. However, zooming in on a region within the QGP that is $2\,\text{fm} \times 2\,\text{fm} = 4\,\text{fm}^2$, the features of the flow (or lack thereof) at switching time become clearer. Indeed, we see that, while neighboring fluid cells usually preserve some form of coherence in their collective flow, neighbors sometimes have practically opposite flow vectors. Therefore, large local fluctuations in energy density translate to large fluctuations in the flow. These large local discrepancies, as explained previously, are mostly due to the nature of the initialization of the color gauge fields - the degrees of freedom of our initial state - which relied on sampling color charges according to quantities which fluctuate from lattice site to lattice site.

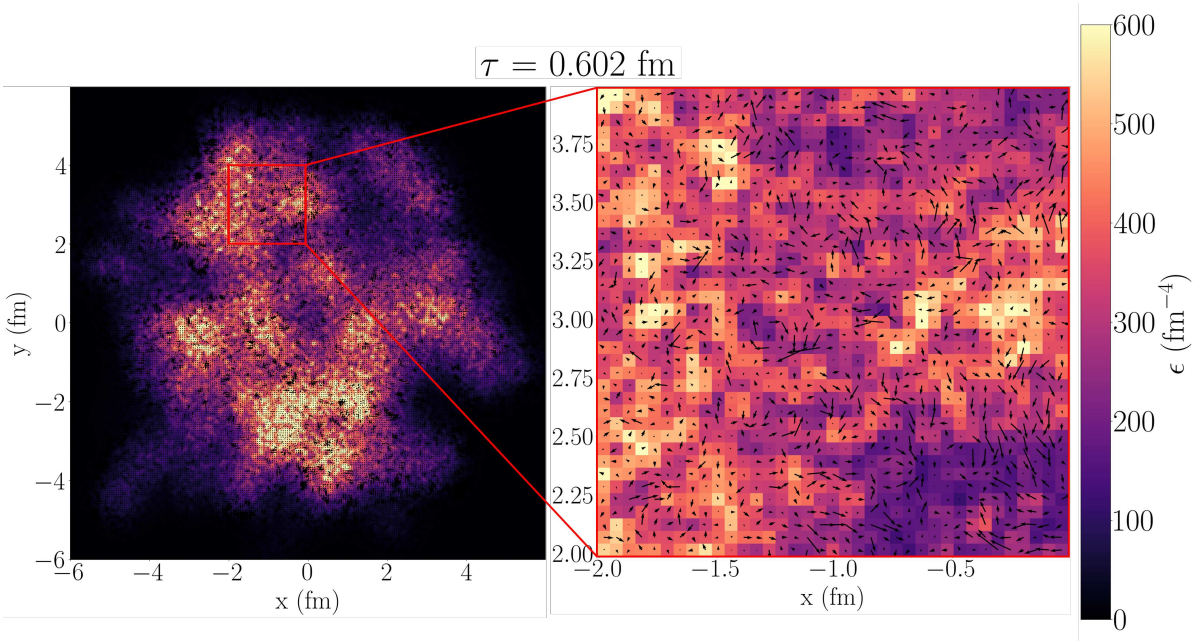


Figure 24: Energy density ($\epsilon$) distribution of a central event at switching time $\tau = 0.602$ fm for Xe+Xe at 5.44 TeV. The flow velocity vectors are overlayed, and an inset is provided to give a clearer picture of the features of the local flow.

Because these gauge fields are evolved according to the CYM equations, these initial time fluctuations in the energy density and flow have not yet had enough time to dissipate and isotropize in the IP-Glasma phase. This spikiness at various levels is a characteristic of IP-Glasma which, as we will now show, the hydrodynamics phase smoothes out by definition.

### 4.1.2 *Hydrodynamical Evolution*

Hydrodynamics is, at its core, concerned with more macroscopic thermodynamic quantities; as such, the stress-energy and shear-stress tensors will encode the fundamental degrees of freedom of the theory themselves. We transition from the color gauge fields to thermodynamic quantities as our degrees of freedom because hydrodynamics is concerned with long-wavelength modes: instead of attempting to track the particles (gluon

fields) in this phase, we turn to more spatially-coarse collective motion, which is better described by thermodynamic quantities [78, 79].

As mentioned, we employ a viscous relativistic hydrodynamics numerical simulation called MUSIC [18] to evolve the QGP. When describing hydrodynamics, it is usually preferred to begin with an ideal description of hydrodynamics, followed by the introduction of deviations from ideal hydrodynamics (here, viscosity) further along. Concretely, ideal hydrodynamics is fully described mathematically through conservation equations. Ignoring other conserved currents (such as baryonic currents) as they make subdominant contributions at the energies we are interested in [79, 80], the first set is given by

$$\begin{aligned} &\partial_\mu T^{\mu\nu} = 0 \\ &\partial_\mu \left( (\epsilon + P) u^\mu u^\nu - P g^{\mu\nu} \right) = 0, \end{aligned} \tag{4.1}$$

where we have used Eq. (3.118) to rewrite the energy-momentum conservation relation into the guiding equation of ideal hydrodynamics. This refactoring makes it clear that the ideal formulation provides five fields to evolve: the energy density $\epsilon$, the pressure $P$ and the flow velocity $u^\mu$. One may notice that the fields we named provide six components. However, given the normalization condition on the flow velocity $u^\mu u_\mu = 1$, the number of independent fields provided by the flow 4-vector $u^\mu$ decreases from 4 to 3. One should also note that, while the pressure $P$ is contained in this conservation equation, given the use of an equation of state in this phase, it is fully determined by the local energy density $\epsilon$, i.e. $P \longrightarrow P(\epsilon)$.

Our description would have ended here if we had used an ideal hydrodynamics framework. However, research conducted as a response to the initialization of RHIC showed that viscous corrections played an important role in producing observables such as elliptic flow [81]. These corrections come in the form of expansions of the stress-energy tensor $T^{\mu\nu}$ in terms of the order of the gradients of the fundamental hydrodynamic quantities ($\epsilon$, $u^\mu$, $P$) found within a given part of $T^{\mu\nu}$. In other words, Eq. (3.118) (written as $T^{\mu\nu}_{\text{ideal}}$ in Section 3.4) would be the $0^{\text{th}}$ order contribution, $T^{\mu\nu}_0$.

Because of the possibility of acausal propagation of information via superluminal flow [82], MUSIC must use second-order viscous hydrodynamics. The expansion of the stress-energy tensor will therefore look like

$$T^{\mu\nu} = T_0^{\mu\nu} + T_1^{\mu\nu} + T_2^{\mu\nu}. \tag{4.2}$$

Following discussions presented in Ref. [83], let us define these deviations.

Using the Landau frame,[2] the frame in which the flow velocity $u^\mu$ is defined as the movement of the energy density $\epsilon$, we have

$$u_\mu T^{\mu\nu} = \epsilon u^\nu. \tag{4.3}$$

Using Eq. (4.3) with Eq. (3.118), we find that

$$u_\mu \left(T_1^{\mu\nu} + T_2^{\mu\nu}\right) = 0, \tag{4.4}$$

since the condition provided by Eq. (4.3) is already fully satisfied by the ideal stress-energy tensor $T_0^{\mu\nu}$. Defining the projection operator $\Delta^{\mu\nu}$ and co-moving derivative $D_\mu$ as

$$\Delta^{\mu\nu} = g^{\mu\nu} - u^\mu u^\nu$$
$$D_\mu = \partial_\mu - u_\mu u^\alpha \partial_\alpha$$

we have, for the first-order deviation,

$$T_1^{\mu\nu} = \eta \left( D^\mu u^\nu + D^\nu u^\mu - \frac{2}{3}\Delta^{\mu\nu}\partial_\beta u^\beta \right) + \zeta \Delta^{\mu\nu}\partial_\beta u^\beta, \tag{4.5}$$

where two new parameters have been added, namely $\eta$, the shear viscosity, and $\zeta$, the bulk viscosity. If we separate the effective hydrodynamic corrections into a traceless and a trace part, we can retrieve the shear-stress and bulk pressures introduced previously, i.e.,

$$T^{\mu\nu} = T_0^{\mu\nu} + \pi^{\mu\nu} + \Delta^{\mu\nu}\Pi, \tag{4.6}$$

[2] There exist other frames which use other quantities as their source for flow. The Eckart frame, for example, uses the velocity of net baryon number flow. However, given we are not considering such conserved currents in this work, the Eckart frame cannot be used here at all.

where the shear-stress tensor $\pi^{\mu\nu}$ and the bulk pressure $\Pi$ have now replaced our first and second order corrections $T_1^{\mu\nu}$ and $T_2^{\mu\nu}$. Therefore, moving away from ideal hydrodynamics implies the addition of viscosity, and our corrections will manifest themselves as further expansions of $\pi^{\mu\nu}$ and $\Pi$. Linking Eq. (4.6) to Eq. (4.5), we find that, to first order,

$$\begin{aligned} \pi^{\mu\nu} &= \eta \left( D^\mu u^\nu + D^\nu u^\mu - \frac{2}{3}\Delta^{\mu\nu}\partial_\beta u^\beta \right) = 2\eta\sigma^{\mu\nu}, \\ \Pi &= \zeta \Delta^{\mu\nu}\partial_\beta u^\beta, \end{aligned} \tag{4.7}$$

where we have defined the velocity shear tensor $\sigma^{\mu\nu}$ and where the names for $\eta$ and $\zeta$ now make sense. We now have definitions for the shear-stress tensor and bulk pressure but no evolution equations. These equations are introduced by moving to second-order and are relaxation-time equations first developed by Israel, Müeller and Stewart [80, 84], and extended through kinetic theory by Denicol, Niemi, Molnar and Rischke (DNMR) more recently [85]. They yield

$$\dot{\pi}^{\mu\nu} = \frac{1}{\tau_\pi}\left( -\pi^{\mu\nu} + 2\eta\sigma^{\mu\nu} - \frac{4}{3}\tau_\pi \pi^{\mu\nu}\Theta + \frac{9}{70P}\pi_\alpha^{\langle\mu}\pi^{\nu\rangle\alpha} - \frac{10}{7}\tau_\pi \pi_\alpha^{\langle\mu}\sigma^{\nu\rangle\alpha} + \frac{6}{5}\tau_\pi \Pi\sigma^{\mu\nu} \right), \tag{4.8}$$

$$\dot{\Pi} = \frac{1}{\tau_\Pi}\left( -\Pi - \zeta\Theta - \frac{2}{3}\tau_\Pi \Pi\Theta + \frac{8}{5}\left(\frac{1}{3} - c_s^2\right)\tau_\Pi \pi^{\mu\nu}\sigma_{\mu\nu} \right), \tag{4.9}$$

where we have introduced the shorthand $\Theta = \partial_\mu u^\mu$ for the expansion rate, $c_s$ is the speed of sound, and where brackets $\langle\ \rangle$ refer to the traceless part of the symmetrized tensors. Furthermore, the dots above $\Pi$ and $\pi^{\mu\nu}$ refer to co-moving derivatives, i.e., $\dot{\Pi} = u^\mu\partial_\mu\Pi$. The relaxation times $\tau_\pi$ & $\tau_\Pi$ characterize the timescales across which the shear-stress tensor and bulk pressure approach their first-order form, Eq. (4.7) [86]. They are set to [85]

$$\begin{aligned} \tau_\pi &= \frac{5\eta}{\epsilon + P}, \\ \tau_\Pi &= \frac{\zeta}{(\epsilon + P)(14.55(1/3 - c_s^2)^2)}. \end{aligned}$$

Like in IP-Glasma, these equations must be respected at every lattice site. The parameters $\eta$ and $\zeta$, introduced above, depend on the site's thermodynamic quantities.

More specifically, they are usually dependent on the temperature $T$, which is itself determined through the equation of state, i.e. $T(\epsilon)$. Following a detailed Bayesian analysis of our workflow conducted in Ref. [77, 87], $\eta/s$, the specific shear viscosity, is constant, while the specific bulk viscosity, $\zeta/s$, is temperature-dependent. Their respective forms are

$$\frac{\eta}{s} = 0.136 \tag{4.10}$$

$$\frac{\zeta}{s}(T) = N \exp\left(-\frac{(T - T_p)^2}{B^2_{(L,G)}}\right), \tag{4.11}$$

where $s$ is the entropy density. In Eq. (4.11), we find an asymmetrical gaussian distribution, with $N = 0.13$, $T_p = 0.18\,\text{GeV}$, $B_L = 0.02\,\text{GeV}$ and $B_G = 0.12\,\text{GeV}$. Whether $B_L$ or $B_G$ is found in the exponent's denominator depends on the relationship between $T$ and $T_p$: if $T < T_p$, we have $B_L$, while we use $B_G$ if $T > T_p$. Figure 25 shows Eq. (4.11) compared to the posterior 90% confidence interval inferred in the Bayesian analysis mentioned above [77, 87]. While its peak falls outside of the confidence interval, our parametrization remains fully consistent with the analysis findings. In Bayesian analysis, a 90% confidence interval provides a general region of space where a particular parameter should lie while allowing some part of the parameter curve to lie outside. Given that some of the beam energies considered in this work are much smaller than those considered in Ref. [77, 87], some of our results are more sensitive to low-temperature bulk features. The bulk viscosity we have used reflects this sensitivity while preserving consistency with the Bayesian analysis in Ref. [77, 87].

We have mentioned the equation of state (EoS) in passing a few times in this section. As established, the EoS is necessary to close the systems of equations developed for use in our hydrodynamics framework. As has been implicitly established, an EoS relates the state variables $(P,\ T,\ s, \epsilon)$ under given conditions. The EoS must be consistent with the properties of QCD matter at different stages of its evolution. It must match lattice calculations when the QGP is extremely hot (i.e. when we move from IP-Glasma to MUSIC) and tend towards conformality in the $T \to \infty$ limit [88]. It must also match that of a hadron gas to be consistent with the transition from MUSIC (hydrodynamics)

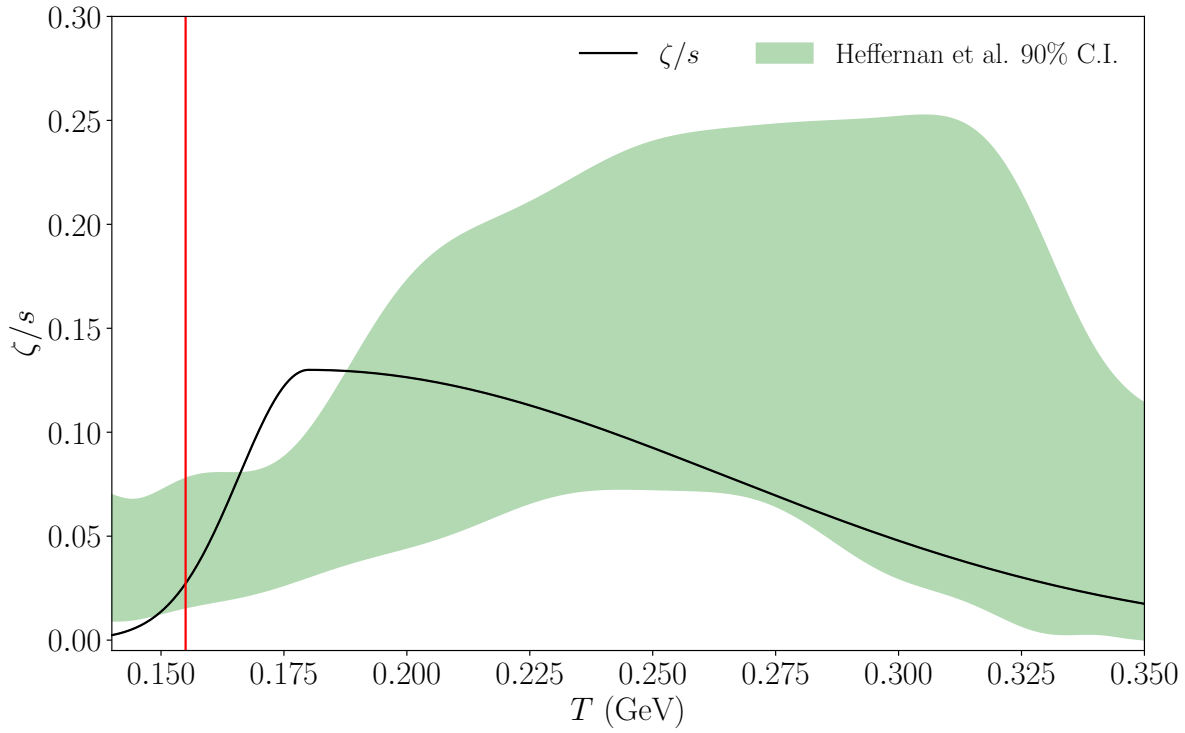


Figure 25: Specific bulk viscosity $\zeta/s$ as a function of temperature. The red vertical line shows the switching temperature $T_{sw} = 155\,\text{MeV}$ below which hydrodynamic cells are frozen out.

to particlization. Therefore, the construction and selection of an appropriate EoS must be taken seriously to preserve consistency across the various stages of our simulations. In this work, we have used an EoS which connects the HotQCD calculation [88] from high- to low-temperatures to a list of general stable resonances selected to reproduce that of Ref. [89]. A more detailed discussion regarding careful EoS construction may be found in Ref. [90].

We have concluded our description of the mathematical underpinnings of the hydrodynamical evolution. However, what does viscous relativistic hydrodynamics do to the spiky initial state configuration that we presented previously? First of all, through fluid expansion across timescales much larger than that of our initial state (generally more than 10× larger), the QGP cools. As we will see a bit further, this cooling is a crucial feature of the hydrodynamics phase, as it brings our highly energetic system of deconfined quarks and gluons - the QGP - back down to energies where color confinement

applies and where the QGP must give way to a gas of hadrons, the final products of the collision. Secondly, fluids described through hydrodynamics are driven by pressure-gradient forces, which drive the expansion we just introduced. Indeed, if we look at the Navier-Stokes equation for a non-relativistic medium which is not being acted on by some external force (i.e. body acceleration is 0), we have

$$\frac{D\vec{u}}{Dt} = \frac{\eta}{\rho}\nabla^2\vec{u} + \nabla\left(\nabla\cdot\vec{u}\left(\zeta + \frac{2}{3}\eta\right)\right) - \frac{\nabla P}{\rho}, \tag{4.12}$$

where $\vec{u}$ is the flow velocity vector (as opposed to its 4-vector), $\rho$ is the fluid's density and $D/Dt = \partial/\partial t + \vec{u}\cdot\nabla$ is the material derivative. Even though this formula applies to non-relativistic fluids, it gives us some insight as to how, generally, viscous fluids behave. Without viscosity, the acceleration of the fluid at any given point is guided by the gradient of the pressure, akin to the force. Looking at the signs of the Navier-Stokes equation, we see that the shear and bulk viscosities $\eta$ and $\zeta$ oppose the flow imposed by the pressure gradient. The viscosity, therefore, serves, in part, as a regulator of the flow of the QGP. This fact, combined with the fact that the relativistic hydrodynamics equations of motion are conservation equations, means that the hydrodynamics phase will regularize the large peaks and variations generated by our initial state fairly quickly within its evolution. Figure 26 shows the 32 first time steps of the hydrodynamics phase. We see that the flow and energy remain fairly disorganized for a few steps before cells with large flow velocities dissipate and give way to more collective flow pockets. This is due to the combination of the surrounding pressure gradients as well as the viscosity of the QGP, which 'penalizes' unregulated and dissonant flow. We see that, at $\tau = 0.762$ fm, the flow is already well-organized and coherent, generally flowing from regions of high energy to areas of low energy. Because of this, the energy has gone from extremely spiky to much more evenly distributed: pockets with large fluctuations have isotropized locally.

As mentioned at the onset of this chapter, the hydrodynamic evolution has a clear exit condition: it evolves the QGP until every cell's temperature has dipped below the freeze-out temperature - a parameter of the model - which is set, in this study, to $T_{\text{freeze}} = 155\,\text{MeV}$. Using our EoS, we can convert this switching temperature to a

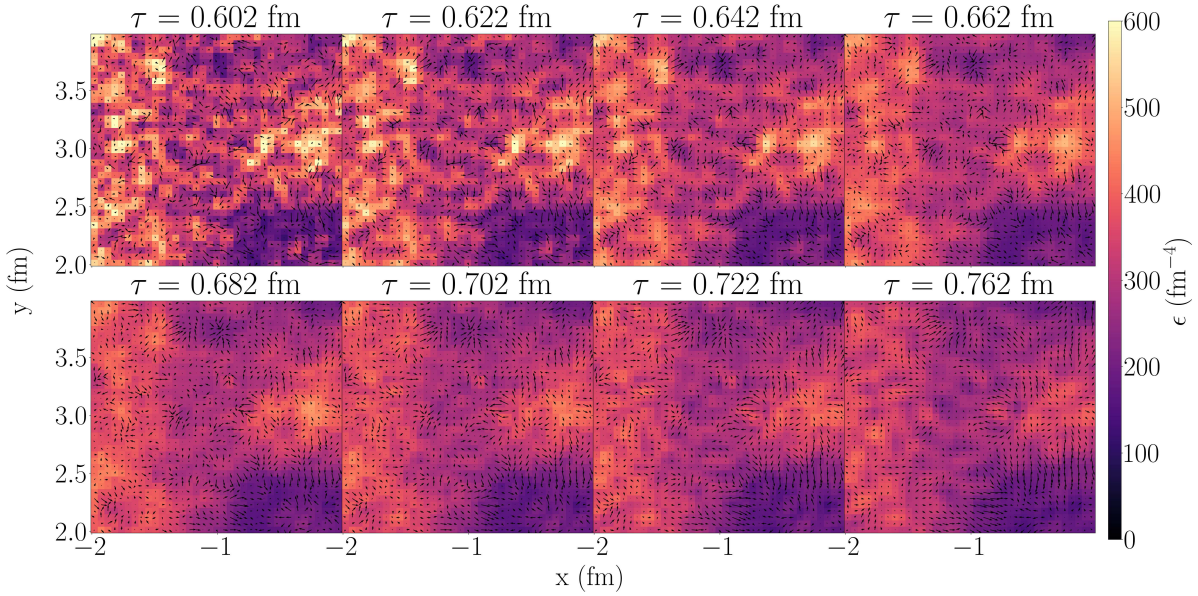


Figure 26: Energy density ($\epsilon$) distribution and flow of a central event from switching time $\tau = 0.602\,\text{fm}$ to $\tau = 0.762\,\text{fm}$ - 32 hydrodynamic time steps, of which only 8 are shown - for Xe+Xe at 5.44 TeV.

corresponding freeze-out energy density $\epsilon_{\text{freeze}} = 0.320\,\text{GeV/fm}^3$. However, given that cells reach this state at different times, a cell reaching freeze-out does not mean it stops contributing to the overall evolution. Rather, once a cell reaches $T_{\text{freeze}}$, its state (flow, shear viscosity, bulk viscosity, position) and the time at which it reaches freeze-out are saved to a file. Once every cell in the transverse grid has reached freeze-out, the evolution terminates, and MUSIC outputs a 4D isothermal hypersurface which serves as input to the particlization stage. Given this exit condition, different events will take different amounts of time to complete freeze-out; more energetic (or central) events will take more time to cool appropriately, and vice-versa. Figure 27 show the entire hydrodynamic evolutions of the central and peripheral events presented in Figs. 20, 22 and 23. As explained above, we can see that the peripheral event reaches freeze-out more than 4 fm sooner than the central event, given its smaller initial total energy. It also catches the eye that the initial state anisotropies, which we have spent time clarifying in the previous two chapters, seem to have unravelled entirely due to the features of the hydrodynamic evolution. This would entail that the differences in collision geometry

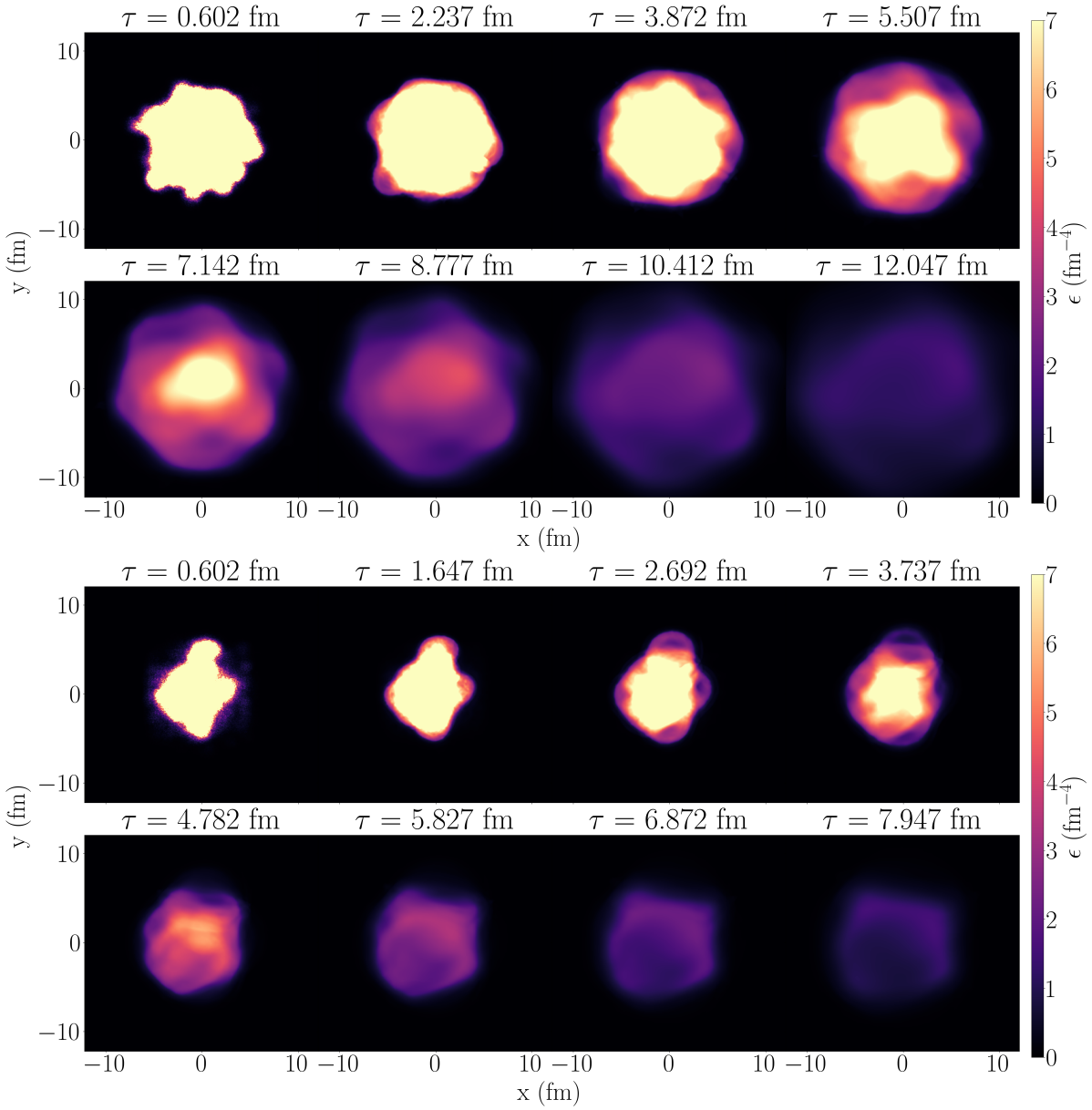


Figure 27: Energy density ($\epsilon$) distribution and flow of (**top two**) central and (**bottom two**) peripheral events from switching time $\tau = 0.602$ fm to complete freeze-out for Xe+Xe at 5.44 TeV. For the **top two** panels, this represents 2,289 hydrodynamic time steps, while for the **bottom two** panels, we have 1,469 hydrodynamic time steps.

could not be detected in final-state particle distributions. However, this is an illusion. Earlier in this paragraph, we explained that freeze-out happens on a cell-by-cell basis and that the freeze-out surface is not simply the thermodynamic configuration of the final slice of the hydrodynamic evolution; instead, it is a 4D hypersurface with points

found at practically *all* times of the evolution. The qualitative shape of the final slice of the evolution of the QGP does not inform us of the anisotropies contained in the distributions of final-state particles.

Figure 28 is inspired by a figure which was first shown in Ref. [30]. We show the transverse positions and transverse flows of all points at freeze-out of the two events - one central and one peripheral - we have been analyzing since Chapter 3. We see that our central event (top panel of Fig. 28), which looked reasonably symmetric in Fig. 22, preserves its symmetries at freeze-out: the spatial distribution of freeze-out points is similar throughout time, and the transverse flow components behave similarly across the entire evolution. Our peripheral event (bottom panel of Fig. 28), on the other hand, shows how the anisotropic energy configuration fed into MUSIC translates to a freeze-out hypersurface which is, itself, quite anisotropic. Firstly, the spatial distribution of freeze-out points reflects the spatial anisotropy found in Fig. 22's right panel, with freeze-out points found in a broader range in the $y$-direction than in the $x$-direction, and this, at all times. Then, the distribution of cell flow velocities also presents a striking asymmetry. Indeed, we see that $u^y$ is generally less broad than $u^x$, and is skewed towards negative flow velocities. Because of the smaller $x$-direction extent of the QGP at the onset of hydrodynamics, the pressure gradients drive flow in that direction more than in the broader $y$-direction, leading to greater flow in the $x$-direction at freeze-out. The asymmetry in the $y$-direction flow is due to the energy density distribution's energetic bulge in its lower-left region at the hydrodynamic onset. This bulge directs flow in the $x$- and $y$-directions simultaneously, leading to more significant residual flow in the negative $y$-direction in the freeze-out hypersurface.

We are now ready to transition to the next phase of our simulations, which we will describe summarily (compared to the two previous phases): particlization and hadron gas evolution.

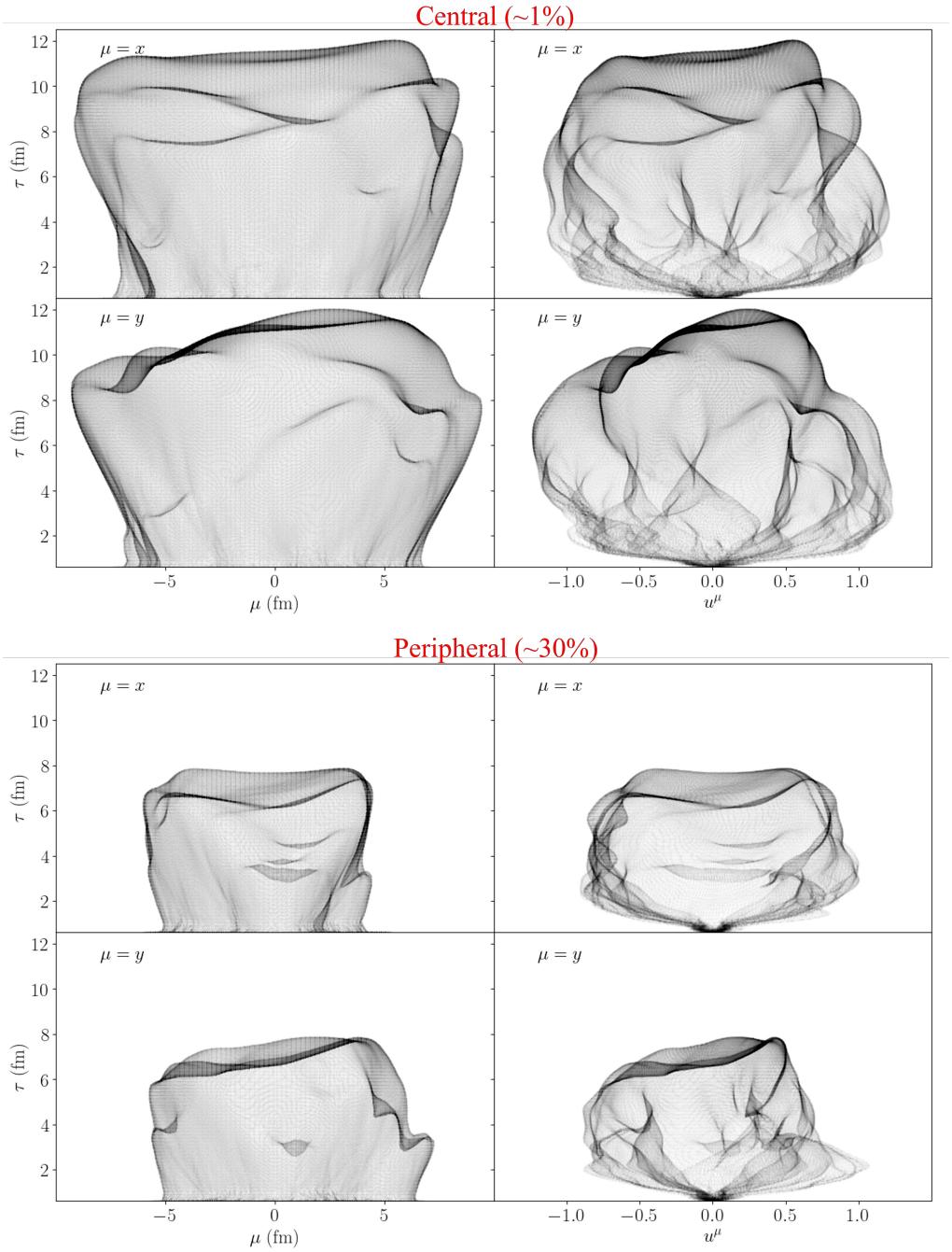


Figure 28: Projections of freeze-out time $\tau$ plotted against various components of the freeze-out hypersurface ((**upper-left**) $x$ position; (**lower-left**) $y$ position; (**upper-right**) $x$-direction flow $u^x$; (**lower-right**) $y$-direction flow $u^y$) for (**top four**) central and (**bottom four**) peripheral Xe+Xe events at 5.44 TeV.

## 4.2 PARTICLIZATION AND HADRON GAS EVOLUTION

With the QGP frozen out, it is time to convert the deconfined state of quarks and gluons to a hadron gas which will be 'detected' by our 'detectors'; this hadron gas is sampled

at the site of the QGP and has properties consistent with that of the freeze-out surface. It must then be evolved kinematically until all of its constituent reach a pre-determined distance - $\sim 1\,\mathrm{m} = 10^{15}$ fm - from the position of the beam ($x = y = 0$), at which point they are frozen and said to have been 'detected'. This process is naturally divided into two moments: we first sample particles from the freeze-out surface using Cooper-Frye sampling [91], and, in the second phase, evolve those particles using kinetic theory. This evolution includes scattering, particle interaction, decays and resonances [21]. Let us describe these two phases in a bit more detail.

### 4.2.1 *Particlization: iSS*

As with our transition from IP-Glasma to MUSIC, we must be careful about preserving consistency across the interfaces of our simulation. As before, the stress-energy tensor will serve as our measure of coherence. We will condense the discussion outlined in Ref. [83]. The condition

$$T^{\mu\nu}_{\mathrm{hydro}} = T^{\mu\nu}_{\mathrm{gas}} \tag{4.13}$$

must be respected at freeze-out. We have established the hydrodynamic stress-energy tensor's form, with second-order bulk and shear viscous corrections taken into account. The stress-energy tensor for a gas of particles at freeze-out time is given by

$$T^{\mu\nu}_{\mathrm{gas}}(x^\mu) = \sum d_r \int \frac{d^4p}{(2\pi)^3}\delta\left(p_\mu p^\mu - m_r^2\right) 2\theta(p^0)p^\mu p^\nu f_r(x^\mu, p^\mu), \tag{4.14}$$

where $d_r$ is the degeneracy factor of particle $r$ and $f_r$ is the on-shell single particle distribution function of particle $r$. This single particle distribution represents the phase space density of on-shell particles, i.e.

$$f_r(\vec{x}, \vec{p}) \propto \frac{dN_r}{d^3p d^3x}. \tag{4.15}$$

Cooper-Frye sampling proposes that the number of particles crossing the surface of an isothermal hypersurface is given by

$$E\frac{dN_r}{d^3p} = \frac{d_r}{(2\pi)^3}\int_\Sigma f_r(\vec{x}, \vec{p})p^\mu d^3\sigma_\mu(x^\mu), \tag{4.16}$$

where $E\frac{dN_r}{d^3p}$ is the momentum spectrum of particle species $r$, $\Sigma$ is the hypersurface - the freeze-out surface generated by MUSIC - and $\sigma^\mu(x^\mu)$ is a vector normal to the hypersurface at position $\vec{x}$ and time $t$ (i.e. at four-vector $x^\mu$). The single particle distributions include in- and out-of-equilibrium parts related to the ideal and viscous parts of the hydrodynamical evolution. We can therefore separate it into an ideal part, and its shear and bulk corrections,

$$f_r(x^\mu, p^\mu) = f_r^0(x^\mu, p^\mu) + \delta f_r^{\text{bulk}}(\vec{x}, \vec{p}) + \delta f_r^{\text{shear}}(\vec{x}, \vec{p}). \tag{4.17}$$

The uncorrected single particle distribution is either a Bose-Einstein (-) or a Fermi (+) distribution, depending on the species, i.e.,

$$f_r^0 = \left(\exp\left(p \cdot u/T\right) \mp 1\right)^{-1}, \tag{4.18}$$

where $u$ is the local flow velocity of the fluid cell and $T$ is its temperature (here, 155 MeV). The corrections are parameters of the model and, given that the second-order viscous expansions used in MUSIC were developed using the 14-moment approximation [92], so are the corrections we use. Their combined form is given by

$$\begin{aligned}\delta f_r = f_r^0 \bar{f}_r^0 \Big(&c_T m_r^2 + b_n \left(c_B(u_\mu p^\mu) + c_V^{\langle\mu\rangle} p_{\langle\mu\rangle}\right) \\ &+ c_E(u_\mu p^\mu)^2 + c_Q^{\langle\mu\rangle}(u_\mu p^\mu) p_{\langle\mu\rangle} + c_\pi^{\langle\mu\nu\rangle} p_{\langle\mu} p_{\nu\rangle}\Big),\end{aligned} \tag{4.19}$$

where $\bar{f}_r^0 = 1 - g_n^{-1}\Theta_n f_r^0$, with $g_n = 2s_n + 1$, the spin degeneracy, and $\Theta_n \in \{-1, 1\}$ to account for the nature (boson or fermion) of the particles. All of the coefficients $c$ are adjusted in order to ensure that the corrections to the single-particle distribution does not contribute to the energy and reproduces the shear-stress tensor and bulk-viscous pressure. Their exact forms are given in Ref. [93]. Concretely, these corrections have a non-negligible effect on the particle yields. Integrating Eq. (4.16) to obtain total yields per species would look like

$$N_r(\vec{x}) = \int \frac{d^3p}{E} E\frac{dN_r}{d^3p}(\vec{x}) = N_r^0 + N_r^{\text{bulk}} + N_r^{\text{shear}} \tag{4.20}$$

with the equilibrium distribution function $f_r^0$ giving [94]

$$N_r^0 = \frac{d_r}{2\pi^2} d^3\sigma_\mu u^\mu m_r^2 T \sum_{n=1}^{\infty} \frac{(\pm 1)^{n-1}}{n} K_2\left(n\frac{m_r}{T}\right), \tag{4.21}$$

where $K_2$ is the modified Bessel function of the second kind. In the end, when equivalence with the hydrodynamic tensor is taken into account, the shear $\delta f$ corrections do not contribute to the yield (i.e. $N_r^{\text{shear}} = 0$), while the bulk corrections do contribute to the yields (i.e. $N_r^{\text{bulk}} \neq 0$).

The Cooper-Frye procedure is included in our simulations through iSS [95, 96], an open-source code [97]. Because of the ensemble average nature of the hydrodynamic evolution and the freeze-out surface it generates, the hypersurface is oversampled 1000 times to ensure that the sampled particle lists converge to the hydrodynamic value of all observables (multiplicity, momenta, flow). Concretely, this means that a single IP-Glasma and MUSIC event, comprised of a unique collision, impact parameter and nuclei configuration, will generate 1000 iSS events, each consisting of its own particle list containing specific species and momenta. These lists are then processed to provide a statistical average of the various observables related to that event. As we will briefly discuss later in this chapter, the moment at which this average is taken can have a real impact on the end-state observables that are calculated.

Once the particle list is generated, the kinetic evolution of the hadron gas produced by our event is initiated.

### 4.2.2 *Hadronic Cascade: SMASH*

The particles generated through the hypersurface must be kinematically evolved until they reach the 'detectors'. The inclusion of such a stage is important: effects borne out of particle interactions, decays, scatterings and resonances can play a considerable role in what the final-state observables look like. Heavy, unstable baryons, which may be sampled by the Cooper-Frye procedure, would make it to the final-state list regularly if it were not for this kinetic phase, where most of them decay fairly quickly. We have opted for the transport code SMASH [21], version 1.8. All interactions and decays

are computed using measured particle properties and channels via coupled Boltzmann equations,

$$p^\mu \partial_\mu f_r(x^\mu, p^\mu) = C\left[f_r\right] . \tag{4.22}$$

We see that the single-particle distribution functions $f_r$ come into play here too. This dynamical stage allows for the decoupling of the QGP medium (which is strongly-interacting) towards a hadron gas which itself goes from fairly dense at hydrodynamic freeze-out to dilute as we progress through the kinetic evolution.

All of the default SMASH parameters were used in this work. For a detailed treatment of the various assumptions of SMASH, one should refer to Ref. [21].

Our simulation is complete at this point, and we are ready to construct observables - quantities that can be compared to experiments - from the final state particle lists. We shall now define primary and secondary observables relevant to our analysis in order to then proceed to large-scale simulation results.

## 4.3 OBSERVABLES

Comparing calculations to experimental data in heavy-ion phenomenology must go through the proper definition of observable quantities, i.e. phenomena that can be measured experimentally; the QGP exists across such narrow timescales ($O(10^{-23}\,\mathrm{s})$) that direct observations of it are impossible. On the other hand, the products of a collision - hadrons propagating in all directions and occupying a large proportion of phase space - are accessible to experimentalists through the calibration and use of detectors which surround the collision areas. Therefore, observables are always exclusively concerned with exposing the coherent trends contained within large collections of particles generated in a collision event.

Before digging into the specifics of our selected observables, it is important to note that observable quantities are usually shared as pertaining to a class of events (rather than to a specific and singular event). There are many reasons why talking about single-event

observables is (mostly) irrelevant, but the main reason is statistical in nature: because collision events generate discreet lists of $N$ particles, any calculated quantity stemming from the analysis of this list will carry an inherent statistical uncertainty with it that would rival the specific and physically-relevant dynamical fluctuations contained in that event. Indeed, the order of statistical fluctuations, via the calculation of the standard error, would be $O(N^{-\frac{1}{2}})$. Grouping events together based on a specific property allows us to increase $N$ drastically and significantly decrease inherent statistical uncertainty. As mentioned in passing in Chapters 2 to 4, events are grouped through their charged particle multiplicity $N_{\text{ch}}$, the amount of charged particles detected within a specific longitudinal range.

### 4.3.1 *Multiplicity & Centrality*

The charged particle multiplicity is the most elementary of observables. In this thesis, when discussing multiplicity, we will talking about charged particle multiplicity *per unit rapidity*, or $dN_{\text{ch}}/d\eta$, also known as the charged particle multiplicity *density*. This specific observable is usually calculated by considering only particles detected within a specific rapidity range, i.e.

$$\frac{dN_{\text{ch}}}{d\eta} = \frac{\int_{|\eta|<X} d\eta N_{\text{ch}}(\eta)}{\eta_{\text{max}} - \eta_{\text{min}}}, \tag{4.23}$$

with $X$ varying from experiment to experiment. In this thesis, depending on the specific experiment we will be comparing to, $X \in \{0.5, 0.8\}$. Therefore, Equation (4.23) counts the number of particles generated in a given rapidity range and then divides it by the its 'length', yielding a charged particle density. As the most elementary observable, the multiplicity also serves as the sole calibration tool for the saturation scale to fluctuation scale proportionality constant $C$ presented in Eq. (3.33), which dictates the amount of energy deposited in the transverse plane at the initial time.

To compare to experimental data, we must segment our collection of events into the same number of centrality classes as it has: if the experiment reports multiplicity at 5%

increments, we must construct 20 centrality classes, all with equal number of events, from the entirety of our dataset. However, as outlined in Chapter 2, certain events generated by our simulations should be complete misses, i.e. events where the impact parameter $b$ is such that the two nuclei do not interact hadronically. To construct our centrality bins, we must reject non-collision events. Intuitively, one could look at the number of binary collisions registered in a given IP-Glasma collision event and reject all events which contain no binary collisions. However, because IP-Glasma does not generate energy density profiles based on binary collisions per se, this method could allow for the inclusion of events that do not generate meaningful amounts of particles and, therefore, would be rejected in an experimental setting.

We employ a centrality binning method first outlined in Ref. [48] to remedy this situation. We start by selecting two experimental centrality bins and their respective multiplicities (i.e. $0-5\%$ and $20-25\%$). We then calculate the ratio of these two multiplicities, $R_{\text{targ}}$. Using our simulation data, we construct a number of centrality bins equal to that presented in the experimental data and extract the multiplicities from our two selected centrality bins ($0-5\%$ and $20-25\%$) to construct a ratio once more, $R_{\text{sim}}$. We then compare the two ratios to one another to inform us on next steps:

1. If $R_{\text{sim}} > R_{\text{targ}}$, we drop our lowest-multiplicity event from consideration and recompute our centrality bins, then $R_{\text{sim}}$. This action necessarily leads to a new and smaller $R_{\text{sim}}$. We repeat this procedure until $R_{\text{sim}} \sim R_{\text{targ}}$, at which point the centralities have been matched.

2. If $R_{\text{sim}} < R_{\text{targ}}$, we could be dealing with one of two things: either $C$, the proportionality constant, leads to too much energy being deposited in the transverse plane (and we should therefore adjust it considerably) *or* we are not truly conducting a minimum-bias study (i.e. our most peripheral events are not complete misses, and we therefore cannot match the entire experimental centrality spectrum). The first issue's solution is self-explanatory, while a resolution to the second issue will be discussed further.

Now, assume we have a collection of events that fits the first presented situation. After having completed the procedure, we compare the nominal multiplicities of all bins to those of the experiment. If the multiplicities themselves are considerably off (be they too large or too small), a recalibration of the proportionality constant $C$ is undertaken, and a new set of results is generated. If the multiplicities are within 5% of all experimental multiplicities, the calibration is complete, and we can move on to calculating the observables relevant to our analysis.

We must diagnose the issue if we find ourselves in the second situation. Suppose our dataset contains events that have $dN_{\mathrm{ch}}/d\eta < 1$. In that case, we are conducting a minimum-bias analysis and must, therefore, strongly recalibrate the proportionality constant to apply the procedure. If, on the other hand, our dataset does not contain events with $dN_{\mathrm{ch}}/d\eta < 1$, we are not conducting a minimum-bias study. Luckily, our procedure contains provisions allowing for matching partial centrality ranges stemming from biased impact parameter ranges. The procedure itself remains quasi-identical, with the important modification being that we are now concerned with finding a proper upper bound for our entire centrality range. In other words, we are now looking for $H$ such that our procedure works for a centrality range $0 - H\%$. To find $H$, one goes through the same procedure outlined above, decreasing $H$ until a bound where the first situation applies is found. From there, $C$ can be calibrated based on how our calculated multiplicities compare to the experiment up to our final upper bound. In the results we will show in the following chapter, biased runs for Au and U were undertaken, calibrated and binned using this technique. Xe results shown further in this thesis will have been binned using the unmodified technique, as they stem from a minimum-bias set of runs.

Once all events are binned into their respective centrality classes, we can compute the following observables on a class-by-class basis.

### 4.3.2 *Mean Transverse Momentum*

This quantity is the second most elementary observable to compare to. It does not figure in the calibration of the model, but it is a good indicator of the overall calibration of a simulation framework, as it is not only sensitive to the amount of energy deposited at the initial time but also to some of the hydrodynamic parameters (such as shear and bulk viscosity) presented earlier in this chapter. Its calculation is straightforward,

$$\langle p_T \rangle = \frac{1}{N_{\text{ev}}} \sum_{j=1}^{N_{\text{ev}}} \frac{1}{N_j} \sum_{i=1}^{N_j} p_{T_i}, \tag{4.24}$$

where $N_{\text{ev}}$ is the number of events in a given centrality class, and $N_j$ is the number of particles sampled in a given event. Mean transverse momentum encodes information about the transverse size of the system. Indeed, at fixed total energy in the transverse plane, a smaller interaction region will lead to larger outward pressure in the hydrodynamic phase, in turn leading to a larger measured $\langle p_T \rangle$.

### 4.3.3 *Multi-particle $p_T$ correlator*

Multi-particle transverse momentum correlators are measures of the dynamical fluctuations contained within the particle distributions. The 2-particle $p_T$ correlator is defined as [98]

$$\langle \delta p \delta p \rangle = \left\langle \frac{\sum_{i \neq j} (p_i - \langle p_T \rangle)(p_j - \langle p_T \rangle)}{N_{\text{ch}}(N_{\text{ch}} - 1)} \right\rangle, \tag{4.25}$$

where $\langle p_T \rangle$ is the mean transverse momentum of the entire centrality class and $\langle \cdot \rangle$ around the ratio symbolizes an average over the entire centrality class, i.e.

$$\left\langle \frac{\sum_{i \neq j} (p_i - \langle p_T \rangle)(p_j - \langle p_T \rangle)}{N_{\text{ch}}(N_{\text{ch}} - 1)} \right\rangle = \frac{1}{N_{\text{ev}}} \sum_{k=1}^{N_{\text{ev}}} \frac{\sum_{i \neq j}^{N_k} (p_i - \langle p_T \rangle)(p_j - \langle p_T \rangle)}{N_k(N_k - 1)}. \tag{4.26}$$

Equation (4.25) is reminiscent of the statistical variance of the centrality class' momentum distribution, but differs from it in a meaningful way: self-correlation (i.e. elements

with $i = j$) are removed. This correlator can, contrarily to the variance, therefore, be a negative quantity.

Implementing Eq. (4.25) numerically as is presented would be extremely costly computationally. Indeed, it would run in at least $O(N_{\text{ev}} \cdot N_{\text{ch}}^2)$, a strikingly taxing process. Instead, we opt to implement a modified version of methods introduced by Giacalone et al. [98]. To do this, we begin by defining the modified moments of the $p_T$ distributions $P_n$,

$$P_n = \sum_{i=1}^{N_{\text{ch}}} (p_i - \langle p_T \rangle)^n \,, \tag{4.27}$$

where, as in Eq. (4.25), $p_i$ is the transverse momentum of the $i^{\text{th}}$ particle of a given event. Then,

$$\begin{aligned}
&\sum_{i \neq j} (p_i - \langle p_T \rangle)(p_j - \langle p_T \rangle) = \\
&\sum_{i=1}^{N_{\text{ch}}} (p_i - \langle p_T \rangle) \left( \sum_{j \neq i}^{N_{\text{ch}}} (p_j - \langle p_T \rangle) \right) = \\
&\sum_{i=1}^{N_{\text{ch}}} (p_i - \langle p_T \rangle) \sum_{j=1}^{N_{\text{ch}}} (p_j - \langle p_T \rangle) - \sum_{i=1}^{N_{\text{ch}}} (p_i - \langle p_T \rangle)^2,
\end{aligned}$$

where in the last step we have allowed for $i = j$ terms in the multiplied sums by subtracting them through the second term. We can then use Eq. (4.27) to rewrite the last line as

$$\sum_{i=1}^{N_{\text{ch}}} (p_i - \langle p_T \rangle) \sum_{j=1}^{N_{\text{ch}}} (p_j - \langle p_T \rangle) - \sum_{i=1}^{N_{\text{ch}}} (p_i - \langle p_T \rangle)^2 = (P_1)^2 - P_2, \tag{4.28}$$

which in turn allows us to rewrite Eq. (4.25)

$$\langle \delta p \delta p \rangle = \left\langle \frac{(P_1)^2 - P_2}{N_{\text{ch}}(N_{\text{ch}} - 1)} \right\rangle . \tag{4.29}$$

The 3-particle $p_T$ correlator can be treated similarly to greatly reduce the computational stress required to extract it. Starting with

$$\langle \delta p \delta p \delta p \rangle = \left\langle \frac{\sum_{i \neq j \neq k} (p_i - \langle p_T \rangle)(p_j - \langle p_T \rangle)(p_k - \langle p_T \rangle)}{N_{\text{ch}}(N_{\text{ch}} - 1)(N_{\text{ch}} - 2)} \right\rangle , \tag{4.30}$$

which requires $O(N_{\text{ev}} \cdot N_{\text{ch}}^3)$ operations, we can write

$$\langle \delta p \delta p \delta p \rangle = \left\langle \frac{(P_1)^3 - 3P_2P_1 + 2P_3}{N_{\text{ch}}(N_{\text{ch}}-1)(N_{\text{ch}}-2)} \right\rangle. \tag{4.31}$$

Equations (4.29) and (4.31) are computable in linear time on an event-by-event basis, which greatly reduces the computational stress required. Furthermore, since both quantities have been reduced to a single term, the calculation of their respective errors has also been greatly simplified. As a price to pay for simplicity, these expressions are prone to cancellation errors. However, given our target precision of $O(1\%)$, these errors are not of much concern. In Chapter 7, we will introduce a composite observable called the 'intensive skewness' which combines the 2- and 3-particle $p_T$ correlators into a single ratio.

### 4.3.4 *Anisotropic Flow*

Anisotropic flow $v_n$ is by now generally accepted as one of the primary evidence of QGP undergoing fluid-like behavior in relativistic heavy-ion collisions [99]. We will start by defining the $n^{\text{th}}$-order anisotropic flow as it will be calculated in this thesis before explaining why it is of great importance to heavy-ion collision phenomenology as a whole, but also specifically for the work carried out in this thesis.

We start by defining the flow vector $Q_n$ for each event [100, 101],

$$Q_n = \sum_{j=1}^{N_{\text{ch}}} e^{in\phi_j}, \tag{4.32}$$

where, as before, $N_{\text{ch}}$ is the event's multiplicity, $j$ runs over all particles registered in the event[3] and $\phi_j$ is the azimuthal angle of the $j^{\text{th}}$ particle. Then, the $2^{\text{nd}}$ order anisotropic flow coefficient (or azimuthal correlation) is given by

$$\langle 2 \rangle_n = \frac{\sum_{i \neq j} e^{in(\phi_i - \phi_j)}}{N_{\text{ch}}(N_{\text{ch}}-1)} = \frac{|Q_n|^2 - N_{\text{ch}}}{N_{\text{ch}}(N_{\text{ch}}-1)}. \tag{4.33}$$

[3] Different experiments have different transverse momentum acceptance windows for their calculations: STAR (at RHIC) only accepts particles with $0.2 \leq p_T \leq 2.0\,\text{GeV}$, while ALICE (at LHC) accepts particles with $0.2 \leq p_T \leq 3.0\,\text{GeV}$.

Equation (4.33) is also called the 2-particle $v_n$, as it calculates anisotropic flow through pair-wise combinations of event particles. The 4$^{\text{th}}$ order azimuthal correlation (or 4-particle $v_n$) for a given event is given by

$$\begin{aligned}\langle 4\rangle_n &= \frac{\sum_{i\neq j\neq k\neq l} e^{in\left(\phi_i+\phi_j-\phi_k-\phi_l\right)}}{N_{\text{ch}}(N_{\text{ch}}-1)(N_{\text{ch}}-2)(N_{\text{ch}}-3)} \\ &= \frac{|Q_n|^4+|Q_{2n}|^4-2\,\text{Re}\left[Q_{2n}\cdot Q_n^*\cdot Q_n^*\right]}{N_{\text{ch}}(N_{\text{ch}}-1)(N_{\text{ch}}-2)(N_{\text{ch}}-3)} - 2\frac{2(N_{\text{ch}}-2)|Q_n|^2-N_{\text{ch}}(N_{\text{ch}}-3)}{N_{\text{ch}}(N_{\text{ch}}-1)(N_{\text{ch}}-2)(N_{\text{ch}}-3)},\end{aligned} \tag{4.34}$$

where $Q_{2n}$ is the flow vector associated with the $2n^{\text{th}}$ harmonic (i.e. if $n = 2$, then $Q_{2n} = Q_4$). Equations (4.33) and (4.34) are formulas for a single event. As with previous observables, we will want to average this quantity over the entirety of events contained in a given centrality class, i.e.

$$\langle\langle\mathcal{V}\rangle\rangle_n = \frac{1}{N_{\text{ev}}}\sum_{i=1}^{N_{\text{ev}}}\langle\mathcal{V}\rangle_{n,i}, \tag{4.35}$$

where $\mathcal{V} \in \{2,4\}$ in our analysis, and the subscript $i$ indicates the $\mathcal{V}$-particle anisotropic coefficient of the $i^{\text{th}}$ event. From these centrality-class averaged quantities, we can construct the quantities $c_n\{2\}$ and $c_n\{4\}$, the 2- and 4-particle cumulants of the azimuthal correlations,

$$c_n\{2\} = \langle\langle 2\rangle\rangle, \tag{4.36}$$

$$c_n\{4\} = \langle\langle 4\rangle\rangle - 2\langle\langle 2\rangle\rangle^2, \tag{4.37}$$

which entails that, to obtain the true 4-particle cumulant of the azimuthal correlations, one must subtract the underlying contributions stemming from 2-particle correlations. We will remind the reader of this fact once we introduce results stemming from 2- and 4-particle cumulants.

The point of constructing these cumulants is to estimate the Fourier coefficients of the azimuthal dependence of the particle yields [102]

$$E\frac{dN}{d^3p} = \frac{1}{2\pi}\frac{dN}{p_T dp_T dy} = \left(1+\sum_{n=1}^{\infty}2v_n\cos\left(n(\phi-\Psi_R)\right)\right), \tag{4.38}$$

where $v_n$ are the coefficients we are interested in and $\Psi_R$ is the reaction plane angle is 0 in our simulations because the nuclei are always shifted along the $x$-axis; experimentally, the reaction plane angle is not known, so estimates of these coefficients *must* be devised. Furthermore, the previously underlined fact that experimental results come in the form of *discrete* collections of particles furthers the need for estimates, as decomposing a discrete distribution into Fourier components creates its own set of errors. Historically, experimentalists have used Eq. (4.33) to estimate the coefficients present in the Fourier decomposition. The issue with these estimates is that they contained so-called non-flow contributions from the lack of information regarding the reaction plane $\Psi_R$, the relatively small number of participating particles and other effects such as momentum conservation, meaning they were really obtaining

$$\langle 2 \rangle = \langle v_n^2 \rangle + \delta_n, \tag{4.39}$$

where the $\delta_n$ are the non-flow contributions we just described, and $v_n^2$ is the square of the Fourier coefficient we are looking to estimate. The idea to decompose the Fourier coefficients into contributions from multi-particle correlations of different orders was first introduced in Ref. [100]: by subtracting non-flow contributions from flow contributions order-by-order, one could improve estimates of the *true* flow coefficients while producing better-defined observables. That is why, in Eq. (4.37), we subtract Eq. (4.33): we are subtracting effects which are already taken into account in an anterior cumulant. To move from Eqs. (4.36) and (4.37) to estimates for multi-particle correlation estimates for $v_n$, we do

$$v_n\{2\} = \sqrt{c_n\{2\}} \tag{4.40}$$

$$v_n\{4\} = \sqrt[4]{-c_m\{4\}}. \tag{4.41}$$

These are the 2- and 4-particle cumulants of the integrated $v_n$.

How does this observable tie into the flow generated in the hydrodynamics phase which we described in Section 4.1.2? When cell flow (and, therefore, momentum) builds up unevenly, particles sampled from the hypersurface will be distributed unevenly in

space: more momentum in one direction means more available energy to sample (or generate) particles in a given direction. Let us look at 3 'toy' particle distributions made up of 300 particles distributed around the beam axis, which are presented in Fig. 29. The **a)** distribution is evenly and randomly distributed (reminiscent of the central event's flow distribution found in Fig. 28); the **b)** distribution has two dense pockets of particles distributed on either side of the $y$-axis and separated by 2 dilute pockets of particle emissions (reminiscent of the peripheral event's flow distribution found in Fig. 28); the **c)** distribution is similar to **b)**, except it has three dense pockets distributed evenly across the transverse plane. Measuring $v_2\{2\}$ for these distributions yields **a)**= 0.03; **b)**= 0.422; **c)**= 0.01. These results make sense since $v_2$ is usually called 'elliptic' flow. If one imagines a histogram depicting the density of particles emitted in a certain direction, the histogram produced by **a)** would be a circle, that of **b)** would look like an ellipse and that of **c)** would resemble a triangle. The specific symmetries of **a)** and **c)** lead to their 2-particle elliptic flow cumulants to be near-0, while that of the elliptically distributed **b)** is orders of magnitude higher. In our results, the spread between isotropic and anisotropic events will be much smaller, but this schematic representation illustrates the mechanics of $v_2\{2\}$. Following this logic, one should assume that a $v_3\{2\}$, the 2-particle cumulant of triangular flow, should be large for **c)** and small for the two others - and one would be right! Experimentally, triangular flow is fairly insensitive to initial state geometry as triangular geometries are not created through reproducible effects - like an increase of the impact parameter $b$ - but rather through fluctuations in nucleon positions and densities at impact. Because of the nature of our distributions, $v_2\{4\}$ is practically equal to $v_2\{2\}$, which does not provide much insight other than that our made-up particle distributions have strong underlying correlations (which we baked in) that stem from the flow. Nevertheless, the previous exercise illustrates the source of $v_n$ in particle distributions.

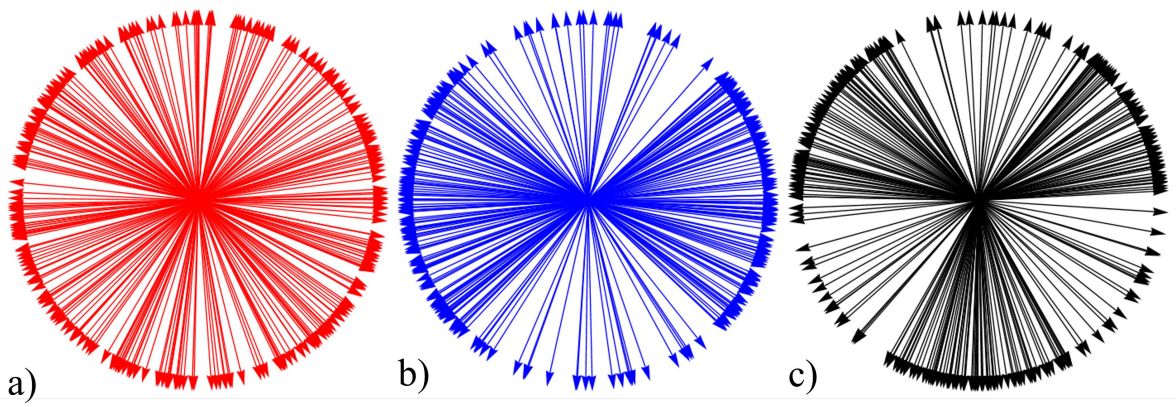


Figure 29: Unit vectors representing 300 generated particles and their azimuthal angle distributed **a)** isotropically and **b) & c)** anisotropically across the transverse plane. The anisotropic flow coefficients $v_n$ aim to measure spatial anisotropies in the particle distributions.

At times, we will be interested in differential anisotropic flow $v_n\{2\}(p_T)$, which is the anisotropic flow contributions of particles within a given narrow $p_T$ range. It is calculated as [101]

$$v_n\{2\}(p_T) = \frac{\mathrm{Re}(\langle Q_n^{\mathrm{PI}}(p_T) \cdot (Q_n^{\mathrm{ref}})^* \rangle)}{\langle N_{\mathrm{ch}}^{\mathrm{PI}}(p_T) N_{\mathrm{ch}}^{\mathrm{ref}} \rangle v_n^{\mathrm{ref}}\{2\}}, \tag{4.42}$$

where 'PI' denotes the particle species of interest (as this is sometimes used to look at identified particle spectra) and the superscript 'ref' denotes the reference flow vector. The idea here is to avoid self-correlations being represented in this observable. Therefore, the flow vector of interest - $Q_n^{\mathrm{PI}}$ - is taken from a mid-rapidity window (generally $|\eta| < 0.5$), while the reference flow vector is taken from a forward (or backward) rapidity window, which is disjointed from that of our particle group of interest. The window parameters will be given on a plot-by-plot basis, as they can change from experiment to experiment.

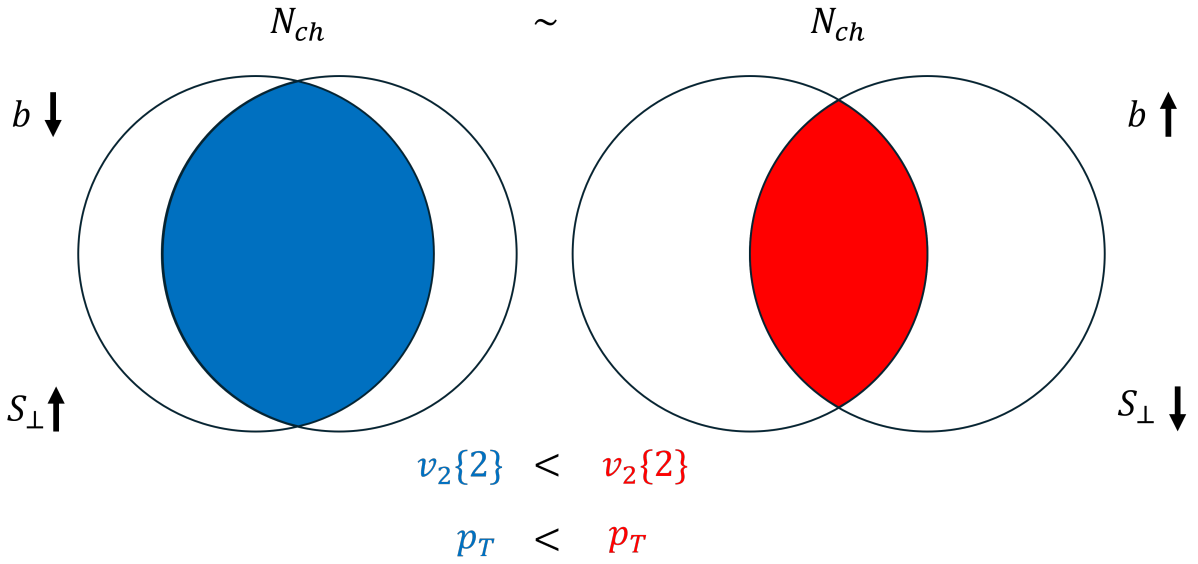


Figure 30: Schematic representation of the relationships between impact parameter $b$, interaction region area $S_\perp$, $v_2\{2\}$ and $\langle p_T \rangle$ for collisions of spherically symmetric nuclei belonging to the same centrality class.

### 4.3.5 *Transverse-Momentum-Flow Correlations*

Transverse-momentum-flow correlations combine two of the 4 observables we have presented to this point, namely the 2-particle cumulant of the anisotropic flow ($v_n\{2\}$) and the mean transverse momentum $\langle p_T \rangle$. This correlator was first developed in Ref. [103] and is given by

$$\rho(v_n\{2\}^2, \langle p_T \rangle) = \frac{\mathrm{cov}(v_n\{2\}^2, \langle p_T \rangle)}{\sqrt{\mathrm{var}\left(v_n^2\right) \cdot \langle \delta p \delta p \rangle}}, \tag{4.43}$$

where

$$\mathrm{cov}(v_n\{2\}^2, \langle p_T \rangle) = \left\langle \frac{|Q_n|^2 - N_{\mathrm{ch}}}{N_{\mathrm{ch}}(N_{\mathrm{ch}} - 1)} \cdot \left( \frac{\sum_{i=1}^{N_{\mathrm{ch}}} p_i}{N_{\mathrm{ch}}} - \langle p_T \rangle \right) \right\rangle \tag{4.44}$$

and

$$\mathrm{var}\left(v_n^2\right) = v_n\{2\}^4 - v_n\{4\}^4, \tag{4.45}$$

while $\langle \delta p \delta p \rangle$ is the 2-particle correlator which we defined in Eq. (4.29).

The elliptic flow flavor of this observable is of particular relevance to collisions of deformed nuclei, as we will show in the following chapter. In short, in central and mid-central ($\sim 0-40\%$) collisions of spherically symmetric nuclei, elliptic flow $v_2\{2\}$ and mean transverse momentum $\langle p_T \rangle$ are positively correlated. To understand why, we must first remind ourselves that this correlator, like all other observables, is calculated within a given centrality class. Therefore, it aims to explore how the two underlying observables, $v_2\{2\}$ and $p_T$, are related to one another within a certain centrality class. Because centrality is synonymous with charged particle multiplicity, and because multiplicity stems primarily from total energy in the interaction region at the moment of the collision, events within a given centrality class have approximately the same amount of total energy deposited in the transverse plane. Therefore, if a particular event within that class generates more elliptic flow, then it must be that the impact parameter for the collision was a bit larger, making the interaction region's area a bit smaller, in turn generating bigger pressure gradients, outward flow and, finally, momentum. Therefore, larger elliptic flow, in collisions of spherically symmetric nuclei and within a given centrality class, generally means larger mean transverse momentum. In other words, these two quantities should be correlated. Figure 30 illustrates this situation schematically. We see that for two events within the same centrality class to differ significantly in elliptic flow, they must also differ significantly in overlap area and, therefore, in mean transverse momentum.

Figure 31 shows a similar schematic representation as Fig. 30, but this time applied to central collisions of deformed nuclei, namely one body-body and one tip-tip collision (configurations we introduced in Chapter 2 and more specifically in Fig. 14). If body-body collisions and tip-tip collisions find themselves in the same centrality class (i.e. generate similar amounts of charged particles), then we should find an anti-correlation between the elliptic flow $v_2\{2\}$ and the mean transverse momentum $\langle p_T \rangle$. Because central body-body collisions generate large amounts of elliptic anisotropy, they will generate large amounts of elliptic flow. On the other hand, central tip-tip collisions will not because they look relatively similar to central collisions of spherically

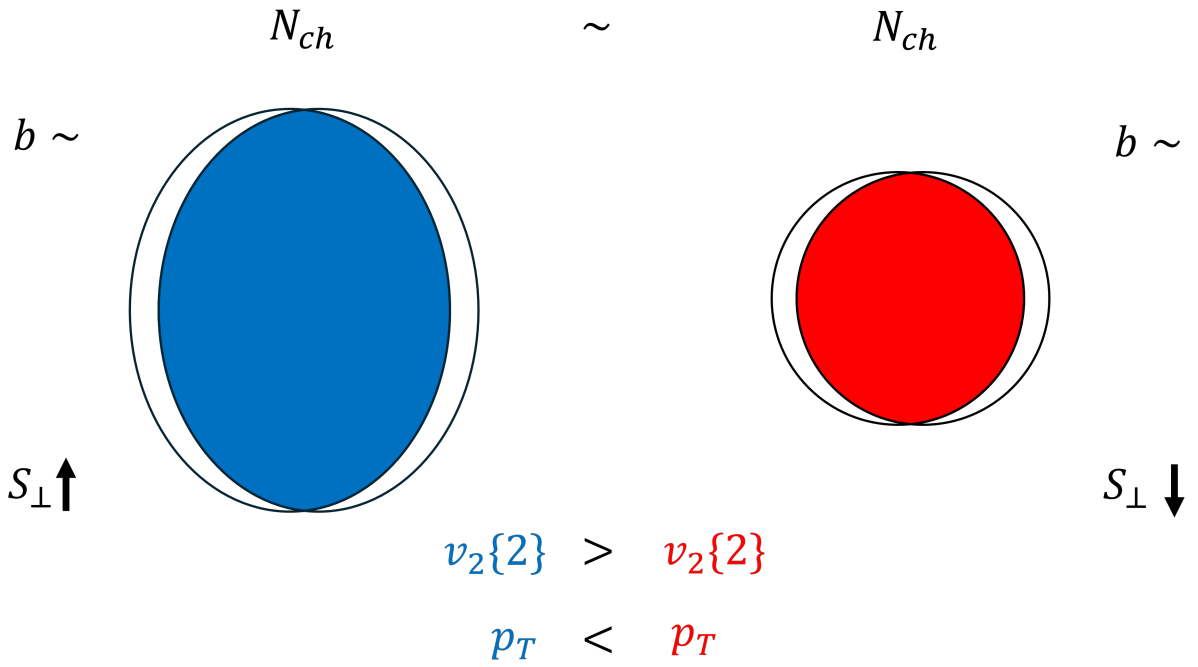


Figure 31: Schematic representation of the relationships between impact parameter $b$, interaction region area $S_\perp$, $v_2\{2\}$ and $\langle p_T \rangle$ for collisions of ellipsoidal (deformed) nuclei belonging to the same central centrality class.

symmetric nuclei. Following the same arguments outlined above, we simultaneously expect the tip-tip collisions to generate a greater mean transverse momentum given their considerably smaller interaction area $S_\perp$, and vice-versa for the body-body collisions. Therefore, in central collisions of considerably deformed nuclei, we should observe an anti-correlation between $v_2\{2\}$ and $\langle p_T \rangle$, i.e. $\rho(v_n\{2\}^2, \langle p_T \rangle) < 0$. This observable is therefore uniquely positioned to detect centrality classes where vastly different initial state anisotropies (and isotropies) coexist, making it a great marker for deformity.

We are now ready to move on to the first results section of this thesis, where we will show results from U+U and Au+Au simulations using two different nuclear parametrizations each, to see if our model is sensitive to deformity across the collection of observables we have just defined.

# 5

# SELECTING APPROPRIATE PARAMETRIZATIONS IN 2D

With the knowledge presented in Chapters 2 to 4, we are ready to share and analyze results stemming from boost-invariant simulations conducted using our framework. The analysis, which was originally published in Ref. [1], is concerned with two systems, namely $^{238}$U and $^{197}$Au, which were selected because of their proximity in mass number $A$ and the different degrees of deformation they exhibit. As explained in detail in Chapter 2, $^{238}$U is a well-deformed, prolate nuclei: low- [25, 104] and high-energy [36, 94, 105] data and simulations have established this fact long ago. However, ambiguity remains regarding the scale of the deformation and of its projection in Woods-Saxon parameter space ($\tilde{\beta}_l^m$), with its quadrupole deformation being allowed to vary by more than 30% from one parametrization to another [36, 106]. On the other hand, $^{197}$Au provides a much more subtle representation of nuclear deformation. Indeed, for some time, given the uncertainty surrounding low-energy HFB calculations (explained in Section 2.2.2), the nuance of deformation signals provided by available experimental data [105], along with early elastic electron scattering experiments [25], the deformation of $^{197}$Au was often overlooked in high-energy simulations [107]. However, low-energy calculations have been confident for some time [108, 109]: $^{197}$Au is somewhat deformed. We therefore set out to use our cutting-edge framework to tackle these questions simultaneously.

We ran simulations using 4 different nuclear parametrizations - 2 for each system. Using multiplicity data collected at RHIC for U+U and Au+Au collisions at $\sqrt{s_{\mathrm{NN}}} = 193\,\mathrm{GeV}$ and $\sqrt{s_{\mathrm{NN}}} = 200\,\mathrm{GeV}$, respectively [105, 110], we calibrated the proportionality constant $C$ (see Eq. (3.33)) to properly reproduce the charged parti-

cle yields. All available experimental observables were compared to our calculations without further calibration or specific tuning. Thanks to this procedure, we simultaneously establish the unique capabilities of our framework to reproduce collections of observables based on a simple calibration procedure and its ability to differentiate clearly between different initial nuclear parametrizations. The latter ability provides us with the opportunity to discriminate between different parametrizations, selecting the Woods-Saxon parametrization for each system that best reproduces available experimental data. In the process, we will provide evidence supporting the use of our framework for constraining other less studied nuclear parametrizations, such as $^{129}$Xe, the other nucleus which we will discuss later in this thesis.

We will first formally introduce the analyzed parametrizations. We will then introduce observables, from the more basic (multiplicity, $\langle p_T \rangle$) to the more intricate ($p_T$ correlators, anisotropic flow), making sure to describe the implications properly of these observables vis-à-vis our final parametrization selections. We will also introduce ratios of observables between our systems, as these ratios have been determined experimentally and provide a further discriminating item for use in our procedure.

## 5.1 BASICS AND CALIBRATION

### 5.1.1 *Initial Parametrizations*

We begin by setting the foundations for our analysis by providing projections of our chosen parametrizations in Fig. 32. There are two collections of projections, differing only in the choice of azimuthal angle - $\phi = 0$ or $\pi/2$. All parametrizations except one are unchanged by the choice of azimuthal angle, which makes sense given that only one parametrization has non-zero triaxiality $\gamma$ (i.e., non-zero $\tilde{\beta}_l^m$ with $m \neq 0$), namely the Def Au parametrization defined in Table 2. It is, however, essential to show these two projections as basing our perception of the Def Au parametrization on only one of these would lead to us forming an inaccurate picture.

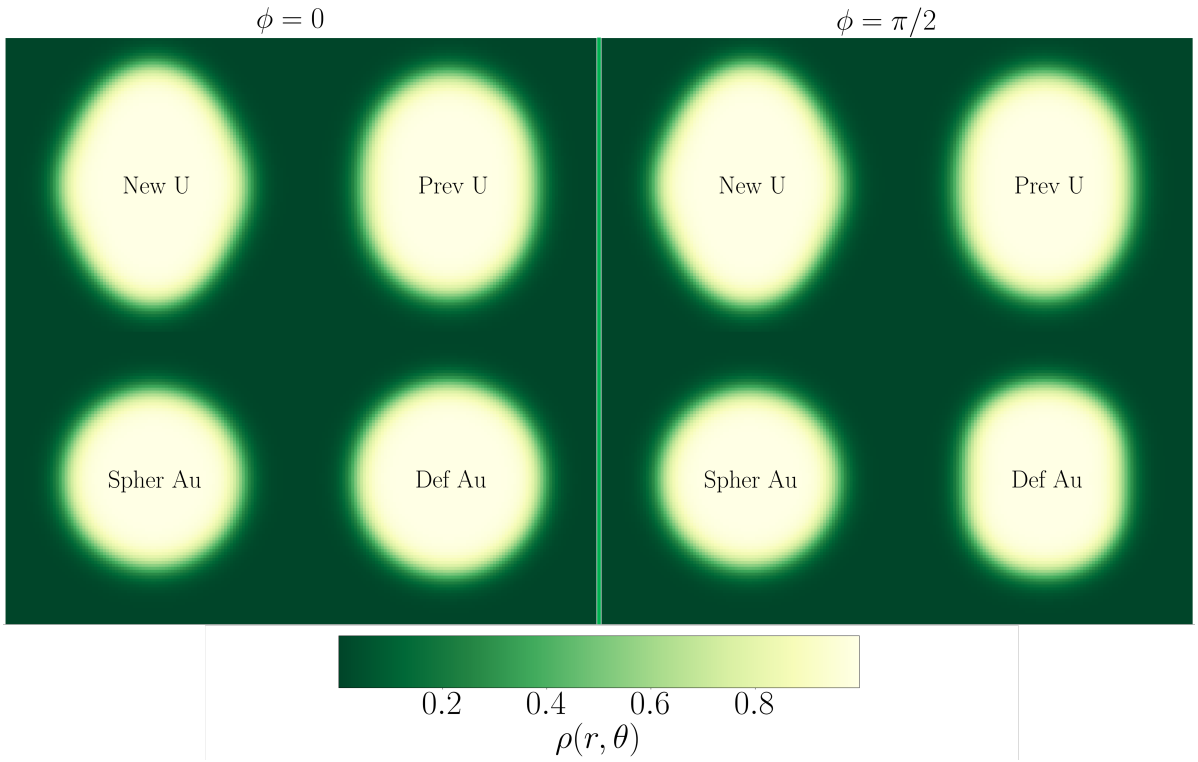


Figure 32: Two-dimensional Woods-Saxon projections taken at (**left**) $\phi = 0$ and (**right**) $\phi = \pi/2$ of the 4 parametrizations subject to our analysis. The details of these parametrizations can be found in Table 2.

Figure 32 also makes it clear that $^{238}$U is considerably more deformed than $^{197}$Au. We also find noticeable qualitative differences between the two $^{238}$U parametrizations, as New U has a diamond shape and Prev U has a much more 'simple' pill shape. This is entirely defined by the large hexadecapole parameter $\tilde{\beta}_4^0$ as well as the absence of non-zero $\tilde{\beta}_4^2$ & $\tilde{\beta}_4^4$ of New U.

As a final observation, the discussion of Section 2.3.2 concerning tip-tip and body-body collisions only seems to apply to our $^{238}$U parametrizations. Indeed, the differences between the short and long axes of Def Au are small when compared to those of our 2 U parametrizations. Furthermore, this asymmetry is only perceivable in the $\phi = \pi/2$ projection, making it much more difficult for the correct combination of conditions - especially in terms of aligning the target and projectile along a specific axis - to occur. Therefore, based on this qualitative assessment, we should not expect to find discernable and significant collections of tip-tip and body-body collisions in our Def

| | $R_0$ (fm) | $a$ (fm) | $\tilde{\beta}_2^0$ | $\tilde{\beta}_2^2$ | $\tilde{\beta}_4^0$ | $\tilde{\beta}_4^2$ | $\tilde{\beta}_4^4$ |
|---|---|---|---|---|---|---|---|
| New $^{238}$U | 7.068 | 0.538 | 0.247 | 0 | 0.081 | 0 | 0 |
| Prev $^{238}$U | 6.874 | 0.556 | 0.2802 | 0 | −0.0035 | 0 | 0 |
| Def $^{197}$Au | 6.62 | 0.519 | 0.098 | 0.076 | −0.025 | −0.018 | −0.018 |
| Spher $^{197}$Au | 6.37 | 0.535 | 0 | 0 | 0 | 0 | 0 |

Table 2: Deformed Woods-Saxon parameters used for sampling nuclei according to Eq. 2.13, taken from [25] (Prev $^{238}$U and Spher Au) and [36] (New $^{238}$U and Def Au).

Au events. Furthermore, our Au events should not produce the anti-correlation described in Section 4.3.5.

Let us examine our calibration via charged particle multiplicity $dN_{\mathrm{ch}}/d\eta$.

### 5.1.2 *Calibrating to Charged Particle Yields*

Before we describe our calibration procedure, it is important to mention two points. Firstly, the calibration was focused on a single system, namely $^{238}$U. We aimed to reproduce the charged particle yields provided for this system specifically and kept the same proportionality constant $C$ for our $^{197}$Au runs to ensure that the results are comparable without any caveats regarding our choice of parameters. This means that our $^{197}$Au curves match their associated experimental yields slightly less well than the $^{238}$U curves, as can be seen in Fig. 33. Secondly, no explicit charged particle multiplicity yield results exist for U+U at $\sqrt{s_{\mathrm{NN}}} = 193$ GeV. Indeed, even though identified particle yields do exist, and charged particle yields probably exist on tape at the Brookhaven National Laboratory, no published charged particle yields exist. We were therefore forced to use a parametrization of the $dN_{\mathrm{ch}}/d\eta$ vs. centrality curve, provided in Ref. [105], to conduct our calibration. While this parametrization is used in that same paper to produce elliptic flow vs. centrality curves (and, therefore, allowed us to reproduce their mapping exactly), it does entail that the experimental charged particle multiplicity curves carry an inherent

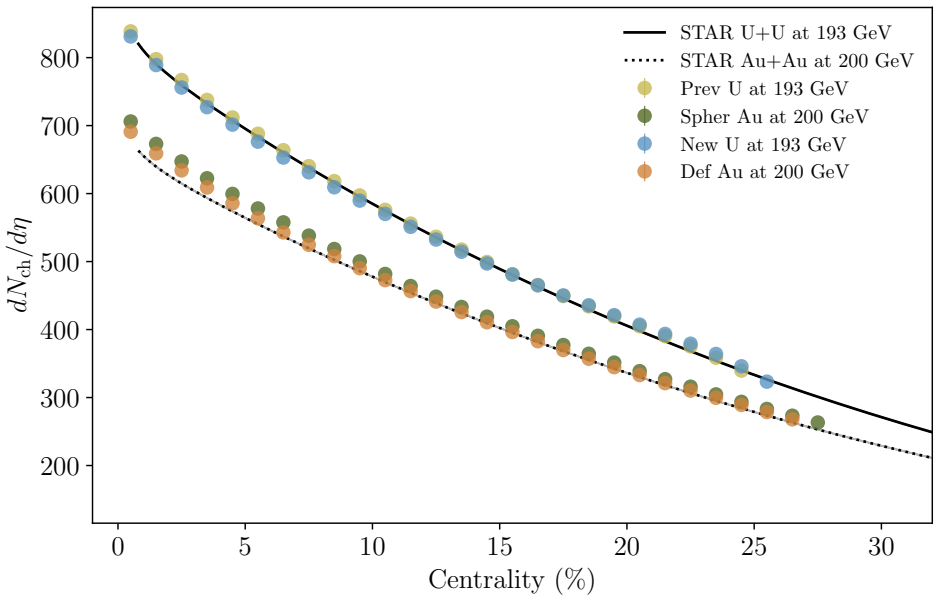


Figure 33: Charged hadron multiplicities in $|\eta| < 0.5$ as a function of centrality. Calculations from our model are compared to parametrizations of charged multiplicity curves for 193 GeV U+U and 200 GeV Au+Au collisions at STAR [105].

uncertainty which is difficult to measure in the absence of the raw experimental data. Nevertheless, this parametrization served as our only calibration tool. Furthermore, the identified particle yields served as a validation of sorts, providing us with raw experimental yields against which to check our calculations, albeit more limited in scope than charged particle yields would have been.

Figure 33 shows the charged particle multiplicity as a function of centrality for our two systems, U+U and Au+Au. Both systems show excellent agreement throughout, and the chosen proportionality constant is $C = 0.505$. The Au curve slightly overestimates the yields provided by the experimental parametrization, which is explained by our calibration's focus on the U yields specifically. It is also interesting to see that nuclear parametrizations - with all other parameters being equal - have a tangible effect on charged particle yields, especially in central collisions. For U, we find that Prev U generates, on average, more charged particles than New U in central (0 - 10%) collisions. The larger yield is due to the slightly higher nucleonic density provided by Prev U's Woods-Saxon parametrization. Indeed, looking at Fig. 32 and Table 2, we see that the

Woods-Saxon radius for Prev U is smaller than that of New U. This will then lead to a smaller volume within which all 238 nucleons must be sampled, yielding in turn a slightly larger nucleonic density. Indeed, taking

$$V_{\mathrm{WS}} = \int_0^{2\pi} \int_0^{\pi} \int_0^{R(\theta,\phi)} r^2 \sin(\theta) d\phi d\theta dr \qquad \text{and}$$
$$R(\theta,\phi) = R_0(1 + \tilde{\beta}_2^0 Y_2^0(\theta,\phi) + \tilde{\beta}_4^0 Y_4^0(\theta,\phi)) \tag{5.1}$$

gives $V_{\text{Prev U}} \sim 1390\,\text{fm}^3$, while $V_{\text{New U}} \sim 1500\,\text{fm}^3$, a $\sim 8\%$ difference. Of course, this is not a fully accurate representation of the nuclear volume of both parametrizations. For one, this quick calculation did not take the diffusiveness $a$ into account: it is smaller for New U than for Prev U, leading to a sharper Woods-Saxon profile for the former and, therefore, a smaller probability of finding nucleons further than $R_0$. For another, the probabilistic nature of the Woods-Saxon distribution means that constraining the nuclear volume for all nuclei generated using a single Woods-Saxon parametrization is a rough approximation. However, to understand the discrepancies between curves of the same system, the point is valid: the Prev U parametrization generally leads to denser nucleonic matter, which, in turn, in central collisions, leads to more charged particles being produced. The same idea holds for the two Au parametrizations. Indeed, we find that Spher Au's yields are larger than those of Def Au and, looking at Table 2, we also find that the Woods-Saxon radius of Spher Au is smaller than that of Def Au. Conducting the same quick integral, we find $V_{\text{Spher Au}} \sim 1080\,\text{fm}^3$ and $V_{\text{Def Au}} \sim 1220\,\text{fm}^3$, another tangible difference of about 12%. One should not, however, give these discrepancies any discriminating power since this step is purely for calibration's sake: if we had wanted, we could have calibrated the constant $C$ to reproduce the charged particle yields perfectly on a system-by-system basis, but this would have made other observables, which have shown sensitivity to this parameter, to become less comparable across systems [77, 87].

Finally, the rightmost points of the U curves dip slightly and break with the curve's trend. This is due to our centrality selection procedure, outlined in Section 4.3.1. For these events, we restricted the impact parameter range from 0 to 8 fm to focus computational resources on generating central events, where, as explained in Chapter 2,

the effects of deformation would be concentrated. We therefore had to use our non-minimum-bias centrality selection procedure to bin our events. While the bins we selected were the ones that reduced the mean-squared-error between the experimental parametrization and our results the most, they did, in the case of the U curves, bring in this dipping artifact. When our procedure is used on non-minimum-bias events, and the selected range is close to the maximal range allowed by the impact parameter range itself, our procedure is bound to allow events which are 'too' peripheral to seep into our most peripheral bins. This erroneous inclusion has a knock-on effect, most visible in the following few peripheral bins until it dissipates. As is apparent from Fig. 33, the Au curves do not share this artifact. This is due to the smaller size of the Au nuclei's Woods-Saxon parametrizations, which, when compared to the chosen impact parameter range for our runs, meant that the maximal centrality allowed by the impact parameter was considerably more extensive than that of our U runs. By limiting our scope to a comparable centrality range, we allowed fewer erroneously classified events into our final bins at the cost of rejecting more events outright because of their peripherality. In other words, the Au curves' most peripheral centrality points and associated impact parameter intervals are well within our impact parameter range, while those of our U events are less well-enclosed. In the end, as we will see with all other observables, this artifact does not affect the conclusions regarding appropriate Woods-Saxon parametrizations, as it does not affect the central bins. Let us move onto observables our model was not explicitly calibrated to match.

## 5.2 U+U AND AU+AU OBSERVABLES

### 5.2.1 *Basic Observables*

Figure 34 shows identified particle yields as a function of centrality for our two systems. We compared our calculations to results published by STAR [111] and PHENIX [112], two experiments based at RHIC. These experiments differ in acceptance and yield

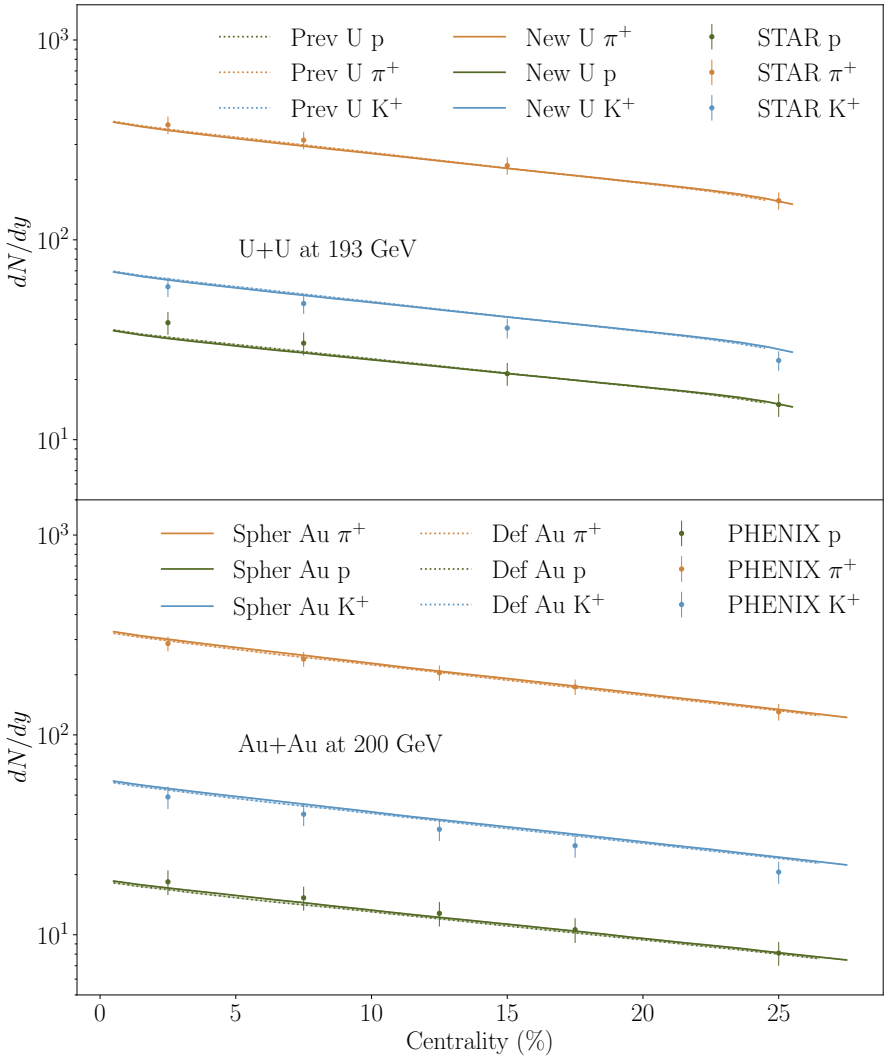


Figure 34: Identified particle multiplicity in $|y| < 0.5$ as a function of centrality. Calculations from our model for (**top**) two U configurations and (**bottom**) two Au configurations are compared to results for 193 GeV U+U collisions at STAR [111] and 200 GeV Au+Au collisions at PHENIX [112].

correction procedures. For example, to be consistent with STAR's experimental procedures, our pion yields were corrected for feed-downs (i.e., contributions to the yields from particles not generated in the original collision event or subsequent inter-particle interactions), while proton yields were not. Conversely, PHENIX's experimental procedures do not correct for feed-downs at all. Clearly, then, we had to carefully analyze which curves should or should not be corrected for such effects to ensure adequate comparisons were being made.

All species considered, our calculations show excellent agreement across the entire centrality window for all configurations and collision systems. This, as mentioned above, proves that our calibration was appropriate and that further results represent our model's current optimal parameter set for the energies at hand. However, the identified particle yields do not show any practical (or potentially discriminatory) sensitivity to our choice of nuclear parametrization. To be clear, there are differences (albeit small) in the yield curves between our different parametrizations. However, all parametrizations fall within the reasonably large error bars provided by the two experiments. It is finally necessary to note that our model does not include a baryon chemical potential $\mu_B$. At these collision energies, $\mu_B$ is small but non-zero, which would affect particle-anti-particle yields.

Figure 35 shows identified particle yields scaled by the average number of participant nucleon pairs in a given centrality class ($\langle N_{\text{part}} \rangle / 2$) as a function of the number of participants $\langle N_{\text{part}} \rangle$. Of course, this observable is highly dependent on the results shown in Fig. 34, as the number of participant nucleons, centrality and yields are all highly correlated. However, this scaled observable identifies how particle production varies from one centrality to another. Because it increases with the number of participant nucleons $N_{\text{part}}$, particle production seems to be guided by a combination of soft and hard processes that scale non-trivially with $N_{\text{part}}$. This result specifically pushes against optical models' (see MC-Glauber) guiding wisdom that multiplicity in a collision is solely determined by the number of binary collisions (and, therefore, the number of participants). Here again, however, different parametrizations give similar results which fall well within the experimental error bars, curtailing any attempt at using it to select appropriate configurations.

Finally, Fig. 36 shows the average transverse momentum $\langle p_T \rangle$ of identified particles against centrality. Contrarily to Figs. 34 and 35, while different parametrizations do give similar results, a more apparent separation emerges. This, like differences in multiplicity found in Fig. 33, is mainly driven by the size differences between configurations. As explained in Chapters 2 and 4, a smaller nucleus leads to a (generally) smaller overlap area in the transverse plane at equal collision energy, which in turn leads to higher energy

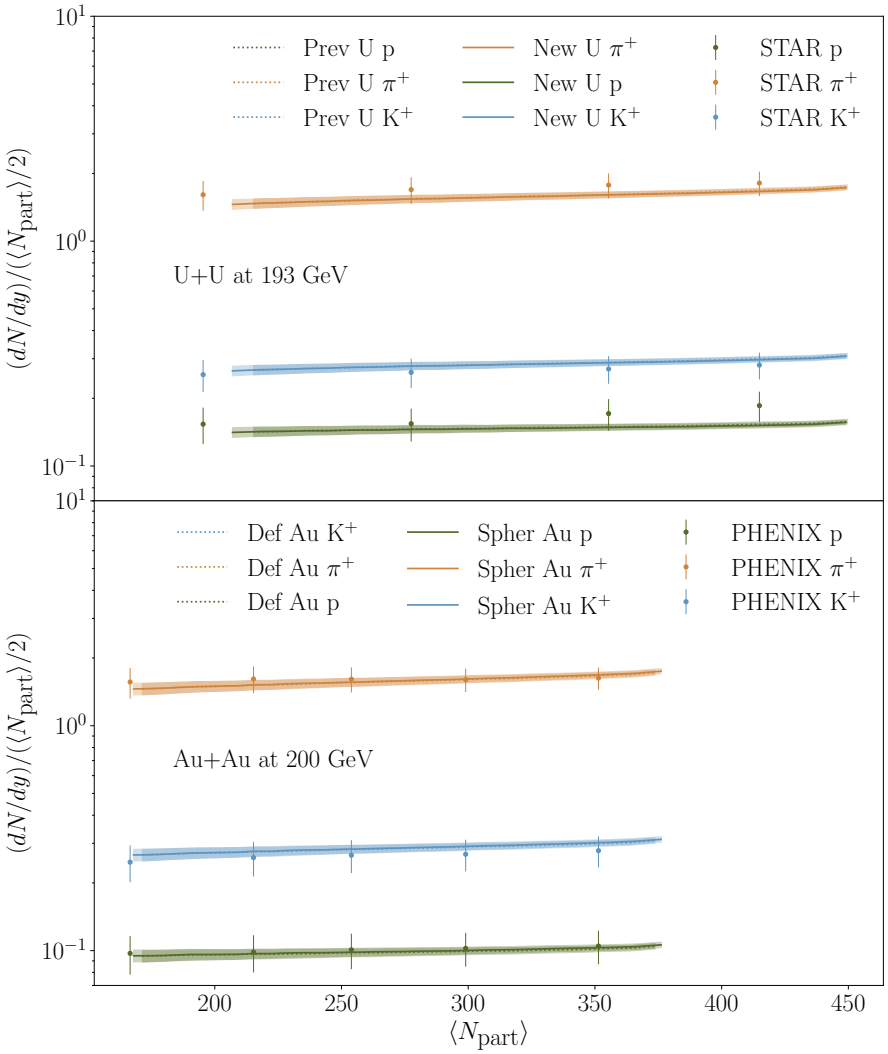


Figure 35: Identified particle multiplicity in $|y| < 0.5$ scaled by average number of participant nucleon pairs in the centrality class $\langle N_{\mathrm{part}}\rangle/2$ as a function of $\langle N_{\mathrm{part}}\rangle$. Calculations from our model for (**top**) two U configurations and (**bottom**) two Au configurations are compared to results for 193 GeV U+U collisions at STAR [111] and 200 GeV Au+Au collisions at PHENIX [112].

densities and larger average transverse momenta at fixed collision energy. Like earlier, the size here does not exclusively refer to the unmodified Woods-Saxon radius $R_0$, but the combination of all Woods-Saxon parameters which contribute to producing specific overlap shapes and sizes. Those overlaps are what is being probed here. The ordering in average transverse momenta between different species is guided entirely by the differences in their respective masses. As in Figs. 34 and 35, all species show significant

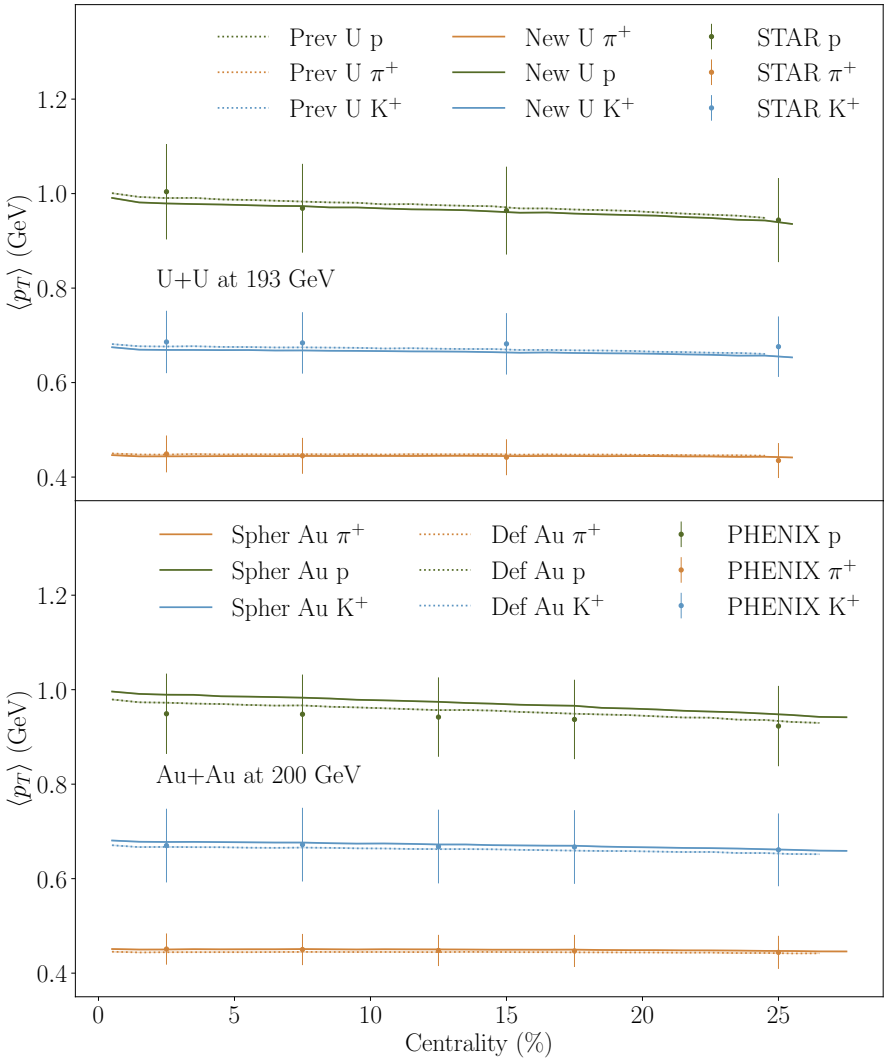


Figure 36: Identified particle mean transverse momentum $\langle p_T \rangle$ in $|y| < 0.5$ as a function of centrality. Calculations from our model for (**top**) two U configurations and (**bottom**) two Au configurations are compared to results for 193 GeV U+U collisions at STAR [111] and 200 GeV Au+Au collisions at PHENIX [112] respectively.

agreement with experimental data. Similarly, sizeable experimental error bars do not allow us to extract any insights regarding which parametrizations are more appropriate, but the marked differences between parametrizations do show that this observable could potentially be used in a discriminating analysis given better-constrained experimental data. Given our use of hydrodynamics, the average transverse momentum puts strong constraints on the $p_T$ spectrum. This entails that good agreement with $\langle p_T \rangle$ is a good indicator of the reproduction of the entire spectrum [113]. Therefore, given our excellent

agreement with experimental data, the shear and bulk viscosity parametrizations and the switching temperature presented in Eqs. (4.10) and (4.11) (and more broadly in Section 4.1.2) seem appropriate.

### 5.2.2 *Elliptic and Triangular Flows*

We are now ready to shift our attention to more sensitive observables, starting with integrated elliptic ($v_2$) and triangular ($v_3$) flows. Figure 37 shows the two- and four-particle cumulants of the elliptic flow $v_2\{2\}$ and $v_2\{4\}$ as functions of charged particle multiplicity and centrality. In both cases, at least one of our parametrizations for both systems matches experimental data well. Both U systems overestimate the elliptic flow at smaller multiplicities or more peripheral collisions. This is a knock-on effect of the artifact described previously, which affected our charged particle yields. Indeed, our most peripheral centrality class contains more peripheral events which weren't rejected by our centrality selection procedure, which in turn leads to an overestimate of the elliptic flow (which generally increases with centrality up to $\sim 40\%$). We also provide a zoomed-in version of the central (0-10%) region of the elliptic flow as a function of centrality in Fig. 38, providing a clearer idea of how parametrizations perform in this critical region of the centrality spectrum.

As explained in Section 4.3.4, this observable served as the first actual signal of the collective nature of particles produced in relativistic heavy-ion collisions. It stands to reason that it should be sensitive to initial state anisotropies, as those are the features carried on to the final state by the hydrodynamic phase. Looking at our U configurations, we find a marked improvement going from Prev U to New U, improvement which is made more evident in Fig. 38. The decrease in $\tilde{\beta}_2^0$ going from Prev U to New U leads to a decrease of the two-particle cumulant of the elliptic flow in central collisions. On the other hand, the four-particle cumulant seems insensitive to changes in parametrizations. This may not be entirely right, as, as explained previously (see Section 4.3.4), further cumulants are meant to isolate pure flow $v_n$ from non-flow effects. However, by con-

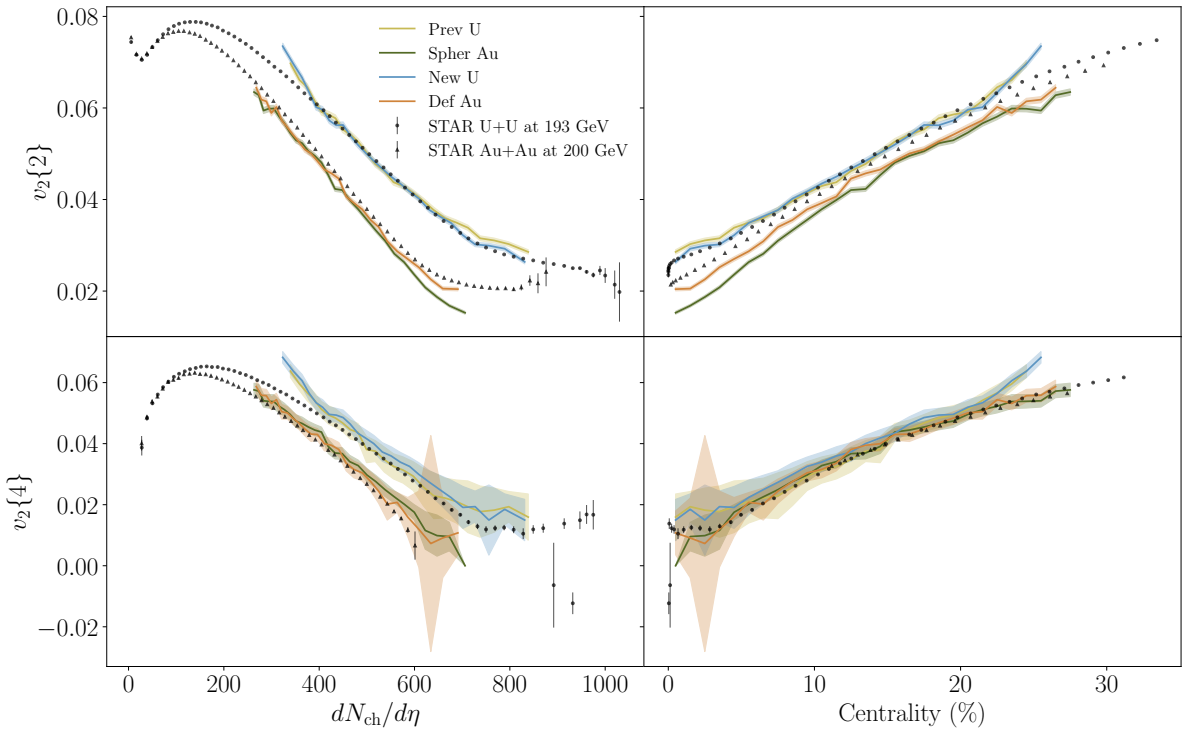


Figure 37: Two- and four-particle cumulants of elliptic flow ($v_2\{2\}$ and $v_2\{4\}$) as functions of (**left**) charged particle multiplicity and (**right**) centrality. Calculations from our model are compared to results for 193 GeV U+U and 200 GeV Au+Au collisions at STAR [105, 114]. The shaded bands represent statistical errors.

struction, these further cumulants do remove contributions from previous cumulants. Therefore, the sensitivity found in the two-particle cumulant will be at least in part subtracted from the four-particle cumulant, which explains the apparent lack of sensitivity (especially when compared to the two-particle cumulant itself).

The Au configurations, on the other hand, show a distinct split in central collisions, which is once again driven by $\tilde{\beta}_2^0$ - this time by its inclusion (Def Au) or exclusion (Spher Au). In central collisions, Spher Au underestimates $v_2\{2\}$ by a wide margin, leading us to conclude unequivocally that $^{197}$Au is deformed. Our deformed parametrization, while it does mirror the experimental data well, still underestimates the experimental curve throughout the entire centrality range. This underestimate, while small, does open the door to future analyses using slightly larger values of $\tilde{\beta}_2^m$. Again, in both Figs. 37 and 38, we find that the four-particle cumulant seems insensitive to the deformation, which at

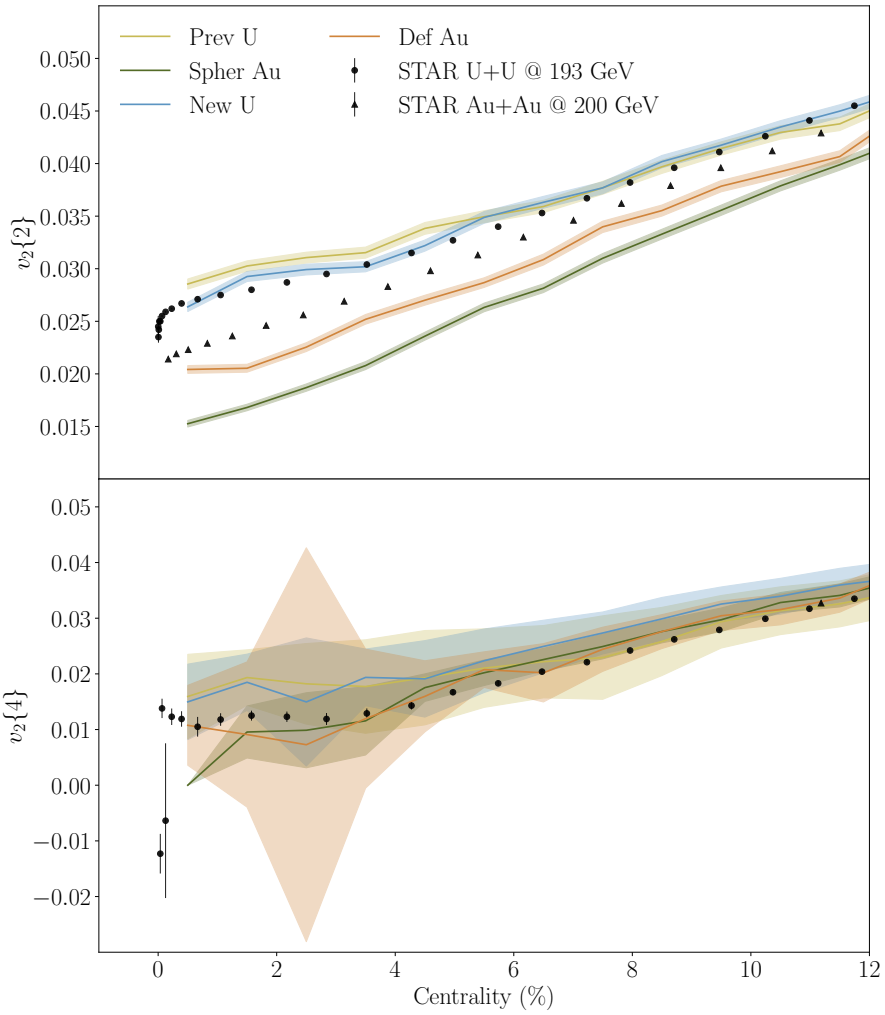


Figure 38: Two- and four-particle cumulants of elliptic flow ($v_2\{2\}$ and $v_2\{4\}$) as functions centrality. Calculations from our model compared to results for 193 GeV U+U and 200 GeV Au+Au collisions at STAR [105, 114]. The shaded bands represent statistical errors.

least in part confirms our hypothesis that the contributions from the quadrupole deformation $\tilde{\beta}_2^m$ are primarily concentrated in the two-particle cumulant, and are subsequently subtracted from this higher-order cumulant.

One may notice that our calculations do not stretch out as far in multiplicity as the experimental data. Looking at Fig. 38 (or the right panels of Fig. 37), we see that the points we do not reach are concentrated between 0 and 0.5% centrality - they are ultra-ultra-central. Furthermore, most of these unmatched points are found within

the top 0.05% centrality. Of course, our runs have events which register multiplicities comparable to those events. However, their number is small and entails bad statistics; we would have to generate many more events to provide a statistically significant picture of what happens within that extremely central, tight window of centrality. Nevertheless, we go down to 0.5% centrality, which is central enough to extract conclusions from the elliptic flow. One should also notice that some of the rightmost, most central experimental points from Fig. 37 are missing in Fig. 38; indeed, we clearly do not see the point comprising large experimental error bars in Fig. 38. This is due to our only having access to a parametrization relating multiplicity to centrality, with these points falling outside of the range mathematically allowed by the form of the parametrization.

The points we are unable to reach tell an interesting story. Indeed, looking at the top panel of Fig. 38, we see that, while the Au elliptic flow does dip in the most central region of the curve, it does not dip as severely as U's elliptic flow. While across the peripheral (10-30%) centrality region, both systems' curves are qualitatively similar, they diverge from one another considerably at about the 5% mark. This is due to the prevalence of body-body and tip-tip events in the most central events of our U event collections. As explained in Section 2.3.2, fully-aligned ($b \sim 0$ fm) collisions of considerably deformed nuclei (such as U) create body-body and tip-tip configurations (see Fig. 14). Body-body collisions will generate slightly less charged particles due to their smaller nucleonic densities and produce more elliptic flow (explaining the marked increase in elliptic flow from 5 to 1% tip-tip collisions produce much less initial state anisotropies (because of the symmetries exhibited by the colliding nuclei about their long axes) while producing more charged particles, populating the most central (1 to 0%) portions of the curve with events having less and less elliptic initial states. The lack of similar features in the Au experimental curve reveals that while $^{197}$Au may be deformed, the scale of its deformity must be small compared to that of $^{238}$U.

Figure 39 shows the ultra-central (and ultra-ultra-central) regions of the $v_2\{2\}$ curves against scaled multiplicity. That is, instead of plotting the elliptic flow against multiplicity directly (as was done in the left panels of Fig. 37), it scales the multiplicities by using

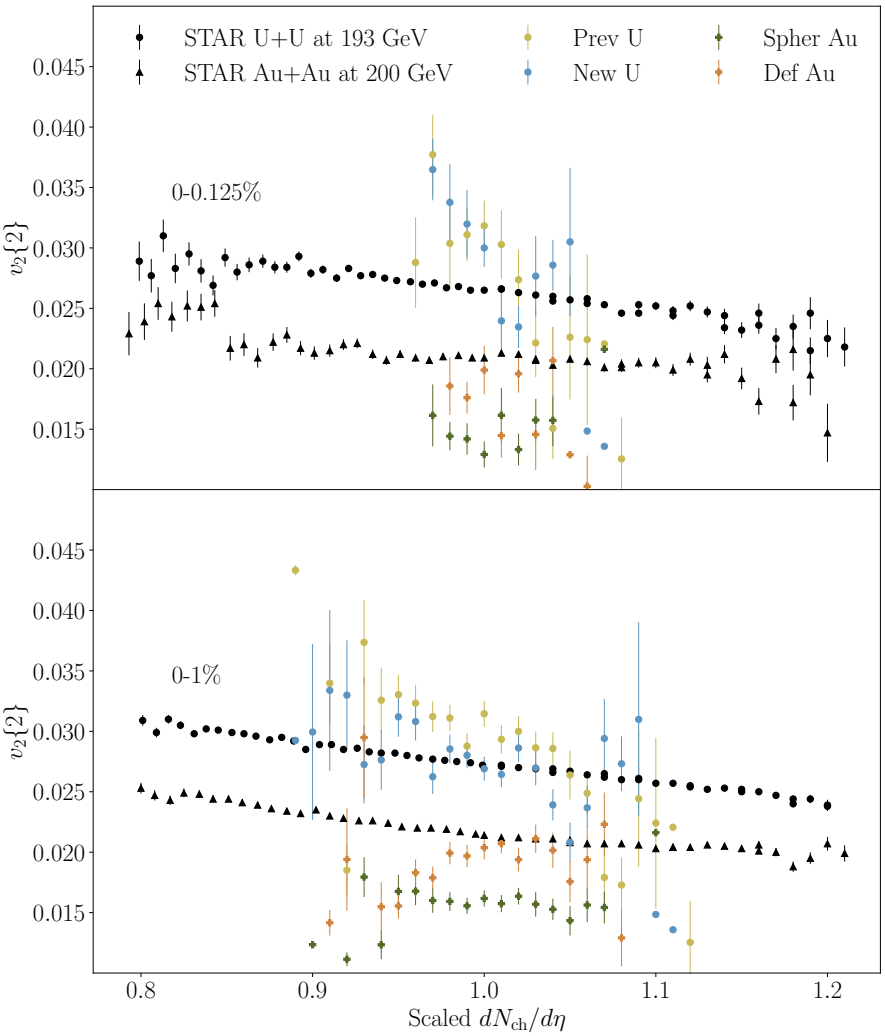


Figure 39: Two-particle cumulant of elliptic flow ($v_2\{2\}$) as functions of scaled charged particle multiplicity for (**top**) $0-0.125\%$ and (**bottom**) $0-1\%$ most cetral events. Calculations from our model are compared to results for 193 GeV U+U and 200 GeV Au+Au collisions at STAR [105].

the average multiplicity in the target centrality ranges (0-1% and 0-0.125%). This reduces the effect of mismatches between our charged particle yields and the experiment's. However, the quoted centralities here are not the same as those presented in the other figures up to this point: these centralities were generated using Zero Degree Calorimeter (ZDC) signals. A ZDC aims to calculate the number of spectator nucleons directly by counting the number of neutrons which did not participate in a given collision. By placing a calorimeter at 0° from the beam direction, neutrons which have not interacted will

continue their route into the calorimeter since the electromagnetic fields responsible for accelerating the ionic beams are ineffective on them. Experimentalists assess the centrality of a collision by counting the number of detected neutrons: the more neutrons were found, the higher the chance that the collision was peripheral. To emulate ZDCs within our framework, we calculated the total number of participating nucleons from a given collision event and subtracted it from the total number of nucleons available to give us the number of spectator nucleons $S$, i.e.

$$S = 2A - N_{\text{Participants}} \tag{5.2}$$

where $A = 238$ for a U+U collision. To obtain the number of neutrons out of the total number of spectator nucleons, we sampled a binomial distribution

$$P(N) = \binom{S}{N} \left(1 - \frac{Z}{A}\right)^{N} \left(\frac{Z}{A}\right)^{S-N} \tag{5.3}$$

where Z is the atomic number (92 for U) and we aim to sample $N$, the number of neutrons, as done in [107]. We average 20 samplings of this distribution per event to reduce variability, giving us the number of spectator neutrons for each event. This method does overlook some points, such as the fact that atomic nuclei have neutron skins (an outer shell where only neutrons are found) [26, 27], which leads to higher probabilities of having spectator neutrons than protons, which are not encapsulated within our simple binomial distribution. These considerations, however, were outside of the scope of this study.

ZDC centralities do carry their own set of inherent uncertainties. However, the experimental data combined with our calculations do show many of the effects described previously. Looking at the top panel of Fig. 39, we find large differences between our two systems not only in the scale of the elliptic flow but also in how it evolves with increasing scaled multiplicity. Indeed, the $^{197}$Au experimental curve is much flatter than that of $^{238}$U, conveying the considerable differences between their deformities: ultra-ultra-central $^{197}$Au collisions present no signs of the body-body-tip-tip dichotomy which is clearly exhibited by the $^{238}$U data (going from $v_2\{2\} \sim 0.03$ to 0.022 within the same extremely

restrictive centrality class). We also find that our statistics could be better, as explained previously. While we do recreate the scale of the elliptic flow in this centrality range, our large error bars and point-to-point fluctuations imply that extracting meaningful conclusions for our $^{238}$U parametrizations would be a stretch. However, looking at the two $^{197}$Au configurations, the Spher Au parametrization (obviously) carries over its considerable underestimation of the elliptic flow from our previous findings. Looking at the bottom panel, which presents a broader (but still ultra-central) centrality range, our calculation's statistics become more reasonable, and the clear separation between parametrizations reemerges. New U and Def Au are the parametrizations that best match the experimental results, reaffirming our previous findings. It is also interesting to note that the $^{197}$Au and $^{238}$U curves' slopes are much more similar than in the ultra-ultra-central range. This means the broader effects of deformity express themselves similarly between the two systems in this range. It also encapsulates the general effect of the impact parameter in generating elliptic flow.

Moving our attention to Fig. 40, we find two new curves for each parametrization stemming from different event averaging techniques. The mixed event curve is generated by taking events from a given centrality class, taking every particle generated in these events and reassigning them to a new event randomly, preserving only event-by-event multiplicities in the process. This procedure aims to determine what underlying correlations (if any) exist between events of a given centrality class. What this curve tells us is that for peripheral events of both systems, mixing all events does not lead to a considerable difference from the actual calculated curves, meaning that all peripheral events essentially look the same. Ergo, mixing them up with one another does not change much. When moving toward the central regime, however, the discrepancies between the mixed event curves and our calculations become appreciably larger, confirming that little underlying relationship exists between these central events: the anisotropy we find in the final state is due largely to event-by-event initial state anisotropies, which cannot be recuperated when mixing all events.

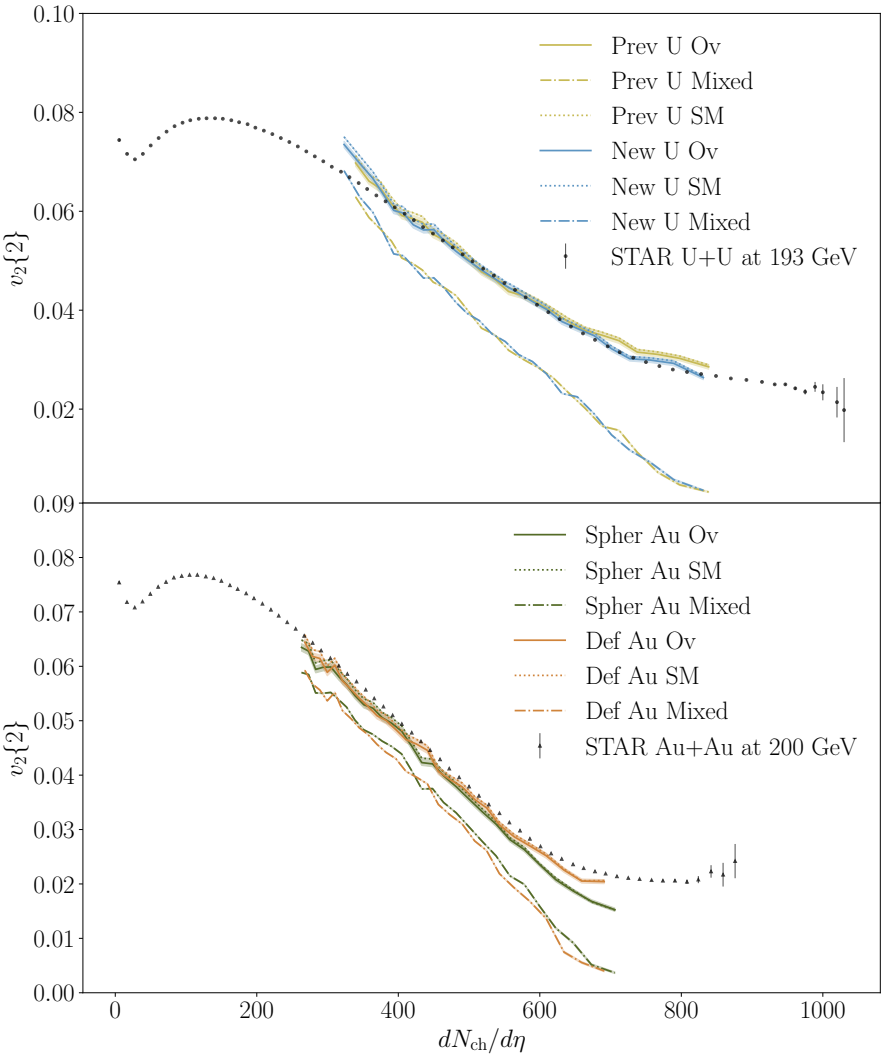


Figure 40: Two- and four-particle cumulants of elliptic flow ($v_2\{2\}$ and $v_2\{4\}$) as functions of charged particle multiplicity. Calculations from our model are compared to results for 193 GeV U+U and 200 GeV Au+Au collisions at STAR [105, 114]. The shaded bands represent statistical errors. We emphasize the addition of Mixed Event and SMASH sub-event average curves compared to Figs. 37 and 38. To differentiate between the different averaging curves, *SM* stands for SMASH sub-event average while *Ov* stands for oversampled average.

The other addition to Fig. 40 is the SMASH sub-event average curve (*SM*). As mentioned in Chapter 4, the hydrodynamic hypersurface is oversampled 1000 times to create a physically accurate picture of the ensemble-averaged state at the interface between hydrodynamics and hadronic transport. However, a choice offers itself when

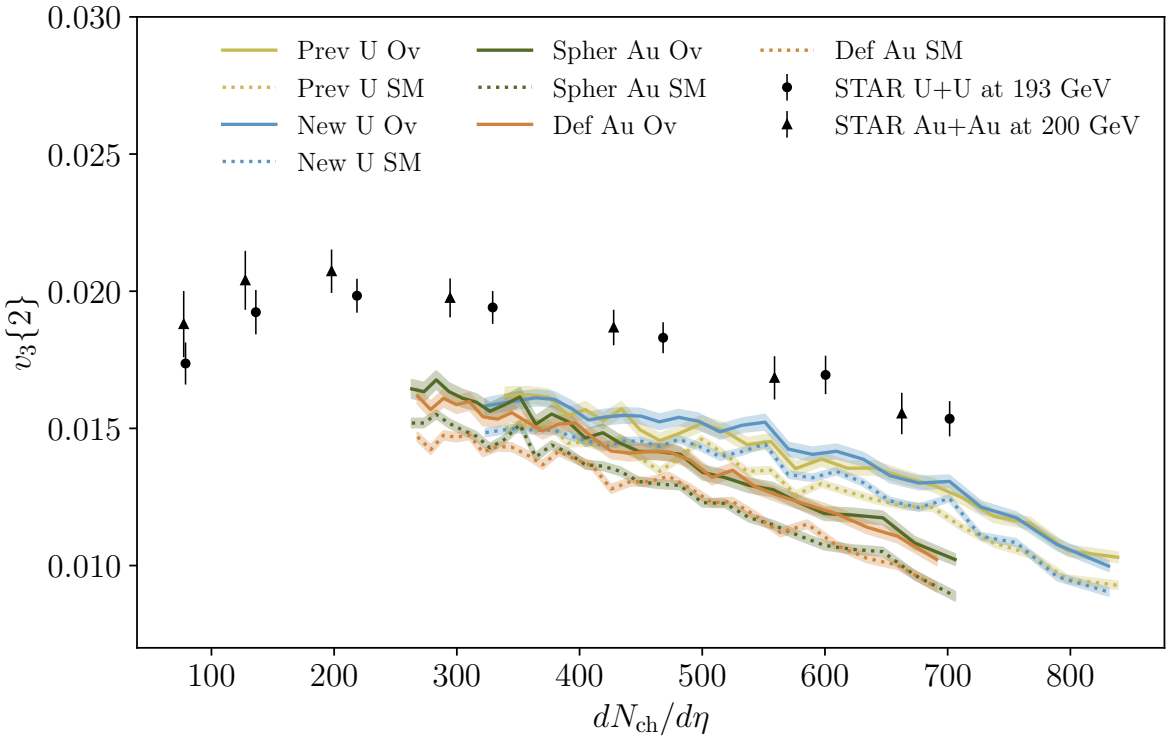


Figure 41: Two-particle cumulant of triangular flow ($v_3\{2\}$) as a function of charged particle multiplicity. Calculations from our model are compared to results for 193 GeV U+U and 200 GeV Au+Au collisions at STAR [110]. Here, *SM* stands for SMASH sub-event average while *Ov* stands for oversampled average.

comes time to analyze the results from a given centrality class: we can either average the oversampled events corresponding to a single hydrodynamic event to create a single event per hydrodynamic evolution (what is usually done), *or* we can preserve all of the oversampled events (with all of their statistical fluctuations intact), build our centrality classes *and then* calculate the average of every single oversampled event belonging to a given centrality class. This slight difference in procedure can considerably impact a given observable, as we will see later in this chapter. Indeed, taking the average at the end of the centrality binning expresses short-range correlations, usually drowned out by taking hydrodynamic event-by-event averages. For elliptic flow specifically, however, Fig. 40 reveals that both averaging techniques are equivalent, indicating that long-range correlations encapsulate the entirety of this observable.

Moving away from elliptic flow, we focus on the two-particle cumulant of triangular flow $v_3\{2\}$. Looking at Fig. 41, we find that the experimental curves practically overlap across the entirety of the charged particle multiplicity range. This reveals the nature of triangular flow as being fluctuation-driven (as opposed to driven by initial state geometry). Our calculation underestimates the observable across both systems and all parametrizations. Taking the SMASH sub-event average decreases the calculated value of triangular flow, meaning that short-range correlations decrease overall triangular fluctuations. Because this observable is driven by initial state fluctuations, a potential solution to our underestimate would be to include sub-nucleonic degrees of freedom (i.e. valence quark configurations) to our initial thickness function $T_A(\vec{x})$ (see Eq. (3.26)), such as those described in Ref. [115]. Including these new sub-nucleonic hot spots could lead to an overall increase in short-range correlations and fluctuations, leading to an increase in the SMASH sub-event averaging results.

The final flow observables we will show are the $p_T$-differential $v_n\{2\}$ for charged hadrons and identified particles. Figure 42 shows our model's calculations across the two systems, compared to existing experimental data. One notices that only one such experimental curve exists, that of $^{197}$Au and published by PHENIX [116]. This implies that our $^{238}$U curves are predictions of our model. One should also note that the PHENIX procedure for calculating the $p_T$-differential anisotropic flow differs from ours, as they do not employ the scalar product (SP) method. Differences due to this discrepancy are, however, minor.

Differential elliptic flow $v_2\{2\}(p_T)$ is larger for $^{238}$U than for $^{197}$Au across all centrality classes, irrespective of parametrization. As expected, the gap gets smaller as we move towards more peripheral collisions. In the 0-10% window, the differences are consistent with the deformation effects described previously: we expect the elliptic flow to be enhanced in this region of the centrality spectrum because of the more marked ellipsoidal shape of $^{238}$U. The two $^{197}$Au configurations overestimate $v_2\{2\}(p_T)$ for $p_T \geq 0.5\,\text{GeV}$. While the discrepancy may point to inadequacies in our hydrodynamic modelling, it is crucial to remember that most produced particles have $p_T \leq 1\,\text{GeV}$,

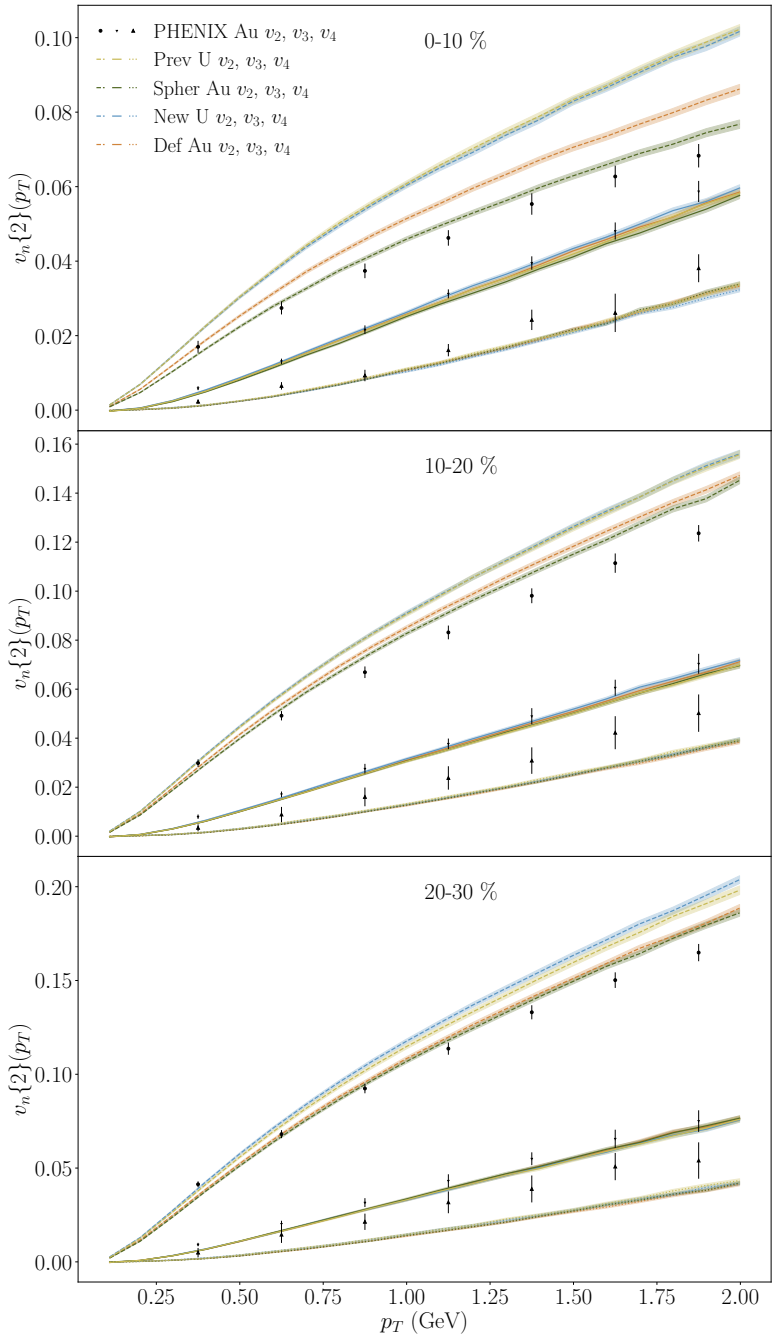


Figure 42: Charged hadron differential anisotropic flow coefficients $v_2\{2\}$, $v_3\{2\}$ and $v_4\{2\}$ as functions of transverse momentum $p_T$ for various centrality classes. Calculations from our model are predictions for 193 GeV U+U collisions, while they are compared to experimental results from PHENIX [116] for 200 GeV Au+Au collisions.

implying that higher $p_T$ contributions to the integrated elliptic flow are small. In the 10-20 % and 20-30 % classes, the differences are minor and are themselves consis-

tent with elliptic flow being noticeably larger for U+U collisions compared to Au+Au throughout the collision spectrum, as evidenced in Fig. 37. The two configurations from both systems overlap $v_2\{2\}$ lines, further confirming that specific nuclear structures do not play an essential role beyond central collisions.

Moving to differential triangular flow $v_3\{2\}(p_T)$, we find that the curves for both systems are very similar throughout. Recalling our analysis of Fig. 41, this is expected, as triangular flow is mostly driven by local fluctuations, which are similar in both systems and are unaffected by the Woods-Saxon parametrizations we have chosen. As for $v_4\{2\}(p_T)$, both collision systems underestimate this observable in peripheral (10 – 30%) collisions. In central (0 – 10%) collisions, both collision systems overlap with themselves and the experimental data. Therefore, our model predicts that $v_4\{2\}$ for U+U collisions at 193 GeV should be similar (if not equal) to that of Au+Au collisions at 200 GeV. This result implies that $v_4\{2\}$ is insensitive to our configurations' specific initial state anisotropies.

Figure 43 shows the differential elliptic flow for identified particles. As with Fig. 42, in the absence of experimental results, the $^{238}$U curves stand as predictions of our model, while the $^{197}$Au curves are compared to experimental results from STAR [117]. This figure only includes 2 parametrizations (New U and Def Au) for clarity, given that conclusions regarding the ordering of the different configurations can be extracted from Fig. 42. Def Au reproduces the experimental data well across all four centrality ranges. Predictably, our calculations yield a more significant differential elliptic flow for $^{238}$U than for $^{197}$Au across all species. The effect is apparent in the ultra-central regions (0 – 5% & 5 – 10%) and crosses hadronic lines. However, in the more peripheral regions (10 – 20% & 20 – 30%), this difference becomes much smaller and varies considerably from one hadron to another; our model's predictions for anti-protons are similar to both $^{197}$Au experimental data and our model's calculation. Higher-$p_T$ differential flow seems to converge consistently across all identified particles.

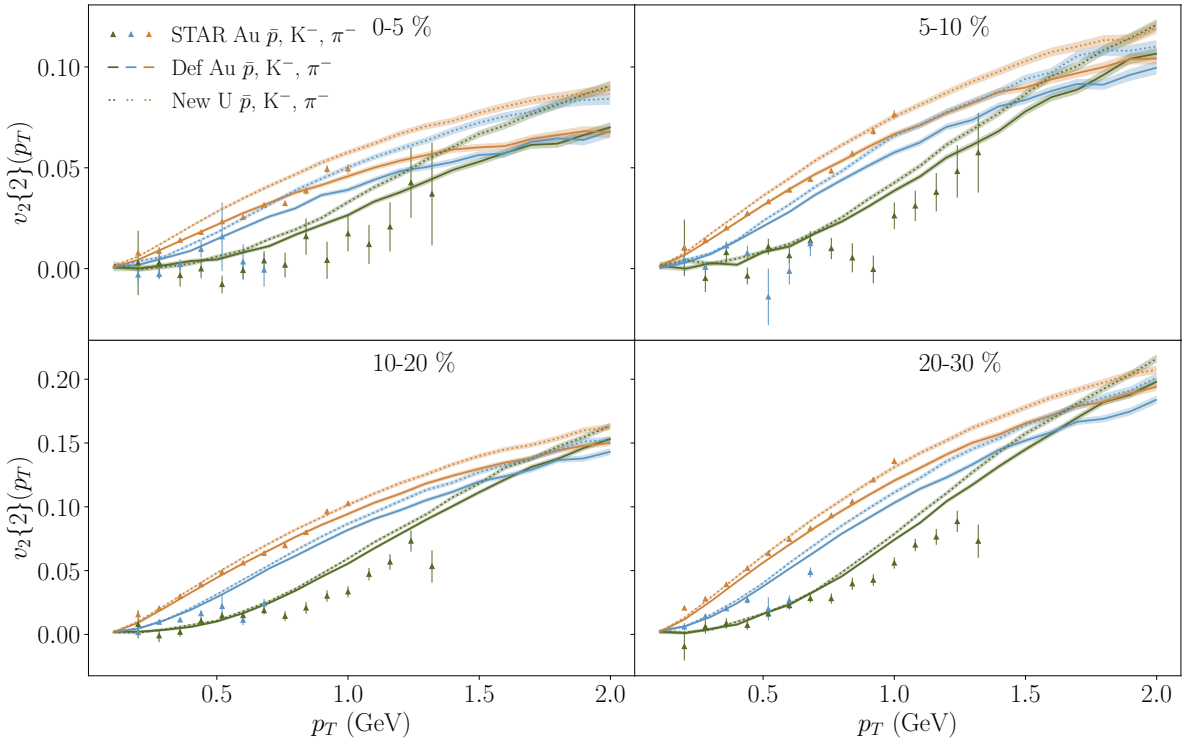


Figure 43: Identified particle differential elliptic flow $v_2\{2\}$ as a function of of transverse momentum $p_T$ for various centrality classes. Calculations from our model are predictions for 193 GeV U+U collisions, while they are compared to experimental results from STAR [117] for 200 GeV Au+Au collisions.

### 5.2.3 *Correlators*

Moving on, we will consider different correlators and how they can differentiate between parametrizations. We start with the 2- and 3-particle correlators described in Section 4.3.3, which can be found in Fig. 44. When used with primary observables such as elliptic flow, these correlators can help constrain a deformed nucleus' Woods-Saxon parameters thanks to their sensitivity [118, 119].

The top panels of Fig. 44 show the 2-particle $p_T$ correlator compared to experimental data from STAR [118], with each collision system having its subplot for clarity. We have included a mixed event curve, just like in Fig. 40, to ensure no underlying $p_T$ correlations exist. Its position on the plot - 0 across the entire range - confirms this. Contrary to our findings with elliptic flow, a sizeable difference exists between our oversampled

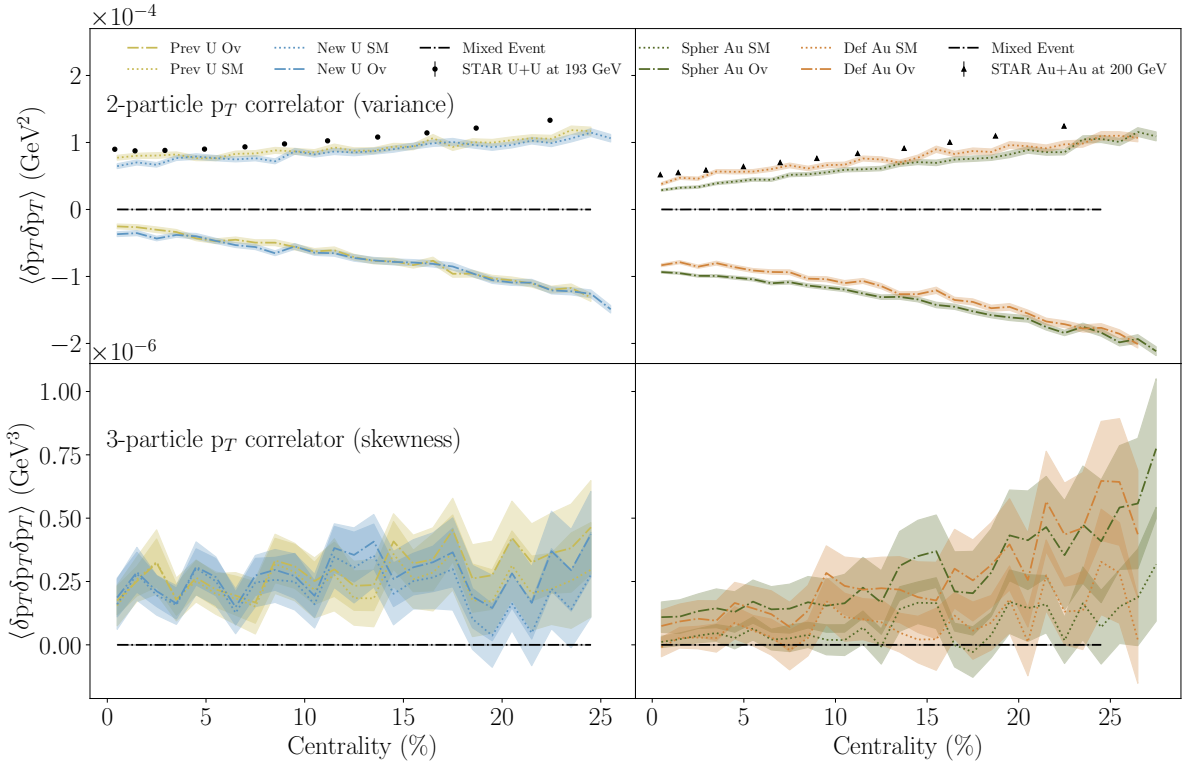


Figure 44: (**top**) 2- and (**bottom**) 3-particle momentum correlators as functions of centrality, with 0.2 GeV $\leq p_T \leq$ 3.0 GeV, for (**left**) U+U at 193 GeV and (**right**) Au+Au at 200 GeV. Calculations from our model are compared to experimental results from STAR [118]. Here, *SM* stands for SMASH sub-event average while *Ov* stands for oversampled average.

and SMASH sub-event averaged curves; they are indeed opposed with respect to the origin. This reveals that including short-range correlations is a crucial determinant of this observable's behaviour across collision systems. Our SMASH sub-event averaged curves match available experimental data well, with Prev U and Def Au as the best matches.

It is also interesting to see how the strength of the correlations changes across collision systems, an ordering dictated by the size and deformity of a given system. Indeed, a hierarchy exists between our curves, going from least deformed (Spher Au) to most deformed (Prev U). The ordering persists at more peripheral centralities, indicating a further dependence on system size ($A$ and $R_0$). One should also notice that in ultra-central $^{238}$U collisions, there is a marked uptick of the 2-particle $p_T$ correlator that

does not appear in the experimental $^{197}$Au curve. This is, once again, due to the larger deformity offered by $^{238}$U compared to $^{197}$Au: the number of pairs of particles with $p_T$ considerably deviating from the centrality class mean ($\langle p_T \rangle$) swells thanks to the distinct groups (body-body and tip-tip) of collision geometries present in said centrality classes. This effect is deconstructed in detail in Ref. [120].

The bottom panels of Fig. 44 show the 3-particle $p_T$ correlator. Again, we opted to include a mixed event curve, reiterating the absence of underlying and all-encompassing $p_T$ correlations in all centrality classes. Contrarily to the 2-particle correlator, the two averaging techniques generally give similar results, with the oversampled average curves giving out slightly larger correlation values than the SMASH sub-event average. The 3-particle correlator is generally larger for $^{238}$U than for $^{197}$Au, especially in central collisions. Interestingly, the SMASH sub-event and oversampled average curves diverge as we move towards more peripheral collisions; the same occurs with the 2-particle correlator, indicating that short-range correlations become increasingly crucial with peripherality. Unfortunately, the lack of experimental data for the 3-particle correlator makes it impossible to use in our constraining procedure. As a final note for this plot, both observables would be sensitive to including sub-nucleonic degrees of freedom (an idea introduced when discussing Fig. 41). Indeed, given their sensitivities to short-range correlations, adding further correlated hot spots (i.e. the quarks) should increase the values of both observables.

Figure 45 shows the transverse-momentum-flow correlation for both systems, an observable which has garnered interest as a tell-tale sign of deformation [98]. This figure does not include the SMASH sub-event averaging technique or the mixed event curves. The former does not lead to a tangible difference (given similar results for the elliptic flow), while the latter is not defined: looking at Eq. (4.43), one notices that a division by $\langle \delta p_T \delta p_T \rangle$ is required, a quantity which is evenly 0 for our mixed event treatment.

Triangular-flow-transverse-momentum (bottom panel) correlations are dominated by fluctuations, with the only real clear trend being that the correlator remains positive

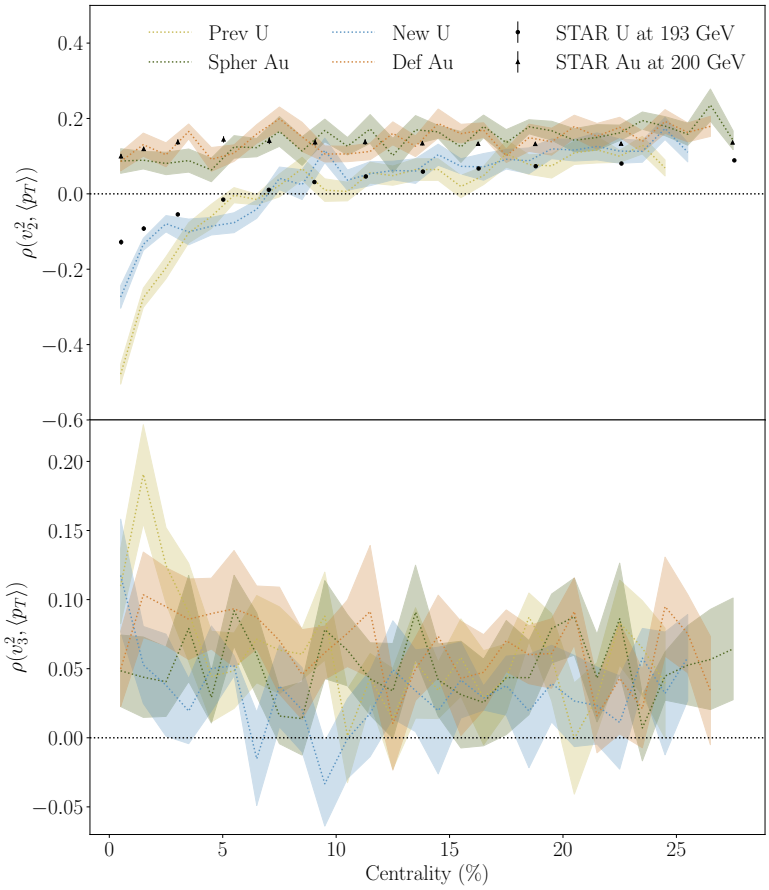


Figure 45: (**top**) Elliptic and (**bottom**) triangular flow and $\langle p_T \rangle$ correlations as functions of centrality. Calculations from our model are compared to experimental results for U+U at 193 GeV and Au+Au at 200 GeV from STAR [118].

throughout the centrality range and across both collision systems and parametrizations. As with the 3-particle correlator, no experimental data was available for this observable.

Elliptic-flow-transverse-momentum correlations, on the other hand, show clear sensitivity to collision systems. Our calculation agrees with experimental data across our entire centrality range. Critically, when our results were first published, this observable stood as a pure prediction of our model: like all other observables except charged particle multiplicity, our model was not explicitly calibrated to match elliptic-flow-transverse-momentum correlations. The experimental data was published afterwards and showed that our model's predictions were accurate. As explained in Section 4.3.5, an anti-correlation is expected to emerge in central collisions of considerably deformed

nuclei, which we find in our calculation and the experimental data. Importantly, when (in the centrality spectrum) this anti-correlation emerges, as well as at what degree of deformity, is still very much unknown. As is apparent in Fig. 45, $^{197}$Au presents no such anti-correlation even though we have determined that deformity is a critical part of reproducing its experimental elliptic flow curve. While their crossovers from correlation to anti-correlation occur at the same centrality ($\sim$ 7%), Prev U's predicted anti-correlation is larger than that presented by the experimental data. On the other hand, New U follows the experimental curve across the entire range. Given the unique sensitivity this observable has concerning deformity, its preference for New U is more important than that of the 2-particle correlator for Prev U, as the latter was only slightly sensitive to deformity, and our lack of inclusion of sub-nucleonic degrees of freedom could have had a considerable effect on this specific observable. For the $^{197}$Au configurations, both fit the experimental data well, making it hard to extract any insight.

### 5.2.4 *Insights from Ratios*

We have hinted a few times that our hydrodynamic modelling could be causing discrepancies. Indeed, even though our hydrodynamic parameters were carefully selected using knowledge produced in an expansive and detailed Bayesian calibration [77, 87], these parameters still have room for improvement. However, it is understood that taking ratios of observables between collision systems can help ease tensions that could arise from loosely constrained hydrodynamic parameters. These new composite observables are mainly independent of the hydrodynamic phase, as they stem from the same hydrodynamic evolution using the same transport properties [118]. We therefore thought it important to calculate ratios of critical observables to ensure that those also matched experimental results, further helping us constrain our choice of nuclear parametrizations as those are fully encapsulated into the initial state. These ratios will be defined as

$$\mathrm{r}_{\mathrm{Au,U}}\left(O\right) = \frac{O_{\mathrm{U}}}{O_{\mathrm{Au}}}, \tag{5.4}$$

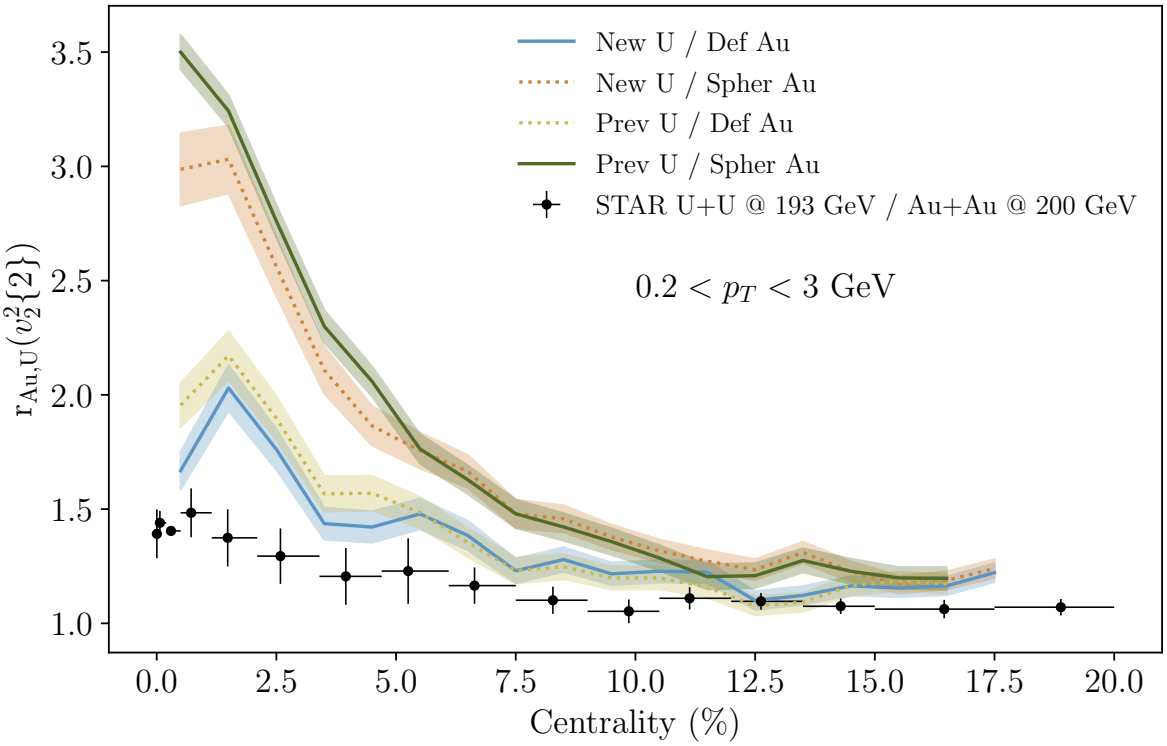


Figure 46: Ratios of the mean squared elliptic flow $v_2\{2\}^2$ as functions of centrality. Calculations from our model are compared to experimental results for 193 GeV U+U and 200 GeV Au+Au collisions at STAR [118].

where $O$ is a placeholder for the specific observable we are rehashing through the ratio.

Starting with elliptic flow, Fig. 46 shows the ratio of $v_2\{2\}^2$ between U+U at 193 GeV and Au+Au at 200 GeV measured at STAR [118]. A clear separation can be seen between ratios which use Def Au and those that use Spher Au. This is perfectly in line with our findings from Figs. 37 and 38, where the gap between the two $^{197}$Au parametrizations was larger than that between the two $^{238}$U configurations. Furthermore, even our best combination of parametrizations, New U / Def Au, overestimates the ratio. This is unsurprising, considering our slight underestimate of the $^{197}$Au elliptic flow. We must reiterate here that, considering a single calibration was undertaken for our two systems, our model reproduces the elliptic flow fairly well. Our calculations between 0-1% and 3-4% follow the data qualitatively and quantitatively, ranges which are particularly sensitive to initial geometry. This still points to the fact that a run with a slightly

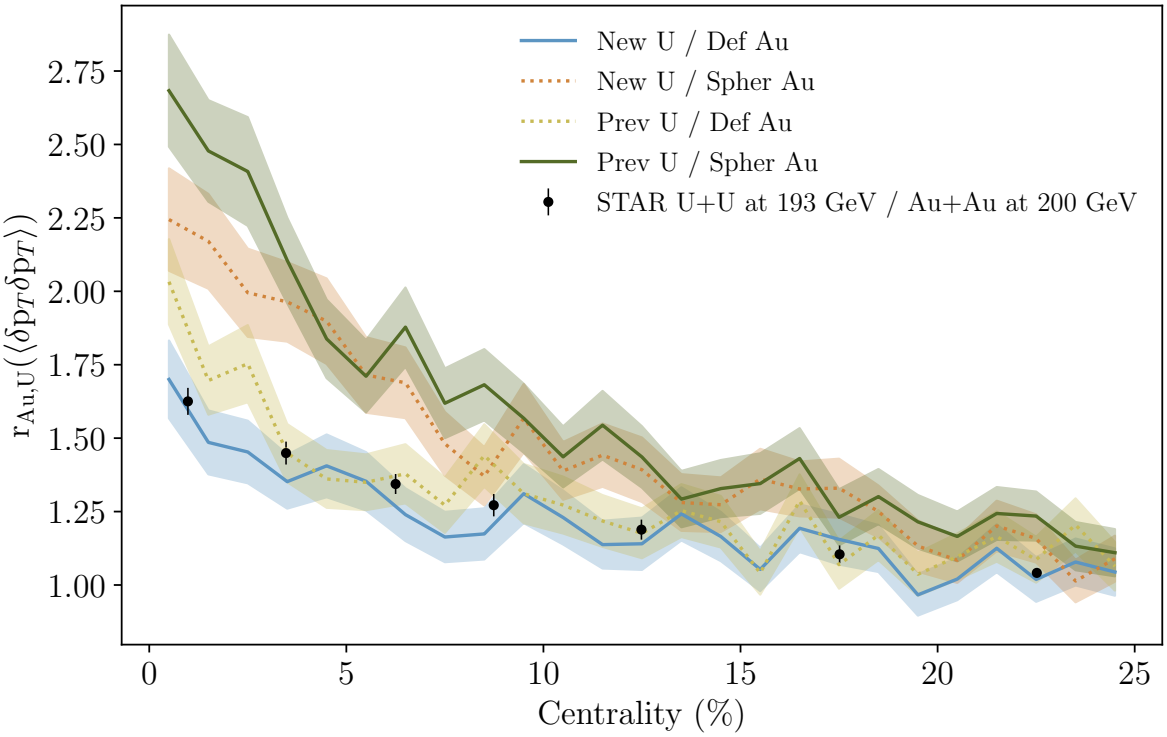


Figure 47: Ratios of the 2-particle $p_T$ correlator as functions of centrality. Calculations from our model are compared to experimental results for 193 GeV U+U and 200 GeV Au+Au collisions at STAR [118].

larger quadrupole deformation for $^{197}$Au might be interesting. It also tells us that an individually calibrated $^{197}$Au run may provide the minor corrections required to perfectly reproduce the ratio (and individual observable).

Moving to Fig. 47, we find the ratios of the 2-particle $p_T$ correlator between U+U at 193 GeV and Au+Au at 200 GeV measured at STAR [118]. Here, only the SMASH sub-event curves from the top panels of Fig. 44 are included, as they were obvious matches for their respective experimental curves. Once again, the best ratios are obtained using Def Au in the denominator, with the ratio using New U being a slightly better match than that using Prev U. This is in contrast to what we had observed in Fig. 44's top-left panel, where Prev U had been the better match when considered individually. This fact exposes one of the caveats of using ratios as observables: this 'new' observable is two independent observations wrapped into one, and two underestimates can turn into a

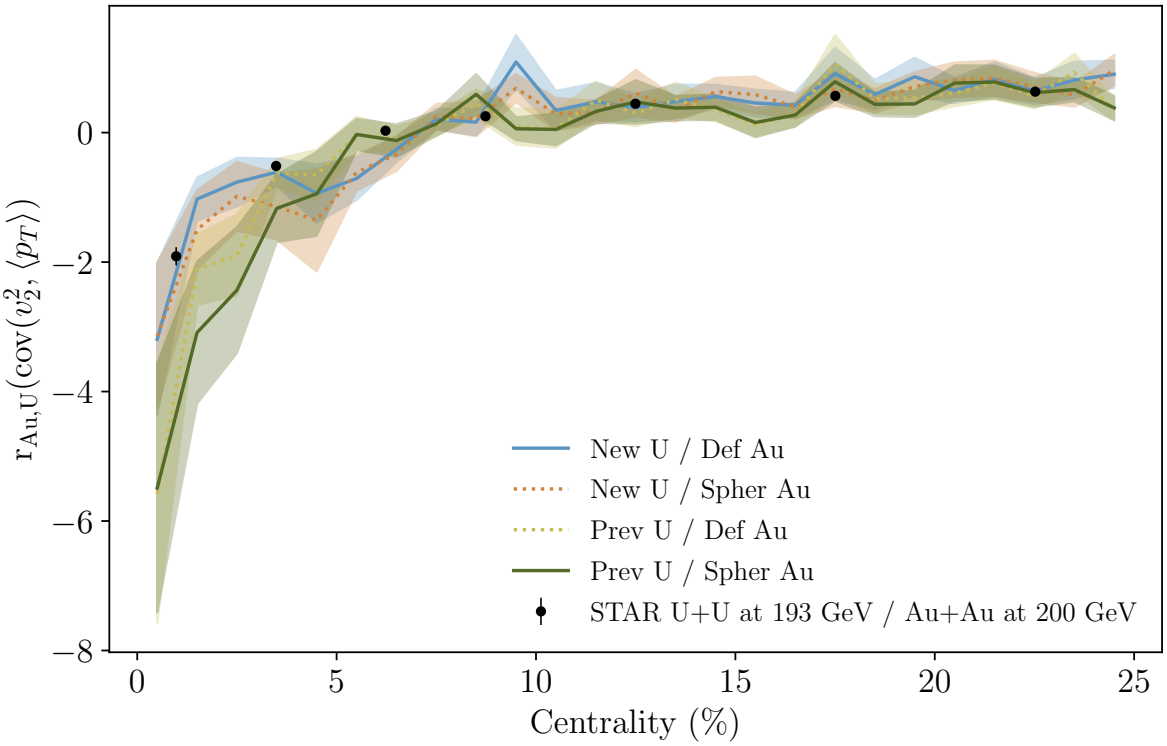


Figure 48: Ratios of the covariances of $v_2\{2\}$ and $p_T$ as functions of centrality. Calculations from our model are compared to experimental results for 193 GeV U+U and 200 GeV Au+Au collisions at STAR [118].

ratio being spot-on. The ratio seems to suggest, however, that our calculations prefer New U and Def Au as long as we isolate our results from our hydrodynamic modelling.

We end this first results chapter by looking at the ratios of the covariances of $v_2\{2\}$ and $p_T$ between U+U at 193 GeV and Au+Au at 200 GeV measured at STAR [118], Fig. 48. Here, the covariances (Eq. (4.44)) and not the entire correlation (Eq. (4.43)) were taken to align with available experimental results. All ratios perform well in peripheral (> 10% centrality) collisions. In central collisions, ratios including Prev U fall sharply lower than the experimental results. Both New U ratios perform well, with a preference, in central collisions, for the New U and Def Au combination - in line with all other ratios. This shows that while Fig. 45 could not meaningfully distinguish our two $^{197}$Au parametrizations, the ratio tells us that Def Au is a more appropriate parametrization, reiterating that $^{197}$Au must truly be deformed.

Therefore, this chapter shows how, with a simple calibration, our model can reproduce many qualitatively different observables simultaneously. Furthermore, it has shown an evident sensitivity to early-stage anisotropies, allowing us to determine that the New U parametrization was an exceptional match for the experimental data, implying it is the best parametrization currently proposed by the literature. It has also allowed us to show, beyond any doubt, that $^{197}$Au is a deformed nucleus. However, the scale of this deformity is still up for debate, as our underestimation of the elliptic flow suggests that a larger deformity could lead to a better match to experimental data. To extract more definitive conclusions, an $^{197}$Au-specific calibration should be undertaken to avoid any underlying biases that may affect end-state observables. All-in-all, our model performed tremendously and has demonstrated how it can be used as a tool to reconcile low-energy deformation estimates with high-energy results, provided that relevant high-energy experimental data exists and allows us to make deductions (i.e. is precise enough).

Throughout this section, the boost-invariant formulation of our model was used. In the following chapter, we will formally extend our initial state and hydrodynamics phase in the longitudinal direction, and will introduce potentially relevant longitudinal observables that could further help us in our pursuit of putting firm constraints on the Woods-Saxon deformation parameters of specific nuclei. We will then use the tools and knowledge acquired during the analysis presented in this chapter to constrain the deformation parameters of $^{129}$Xe, an isotope which has had limited runs at the LHC and is considered deformed but with much uncertainty surrounding its most appropriate Woods-Saxon parametrization.

# 6

# LONGITUDINAL DYNAMICS

After the success of the boost-invariant analysis presented in Chapter 5, we sought to determine if including longitudinal dynamics (i.e. moving away from a purely boost-invariant simulation) could provide new insights and discerning capabilities regarding deformed systems, specifically $^{129}$Xe. Before answering this question, we must generalize our framework to 3+1 dimensions; thankfully, the evolution equations derived in Chapter 3 are entirely valid in this new regime. However, a few critical questions do arise. Firstly, now that we are moving away from a system at mid-rapidity, how do the CGC assumptions and the color charge sampling procedure, both relying on the small momentum fraction of our system, hold up? How are different parts of the rapidity space related to one another in a coherent evolution? Then, in our initial conditions, shown in Section 3.3.2, our boost-invariant assumption led to the initial longitudinal color gauge fields being evenly 0 at $\tau = 0^+$. Does this presumption continue to be true in a 3+1D initialization? And finally, how does our hydrodynamic model accommodate the new longitudinal extent and degree of freedom?

In this chapter, we will answer the above questions by following the work presented in Refs. [17, 54, 55, 67, 121–123]. We will first show how the momentum fraction probed at a given rapidity can be found. We will then explain how the saturation scale and the color charge distribution are translated in rapidity space via the JIMWLK (Jalilian-Marian, Iancu, McLerran, Weigert, Leonidov, Kovner) equation. Leveraging this new formalism, we will rederive our initial conditions in 3+1D. We will discuss how the interface between the initial state and the hydrodynamics phase changes in a 3+1D setting, and how the hydrodynamic evolution of different rapidity slices differ from

one another. Finally, we will define new observables which leverage the longitudinal dynamics to allow us to interpret our second set of results, which will be presented in the next chapter, in the hopes of finding new signals of nuclear deformity to be detected in future experiments.

## 6.1 INITIAL STATE IN 3+1D

### 6.1.1 *Momentum Fraction x*

We begin our redefinition of the initial state by analyzing one of the foundational assumptions of the CGC, namely that heavy-ion collisions produce conditions where the relevant degrees of freedom are purely gluonic and are so dense that classical field theory can be used to describe them. Referring back to Fig. 15, we find that gluons dominate for $x \leq 0.01$. Given that different values of spacetime rapidity $\eta$ will be probed, it stands to reason that we will need to redefine the momentum fraction in terms of the value of $\eta$ of a given transverse region.

We begin by defining kinematic rapidity $y$, an analog to spacetime rapidity $\eta$,

$$y = \frac{1}{2} \ln \left( \frac{E + p_z}{E - p_z} \right) \tag{6.1}$$

which, using the hyperbolic cosine function cosh, can be transformed into

$$y = \cosh^{-1} \left( \frac{E}{m_T} \right), \tag{6.2}$$

where $m_T$ is the transverse mass of the nucleon ($m_T = \sqrt{m_N^2 + p_T^2}$) having energy $E$. Using the fact that the energy in a given collision is given by $\sqrt{s}/2$, we can use Eq. (6.2) to obtain the kinematic rapidity of our heavy-ion beam,

$$y_{\text{beam}} = \cosh^{-1} \left( \frac{\sqrt{s}}{2m_N} \right), \tag{6.3}$$

where $m_T = m_N$ here because the nucleon's motion is purely in the $z$-direction.

Rapidity is an additive quantity, meaning that to obtain the rapidity of an observer in a frame $S'$ moving relative to a frame $S$ (in which our beam rapidity is defined), one simply takes [124]

$$y\,(\text{in frame } S') = y\,(\text{in frame S}) - y(S' \text{ relative to } S). \tag{6.4}$$

In other words, the measured rapidity of the particle in two different frames differs by the rapidity of the boost between the two frames, making kinematic rapidity a useful and powerful tool for describing relativistic particles.

In the boost-invariant case, the momentum fraction $x$ of a gluon cloud of saturation scale $Q_s$ at a given collision energy is [60]

$$x = \frac{Q_s}{E_{\text{beam}}}. \tag{6.5}$$

Moving away from boost-invariance, one can look at the momentum fraction probed in this new frame $S'$ by taking

$$x = \frac{Q_s}{m_N \cosh\left(y_{\text{beam}} - y_{S\to S'}\right)}. \tag{6.6}$$

However, how does one move from kinematic rapidity $y$ to spacetime rapidity $\eta$? After all, our coordinate system uses $\eta$ - which includes $t$ and $z$ coordinates - and not $y$. It follows naturally that we would want to convert between rapidities for use in our simulation framework. The conversion is rather simple, given our work on ultra-relativistic systems. Indeed, recalling Eq. (3.52), we have

$$\eta = \frac{1}{2}\ln\left(\frac{t+z}{t-z}\right),$$

which is Eq. (6.1) with substitutions $E \to t$ and $p_z \to z$. Now, expanding $E$ and $p_z$ in Eq. (6.1) gives

$$y = \frac{1}{2}\ln\left(\frac{\gamma m + \gamma m v_z}{\gamma m - \gamma m v_z}\right) = \frac{1}{2}\ln\left(\frac{1+v_z}{1-v_z}\right).$$

Setting $v_z \sim z/t$, we obtain

$$y \sim \frac{1}{2}\ln\left(\frac{t+z}{t-z}\right) = \eta.$$

Therefore, in the highly-relativistic limit, $\eta$ can be substituted with $y$ interchangeably. This means that Eq. (6.6) can be modified to incorporate some $\eta$ dependence. Indeed, considering we (the observers) are in the lab frame, any boost away from us will be relative to the lab frame, and therefore, will be well-defined in terms of spacetime rapidity $\eta$ (since the lab frame is also at the origin). We will have

$$x = \frac{Q_s}{m_N \cosh\left(y_{\text{beam}} - \eta\right)}, \tag{6.7}$$

which gives us a hint that now, given the known interdependence between the momentum fraction $x$ and the saturation scale $Q_s$, and the spacetime rapidity $\eta$, $Q_s$, in our simulation, is now a function of both the transverse position $\vec{x}$ on the lattice *and* the rapidity $\eta$. However, given this intricate interdependence, we can not, in the absence of a framework to evolve the saturation scale to different values of spacetime rapidity, estimate the value of $x$ probed at different rapidities. Before going any further, then, we must introduce the JIMWLK [121] renormalization equation and how it fits into IP-Glasma.

### 6.1.2 *CGC in 3+1D*

At the onset of this chapter, we asked how the separation of scales, the underlying assumption of the CGC formalism, would hold up to our inclusion of a longitudinal direction. As a reminder, the argument was that hard partons remain undeflected in a collision event and keep moving on the light cone. Their extremely high velocity ($\sim c$) would allow us to consider them as frozen-out sources for mid-rapidity gluons, which dominate the Parton Distribution Function at small momentum fraction $x$ (as seen in Fig. 15). Incorporating longitudinal structure in the initial state complicates things from the start, as we are no longer concerned exclusively with mid-rapidity evolution, which is inherently composed of matter at small momentum fraction $x$. Indeed, we will now have to consider matter which is moving longitudinally at velocities which are much greater than those found at mid-rapidity, making its velocity relative to the high-$x$ partons smaller and, therefore, stretching the assumption that these same high-$x$ partons

can be considered frozen-out temporally. To have a sense of how quickly longitudinal velocities scale with rapidity, consider the following: when $z = t$, a parton is moving at the speed of light and $\eta \to \infty$. Consider now a finite value of $\eta$. Solving for $z/t$, we have

$$\frac{z}{t} = \frac{e^{2\eta} - 1}{e^{2\eta} + 1} = 1 - 2e^{-2\eta} + \mathcal{O}\left(e^{-4\eta}\right) \tag{6.8}$$

The main takeaway of Eq. (6.8) should be how quickly this function converges to 1. Indeed, $\eta = 4$ already yields a longitudinal velocity of $0.9993c$. How, then, can we build an argument for the validity of the CGC in a fully 3+1D simulation? The JIMWLK [121] renormalization equations provide a framework through which we progressively integrate out modes at higher and higher rapidities. What this means is that the separation of scales itself becomes rapidity dependent, leading to different rapidity slices having different gluon densities (and, therefore, color charge fluctuations) depending on their velocity with respect to the hard-$x$ partons. The Lagrangian itself remains essentially unchanged, with the only (crucial) difference being that the color charge density $\rho$ now becomes rapidity dependent, fluctuating as we move along the longitudinal direction, i.e. $\rho(\vec{x}_\perp) \to \rho(\vec{x}_\perp, \eta)$. This also aligns with what we found in the previous section regarding the saturation scale.

Before we show how this procedure works, let us quickly outline the logic behind this renormalization procedure (a more detailed description can be found in Ref. [121]). The effective Lagrangian utilized in the CGC framework as given in Eq. (3.14) is concerned with momenta at scale $p^+ \lll P^+$, where $P^+$ is the scale of the momentum of the nucleons travelling in the beam direction. We consider some new scale, $q^+$, such that $p^+ \leq q^+ \leq P^+$. Instead of integrating out all modes $\leq P^+$, we integrate out all modes $\leq q^+$, a scale closer to the scale of the fields we are trying to describe. This Lagrangian is self-similar to the 'regular' CGC Lagrangian, simply having more modes integrated out (and, therefore, fewer quantum fluctuations from which to generate color charge). In essence, the JIMWLK equations dictate how the squared color charge per unit area

$\mu^2$ (not the scale of fluctuations $\mu_A$) evolves with rapidity $\eta$ and the transverse resolution scale $Q^2$. The additional charge per unit area at each longitudinal iteration is

$$\sim \mu^2(\eta, Q^2)d\eta = \mu^2(\eta, Q^2)\ln\left(\frac{1}{x}\right)dx. \tag{6.9}$$

By implementing an iterative procedure (which we will describe shortly), we can treat the additional amounts of fluctuations perturbatively, allowing us to solve for the color charge densities at different rapidities. Understanding that we go from the most negligible squared color charge per unit area to the largest tells us that the initial longitudinal evolution of both nuclei must be done separately. Indeed, since both nuclei propagate in opposite directions, their respective cutoff scales progress opposite one another as well. Therefore, the JIMWLK evolution is done to both nuclei individually and separately, directly after IP-SAT has been run on each nucleus. Only after the JIMWLK evolution is complete can we set the initial conditions on the lattice and begin the 3+1D evolution. Explicitly, let us consider a nucleus propagating from $-z$ to $+z$. We will start by sampling the colour charge density at our maximal value of $\eta$, close to the rapidity of the hard parton sources. We would then iteratively bring in more color charge fluctuations by progressively integrating out higher modes until we reach the minimum $\eta$ bound of our evolution (where the smallest-$x$ and largest color fluctuation scales are found).

We will follow the procedure outlined in Ref. [17] to describe how the JIMWLK evolution is implemented. After sampling the color charge distributions and generating the initial gauge fields following the boost-invariant procedure, the JIMWLK evolution targets the Wilson lines $V$ via the Langevin step [122],

$$\begin{aligned} V(\vec{x}_\perp, Y+dY) = \exp\left(-i\frac{\sqrt{dY}}{\pi}\int_{\vec{u}} \vec{K}_{\vec{x}-\vec{u}}\cdot\left(V_{\vec{u}}\zeta_{\vec{u}}V^\dagger_{\vec{u}}\right)\right) \\ V(\vec{x}_\perp, Y)\exp\left(i\frac{\sqrt{dY}}{\pi}\int_{\vec{v}} \vec{K}_{\vec{x}-\vec{v}}\cdot\zeta_{\vec{v}}\right), \end{aligned} \tag{6.10}$$

where $\zeta_z = \left\{\zeta_1^a(\vec{z}, Y)t^a, \zeta_2^a(\vec{z}, Y)t^a\right\}$ is a random variable and $V_{\vec{z}} = V(\vec{z}, Y)$. We have opted to keep $Y$, the kinematic rapidity, instead of $\eta$ to align ourselves with the liter-

ature. However, as established previously, these two can be used interchangeably. The correlation between the random $\zeta$ variables is given by

$$\left\langle \zeta_i^a(\vec{x}_\perp, Y_1)\zeta_j^b(\vec{x}_\perp, Y_2)\right\rangle = \delta^{ab}\delta^{ij}\delta^{Y_1Y_2}\int \frac{d^2\vec{k}}{(2\pi)^2}\exp\left(i\vec{k}\cdot(\vec{x}-\vec{y})\right)\alpha_s(\vec{k}). \tag{6.11}$$

These random variables are noise terms which represent the stochastic nature of gluon emission, which serve as part of the quantum mechanical corrections to the color charge that sources the classical fields. $\vec{K}_{\vec{x}-\vec{z}}$, which is the modified kernel [125], has the form

$$\vec{K}_{\vec{x}-\vec{z}} = m|\vec{x}-\vec{z}|K_1(m|\vec{x}-\vec{z}|)\frac{(\vec{x}-\vec{z})}{|\vec{x}-\vec{z}|^2}, \tag{6.12}$$

with $K_1(x)$ being the Bessel function of the second kind and $m = 0.4\,\text{GeV}$ is an infrared regulator [125].

The exponent in Eq. (6.10) is solved by Fourier transforming the kernel (Eq. (6.12)) and the noise term (Eq. (6.11)). The kernel becomes

$$\vec{K}_{\vec{k}} = \frac{2\pi i\vec{k}}{\vec{k}^2+m^2}. \tag{6.13}$$

Given the form of the noise term, the move to Fourier space amounts to a convolution [126]. In Eq. (6.11), we find a momentum-dependent running coupling $\alpha_s(\vec{k})$, which takes the form

$$\alpha_s(\vec{k}) = \frac{4\pi}{(11-2N_f/3)\ln\left[\left(\frac{\mu_0^2}{\Lambda_{\text{QCD}}^2}\right)^{1/c}+\left(\frac{\vec{k}^2}{\Lambda_{\text{QCD}}^2}\right)^{1/c}\right]^c}, \tag{6.14}$$

where $N_f = 3$, $\Lambda_{\text{QCD}} = 200\,\text{MeV}$, $c = 0.2$ and $\mu_0 = 400\,\text{MeV}$ [122]. This differs from Eq. (3.32) in the inclusion of a second term relating the momentum $\vec{k}$ of the mode in Fourier space to the QCD scale $\Lambda$.

Incorporating a running coupling constant $\alpha_s(\vec{k})$ has a few effects. First, it filters out higher energy modes fairly quickly, which links the scale of the running coupling to that of radiated gluons. Second, the inclusion of a running coupling constant dampens the effect of the JIMWLK evolution, leading to more correlation between neighboring $\eta$ slices when compared to a constant $\alpha_s$ implementation.

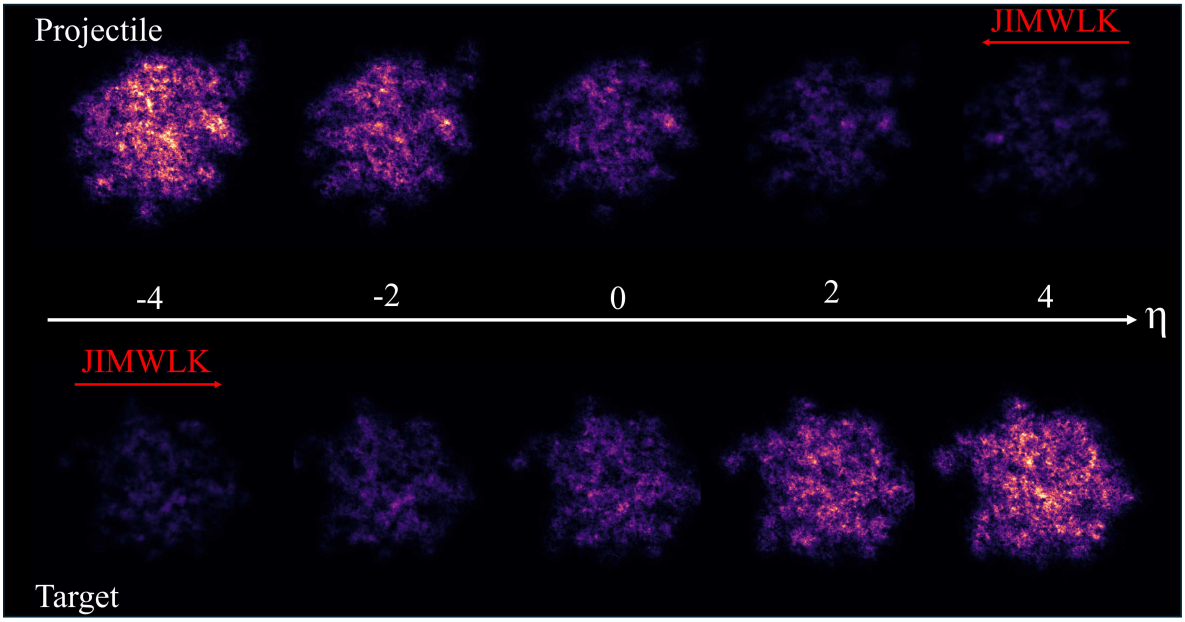


Figure 49: Two nuclei evolving longitudinally (in rapidity space) using the JIMWLK equations. The two nuclei constitute the central event we have been studying (see Figs. 20, 27 and 28). Plotted is $\frac{\mathrm{Tr}(1-V)}{N_c}$, a measure of gluon density. As explained, the JIMWLK evolution of the projectile nucleus proceeds in the opposite direction of that of the target nucleus.

Figure 49 shows how the gluon distribution of two nuclei involved in the central event we have been examining (see Figs. 20, 27 and 28) evolve in rapidity space thanks to the JIMWLK equations. Two things should be remarked regarding Fig. 49: first, the JIMWLK evolution goes from high-$x$ to small-$x$, as established previously; secondly, the general structure of the nucleus is preserved across the rapidity spectrum, with fluctuations occurring at smaller scales.

Now that the color charge densities have been established at all rapidities let us quickly circle back to the the initialization procedure for our color gauge fields $A^\mu$ in this 3+1D formulation.

### 6.1.3 $A^\mu$ *in 3+1D*

The initial conditions introduced in Section 3.3.2 were specific to the boost-invariant assumption. As a reminder, the transverse gauge fields $A_i$ of both nuclei were pure gauge, and the resulting transverse gauge field post-collision was simply the sum of the two pre-collision pure color gauge fields. In the transverse direction, we had made the color gauge field vanish (i.e. $A_\eta = -\tau^2 A^\eta = 0$). The boost-invariant assumption motivated this vanishing longitudinal component, since all longitudinal derivatives vanish. Now that we are looking to build a fully 3+1D formulation of IP-Glasma, however, longitudinal derivatives must be treated carefully. From Section 3.4, we know that the energy density in a given region of space is proportional to the chromo-electric and -magnetic fields in a given region, which themselves are dependent upon the field strength tensor $F_{\mu\nu}$ in that same region. Let us assume the initial conditions described in Section 3.3.2 are appropriate in 3+1D. Calculating the field strength tensor for a single nucleus with this initial condition, we would have

$$\begin{aligned}
F_{\mu\nu} &= \partial_\mu A_\nu - \partial_\nu A_\mu + ig\left[A_\mu, A_\nu\right], \\
F_{ij} &= -\frac{i}{g}\left(\partial_i V\right)\left(\partial_j V^\dagger\right) + \frac{i}{g}\left(\partial_j V\right)\left(\partial_i V^\dagger\right) - \frac{i}{g} V\left(\partial_i V^\dagger\right) V\left(\partial_j V^\dagger\right) + \frac{i}{g} V \partial_j V^\dagger V \partial_i V^\dagger, \\
F_{i\eta} &= \partial_i A_\eta - \partial_\eta A_i + ig\left[A_i, A_\eta\right],
\end{aligned} \tag{6.15}$$

where in the $F_{ij}$ line we substituted $A_i = -\frac{i}{g} V \partial_i V^\dagger$, as established in Eq. (3.49). With a bit of algebraic manipulation, and using the fact that $\partial_\mu V V^\dagger = -V \partial_\mu V^\dagger$, we arrive at a vanishing transverse field strength tensor, i.e. $F_{ij} = 0$, where the transverse fields are pure gauge. In the longitudinal direction, however, we are left with

$$F_{i\eta} = -\partial_\eta A_i \neq 0. \tag{6.16}$$

While the $A_\eta$ term and the commutator go to 0, the longitudinal derivative does not vanish here, and we have a non-zero longitudinal component to the field strength tensor. Given the dependence of the stress-energy tensor $T^{\mu\nu}$ on $F_{\mu\nu}$, a non-vanishing component

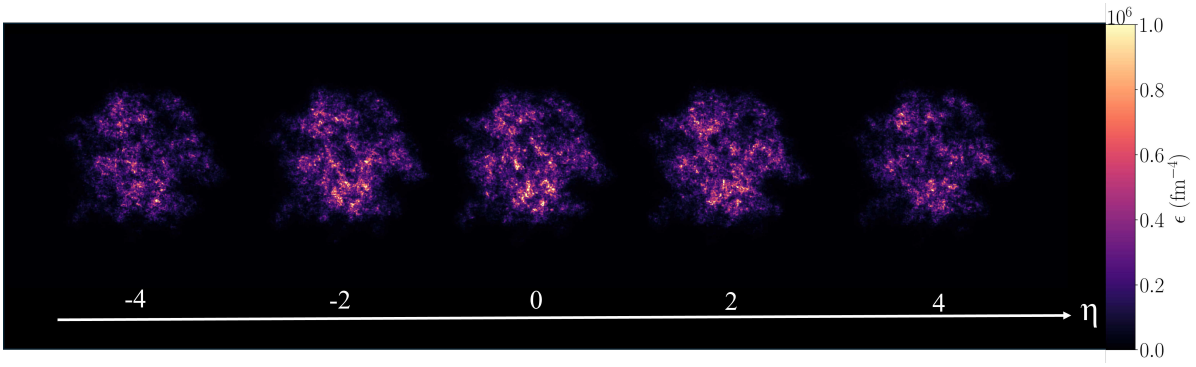


Figure 50: Energy density (in fm$^{-4}$) deposited in the transverse plane at initial time $\tau_0 = 0.01$ fm at different values of $\eta$ for our central event. While fluctuations can be found from slice to slice, the general geometric features of the overlap region persist across the rapidity spectrum.

would mean energy deposition from our one nucleus initial condition - even without a collision - which would obviously be an issue. Indeed, if a single nucleus is initialized in 3+1D with pure gauge transverse color gauge fields and vanishing longitudinal color gauge fields, that nucleus' gauge fields alone could lead to energy deposition, meaning that energy deposits would occur everywhere around the nucleus, and not only where it overlaps with another nucleus.

Let us clarify this last statement a bit: while the pre-collision gauge fields of the two nuclei in the boost-invariant formulation *are* pure gauge, their superposition post-collision *is not*, which leads to energy deposition where they overlap (i.e. where the resulting color gauge fields are not pure gauge) and no energy deposition where they don't. However, allowing the field strength tensor to have non-vanishing components due to a single nucleus would lead to energy deposits everywhere the color charge is non-zero, i.e. surrounding both nuclei. Thankfully, a simple answer to this conundrum, which we have already utilized in the boost-invariant formulation, exists: set the initial longitudinal gauge fields of both nuclei to be pure gauge, i.e.,

$$A_\eta = -\frac{i}{g} V \partial_\eta V^\dagger. \tag{6.17}$$

This solves the issue of non-vanishing field strength for a single nucleus while also reducing the 2D limit in the case of vanishing $\eta$ derivatives. The ansatz for initializing

the longitudinal color gauge fields for both nuclei combined follows that of the transverse fields, i.e.,

$$A_\eta = A_\eta^A + A_\eta^B, \tag{6.18}$$

with the initial condition for the longitudinal electric field remaining the same as Eq. (3.70).

Figure 50 shows the initial energy deposits for our central event at different values of spacetime rapidity $\eta$. Once again, much like in Fig. 49, we find that the general geometric features of our overlap region persist from slice to slice, with fluctuations taking place locally. However, one of the caveats of the JIMWLK evolution has now become clear: the total amount of energy deposited from rapidity slice to rapidity slice does not vary much. While this can make sense for slices close to mid-rapidity ($|\eta| \leq 2$), we should expect less interaction energy moving at higher rapidities. Indeed, as established in Eq. (6.8), at $\eta = 4$, matter travels at $> 99\%$ the speed of light in a given direction. We should, therefore, not expect interactions between our colliding nuclei to persist with such intensity along the beam direction. However, looking at Fig. 50, we see that while more energetic pockets may be absent at larger rapidities, the energy scale remains consistent across the rapidity spectrum, meaning that the JIMWLK evolution equations do not lead to significant differences in interaction energy deposition across the rapidity spectrum. This issue, as we will see in the next chapter, is critical, as we will want to reproduce charged particle distributions longitudinally. Charged particle yields generally peak between $\eta = -1$ and $\eta = 1$, with a considerable drop-off occurring for $|\eta| > 2$. We must normalize the initial state energy density at high rapidities to reproduce these yields. This normalization occurs at the interface between our initial state model IP-Glasma and our hydrodynamic model MUSIC. Let us describe it quickly, before moving on to our description of observables enabled by our 3+1D modeling.

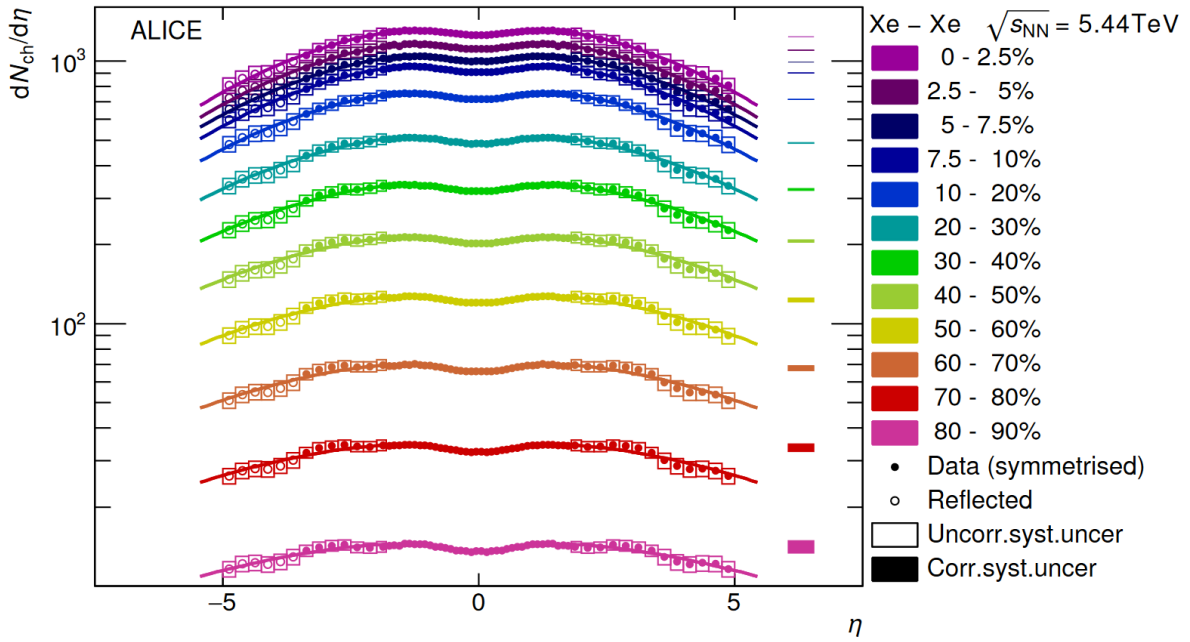


Figure 51: Experimental charged hadron multiplicity as a function of rapidity $\eta$ for 12 centrality classes for Xe+Xe collisions at 5.44 TeV. Data gathered by ALICE and figure taken from Ref. [127]. As we move to larger absolute rapidities, the yields go down. Solid curves represent Gaussian fits to the experimental data points.

## 6.2 HYDRODYNAMIC NORMALIZATION

The detailed description of the hydrodynamic phase provided in Chapter 4 is not affected by our move to 3+1D. None of the theoretical underpinnings of our prescription of viscous relativistic hydrodynamics relied on boost-invariance, contrarily to our initial description of the initial state. Therefore, adding a longitudinal component to the evolution is as simple as providing $T^{\mu\nu}(\eta)$ for all $\eta$ relevant to our evolution and going through the same hydrodynamic evolution as the mid-rapidity slice does in a boost-invariant simulation. However, as established in the previous subsection, while the JIMWLK evolution does provide a physical framework through which the longitudinal evolution of the initial state can proceed, it does not provide meaningful differences in total energy deposition between rapidity slices at or close to mid-rapidity and those at large rapidities.

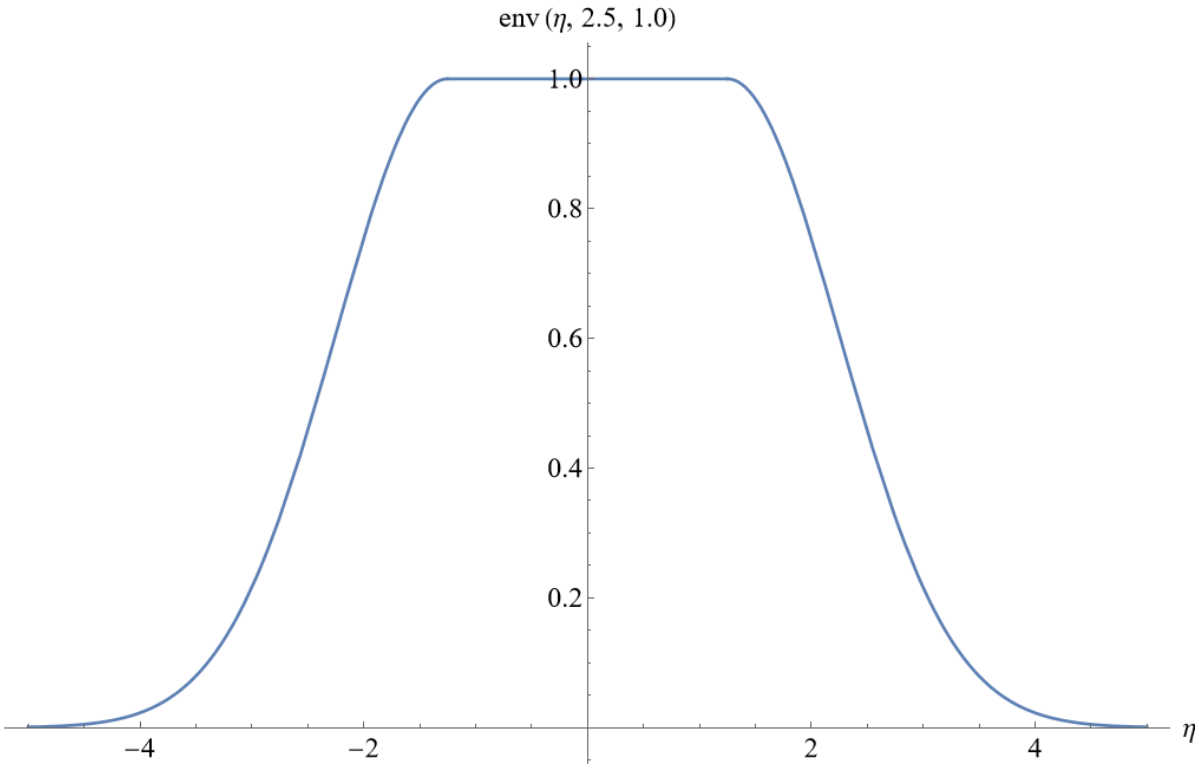


Figure 52: Rapidity-dependent envelope used for energy and shear-stress tensor normalization between 3+1D IP-Glasma and MUSIC. The envelope, defined in Eq. (6.19), plateaus at mid-rapidity and falls off steeply at higher rapidities, ensuring charged particle yields mirror experimental results.

Figure 51 shows the charged particle multiplicity as a function of $\eta$ for Xe+Xe collisions at the LHC [127]. We see that while a meaningful amount of particles is produced at high rapidities, for a given centrality class, the multiplicity can drop by more than 20% beyond $\eta = 3$ compared to the mid-rapidity yields. Because charged particle multiplicity is a proxy for the total energy contained in a given rapidity slice, Fig. 51 tells us that the energy should decrease significantly when moving away from mid-rapidity, something that is not observed in Fig. 50. Therefore, to correctly reproduce the longitudinal structure of the charged particle yields, we must apply some form of normalization to the energy density profiles generated by our initial state. Without such a normalization, the yields predicted by our model would be far too high at large rapidities, rendering any further comparison to experimental data difficult.

As mentioned previously, the normalization procedure occurs at the interface between 3+1D IP-Glasma and MUSIC. When reading in the rapidity slices generated using IP-Glasma, MUSIC builds the initial shear-stress tensor $\pi^{\mu\nu}$ and multiplies all of its components and the energy density $\epsilon$ by a rapidity-dependent envelope function. This envelope function has the form

$$\mathrm{env}(\eta, \eta_0, \sigma_\eta) = \exp\left(-\frac{1}{2}\left[\frac{|\eta| - \frac{\eta_0}{2}}{\sigma_\eta}\right]^2 \Theta\left(\frac{|\eta| - \frac{\eta_0}{2}}{\sigma_\eta}\right)\right), \tag{6.19}$$

where $\eta$ is the rapidity, $\eta_0$ controls the width of the normalization plateau at mid-rapidity, $\sigma_\eta$ controls the steepness of the fall-off in rapidity beyond this plateau, and $\Theta$ is the heavyside function. The parameters used in the runs we will present in the next chapter are $\eta_0 = 2.5$ and $\sigma_\eta = 1$, which were selected to mirror the parameters used in a previous 3+1D analysis at similar energies conducted with our model [17]. Figure 52 shows what Eq. (6.19) looks like with our chosen parameters. We find a plateau for $|\eta| \leq 1.5$, which falls steeply once we move away from mid-rapidity, hitting close to 0 further out. While the fall-off may seem steep, especially when comparing the shape of the envelope to the distributions shown in Fig. 51, it is appropriate given the rapidity range we will be matching to. Figure 53 shows our central event before and after the application of our envelope function at the interface between IP-Glasma and MUSIC. Without the envelope, while differences can be found in the overall scale of the energy deposit, those differences are fairly small, meaning that differences in total energy (and, therefore, multiplicity) would themselves also be small, leading to a mismatch between our rapidity-dependent yield curves and those of experiment. The scaling provided by the envelope function ensures that our simulation can reproduce the relationship observed experimentally.

We are now ready to describe the longitudinal observables, which will serve as our basis for comparison with experiments.

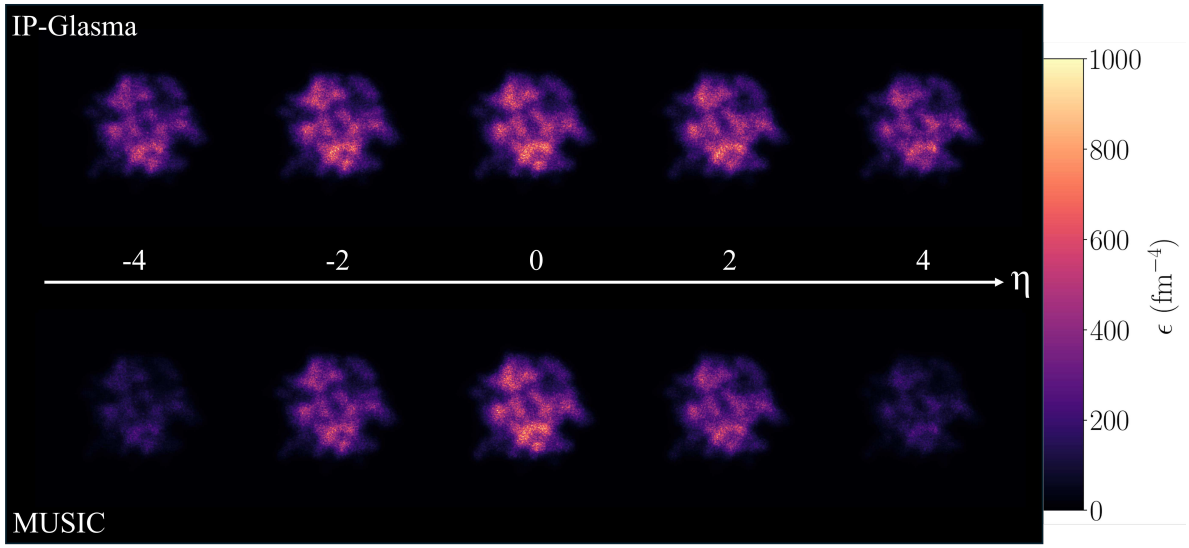


Figure 53: Energy density distribution at switching time ($\tau_{\text{switch}} = 0.602$ fm) in (**top**) IP-Glasma and (**bottom**) MUSIC after applying the envelope function Eq. (6.19). The energy density distribution at mid-rapidity is unaffected, while at higher rapidities, it is brought down considerably.

## 6.3 LONGITUDINAL OBSERVABLES

### 6.3.1 *Rapidity-dependent Multiplicity*

We start by quickly and formally defining the rapidity-dependent multiplicity. Simply put, the charged hadron multiplicity described in Section 4.3.1 was in and of itself rapidity-dependent; our boost-invariant description of observables set the rapidity range for the multiplicity to $|\eta| \leq 0.5$. With longitudinal structure included, particles will be sampled in meaningful quantities across the rapidity spectrum. Therefore, the rapidity-dependent multiplicity density is concerned with counting particles generated in a given rapidity range, i.e.,

$$\frac{dN_{\text{ch}}}{d\eta}|_{\eta_0 \leq \eta \leq \eta_1} = \frac{\int_{\eta_0}^{\eta_1} d\eta N_{\text{ch}}(\eta)}{\eta_1 - \eta_0}, \tag{6.20}$$

where $\eta_0$ and $\eta_1$ are, respectively, the lower and upper bounds of the rapidity range being considered, and $N_{\text{ch}}(\eta)$ is the number of charged particles detected having rapidity $\eta$.

This is of course almost the same definition as Eq. (4.23), differing only in the fact that the integration bounds are asymmetrical. By measuring multiplicities across the rapidity spectrum, multiplicity densities can be turned into a function of $\eta$, generally with fixed $\eta$ gaps $\Delta\eta$. We would therefore have

$$\frac{dN_{\text{ch}}}{d\eta}(\eta) = \frac{dN_{\text{ch}}}{d\eta}|_{\eta-\Delta\eta/2\leq\eta\leq\eta+\Delta\eta/2}. \tag{6.21}$$

The same calibration procedure outlined in Section 4.3.1 still applies for 3+1D simulations. We used the charged particle multiplicity measured at mid-rapidity, i.e. $|\eta| \leq 1$, as our calibration tool. It is interesting to note here that the boost-invariant assumption, which may seem farfetched at first, actually holds up fairly well up to $|\eta| = 2$. Indeed, looking at Fig. 51, we find that the charged-particle yields stay relatively flat up to that rapidity, which includes matter moving at up to 96% of the speed of light. It is only once we move past this relatively large $\eta$ gap that a sustained drop is observed. The assumption of boost-invariance is therefore proven here to be rather fair.

### 6.3.2 *Rapidity-dependent Anisotropic Flow*

Much like the multiplicity, we will want to determine how the anisotropic flow evolves with rapidity. Naively, given the considerable dependence on the geometrical features of the initial state, one may assume that the elliptic flow should remain constant as we move from mid-rapidity outwards to larger rapidities. However, that is not the case, as we will show in the next chapter. For now, however, let us formally define the $\eta$-differential 2-particle cumulant of the anisotropic flow, i.e.,

$$v_n\{2\}(\eta) = \frac{\text{Re}(\langle Q_n^{\text{PI}}(\eta) \cdot (Q_n^{\text{ref}}(\eta_{\text{ref}}))^*\rangle)}{\langle N_{\text{ch}}^{\text{PI}}(\eta) N_{\text{ch}}^{\text{ref}}\rangle v_n^{\text{ref}}\{2\}}. \tag{6.22}$$

One may notice similarities between the $p_T$-differential (Eq. (4.42)) and $\eta$-differential formulas because they are defined in the same way, with only the differential element changing. We, therefore, set a reference flow (mimicking that set by experimentalists) and calculate the rapidity-dependent flow at different values of $\eta$ from there (those

should be understood as $\eta$ ranges rather than specific values). The reference flow is generally taken from a wide rapidity range, while the Particle of Interest (PI) flow is taken from a much narrower range. The rapidity gap between the reference flow and the flow of interest is important, as it ensures that we remove most non-flow effects from the calculation. But if flow fluctuations occur in the longitudinal direction, we should adequately investigate their scale and attempt to understand what causes longitudinal decorrelations. That is where the decorrelation ratio $r_{n|n}$ comes in.

### 6.3.3 *Decorrelation Ratio*

To quantify the amount of decorrelation exhibited by a given anisotropic flow coefficient, we compare the flow in two symmetrically opposed rapidity regions (relative to $\eta = 0$) - one in forward rapidity and the other in backward rapidity. The CMS collaboration was the first to introduce a definitive and quantitative measure of decorrelation called the factorization ratio, which is defined as [128]

$$r_{n|n}(\eta, \eta_{\text{ref}}) = \frac{\left\langle v_n(-\eta) v_n^*(\eta_{\text{ref}}) \cos\left(n\left(\Psi_n(-\eta) - \Psi_n(\eta_{\text{ref}})\right)\right)\right\rangle}{\left\langle v_n(\eta) v_n^*(\eta_{\text{ref}}) \cos\left(n\left(\Psi_n(\eta) - \Psi_n(\eta_{\text{ref}})\right)\right)\right\rangle}, \tag{6.23}$$

where $v_n$ are the $\eta$-differential flow coefficients measured at different rapidity values, $\eta_{\text{ref}}$ is the reference $\eta$ range, and $\Psi_n$ are the $n^{\text{th}}$ order event plane angles at $\eta$. This decorrelation (or factorization ratio) can be understood in two parts. First, the flow magnitude part, guided by the inclusion of rapidity-dependent anisotropic flow coefficients $v_n(\eta)$, and then, the decorrelation arising from event plane angle fluctuations, given by the cos of the difference in event plane angles at different rapidities. Differences in flow magnitude will be made clear in plots of the $\eta$-dependent anisotropic flow. Fluctuations in event plane angles, on the other hand, are more subtle. As is evident in Fig. 53, the different energy density slices show only slight rotations about the beam axis, which is what the event plane angle measures. While the event plane angle is not a quantity which can be measured experimentally, it can be inferred on an event-by-event and rapidity-by-rapidity basis by comparing anisotropic flow coefficients at different rapidi-

ties: fluctuations in $v_n$ lead to non-zero differences in the inferred event plane angles. This observable therefore measures two different types of flow fluctuations simultaneously, creating a picture of how particle flow progresses in rapidity space and how well initial state structure is preserved at different rapidities.

Now that the relevant longitudinal observables have been described, we are ready to show results from simulations of Xe+Xe collisions at 5.44 TeV using 5 considerably different nuclear parametrizations in an attempt to use experimental data to properly constrain $^{129}$Xe's shape for future analyses.

# 7

# CONSTRAINING PARAMETRIZATIONS IN 3D

We now turn to the final results section of this thesis, which summarizes the theory and work presented so far. In 2017, the LHC announced that it had ran $^{129}$Xe nuclei through its beam pipe at a center-of-mass energy of 5.44 TeV. Compared to the $^{208}$Pb runs that had been conducted there previously, these runs would feature a much smaller (almost half the mass number of lead) and, as far as low-energy experiments and models are concerned [109], deformed nucleus. This short collision program has yielded results which have been contrasted with those obtained in the much longer $^{208}$Pb program, attempting to characterize how much system size and fluctuations affect end-state observables at a given energy. However, modelling efforts have been pulling in many different directions without proper constraints on $^{129}$Xe's geometric properties and their projections in Woods-Saxon space. Indeed, while there is some understanding as to the general features of $^{129}$Xe, proposed quadrupole deformation parameters have ranged from $\tilde{\beta}_2^0 = 0.139$ [109] up to $\tilde{\beta}_2^0 = 0.207$ [129], with some parametrizations including triaxial deformation and hexadecapole deformation as well. It is therefore obvious that there is considerable uncertainty regarding $^{129}$Xe's appropriate Woods-Saxon parametrization; comparing this gap to that of the $^{238}$U parametrizations utilized in the analysis provided in Chapter 5, we find that the differences exhibited by currently accepted $^{129}$Xe parametrizations are considerably larger. Therefore, the current large-scale analysis will serve as the first of its kind for $^{129}$Xe, allowing future research to integrate our findings and further our understanding of the structure of mid-sized nuclei. As mentioned in the previous chapter, it will determine if longitudinal observables

obtained through more involved computations exhibit additional sensitivity to the initial state fluctuations from nuclear deformity.

We will present results produced using five different $^{129}$Xe parametrizations, 4 of which are deformed and the last being undeformed and serving as a baseline for comparison's sake. Using charged particle multiplicity data from ALICE [127], we calibrated the saturation scale to color charge fluctuation scale proportionality constant $C$. It is important to note here that the value we found for this constant is considerably different from that which we found for our $^{238}$U and $^{197}$Au analysis, as those runs were done in 2+1D; the additional non-trivial longitudinal component in the current analysis leads to extra energy being deposited longitudinally, requiring that the proportionality constant lead to *less* color charge fluctuations than in 2+1D. Once again, this was our only calibration tool. Once the charged particle yields were reproduced accurately, the rest of the observables were calculated and compared to experimental results, without any additional intervention or parameter modulation.

This chapter's structure will resemble that of Chapter 5. We will introduce the different $^{129}$Xe parametrizations used in our analysis. We will then show basic observables, from the calibration-specific multiplicity to average transverse momentum and identified particle observables. Following these introductory observables, we will analyze anisotropic flow, both integrated and differential in $\eta$ and $p_T$, as well as transverse-momentum-flow observables, standardized skewness (which we will define in due time) and the factorization ratios $r_{n|n}$. Finally, using our model's calculations, we will use previous research [118, 120] to formally constrain $^{129}$Xe's quadrupole deformation parameters.

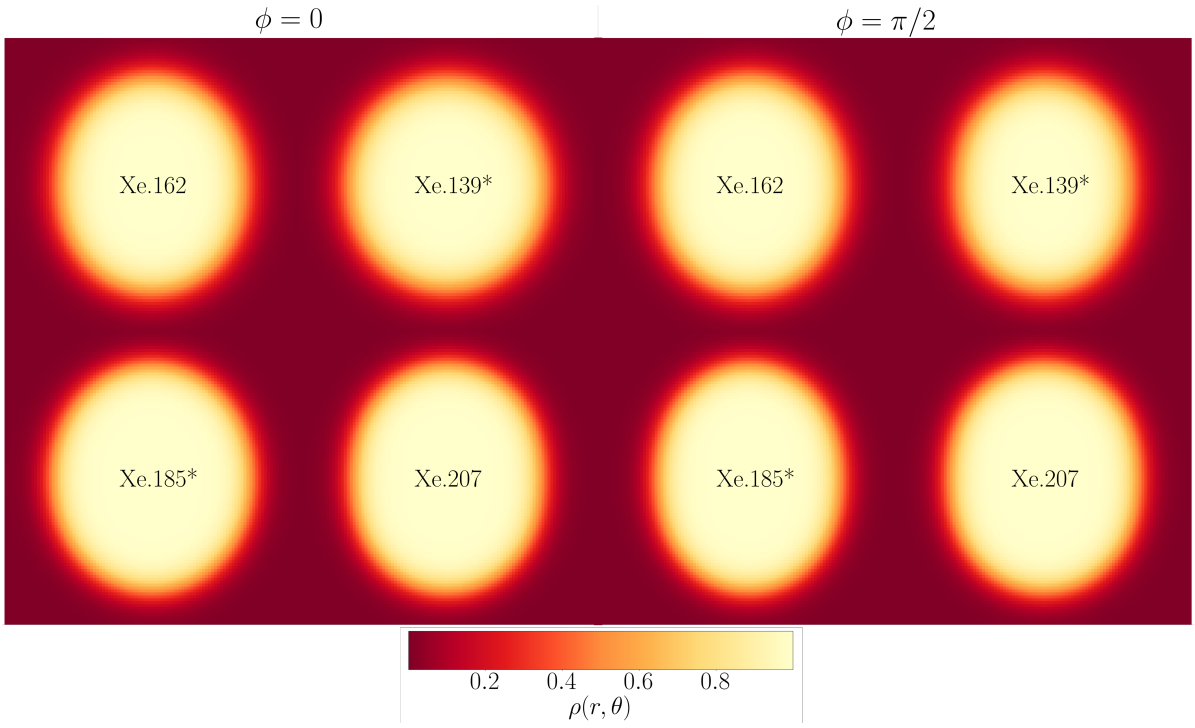


Figure 54: Two-dimensional Woods-Saxon projections taken at (**left**) $\phi = 0$ and (**right**) $\phi = \pi/2$ of the 4 deformed $^{129}$Xe parametrizations subject to our analysis. The details of these parametrizations can be found in Table 3. We have excluded the undeformed parametrization. '*' mark parametrizations which include triaxial deformation.

## 7.1 BASICS AND CALIBRATION

### 7.1.1 *Initial Parametrizations*

To equip ourselves with a more intuitive idea of the shapes of our chosen parametrizations, we constructed Fig. 54, similarly to Fig. 32. The four deformed parametrizations are shown side by side and viewed from different azimuthal angles $\phi$; parametrizations exhibiting triaxial deformation are marked with an asterisk. As a reminder, triaxial deformation breaks the azimuthal symmetry of the Woods-Saxon distribution. Therefore, the 2D projections of triaxial parametrizations change based on the azimuthal angle. It is also important to note that the scale for these plots was changed compared to that

of Fig. 32; while $^{129}$Xe nuclei may appear larger than $^{238}$U or $^{197}$Au based exclusively on these plots, they are not. One should only use these plots to compare the provided parametrizations between themselves. Finally, the names of the parametrizations themselves are related to their quadrupole deformity coefficient $\tilde{\beta}_2^0$, with the decimals being those of the parameters themselves.

The scale of the triaxial deformations of Xe.185* (here, the '*' mark means that this parametrization incorporates triaxial deformation) leads to slight but perceptible differences between its cross-sections. Xe.139*, on the other hand, exhibits much more perceptible changes between its two cross-sections. For both, going from $\phi = 0$ to $\phi/2$ leads to a more elliptical 2D projection. While this change may seem too subtle to influence large-scale results, triaxiality has been found to have a critical impact in reproducing transverse-momentum-flow correlations in $^{129}$Xe collisions [129]. There is, however, an intricate balance to strike between triaxiality and its effects on specific observables and compromising the general elliptic shape of $^{129}$Xe, which is critical to reproducing a more primary observable like the elliptic flow.

We also note that the sizes of the parametrizations are comparable across the board, with only Xe.139* being perceivably smaller. Finally, the considerable quadrupole deformation, while not as marked as that of $^{238}$U, could potentially generate the tell-tale tip-tip and body-body collisions required to generate an anti-correlation in the transverse-momentum-elliptic-flow correlator $\rho(v_2\{2\}, \langle p_T \rangle)$. The chosen parametrizations form a spectrum of prolate shapes, going from the least consistently prolate (Xe.139*) to the most pill-shaped parametrization (Xe.207). Therefore, our calculation of $\rho(v_2\{2\}, \langle p_T \rangle)$ should lead to contrasting values between our different parametrizations, meaning reproduction of the experimental values will be key.

### 7.1.2 *Calibrating to Charged Particle Yields*

Figure 55 shows the charged particle rapidity at mid-rapidity ($|\eta| < 0.5$) for Xe+Xe collisions at 5.44 TeV. All of our parametrizations, including the undeformed Xe.0,

| | $R_0$ (fm) | a (fm) | $\tilde{\beta}_2^0$ | $\tilde{\beta}_2^2$ |
|---|---|---|---|---|
| Xe.0 | 5.601 | 0.492 | 0 | 0 |
| Xe.162 | 5.42 | 0.57 | 0.162 | 0 |
| Xe.139* | 5.36 | 0.59 | 0.1394 | 0.081 |
| Xe.185* | 5.601 | 0.492 | 0.185 | 0.0469 |
| Xe.207 | 5.601 | 0.492 | 0.207 | 0 |

Table 3: Deformed Woods-Saxon parameters used for sampling nuclei according to Eq. 2.13, taken from Ref. [109] (Xe.162), Ref. [130] (Xe.139*), and Ref. [129] (Xe.185* and Xe.207). The undeformed parametrization's (Xe.0) radius and diffusiveness are based off of Xe.185* and Xe.207.

accurately reproduce the yields. A calibrated value of $C = 1.415$ was used, almost three times that which was used for our boost-invariant runs. Contrarily to the experimental yield parametrizations used to calibrate the $^{238}$U runs, the results published by ALICE and used here are actual experimental multiplicity measurements. Given that these runs are minimally biased, our multiplicity calibration procedure does not lead to incorrect centrality binning in peripheral collisions, such as were generated in the U curves of Fig. 33. However, we find that the curves' agreement with the experimental data and with one another systematically weakens as we move beyond the 35% centrality mark. This, as we have described in Chapter 5 and will come to redescribe here, is due to the nucleonic density of the different parametrizations. Indeed, in peripheral collisions, a nucleus with a smaller Woods-Saxon radius $R_0$ generally has a denser nucleonic configuration, leading the overlap region to contain more nucleons at a given peripheral impact parameter $b$. This slight change in nuclear density is sufficient to drive a noticeable splitting between the curves as we move towards more peripheral collisions; just like tip-tip collisions lead to greater multiplicities in ultra-central collisions, the increase in nuclear density creates differences between our different parametrizations in peripheral collisions. However, this splitting does not provide any discriminatory power, as the calibration could be

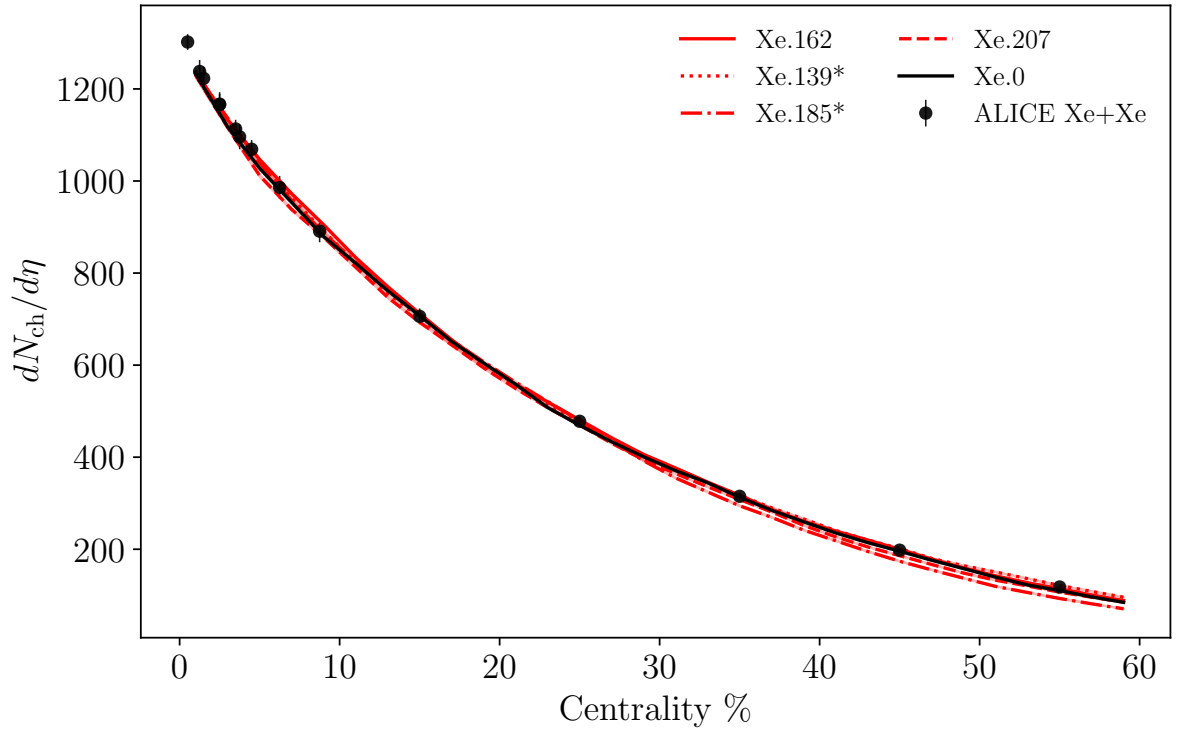


Figure 55: Charged hadron multiplicities in $|\eta| < 0.5$ as a function of centrality. Calculations from our model compared to results for 5.44 TeV Xe+Xe collisions at ALICE [127].

tweaked to perfectly reproduce the yields for a given parametrization. Just like with our results from Chapter 5, conducting multiple independent calibrations could affect other observables which would be difficult to quantify, and would hinder our ability to compare and contrast the results stemming from different Woods-Saxon configurations. All-in-all, the yields are faithfully reproduced by our model across the entirety of the centrality range, with the best agreement occurring in the central to semi-peripheral regions, regions which are most important to the analysis we are conducting.

Once calibrated to the mid-rapidity multiplicity, our results were compared to the rapidity-dependent charged particle multiplicity $dN_{\rm ch}/d\eta(\eta)$. Obviously, at and around mid-rapidity, our results should agree with the experimental yields. However, away from mid-rapidity, our results depend on the evolution of the gluon fields and the envelope function described in Chapter 6. Figure 56 shows our calculation against experimental results gathered at ALICE [127]. Because this is a rapidity-dependent observable, curves are separated based on their centrality: the top curve is the most central (0-

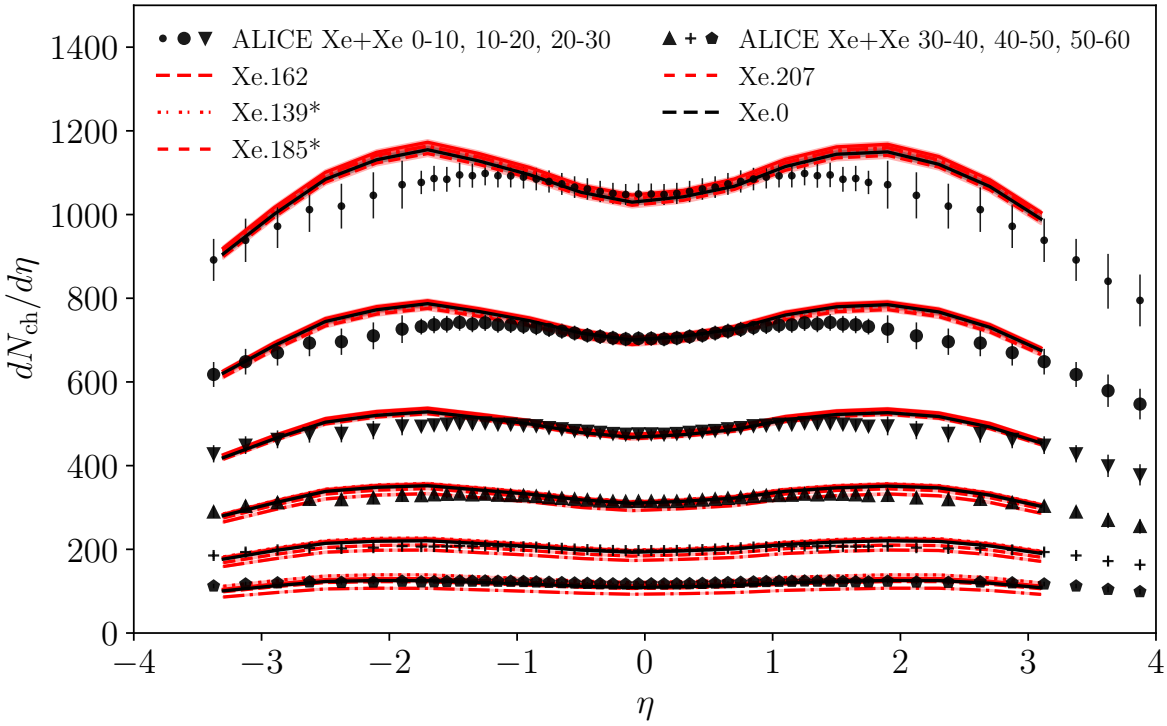


Figure 56: Rapidity-dependent charged hadron multiplicities for $|\eta| \leq 3.5$. Calculations from our model compared to results for 5.44 TeV Xe+Xe collisions at ALICE [127].

10%) collection of events, while the lowest curve is the most peripheral centrality bin relevant to our analysis (50-60%). As hypothesized above, the mid-rapidity calculations agree with the experimental results well, with the splitting between parametrizations appearing in the 30-40% slice. However, our calculation slightly overestimates the yields away from mid-rapidity, with the worst overestimate coming in the most central centrality bin. While our model produces results that fall close to the error bars for $1 \leq |\eta| \leq 2.5$, the calculations overestimate the yields in central and semi-peripheral collisions. While one could potentially look at the initial state to rectify the situation, the envelope function presented in Section 6.2 should be regarded as the main culprit for the mismatch between our calculation and experimental results. Indeed, given that the envelope function serves as a longitudinal normalization tool, the parameters used can be calibrated on a system-by-system basis; to save compute time, we had opted to use the envelope function proposed in Ref. [17], which yielded great results for Pb+Pb collisions at 2.76 TeV. However, the jump in beam energy and potentially even the

change in system size and geometry had unforeseen effects on the longitudinal structure of the energy density distributions. These effects led to the overestimation of the yields around the shoulders of the distribution. Implementing a shorter plateau size and a less steep fall-off could mend the gap between our calculation and the experimental data. Nevertheless, the discrepancy remains small and fairly contained to central collisions and a relatively narrow rapidity gap, making our distributions appropriate overall.

Now that the calibration of our model has been settled, let us move to observables which were calculated only once the calibration had been completed.

## 7.2 XE+XE OBSERVABLES

### 7.2.1 *Basic Observables*

We begin by looking at Fig. 57, which shows the charged particle multiplicity scaled by the average number of participants in a given centrality class, $\langle N_{\text{part}} \rangle / 2$. All parametrizations overlap across the entire centrality range without showing meaningful or sustained ordering between themselves. Our calculation reproduces the experimental data fairly well, even though all parametrizations underestimate the experimental values. It is, however, important to note that the number of participants can not be calculated experimentally. Therefore, experimental collaborations run Glauber simulations to produce an expected centrality-dependent $\langle N_{\text{part}} \rangle$ spectrum from which they calculate this observable. Therefore, whatever nuclear parametrization was used experimentally biased the results towards an assumption regarding the shape of $^{129}$Xe which is inherently uncertain. Furthermore, the general shape and slope of the experimental curve in the central to semi-peripheral regions is reproduced by all parametrizations, supporting the conclusion that particle generation processes are emulated correctly by our model.

Proceeding to identified particle observables, starting with the yields. Figure 58 shows our model's calculations compared to experimental results gathered at ALICE [131]. Our model's calculation is in excellent agreement with the experimental data across

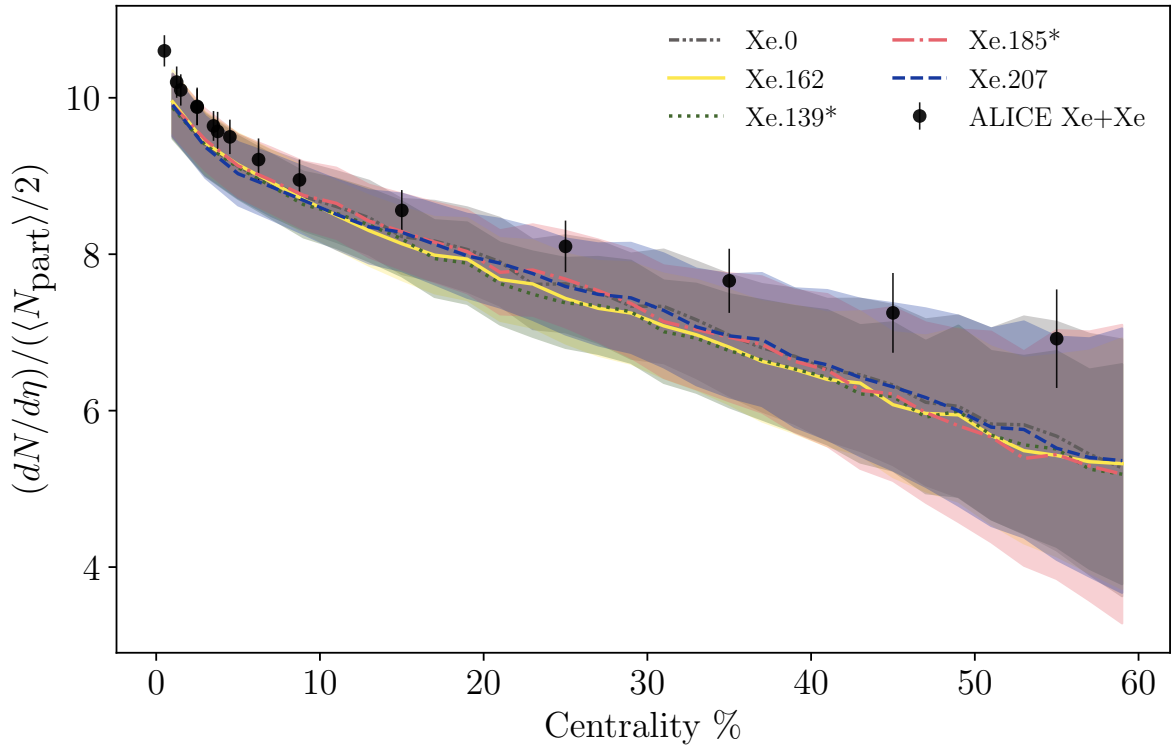


Figure 57: Charged particle multiplicity in $|\eta| < 0.5$ scaled by the average number of participant nucleon pairs in the centrality class $\langle N_{\rm part}\rangle/2$ as a function of $\langle N_{\rm part}\rangle$. Calculations from our model are compared to results for 5.44 TeV Xe+Xe collisions at ALICE [127].

the entirety of the centrality range, with - once again - a splitting occurring between all parametrizations in peripheral collisions. This splitting, much like that which we observed in Figs. 55 and 56, is mostly driven by nucleonic density and should not be treated as a discriminating element as not only is the nucleonic density expressly *not* what we seek to constrain, but also peripheral collisions find themselves at the very boundary of applicability of hydrodynamics and, therefore, carry with them some inherent uncertainties that are difficult to quantify. We reiterate that our model reproduces the identified particle yields across a considerable centrality range.

Moving on to Fig. 59, we find the mean transverse momentum of identified particles plotted against centrality. Once again, our model reproduces the experimental data fairly well across the entire centrality range. While our calculated proton $\langle p_T\rangle$ diverges

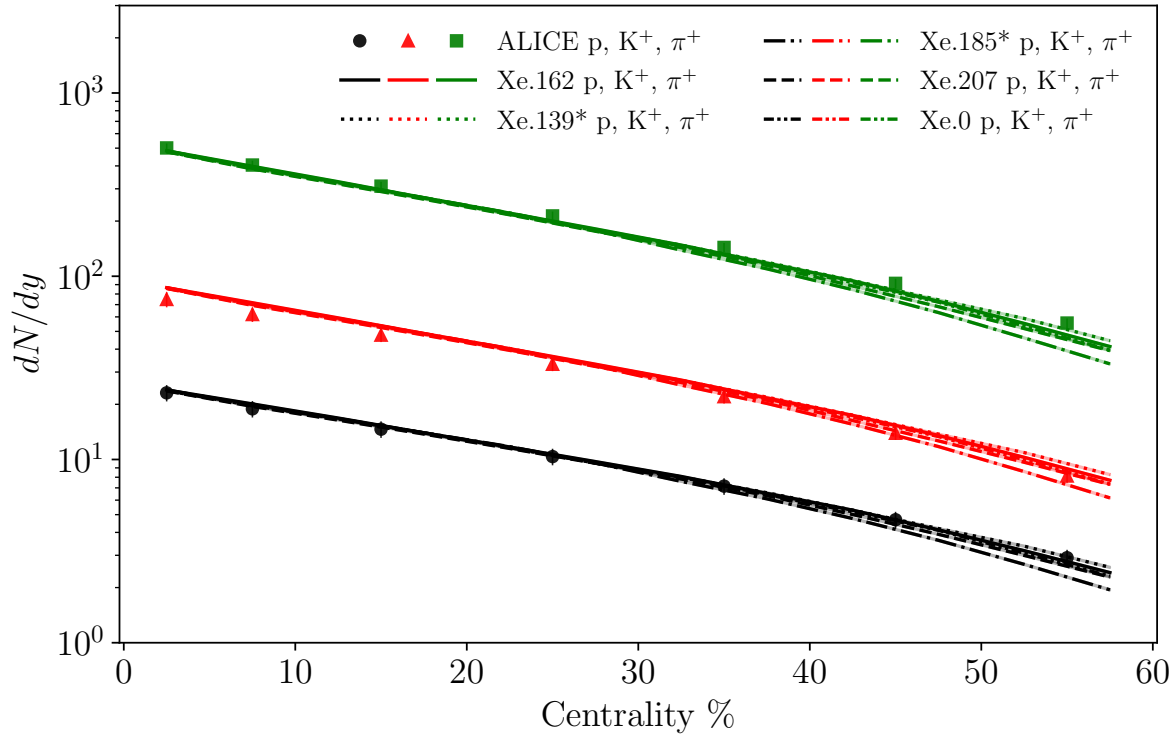


Figure 58: Identified particle multiplicity in $|y| < 0.5$ as a function of centrality. Calculations from our model are compared to results for 5.44 TeV Xe+Xe collisions at ALICE [131].

appreciably from the experimental data in more peripheral collisions, this is not, as with previous underestimates, cause for concern. Indeed, the mean transverse momentum for heavier particles - such as pions and protons - is sensitive to hydrodynamic quantities such as the bulk viscosity and freeze-out temperature and the specifics of the Cooper-Frye sampling procedure. In a hydrodynamic system, the bulk viscosity dampens the radial flow velocity of the QGP significantly, leading to smaller $\langle p_T \rangle$ for heavier particles when compared to expansion which is not hindered by viscosity. The bulk viscosity is therefore of great importance to reproducing the average transverse momentum in central collisions. However, as we move towards more peripheral centralities and that, much like we described earlier, the hydrodynamic assumption begins to wear thin, the inclusion of bulk viscosity actually leads to an underestimation of the mean transverse momentum for heavier particles; this is yet another indication of the coexistence of

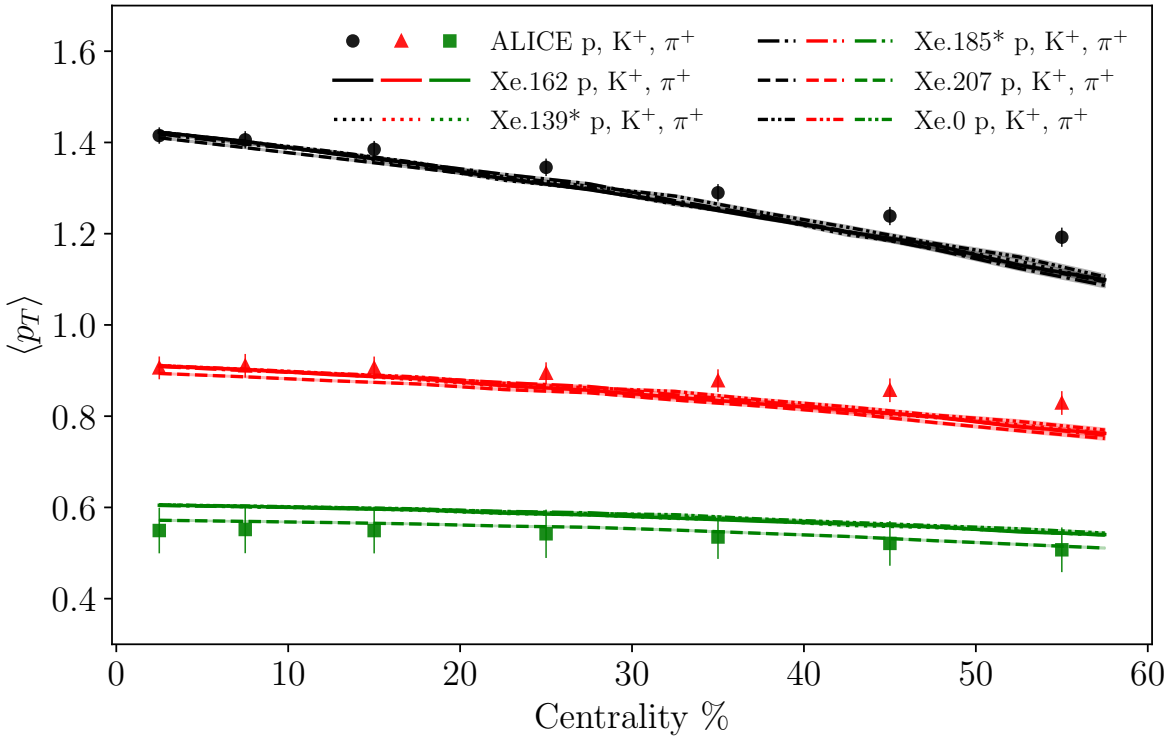


Figure 59: Identified particle mean transverse momentum $\langle p_T \rangle$ in $|y| < 0.5$ as a function of centrality. Calculations from our model are compared to results for 5.44 TeV Xe+Xe collisions at ALICE [131].

hydrodynamic and non-hydrodynamic modes of evolution in heavy-ion collisions, with the transition between the two progressing with centrality.

It is also interesting to note how Xe.207 (the dashed curve), our parametrization with the largest transverse cross-section, leads to noticeably smaller mean transverse momentum across all species, with the effect being most obvious for pions. To a lesser extent, this effect was also observed in Fig. 36. At constant collision energy, a larger overlap area between the colliding nuclei will lead to less energetically dense QGP and particles having less momentum. In other words, the flow of the QGP generated in Xe.207 collisions is markedly smaller than that generated in collisions of our other systems, leading to less momentum once particles are sampled. However, a valid question would be why the undeformed system Xe.0 or the triaxially deformed Xe.185* do not show similar dips in mean transverse momentum given they share $R_0$ with Xe.207. Measuring the transverse size of each parametrization gives us an answer. Indeed, much like we did in

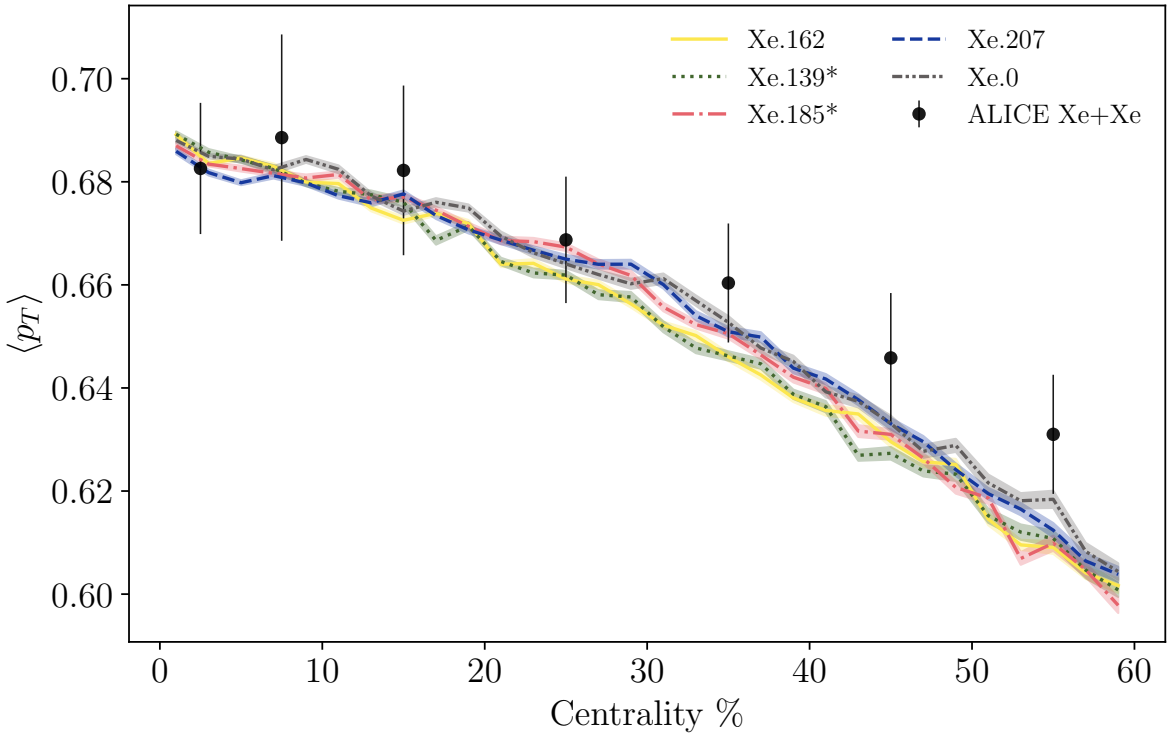


Figure 60: Charged particle mean transverse momentum $\langle p_T \rangle$ in $|\eta| < 0.8$ as a function of centrality. Calculations from our model are compared to results for 5.44 TeV Xe+Xe collisions at ALICE [132].

Section 5.1.2, we can estimate the transverse extent of these configurations by taking the following integral,

$$A_{\mathrm{WS}} = \int_0^{2\pi} \int_0^{R(\theta,\phi)} r d\theta dr$$
$$R(\theta,\phi) = R_0(1 + \tilde{\beta}_2^0 Y_2^0(\theta,\phi) + \tilde{\beta}_4^0 Y_4^0(\theta,\phi)). \tag{7.1}$$

Using this, we find that the transverse area of Xe.207 is the largest, at 106 fm$^2$. Xe.185* has two values, one taken at $\phi = 0$, and the other at $\phi = \pi/2$. The first yields a larger transverse area, 109 fm$^2$, while the second yields a smaller transverse area, 101 fm$^2$. This may seem like a contradiction to our argument. However, given that the orientations of the colliding nuclei determine the size of the overlap, the smaller transverse size will be more representative of the average shape of the overlap region across all centralities as the smaller transverse area is fully contained in the larger one. Finally, the same integral yields 99 fm$^2$ for Xe.0, providing an intuitive understanding of the ordering in Fig. 59.

We conclude this part of the results by providing results for charged particle mean transverse momentum compared to the experiment. This observable was not available in U+U and Au+Au runs. However, it gives us a more general picture of our systems' dependencies and shortcomings. Looking at Fig. 60, we find that our model once again reproduces the mean transverse momentum across most of the centrality range, with, again, an underestimate in the most peripheral plotted region. Interestingly, the ordering in Fig. 59 does not apply here. This is probably driven by particles not included in our identified particle analysis and may contribute significant amounts of momentum to the averages, skewing the results away from the specific ordering we observed previously. It could also be driven by changes in the kinematic cuts used in calculating this observable, which differed considerably from those used in Fig. 59; Ref. [132] used $0 \leq p_T \leq 10\,\text{GeV}$, while Ref. [131] restrained itself to $0 \leq p_T \leq 7\,\text{GeV}$. The large experimental error bars indicate that the underlying charged particle distribution must be broad, supporting our theory. Nevertheless, our model does reproduce the experimental results quantitatively, which is, once again, a confirmation that our calibration was adequate.

### 7.2.2 *Elliptic and Triangular Flows*

With our model calibrated and baseline observables reproduced, we can shift our attention to more sensitive and discriminating observables, starting with the elliptic flow $v_2$. Figure 61 shows the elliptic flow's 2- and 4-particle cumulants, $v_2\{2\}$ and $v_2\{4\}$, as functions of centrality. Our model's calculation is compared to data gathered at ALICE [133]. We see that, in both observables, our collection of parametrizations reproduces the experimental data faithfully. In central (0-10%) collisions, a clear separation driven by the Woods-Saxon quadrupole deformation parameter $\tilde{\beta}_2^0$ can be seen. Once we move past that mark, however, differences in our model's calculation become driven by the Woods-Saxon radius $R_0$ and diffusiveness $a$. Indeed, one finds that the undeformed parametrization Xe.0 jumps over two deformed parametrizations, namely Xe.162 and

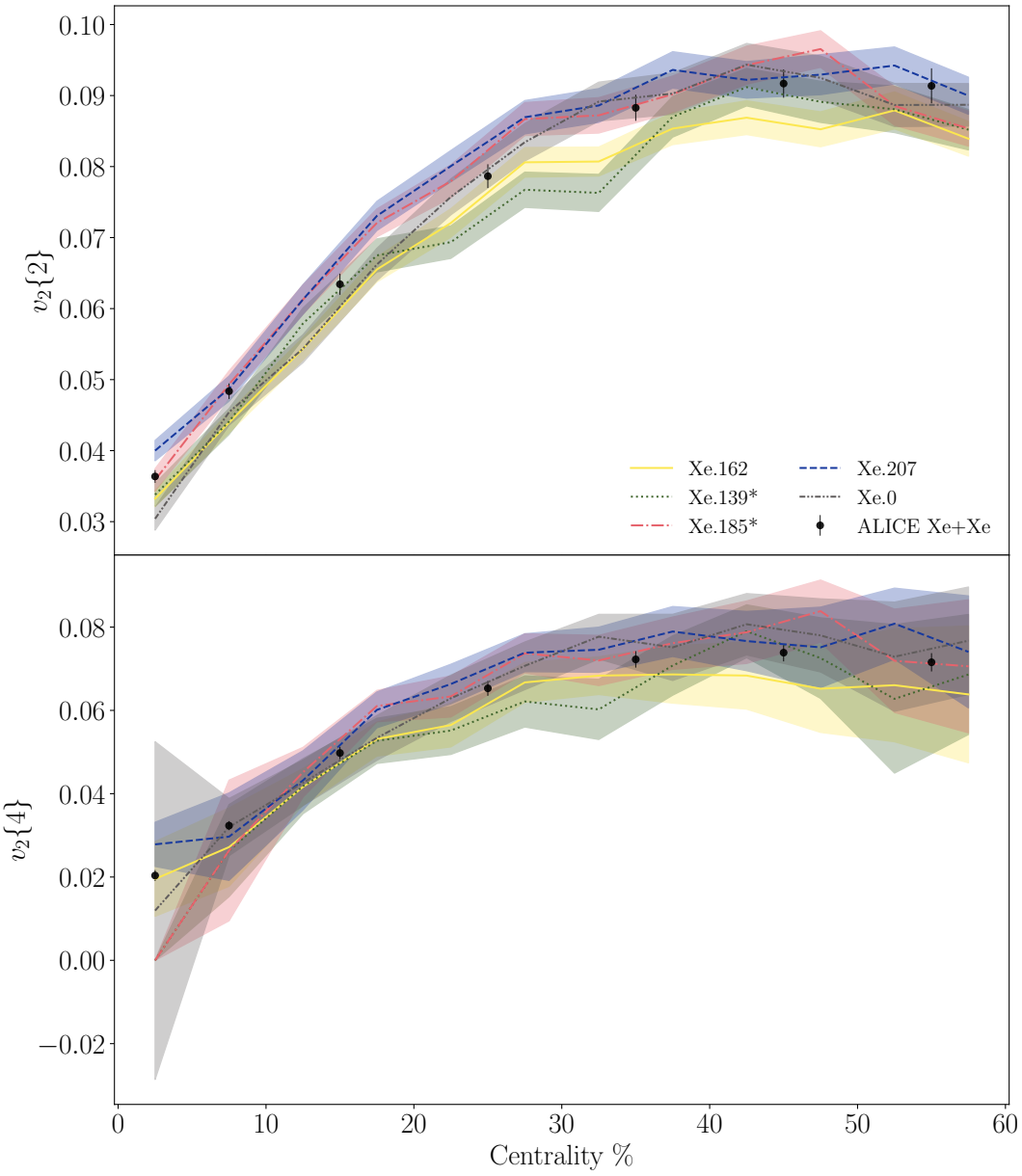


Figure 61: Two- and four-particle cumulants of elliptic flow ($v_2\{2\}$ and $v_2\{4\}$) as functions of centrality, for $0.2 < p_T < 3$ GeV. Calculations from our model compared to results for 5.44 TeV Xe+Xe collisions at ALICE [133].

Xe.139*, to join parametrizations which share its values of $R_0$ and $a$ (which are tabulated in Table 3). While the undeformed parametrization behaved as expected in the central region, producing less elliptic flow than other parametrizations, it quickly converges towards the Xe.185* and Xe.207 curves in more peripheral (25-60%) collisions. The 4-particle cumulant demonstrates similar qualitative features as the 2-particle cumulant.

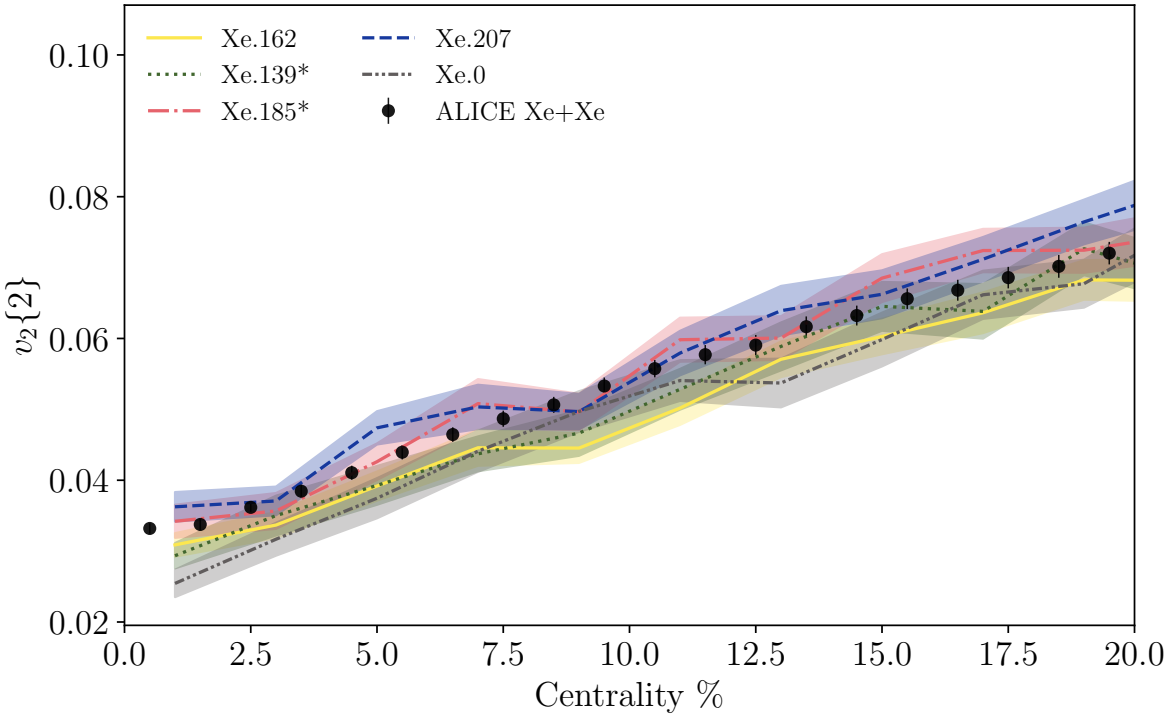


Figure 62: Two-particle cumulant of elliptic flow $v_2\{2\}$ as a function of centrality, for central to semi-peripheral collisions (0-20%) and $0.2 < p_T < 3$ GeV. Calculations from our model compared to results for 5.44 TeV Xe+Xe collisions at ALICE [133].

Given the large error bars, the parametrization ordering in ultra-central collisions is hard to make out. However, the ordering in peripheral collisions mirrors that which was found in the 2-particle cumulant. All-in-all, our model manages to recreate both observables very well across a very wide centrality range.

Shifting our attention to Fig. 62, we find the same 2-particle cumulant of the elliptic flow $v_2\{2\}$ as a function of centrality, but focused on central and semi-peripheral collisions (0-20%). This enlarged plot features finer centrality bins for our model and the experimental data. Figure 62 makes it clear that Xe.0, the undeformed parametrization, is inappropriate for describing the experimental data in central collisions, results which are most sensitive to the shape of the colliding nuclei. Furthermore, both Xe.162 and Xe.139* fail to generate sufficient elliptic flow to match the experimental data. They also fail to register the noticeable uptick in the trend of the elliptic flow in ultra-central (0-2.5%) collisions. Xe.185* and Xe.207, stemming from similar parametrizations, are

the best matches for the experimental elliptic flow data, with a slight preference for the triaxial Xe.185*. Indeed, including triaxiality inhibits elliptic flow in central collisions just enough to overlap perfectly with the experimental data. Xe.207 slightly overestimates the elliptic flow toward semi-peripheral collisions, furthering the experimental data's preference for the Xe.185* parametrization.

Interestingly, looking at the experimental data's most central point, we notice a slight uptick of the elliptic flow in ultra-ultra-central collisions. This uptick was not observed in Fig. 38, which suggests that this is due to the true triaxial nature of $^{129}$Xe. Indeed, if a nucleus is sufficiently triaxially deformed, tip-tip collisions (refer to Figs. 14 and 31) do not actually always generate a circular overlap region. Instead, they can generate any of a wide range of overlap shapes, ranging from elliptical to circular. Therefore, ultra-ultra-central collisions of considerably triaxially deformed nuclei should generate non-negligible amounts of elliptic flow, in stark contrast with the $^{238}$U experimental data seen in Fig. 38, which dives towards 0 elliptic flow in ultra-ultra-central collisions. This slight uptick in ultra-ultra-central collisions is, therefore, a strong signal of $^{129}$Xe exhibiting considerable triaxial deformity.

We now focus on the 2-particle cumulant of triangular flow $v_3\{2\}$, shown in Fig. 63. Much like what we found in Fig. 41, we underestimate the triangular flow in central collisions across all parametrizations. Furthermore, the Xe+Xe triangular flow displays the same fluctuation-driven behavior observed in U+U and Au+Au collisions. Indeed, no real ordering between parametrizations emerges, with curves varying considerably across the entirety of the centrality range. Interestingly, in peripheral collisions, the ordering found in Fig. 61 is partially reversed, with Xe.162 and Xe.139* finding themselves above Xe.0, Xe.185* and Xe.207. Because of their smaller system size, fluctuations in nucleon positions play a comparatively larger role than the same fluctuations play in the larger systems, driving a slight increase in triangular flow. Once again, for central collisions, the inclusion of sub-nucleonic degrees of freedom should help enhance this observable [115]. This observable, however, does not seem to hold any discriminatory power in terms of the parameters we are looking to constrain.

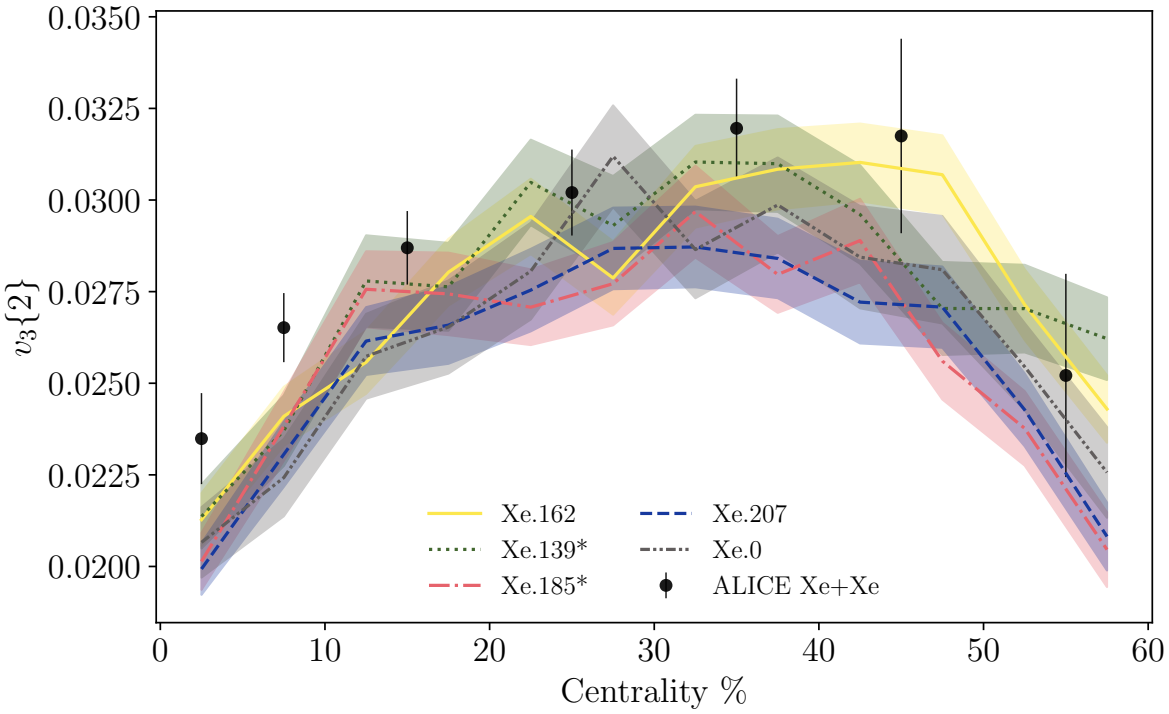


Figure 63: Two-particle cumulant of triangular flow $v_3\{2\}$ as a function of centrality, for $0.2 < p_T < 3$ GeV. Calculations from our model compared to results for 5.44 TeV Xe+Xe collisions at ALICE [133].

Moving to differential observables, we begin with the $p_T$-differential 2-particle cumulant of elliptic flow $v_2\{2\}(p_T)$, shown in Fig. 64. The conclusions here resemble those of our analysis of U+U and Au+Au differential flow and those of Fig. 61. Indeed, while the most central panel, 0-5%, provides some discriminating potential between our parametrizations, the curves quickly converge as we move towards more peripheral bins. Additionally, the behavior of the 5-10%, 10-20% and 20-30% slices is quasi-identical; we find that our model underestimates the differential elliptic flow for $p_T < 0.5$ GeV and overestimates it at higher $p_T$. Because our model only goes up to $\sim p_T = 4$ GeV, it seems like it compensates for its truncated distribution by generating more elliptic flow at these higher values. The underestimate at lower $p_T$ is less prominent than the overestimate at high $p_T$, in line with the fact that a much larger number of particles have $p_T < 1$ GeV than $p_T > 2$ GeV, ensuring that the integrated flow presented in Figs. 61 and 62 remain consistent with experimental results. Shifting our focus to the ultra-central slice 0-5%,

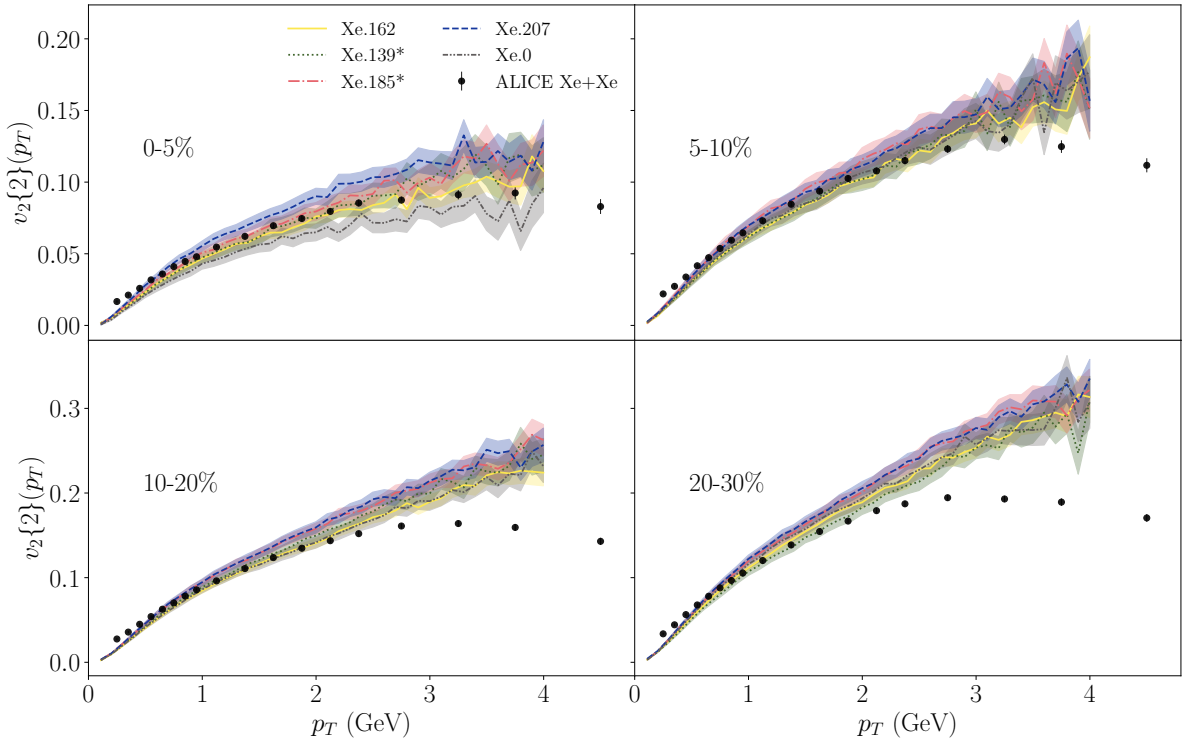


Figure 64: Two-particle cumulant of $p_T$-differential elliptic flow $v_2\{2\}(p_T)$ as a function of transverse momentum $p_T$. Calculations from our model compared to results for 5.44 TeV Xe+Xe collisions at ALICE [133].

we find that the behavior of the different parametrizations unsurprisingly mirrors that which we found in Fig. 62. The undeformed parametrization systematically underestimates the differential elliptic flow across the entire range, providing added evidence of $^{129}$Xe's deformity. Moreover, Xe.162 and Xe.139* both considerably underestimate the differential elliptic flow in the critical low-$p_T$ region, while Xe.185* and Xe.207 coalesce much quicker towards the experimental data points. Figure 64 provides further evidence of a preference emerging for the Xe.207 and Xe.185* parametrizations.

Proceeding to Fig. 65, we find our first rapidity-dependent observable, $v_2\{2\}(\eta)$. Because the results shown in Figs. 61 and 62 were taken at mid-rapidity, our calculation at and around mid-rapidity is expected to mirror the results shown in those figures. Indeed, we find that the initial parametrization ordering and the progression as we move to more and more peripheral collisions are similar to that seen in our integrated flow figures. However, it seems that our model is unable to reproduce the experimental

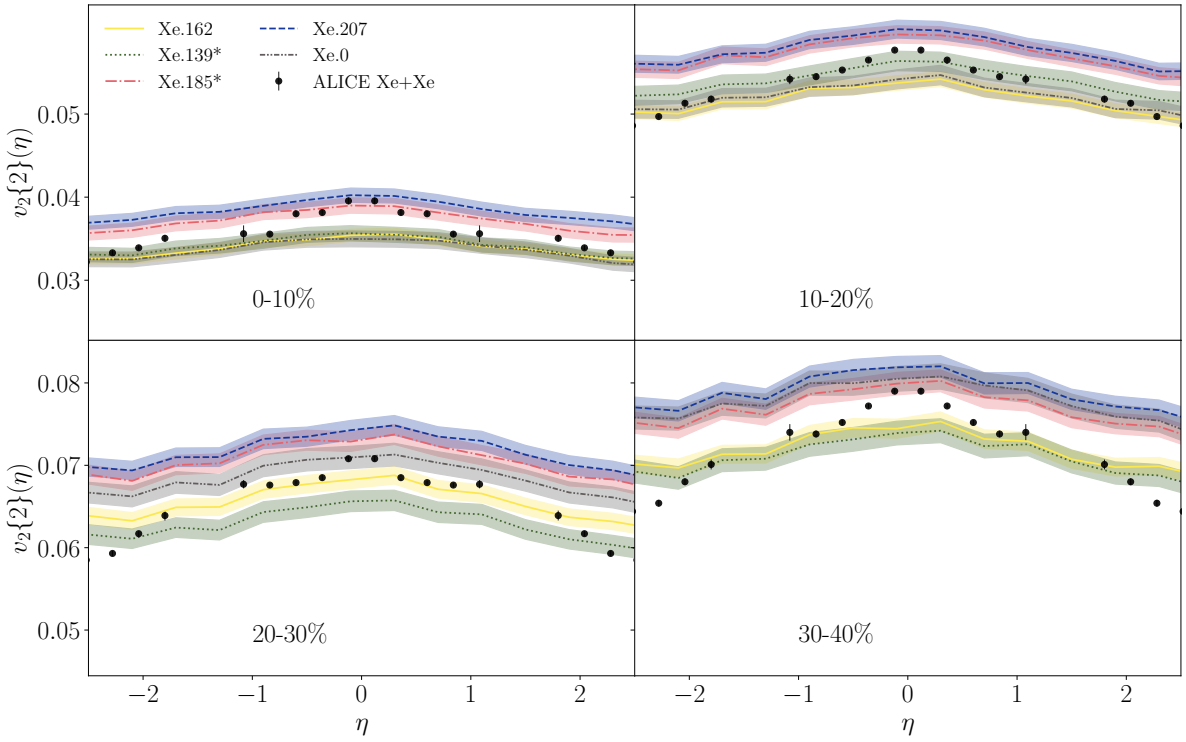


Figure 65: Two-particle cumulant of $\eta$-differential elliptic flow $v_2\{2\}(\eta)$ as a function of pseudorapidity $\eta$, for $0.2 < p_T < 5\,\text{GeV}$. Calculations from our model are compared to results for 5.44 TeV Xe+Xe collisions at ALICE [134].

slope in elliptic flow in the $\eta$ direction. This is linked to our overestimating the charged particle yields for $|\eta| > 1$ seen in Fig. 56. Indeed, overestimating the yields is equivalent to overestimating the total energy contained in a given rapidity slice, spreading across all components of the stress-energy tensor $T^{\mu\nu}$. More energetic slices will take more time to reach freeze-out, allowing for the development of more and more coherent flow, in turn leading to an overestimate of the anisotropic flow away from mid-rapidity. It is also certainly caused by our early-stage longitudinal evolution - the JIMWLK evolution - generating too much correlation between different slices; it seems likely that, in experiments, the longitudinal structure of the QGP generated in a collision event exhibits some form of rotational decorrelation [135], in addition to the gluonic field fluctuations included in the JIMWLK evolution. This decorrelation should lead to less coherence in flow and, therefore, less elliptic flow at larger absolute rapidities. Looking at Fig. 66, we find the $\eta$-dependent triangular flow. Once again, our results

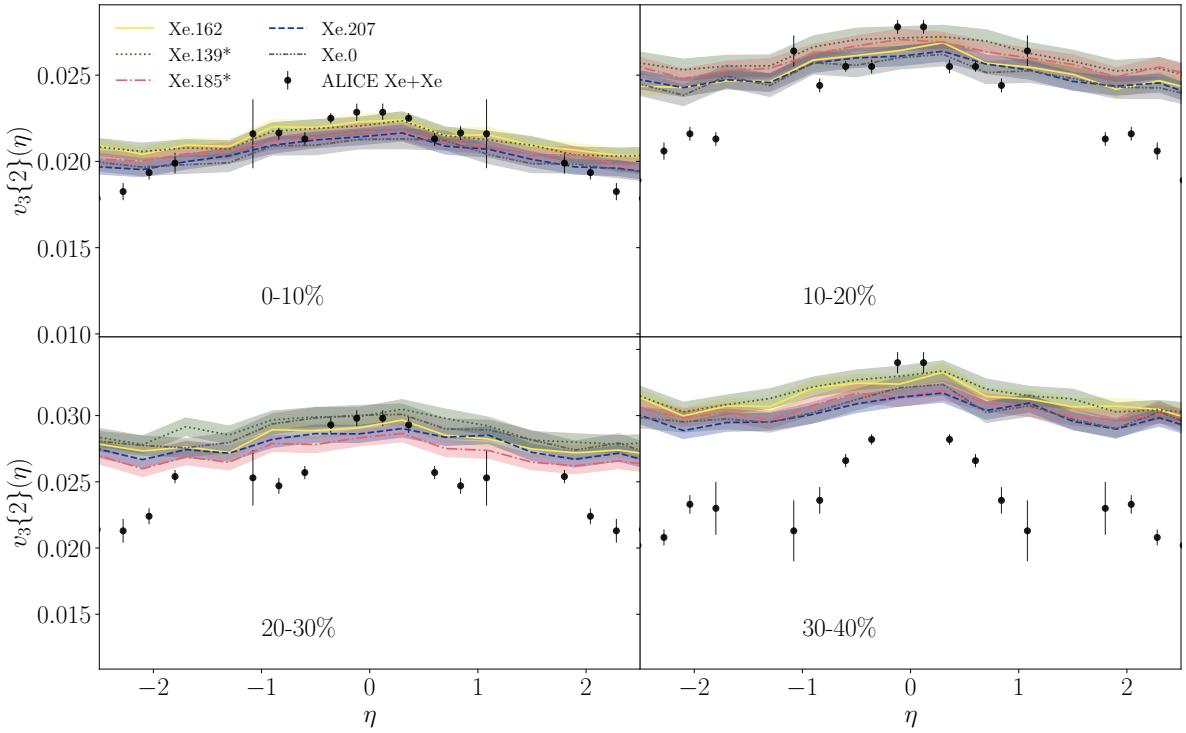


Figure 66: Two-particle cumulant of $\eta$-differential triangular flow $v_3\{2\}(\eta)$ as a function of pseudorapidity $\eta$, for $0.2 < p_T < 5$ GeV. Calculations from our model are compared to results for 5.44 TeV Xe+Xe collisions at ALICE [134].

mirror those found in the integrated observable Fig. 63: no consistent ordering can be determined, and fluctuations dominate the curves. While our model's calculation's slope seems consistent across centrality slices, it is interesting to note how much the experimental curves' slopes vary from centrality class to centrality class. Indeed, while our calculation matches up fairly well with the experimental data across the entire rapidity range for 0-10% centrality, the experimental curves demonstrate much greater triangular flow suppression as we move towards larger absolute rapidities in all the other centrality slices. Much like the $\eta$-dependent elliptic flow, this is driven by our charged yields overestimates, for much the same reason, with the added fact that triangular flow is mainly driven by small fluctuations - be they geometric or energetic - whose signals would get further suppressed if we had normalized the longitudinal energy content more appropriately. This effect deserves an investigation, which could shed light on the exact

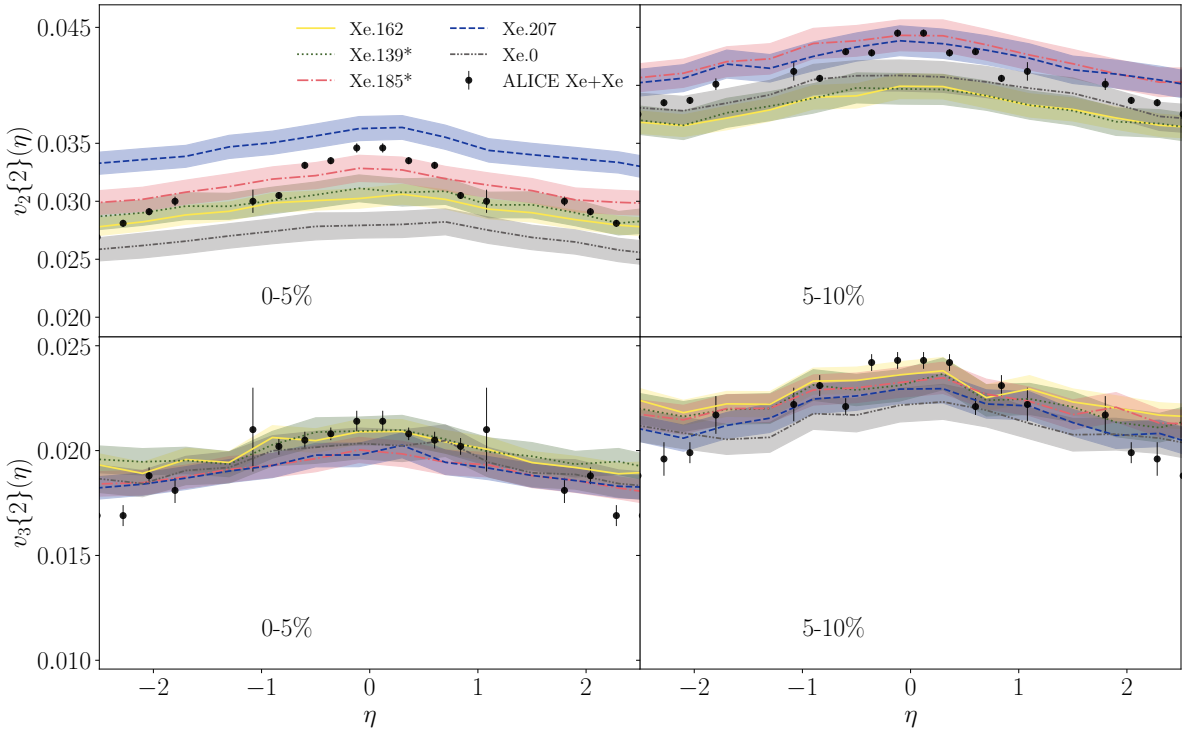


Figure 67: Two-particle cumulant of $\eta$-differential (**top**) elliptic flow $v_2\{2\}(\eta)$ and (**bottom**) triangular flow $v_3\{2\}(\eta)$ as a function of spacetime rapidity $\eta$, for ultra-central (0-5%) and central (5-10%) collisions and $0.2 < p_T < 5\,\text{GeV}$. Calculations from our model compared to results for 5.44 TeV Xe+Xe collisions at ALICE [134].

dependency of color charge fluctuations on spacetime rapidity and on the longitudinal suppression of flow.

Examining Fig. 67, we find the 0-10% centrality bins from Figs. 65 and 66 segmented into ultra-central (0-5%) and central (5-10%) bins, allowing us to further differentiate between our different parametrizations. It is interesting to note how quickly the different $v_2\{2\}(\eta)$ curves converge onto one another beyond the ultra-central region. Of course, the ordering observed in Fig. 62 is maintained, with Xe.0 being wholly inadequate in describing the ultra-central region of this observable. Interestingly, while this observable still prefers Xe.207 and Xe.185*, both fall on either side of the ultra-central experimental data, providing the first signal that, potentially, neither of these parametrizations delivers an accurate projection of the shape of the quantum fluctuations of $^{129}$Xe. Nevertheless, similar conclusions regarding our model's capabilities and shortcomings can be

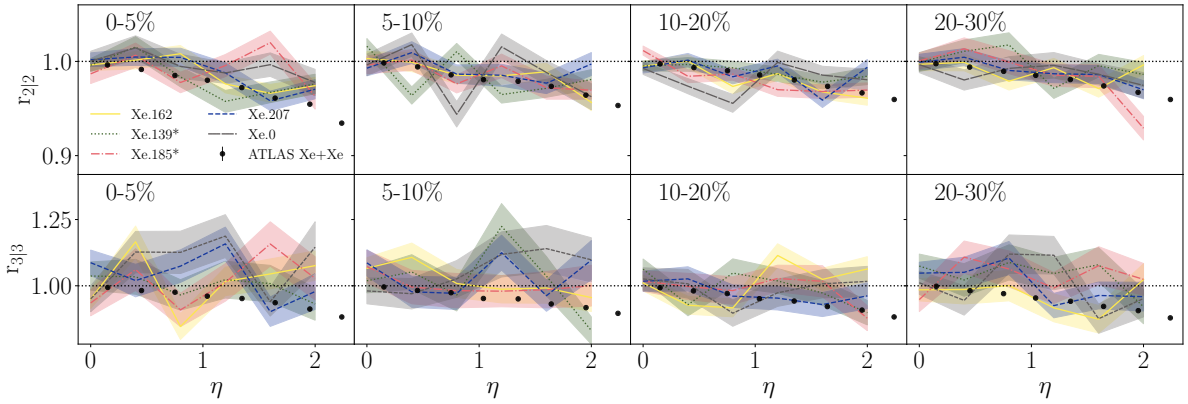


Figure 68: (**Top**) Elliptic and (**bottom**) triangular flow decorrelation ratio $r_{2|2}$ and $r_{3|3}$ as functions of spacetime rapidity $\eta$, for $0.2 < p_T < 5$ GeV. Calculations from our model compared to results for 5.44 TeV Xe+Xe collisions at ATLAS [136].

extracted from Fig. 67, namely that we are able to reproduce central $v_3\{2\}(\eta)$ faithfully, and that elliptic flow decorrelations in the $\eta$ direction may be insufficient; the scale of the elliptic flow is, however, well-reproduced in the mid-rapidity region across all centralities.

To properly quantify the scale of decorrelations measured in experiment, we turn to the decorrelation ratio $r_{n|n}$ described in Section 6.3.3. Obviously, given its definition, this observable is intrinsically tied to the rapidity-dependent anisotropic flow $v_n\{2\}(\eta)$; as mentioned above, one can see from the results presented in Figs. 65 to 67 that our model's calculation, especially in peripheral collisions, leads to a flatter slope in the $\eta$ direction than the experimental results. This flatter slope, interpreted under the lens of correlations, indicates that our anisotropic flow away from mid-rapidity is too correlated with that of mid-rapidity and the opposite rapidity. However, given the inclusion of a specific reaction plane term in the experimental observable's calculation, one can expect some differences between the values inferred from Figs. 65 to 67 and those obtained using Eq. (6.23). Therefore, comparing this observable remains relevant to our analysis and understanding where our model may be improved. Looking at Fig. 68, we find the elliptic and triangular flow decorrelations for 4 centrality slices. Calculations from our model are compared to experimental results from ATLAS [136]. From the start,

it is important to note that the move from one experiment (ALICE, in the case of all previous figures) to another is not trivial; different experiments use different kinematic cuts, acceptance ranges and reference flow vectors which need to be considered. These differences can (and should) lead to differences in the end-state observables - if they did not, the specificities of each experiment would not be mentioned. Therefore, when comparing the decorrelation ratios measured at ATLAS to the $\eta$-dependent anisotropic flows shown in Figs. 65 to 67 should be done cautiously, as the calculations of $r_{n|n}$ made at ATLAS use a different collection of events than that measured at ALICE, analyzed using different cuts. Concretely, ALICE use particles with $0.2 \leq p_T \leq 5\,\text{GeV}$ for its analysis, with pseudorapidity separation $|\Delta\eta| > 0.4$ for mid-rapidity and $|\Delta\eta| > 2.2$ for forward-rapidity reference flow particles (see Eq. (6.22)). ATLAS, on the other hand, uses particles with $0.5 \leq p_T \leq 3\,\text{GeV}$, with $4.0 < |\eta_{\text{ref}}| < 4.9$ for $r_{2|2}$ and $3.2 < |\eta_{\text{ref}}| < 4.9$ for $r_{3|3}$. When comparing to data from different experiments, we must tailor our analysis to take these different kinematic cuts into account. In the end, this means that trying to understand the decorrelation ratios presented in Fig. 68 through Figs. 65 to 67 is of no practical use as the $v_n\{2\}(\eta)$ curves generated by an ATLAS analysis may look very different (potentially much flatter) than those of ALICE, especially given ALICE uses a narrow mid-rapidity window for its reference flow vector which generates a larger peak in that region. Our model can reproduce the decorrelation trends of both the elliptic and the triangular ratios. However, it does present a noticeable overestimation of both observables. This is to be expected when we consider how our initial state determines different slices in rapidity; while the gluon field is sensible, the shape of the interaction region, which is a primary marker of how flow builds up in the QGP, is determined by the overlap of the nuclei thickness functions in the transverse plane. From one rapidity to another, the overlap region's features remain unchanged. Gluonic field fluctuations affect how much energy is deposited and how much flow builds up before the hydrodynamic phase. However, given similar total energy and overlap shape, two rapidity slices at opposing sides of mid-rapidity will generate very similar amounts of flow, especially elliptic flow (which is not mainly

driven by fluctuations, contrarily to triangular flow). The flows, then, are correlated with one another even though a considerable rapidity gap separates the two regions. As shown in Fig. 68, this is an inadequate representation of reality: flow decorrelates appreciably as we move to larger and larger gaps in rapidity.

There are simple and not-so-simple ways one could improve decorrelation calculations. For one, the use of our envelope function Eq. (6.19) produces decorrelations on its own: by reducing all components of $T^{\mu\nu}$ by some multiplicative constant, one reduces the total energetic content of a given rapidity slice of QGP and, in turn, reduces the amount of time required for that rapidity slice to reach freeze-out. This diminishes coherent flow build-up and, therefore, reduces the amount of anisotropic flow generated in a given slice. Our overestimates of the rapidity-dependent yields are thus related to underestimating the amount of decorrelation. Further calibrating our $\eta$ envelope could help us close the gap between our calculation and the experimental results. One could also use this envelope to introduce some rotational decorrelation to the hydrodynamic evolution, partially rotating each rapidity slice in the transverse plane to generate slice-to-slice anisotropies and, more generally, provide a numerical equivalent to the event-plane angle $\Psi_R(\eta)$ which is captured implicitly by these observables. Then, there are more complex sources of decorrelations which are overlooked by our model in its current state, such as the inclusion of mini-jets. Mini-jets are initial semi-hard scatterings which have energy greater than the typical QGP temperature scale. Mini-jets can potentially contribute to the total energy of the system. Including a mini-jets simulator concurrently with the hydrodynamic evolution provided by MUSIC should provide considerable decorrelations from one rapidity slice to another. This is, however, left as future work.

In terms of the objectives of this analysis, the decorrelation ratio, as calculated by our model in its current state, does not provide any discriminating potential between the different parametrizations; the curves stemming from different parametrizations overlap considerably across centralities and rapidities, providing no insights. It is therefore safe

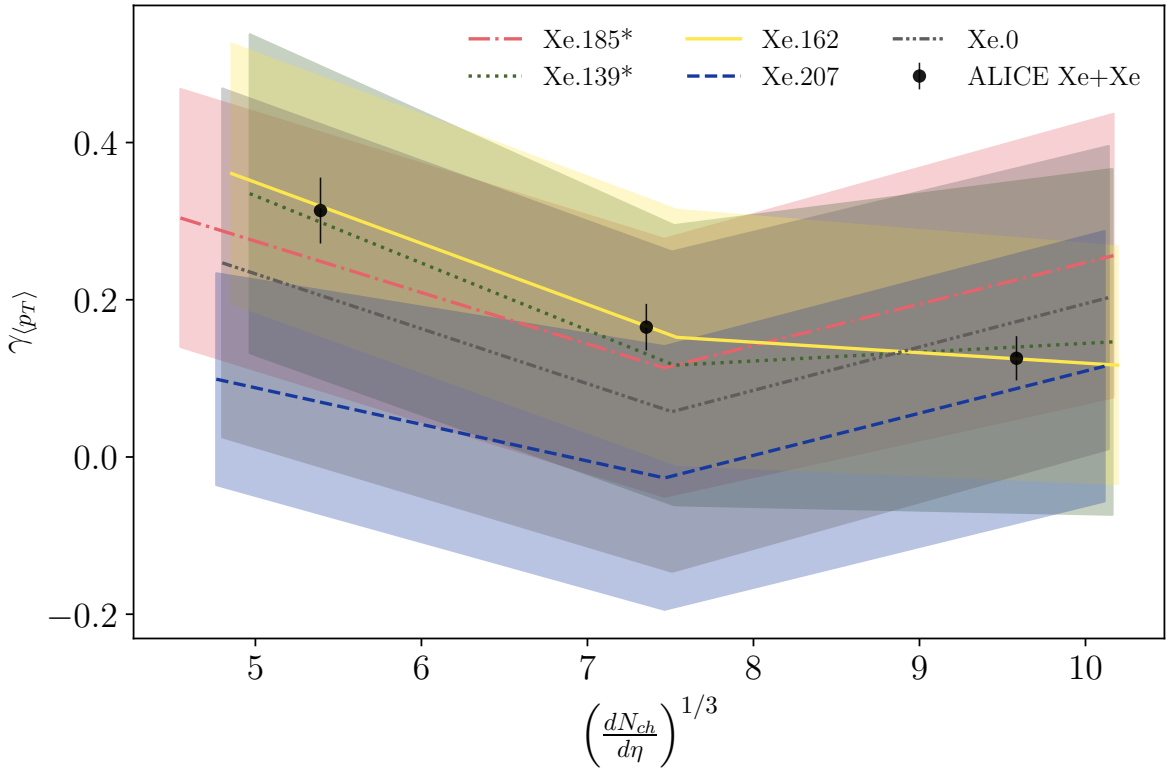


Figure 69: Standardized skewness $\gamma_{\langle p_T \rangle}$ as a function of the cubic root of charge particle multiplicity $(dN_{\mathrm{ch}}/d\eta)^{1/3}$. Calculations from our model compared to results for 5.44 TeV Xe+Xe collisions at ALICE [137].

to say that, in order for longitudinal observables to be used in a nuclear shape calibration procedure, models will need to be improved.

Let us now move on to the different momentum and flow correlators which provided us with valuable insights regarding the appropriateness of a given parametrization.

### 7.2.3 *Correlators*

We begin by introducing the standardized skewness $\gamma_{\langle p_T \rangle}$; it is a composite observable made up of the 2- and 3-particle $p_T$ correlators introduced in Section 4.3.3. Formally, it is defined as

$$\gamma_{\langle p_T \rangle} = \frac{\langle \delta p_T \delta p_T \delta p_T \rangle}{\langle \delta p_T \delta p_T \rangle^{3/2}}. \tag{7.2}$$

While we may have preferred individual comparisons to the 2- and 3-particle $p_T$ correlators based on our previous findings, the experimental data was only given in terms of the standardized skewness $\gamma_{\langle p_T \rangle}$. Figure 69 shows our model's calculation against the experimental data gathered at ALICE [137]. Across all parametrizations, our model replicates the experimental data across the provided multiplicity range. The general lack of experimental data however undermines our efforts at differentiating between our parametrizations using central collisions. Indeed, each experimental data point represent a very wide centrality range, meaning that any sensitivity to specific initial state anisotropies is averaged out. Our finding from Chapter 5 seem to be repeated here as well; indeed, the ordering exhibited by our most central (rightmost points) collisions suggests that system size drives this observable. However, the lack of experimental data at such multiplicities leaves us guessing whether such dependencies persist in an experimental setting. Nevertheless, as mentioned previously, our model does generate appropriate multi-particle $p_T$ correlations, although they do not seem to hold any discriminatory power. In the end, our model holds slight preferences for Xe.162, Xe.139* and Xe.185*, although the error bars overlap for all parametrizations across the entire range.

Moving to transverse-momentum-flow correlators now, we turn our attention to Fig. 70, which shows the transverse-momentum-elliptic-flow correlator $\rho(v_2\{2\}, \langle p_T \rangle)$ as a function of centrality. As a reminder, nuclei presenting large quadrupole deformations should generate an anti-correlation between mean transverse momentum $\langle p_T \rangle$ and elliptic flow $v_2\{2\}$. However, based on Fig. 45, we could not determine how much quadrupole deformity was minimally required to generate anti-correlation. We were also unsure whether the transition between correlation and anti-correlation would be smooth, moving linearly with increasing $\tilde{\beta}_2^0$.

Figure 70 shows $\rho(v_2\{2\}, \langle p_T \rangle)$ for our 5 parametrizations compared to experimental data from ATLAS [138]. Given key differences in behavior, we include, for the first time in our $^{129}$Xe results, curves stemming from the two averaging techniques described in Chapter 5, namely the SMASH Sub-Event (SM) average and Oversampled

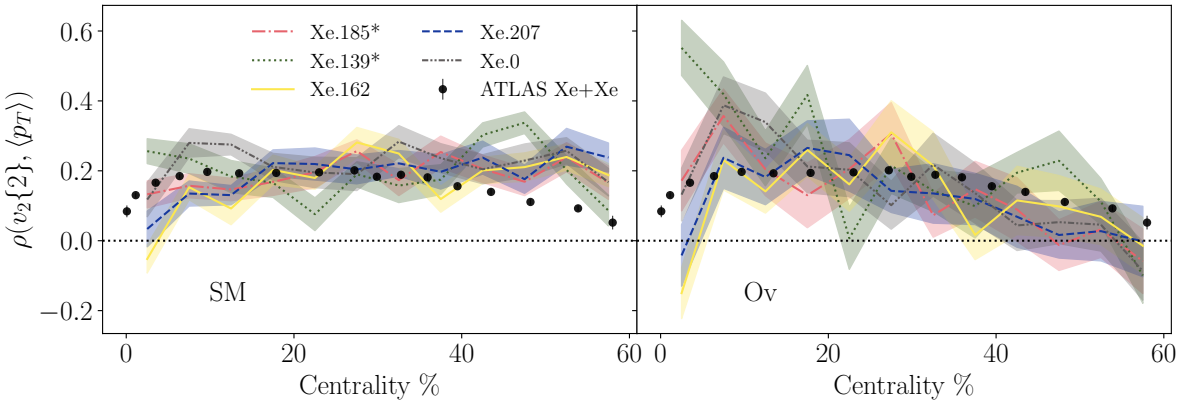


Figure 70: Transverse-momentum-elliptic-flow correlator $\rho(v_2\{2\}, \langle p_T \rangle)$ as a function of centrality. The **left** panel shows calculations done with the SMASH Sub-Event (SM) averaging method, while the **right** panel shows calculations made with the more common Oversampled (Ov) averaging technique. Calculations from our model compared to results for 5.44 TeV Xe+Xe collisions at ATLAS [138].

(Ov) average. While all parametrizations seem to overlap for more peripheral collisions, a splitting occurs at around the 10% centrality mark; we find that Xe.162 and Xe.207 - our two non-triaxially deformed parametrizations, dive down towards anti-correlation. Xe.185* and, interestingly, Xe.0 - our undeformed parametrization - provide fair agreement with experimental data, both qualitatively and quantitatively. Finally, Xe.139* generates far too much correlation in central collisions. Interestingly, the SM curves are much smoother than the Ov curves while preserving the same ordering throughout. Also of note, while the SM curves overestimate the experimental data in peripheral (>40%) collisions, the Ov averaging leads to an underestimate, which entails that the simple dichotomy between the inclusion or exclusion of short-range correlations is inadequate in our quest to describe these correlations in the peripheral centrality region. Furthermore, some non-trivial effects are clearly at play here, as in the central region, the Ov curves lead to more extreme values when compared to the curve stemming from the same parametrization but calculated using the SM average. This seems to indicate that the short-range correlations and fluctuations inherently included in the SM average work to 'reign in' long-range fluctuations and correlations which guide the Ov curves.

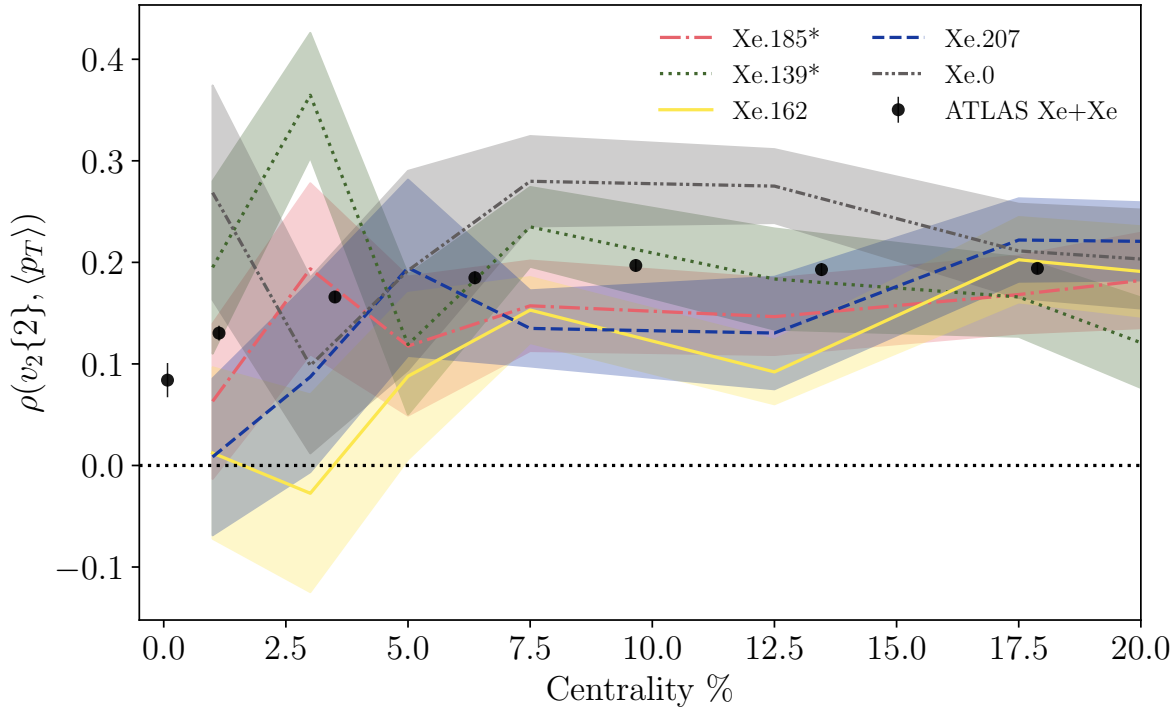


Figure 71: Transverse-momentum-elliptic-flow correlator $\rho(v_2\{2\}, \langle p_T \rangle)$ as a function of centrality for central (0-20%) collisions. Calculations from our model stemming from the SM averaging method compared to results for 5.44 TeV Xe+Xe collisions at ATLAS [138].

Because the central region is of utmost interest, we provide an enlarged plot of said region using finer centrality bins provided by ATLAS [138]. Figure 71 shows our SM average curves for central collisions. The fluctuations exhibited by our different curves in the ultra-central (0-5%) region are driven by the use of finer centrality bins for comparison's sake. Once again, all parametrizations fit the experimental data well across the entire range. However, in ultra-central collisions, the curves settle at different values. Notably, we find that the Xe.139* curve, which in Fig. 70 appeared to overestimate the correlator, dives back down towards the experimental curve in our most central bin. Comparing the results from our two triaxially-deformed parametrizations, Xe.139* and Xe.185*, to those of our two other deformed parametrizations Xe.162 and Xe.207, we find that our model prefers triaxial parametrizations in reproducing the experimental correlator. This finding is in line with what was found with a simpler model [129] and

hypothesized by the experimentalists [138]. The Xe.185* parameterization comes the closest to reproducing the entire central range for this observable, following step with the other observables shown to this point, which suggests that it is the most appropriate parametrization we have used.

Regarding our question concerning the specific relationship between the scale of deformity and an emerging anti-correlation in central collisions, our model suggests that this transition is smooth and simply requires sufficient quadrupole deformation to surface. Indeed, we find that both the Xe.207 and Xe.162 - both non-triaxially-deformed parametrizations - show signs of anti-correlations in ultra-central collisions. It is however interesting to note that these two parametrizations present considerably different quadrupole deformations, and that Xe.162's $\tilde{\beta}_2^0$ is much smaller than that of Xe.185*. Therefore, not only does triaxiality play a significant role in how these correlations develop, but it seems like system size could also play a significant role. Indeed, looking back at our $^{197}$Au curves, we see that, even though their parametrizations differ significantly, they both reproduce the experimental data well, hinting at non-trivial interplay between the deformity of a nucleus, its size, and the correlator.

As a final observable, we move our attention to the transverse-momentum-triangular-flow correlator $\rho(v_3\{2\}, \langle p_T \rangle)$, shown in Fig. 72. As with Fig. 45's bottom panel, we find that $\rho(v_3\{2\}, \langle p_T \rangle)$ is dominated by fluctuations. The correlator hovers just above 0 across the entire centrality range, with a slight uptick in central collisions which is caused by small overlap area events (which lead to higher $\langle p_T \rangle$) being more prone to geometric fluctuations (which lead to triangular flow $v_3\{2\}$). Notably, the differences between the SM and Ov averaging techniques persist in this observable, with SM overestimating the correlation in peripheral collisions and Ov underestimating it. As mentioned in the previous statement, it is also interesting to note that both Ov and SM techniques produce similar results in the central region while diverging in peripheral collisions. No real ordering emerges in our parametrizations, confirming that $\rho(v_3\{2\}, \langle p_T \rangle)$ is insensitive to initial state geometric features stemming from deformed nuclear parametrizations.

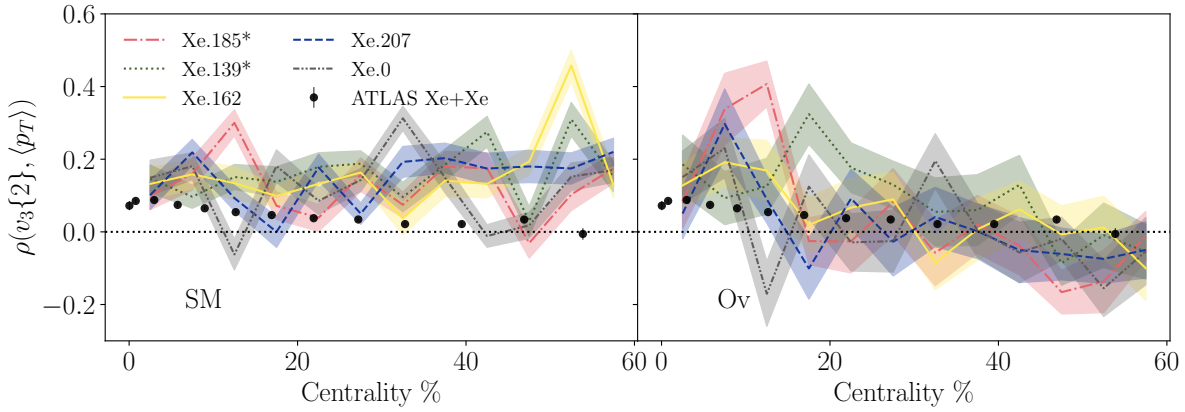


Figure 72: Transverse-momentum-triangular-flow correlator $\rho(v_3\{2\}, \langle p_T \rangle)$ as a function of centrality. The **left** panel shows calculations done with the SMASH Sub-Event (SM) averaging method, while the **right** panel shows calculations made with the more common Oversampled (Ov) averaging technique. Calculations from our model stemming from the SM averaging method compared to results for 5.44 TeV Xe+Xe collisions at ATLAS [138].

The results presented now constitute a complete overview of our model's capabilities vis-à-vis reproducing a wide catalogue of experimental observables while only explicitly calibrating to reproduce the charged particle multiplicity at mid-rapidity. Using Bayesian-calibrated shear and bulk viscosities contributes to our model's success in reproducing these observables. Given the success of our physics-based approach and the wide reach and depth of the current analysis, we may now use our model's calculations to attempt to constrain the quadrupole and triaxial deformation of $^{129}$Xe based entirely on our model's predictions.

## 7.3 QUADRUPOLE AND TRIAXIAL CONSTRAINTS

Following work done in Ref. [119, 120], we now have basic foundations for understanding how initial state properties affect specific end-state observables, namely $v_2\{2\}$, $\langle \delta p_T \delta p_T \rangle$ and $\rho(v_2\{2\}, \langle p_T \rangle)$. In essence, simple parametric dependencies have been

discovered, which, in theory, should allow us to determine the most appropriate value of $\tilde{\beta}_2^0$ and $\tilde{\beta}_2^2$. These relationships are [120]

$$\begin{aligned}
(v_2\{2\})^2 &= a_1 + b_1(\tilde{\beta}_2)^2, \\
\langle \delta p_T \delta p_T \rangle &= a_2 + b_2(\tilde{\beta}_2)^2, \\
\rho(v_2\{2\}, \langle p_T \rangle) &= a_3 + b_3 \cos(3\gamma)(\tilde{\beta}_2)^3, \\
\langle \delta p_T \delta p_T \delta p_T \rangle &= a_4 + b_4 \cos(3\gamma)(\tilde{\beta}_2)^3,
\end{aligned} \tag{7.3}$$

where parentheses have been added for clarity, $\tilde{\beta}_2$ is the *total* quadrupole deformation and $\gamma$ is the triaxiality angle or parameter. Explicitly, it is defined in terms of the Woods-Saxon parameters described in Chapter 2 as

$$\begin{aligned}
\tilde{\beta}_2 &= \sqrt{(\tilde{\beta}_2^0)^2 + 4(\tilde{\beta}_2^2)^2}, \\
\gamma &= \arctan\left(\frac{2\tilde{\beta}_2^2}{\tilde{\beta}_2^0}\right).
\end{aligned} \tag{7.4}$$

Therefore, Xe.139* has $\gamma = 49°$ and $\tilde{\beta}_2 = 0.213$, while Xe.185* has $\gamma = 27°$ and $\tilde{\beta}_2 = 0.207$. This makes it obvious that the second of these parametrizations was generated by adding triaxial deformation to Xe.207. Xe.139*, on the other hand, uses a similar radius to Xe.162 but includes large triaxial deformation. Having five statistically significant runs stemming from different parametrizations - including an undeformed run - provides us with a unique opportunity to determine the various parameters of Eq. (7.3) with respect to our model and extract most likely values of $\tilde{\beta}_2$ and $\gamma$ in the process. However, given that the experimental data provided by ALICE [137] does not contain the individual 2- and 3-particle $p_T$ correlators, and that the standardized skewness $\gamma_{\langle p_T \rangle}$ is only provided for a wide centrality range (0-20%), we will need to overlook this observable in our analysis, as considering it would lead to a breakdown of many assumptions which are key to the extraction of Eq. (7.3).

As with the application of these linearizations shown in Ref. [118], we will use averaged calculations and experimental data in the 0-5% centrality range. Because Eq. (7.3)'s parameters measure the dependency of an observable on the geometry of the Woods-Saxon parametrization for a specific model, our aim is to fit a single pair of

parameters $(a_i, b_i)$ such that it is representative of a specific observable's dependencies on our model's parameters. The first parameter, $a_i$, should be viewed as measuring our model's baseline value for an observable based mostly on collision energy and collision system properties like nucleon number and size. The second parameter, $b_i$, measures how our model reacts to specific anisotropies in the initial state and, since we are focusing on ultra-central collisions, on the deformity of the collision system itself. As such, our undeformed run Xe.0 will serve as the very baseline for our model, allowing us to extract $a_i$ instantly using its value for a given observable. Then, using both the observable values and deformation parameters from our four deformed parametrizations, we will be able to fit a value of $b_i$ representative of our model's properties. Finally, using the ultra-central experimental data point, we will be able to extract values of $\tilde{\beta}_2$ and $\gamma$ predicted by our model given its specific dependencies on these deformation parameters and on our explicit goal of reproducing the experimental data exactly.

We begin with the elliptic flow, which exclusively constrains $\tilde{\beta}_2$. As mentioned above, our undeformed parametrization will serve us greatly, allowing us to set $a_1$ directly. Indeed, given that Xe.0 has $\tilde{\beta}_2 = 0$, we will have $v_2\{2\}^2_{\text{Xe.0}} = a_1$. This leads to $a_1 = (9 \pm 1) \times 10^{-4}$.

We can then use this value of $a_1$ to find a value of $b_1$ for our model, providing us with a path towards a first estimate. Taking into account our four deformed parametrizations, we find

$$b_1 = 0.010 \pm 0.002. \tag{7.5}$$

The experimental data point in 0-5% is $(v_2\{2\})^2 = 0.00132 \pm 0.00007$. Using our fitted values of $a_1$ and $b_1$, we find our model predicts

$$\tilde{\beta}_2 = 0.205 \pm 0.029. \tag{7.6}$$

As explained above, however, this value does not mean much without finding a corresponding value of $\gamma$, as the triaxiality parameter translates $\tilde{\beta}_2$ into $\tilde{\beta}^0_2$ and $\tilde{\beta}^2_2$. Therefore, we need to pursue a similar fitting with the correlator $\rho(v_2\{2\}, \langle p_T \rangle)$ to constrain $\gamma$.

Once again, our undeformed parametrization will greatly facilitate the task at hand. Much like above, we find, using Xe.0,

$$\begin{aligned} &\rho(v_2\{2\}, \langle p_T \rangle) = a_3 \\ \Rightarrow &a_3 = 0.12 \pm 0.04. \end{aligned} \tag{7.7}$$

Following the same logic as before, we can fit $b_3$ using this value of $a_3$. Doing so yields

$$b_3 = -15 \pm 12. \tag{7.8}$$

Here, the error is much larger than the one we extracted for $b_1$. This is driven by the relatively large error bars held by our $\rho(v_2\{2\}, \langle p_T \rangle)$ calculation. Using the value of $\tilde{\beta}_2$ obtained through our first procedure, we find

$$\begin{aligned} &\cos(3\gamma) = -0.18 \pm 0.27 \\ \Rightarrow &\gamma = (34 \pm 5)^\circ. \end{aligned} \tag{7.9}$$

Therefore, our multiple runs suggest that $^{129}$Xe has $\tilde{\beta}_2 = 0.205 \pm 0.029$ and $\gamma = (34 \pm 5)^\circ$. These parameters are fairly close to those presented in Ref. [129], showing a larger triaxiality coupled to a smaller quadrupole moment. Converting these estimates to $\tilde{\beta}_2^0$ and $\tilde{\beta}_2^2$ using Eq. (7.4), we obtain

$$\begin{aligned} \tilde{\beta}_2^0 &= \sqrt{\frac{(\tilde{\beta}_2)^2}{(1 + \tan^2(\gamma))}} = 0.170 \pm 0.033, \\ \tilde{\beta}_2^2 &= \frac{\tilde{\beta}_2^0 \tan(\gamma)}{2} = 0.057 \pm 0.010. \end{aligned} \tag{7.10}$$

Comparing our fitted values to those of Table 3, we find that our fits include Xe.185*'s parameters within their error bars. Given that this parametrization performed best across the board, it makes sense that the fitted parameters would end up being close to those. However, these fits provide further support to the low-energy HFB calculations undertaken in Ref. [129] which suggested $^{129}$Xe be triaxially deformed. Given that these HFB calculations incorporate many assumptions discussed in Chapter 2, we know that their output values must be validated and improved upon. By utilizing high-energy experimental data and our state-of-the-art framework, we were able to show that,

while recent HFB calculations do provide good baseline parametrizations, high-energy data suggests that these may be improved further, especially in the context of nucleon sampling using a Woods-Saxon distribution.

These techniques can be applied to any system purporting sufficient experimental data to extract proper bounds for two critical Woods-Saxon parameters. Using an undeformed parametrization is key to understanding what the different constant offsets $a_i$ should be, as they provide a direct representation of a specific observable's dependency on parameters unrelated to system geometry, such as collision energy and nucleonic content. Furthermore, utilizing a group of parametrizations which provide specific modulations to the different quadrupole deformation parameters ensures that the entirety of the observable spectrum is covered, providing simpler and more reliable fitting. Access to the 2- and 3-particle correlators could help further constrain both parameters and support our analysis. However, given the available experimental data, our model provides sensible and trustworthy bounds on deformation parameters which can be sharpened as more data becomes available while reproducing all provided experimental observables simultaneously. This shows clearly our framework's potential to bridge the gap between low-energy studies of nuclear wavefunctions and their fluctuations and high-energy nuclear physics, allowing one to test multiple nuclear structure parametrizations against one another in a self-consistent manner, providing valuable insights regarding the very structure of atomic nuclei at all energy scales.

# 8

# FINDINGS, IMPLICATIONS AND FINAL REMARKS

In this thesis, our state-of-the-art heavy-ion collision simulation framework was used as a tool to infer accurate parametric representations of nuclear shape fluctuations for multiple collision systems ($^{238}$U, $^{197}$Au, and $^{129}$Xe) at three different collision energies (193 GeV, 200 GeV, and 5.44 TeV). The recent advances in fully self-consistent and physically motivated initial state and hydrodynamic models IP-Glasma [16, 17] and MUSIC [**Schenke:2010nt**] coupled to a thorough Bayesian calibration of our entire framework's relevant parameter space [77, 87] made initial state anisotropies the next frontier in properly describing the entirety of heavy-ion collisions theoretically and computationally. As described in Chapter 2, the main sources of unconstrained initial state anisotropies are the geometrical properties of the colliding nuclei and their wavefunctions. More specifically, fluctuations in these wavefunctions are captured by the extremely short interaction timescale offered by heavy-ion collisions. These fluctuations exhibit specific shapes which generate characteristic anisotropies in the interaction region and the QGP. These anisotropies then generate observable signatures that can not be explained through mere model calibration: these shapes, as deeply hidden inside the nuclear wavefunction as they may be, have become necessary inclusions to theoretical frameworks seeking to understand heavy-ion collisions completely. Furthermore, historic tensions between low-energy pictures of nuclear structure and high-energy models and inferences have only just begun to be disambiguated [1, 36, 118]. By building on recent work using our fully-calibrated framework, we sought to help bridge the existing

gap and assist future low- and high-energy experiments in, at first, understanding the specifics of the underlying quantum states which make up the total nuclear wavefunction, and then providing properly constrained and verified nucleon density distributions which can be used to improve modern simulation calculations' agreement with experimental data and, in turn, enhance our understanding of nuclear and quark matter.

After thoroughly describing the theoretical and numerical framework we would be employing, we began our study by conducting a large-scale analysis of existing $^{238}$U and $^{197}$Au data from RHIC to establish our model's capabilities regarding simultaneous reproduction of a wide variety of observables via a single calibration. We also set out to determine how sensitive our model was to specific changes in nuclear parametrizations. To do so, we selected four parametrizations (two each) listed in Table 2. Critically, we used two largely deformed $^{238}$U parametrizations which presented subtle differences to one another and an undeformed and a deformed $^{197}$Au parametrization. Then, following an initial calibration against experimental charged particle multiplicity curves [105], we generated a statistically significant set of central to semi-peripheral events for our two systems. From there, we were able to reproduce available fundamental observables such as identified particle yields, mean transverse momentum, and scaled multiplicity. We found that, while our model did lead to differences in calculated curves between parametrizations, large experimental error bars coupled to our model's thorough calibration meant that these more 'basic' observables could not shed light on which parametrizations were more appropriate than others. With only the basic observables in hand, then, one could not use the experimental data to determine whether an undeformed or a significantly deformed $^{197}$Au parametrization was more appropriate. The inclusion of more sensitive and involved observables changed that. Indeed, elliptic flow calculations showed that deformity was a key feature of an appropriate $^{197}$Au parametrization. It also showed that our model was extremely sensitive to initial state parametrizations, especially in central collisions; we found that the slightly less deformed New U parametrization performed noticeably better than the Prev U parametrization, overlapping the experimental results across the entirety of the relevant

centrality range. The fact that this parametrization came from recent low-energy estimates coupled to proper projection onto the nuclear density distributions sampled in our simulations [36] supported the idea that our framework could be used as a tool for determining credible ranges for various deformation parameters given its accuracy and sensitivity.

Although the elliptic flow provided ample observable evidence of our model's capabilities, we moved on to yet more observables. We determined that the 2-particle $p_T$ correlator (Eq. (4.25)) could not be reproduced without modifying our event averaging procedure. This entailed that short-range fluctuations and correlations dominated this observable, the first observable which we had found to be meaningfully sensitive to the inclusion or exclusion of such short-range fluctuations. We also established this observable's sensitivity to deformity; when comparing between our model's $^{197}$Au and $^{238}$U curves, we noted an increase in correlation in the ultra-central region of this observable, coupled to a considerable underestimate of the experimental curve for the undeformed $^{197}$Au curve. These features were also linked to system size.

Providing further support to our process, we shared a true prediction of our model for transverse-momentum-flow correlations (in Fig. 45), a prediction which ended up being validated by experimental data published after the fact (for $\rho(v_2\{2\}, \langle p_T \rangle)$). We noted the distinctions between the $^{197}$Au and $^{238}$U curves. While both Def Au and our two $^{238}$U parametrizations were deformed, the latter present much larger quadrupole deformation. This discrepancy, while responsible for more subtle differences in other observables, leads to a complete divergence of the curves based on collision system. As described in Section 4.3.5, $^{238}$U's large prolate deformation leads to an anticorrelation between elliptic flow and mean transverse momentum in collisions below the $\sim 7\%$ centrality mark. While both $^{238}$U parametrizations did reproduce the cross-over point, New U provided better agreement beyond that mark.

To complete those initial results, we looked at experimentally available ratios of previously analyzed observables. These ratios allowed us to compare our different parametrizations in a pair-wise manner. These comparisons' main contributions were

in cementing the fact that not only did $^{197}$Au need to present some form of quadrupole deformity, but that the deformity used in $^{197}$Au was insufficient, hinting at the fact that further analyses should be conducted with a more deformed parametrization of $^{197}$Au.

Following the success of the boost-invariant formulation of our model in describing all available experimental data accurately and in discriminating between different nuclear parametrizations, we moved on to results stemming from fully 3+1D runs of our model. Aiming to determine whether or not new sensitivities to nuclear structure could be extracted from longitudinal observables, we ran a much less studied system ($^{129}$Xe) at a much larger beam energy (5.44 TeV) to align ourselves with current experimental programs.

All of these results were produced using a boost-invariant simulation. Considering the sensitivities of most observables on nuclear configurations, we became interested in determining if the inclusion of longitudinal observables - through the use of a fully 3+1D version of our framework - could provide additional insights regarding observable dependencies on specific initial state anisotropies. Therefore, extending our successful analysis to 3+1D, using a smaller and much less constrained system ($^{129}$Xe) at a much larger beam energy (5.44 TeV).

The lack of pre-established firm constraints on $^{129}$Xe's Woods-Saxon parameters allowed us to probe a wide area of the quadrupole deformation space. Indeed, given we focused on a single system and collisions energy, we were able to produce statistically significant results for five different parametrizations, listed in Table 3. Given the relevance of the undeformed run in our $^{197}$Au runs, we opted to include a similarly undeformed parametrization in our $^{129}$Xe runs. The other parametrizations stemmed from low-energy experiments and calculations, aligned with our goal to probe as wide a combined range of $\tilde{\beta}_2^0$ *and* $\tilde{\beta}_2^2$ as possible.

Following the same steps as our initial analysis, our model reproduced the charged particle yields at mid-rapidity across all of our parametrizations and a centrality twice as large as that of our previous analysis. The rapidity-dependent yields were also reproduced, albeit with a noticeable and consistent overestimate of the yields in central

(0-20%) collisions away from mid-rapidity ($|\eta| > 1$). This overestimate was attributed to the envelope function used to normalize the longitudinal energy distributions at the interface between IP-Glasma and MUSIC. The scaled charged particle multiplicity was also plotted (Fig. 57), supporting the conclusions drawn in our first analysis that nuclear structure did not meaningfully affect particle production mechanisms across centralities.

Other basic observables were also reproduced, with a similar lack of conclusive power as those of our $^{238}$U and $^{197}$Au runs. Interestingly, the Xe.207 showed a suppression of identified particle momentum which we attributed to the size of the system being collided. A more thorough investigation of this effect could be worthwhile. However, even though the suppression was noticeable, all parametrizations still fell within the experimental error bars, nullifying any potential constraining power.

More predictive observables, such as the elliptic flow, were also shown. $v_2\{2\}$ once again allowed us to discriminate between our different parametrizations, determining on the one hand that $^{129}$Xe, much like $^{197}$Au, had to be deformed given Xe.0's - the undeformed parametrization - disagreement with experimental data. Furthermore, it suggested that Xe.185*, stemming from recent low-energy parametrizations, was the best match amongst our chosen parametrizations. The differential elliptic flow underlined the fact that, away from central collisions, the effects of nuclear structure are washed out by more definite and consistent anisotropies due to the increase of the impact parameter $b$. The rapidity-dependent anisotropic flows, on the other hand, held little discriminating power. Indeed, while the scale of the flow was reproduced at mid-rapidity, the evolution of the flow with rapidity was not captured accurately by our model, especially away from central collisions. While this hints at model-improvement opportunities, it also tells us that, in its current state, our model is unable to use the rapidity-dependent anisotropic flow to differentiate between nuclear parametrizations. Unsurprisingly, the decorrelation ratios $r_{n|n}$ were also unable to shed light on the specific structure of $^{129}$Xe, with calculated curves fluctuating and congregating across the entirety of the $\eta$ range.

While our comparisons to multi-particle $p_T$ correlators had been promising in our initial, boost-invariant analysis, the lack of experimental data for specific $n$-particle correlators in $^{129}$Xe collisions forced us to overlook a potentially-predictive observable. Instead, we compared to the standardized skewness $\gamma_{\langle p_T \rangle}$. The sparse experimental data combined to our fairly large error bars inhibited the potential predictive power of this observable. Nevertheless, it did seem like Xe.185* was once again preferred by our model and the experimental data.

Using our five distinct parametrizations, we were able to paint a better picture of how transverse-momentum-elliptic-flow correlations are affected by differences in nuclear parametrizations, and if the cross-over to anticorrelation in central collisions occurs smoothly with increasing quadrupole deformation. Indeed, we were able to determine that quadrupole deformation and triaxiality were insufficient to fully understand the behavior of the correlator, and that considerations of system size and other structure properties were also involved in the development of transverse-momentum-elliptic-flow correlations. Nevertheless, it did, much like the $^{238}$U curves in our previous analysis, provide great discriminating power between our parametrizations, clearly favoring the Xe.185* parametrization in the central region.

Using this wealth of calculations, we were able to provide firm constraints for $\tilde{\beta}_2^0$ and $\tilde{\beta}_2^2$, the deformation parameters modulated during our analysis. Indeed, building on work presented in Ref. [120], we showed that our model could be used to extract specific values and errors for these parameters based on simulated results and comparisons to experiment. We showed that the inclusion of an undeformed parametrization greatly simplified the fitting procedure and improved constraints, providing a solid baseline from which deformation effects could be seen as emerging. Our fitted parameters for $^{129}$Xe were $\tilde{\beta}_2^0 = 0.170 \pm 0.033$ and $\tilde{\beta}_2^2 = 0.057 \pm 0.010$, which are consistent with Xe.185*'s parametrization. These constraints can be used to motivate and guide future runs using parametrizations stemming from a much smaller parameter space, further constraining $^{129}$Xe's shape through similar methods.

Our model, composed of IP-Glasma, MUSIC, iSS and SMASH, can therefore be used to differentiate and constrain nuclear parametrizations. We have also shown that it is simultaneously capable of reproducing critical observables which rely on physics which are foundational to our understanding of QCD and of nuclear physics at large. Furthermore, the excellent agreement with experimental data demonstrated by our framework across many systems and collision energies shows that our approach, while demanding computationally, generates reliable phenomenological insights using entirely physically-motivated simulations which are open to improvements with our understanding of fundamental physics. In this sense, our methodology truly bridges the existing gap between low-energy and high-energy nuclear physics, as our constraints on the realms of quark matter intrinsically rely on our deep understanding of low-energy nuclear structure; furthering one inevitably leads to a better understanding of the other.

While the work presented in this thesis is complete, self-consistent and provides significant improvements on methods used previously, it does allow for both improvements and extensions. First, our $^{197}$Au results; while we did prove that this nucleus is deformed, the deformation parameters used in our analysis led to underestimates of $v_2\{2\}$, the observable most sensitive to quadrupole deformation. Using the same process as we developed for $^{129}$Xe, we could conduct a system-specific calibration and a set of runs using parametrizations which span the credible deformation parameter space for $^{197}$Au, which would allow us to set strong constraints on its shape. The availability of experimental data for both the 2- and 3-particle $p_T$ correlators would provide added constraints to both $\tilde{\beta}_2^0$ and $\tilde{\beta}_2^2$. Secondly, an independent re-calibration of the $\eta$ envelope used in our 3+1D simulations could certainly help improve longitudinal observables. Indeed, our calculations ended up consistently overestimating the yields in collisions away from mid-rapidity ($|\eta| > 1$). While our curves fell within the experimental error bars, the yield overestimates point to a more fundamental problem related to the envelope: longitudinal slices away from mid-rapidity contain too much energy. This extra energy, distributed throughout the stress-energy tensor $T^{\mu\nu}$, has effects on other longitudinally-dependent observables, such as $v_2\{2\}(\eta)$. Indeed, more energetic longitudinal slices

will spend comparatively more time in the hydrodynamic phase, allowing for flow to develop more than if they had had less energy. Therefore, re-calibrating the $\eta$ envelope to properly contain the sources of errors in our longitudinal observables would be an important step in a future extension. Finally, related to this last point, an improvement of our understanding of the sources of longitudinal decorrelations is paramount to decidely ruling out $r_{n|n}$ and $v_n\{2\}(\eta)$ as observables sensitive to nuclear structure. Given our model's poor performance against these observables, it is impossible to determine if when all sources of decorrelation are taken into account our model's calculation will behave similarly. Therefore, while our model's current iteration suggests that longitudinal observables do not offer added insights regarding early-stage properties, future work will be required to modify our model so that it encompasses most primary sources of longitudinal decorrelations appropriately.

This thesis significantly advances the field of heavy-ion collision research. By improving and pioneering novel methods in high-energy nuclear physics simulations, it provides useful and accurate estimates of the fundamental geometric properties of atomic nuclei. The simulation framework and large-scale data analysis and comparison described in this thesis sets a new standard in bridging low-energy estimates of nuclear properties and high-energy experimental data.

The production of strongly-interacting matter in terrestrial colliders is a remarkable achievement, akin to recreating the conditions of the early universe. Inferring its properties along with those of stable nuclear matter is a complex task. This thesis contributes significantly to our understanding of the building blocks of matter, their different states and how the rules guiding their interactions change through phase space. As research continues and new physical insights emerge, our knowledge of hot QCD matter will undoubtedly deepen. This thesis represents a milestone in this ongoing journey.

# APPENDIX: CALCULATIONS AND SANITY CHECKS

# A

# GAUGE THEORY CLARIFICATIONS

## A.1 MOTIVATING GAUGE LINKS

When in Section 3.3.1 we introduced the following ansatz for the gauge links

$$U(x) = \exp\left(igaA_\mu^a(x)t^a\right) \tag{A.1}$$

we did not provide many first-principles explanations for this specific choice. In that same chapter, we established how this choice produces neat relationships which can lead to the extraction of useful physical quantities, such as the field strength tensor $F^{\mu\nu}$, through products of adjacent links. This choice is much more fundamental than our lack of explicit explanation in the body of the thesis let on.

Let us define $\Psi(x)$, a complex Dirac field representing some particle. Gauge theories require invariance under specific local transformations, such as

$$\Psi(x) \to \exp(i\alpha(x))\Psi(x) \tag{A.2}$$

where $\alpha(x)$ is some local phase space rotation. $\Psi(x)$'s derivatives must also be invariant under gauge transformations, complicating things. Indeed, given that the phase space rotations $\alpha(x)$ may vary locally, defining an invariant derivative is not trivial. Explicitly, starting from a basic formulation of $\Psi$'s derivative at some point $x$, we have

$$n^\mu \partial_\mu \Psi(x) = \lim_{\epsilon \to 0} \frac{\Psi(x+\epsilon n) - \Psi(x)}{\epsilon} \tag{A.3}$$

where $n^\mu$ is some four-vector introducing a small change in every allowed direction. Obviously, based on Eq. (A.2), $\Psi(x+\epsilon n)$ and $\Psi(x)$ can (and most probably will)

have incurred different transformations. We, therefore, need to introduce terms to take these different transformations into account. To do so, the gauge link $U$ is introduced. Formally, it links to points in spacetime such that their transformations are connected, ensuring that our field at different places is comparable. When transformed, the gauge link becomes

$$U(x,y) \to \exp(i\alpha(x))U(x,y)\exp(-i\alpha(y)). \tag{A.4}$$

By definition, $U(x,x) = 1$. Using this link, we can make it so that $\Psi(x)$ and $U(x,y)\Psi(y)$ transform in the same way under gauge transformations. Indeed, the $\exp(-i\alpha(y))$ term will cancel the corresponding $\exp(i\alpha(y))$ rotation from $\Psi(y)$'s transformation, leaving only $\exp(i\alpha(x))$ as the rotation. Incorporating the gauge link, the previous simple derivative can finally be taken, i.e.

$$n^\mu D_\mu \Psi(x) = \lim_{\epsilon\to 0} \frac{\Psi(x+\epsilon n) - U(x+\epsilon n, x)\Psi(x)}{\epsilon}. \tag{A.5}$$

Under gauge transformations, both $\Psi(x+\epsilon n)$ *and* $U(x+\epsilon n, x)\Psi(x)$ transform in the same way (i.e. they both gain an $\exp(i\alpha(x+\epsilon n))$ term), allowing us to take the difference between these two quantities in a meaningful and consistent way. In QCD, the gauge link $U_\mu(x)$ is defined as

$$U_\mu(x) = \mathcal{P}\exp\left(ig\int_{x_i}^{x_{i+1}} dx^\mu A^a_\mu(x)t^a\right) \approx \exp\left(igA^a_\mu(x)t^a\right) \tag{A.6}$$

which is the same form used in this thesis. In IP-Glasma, the only evolve fields are the color gauge fields themselves, meaning that there are not any Dirac fields to transform from lattice site to lattice site, explaining why the gauge links themselves are the only degrees of freedom in our theory and, finally, resolve this tension.

## A.2 NUMERICAL ERRORS IN IP-GLASMA

In simulations, numerical errors must be treated carefully to ensure results' reliability. This short section will list the most significant error terms found in different expansions

used in IP-Glasma. We begin with the gauge link itself. Expanding the exponential, we have

$$U_\mu(x) \approx 1 + igaA^a_\mu(x)t^a - g^2a^2A^a_\mu t^a A^b_\mu t^b + O(a^3) \tag{A.7}$$

where we keep only terms up to quadratic order as those are relevant for the calculation of the plaquettes (see Eq. (3.80) and Fig. 21). Therefore, in our simulations, the gauge links themselves carry an inherent $O(a^3)$ error, which leads to $O(10^{-6}\,\text{fm})$ given we used $a = 0.05\,\text{fm}$ in our runs. By extension, $F^{\mu\nu}$ will carry a similar error, while the squared field strength tensor - a critical component of the stress-energy tensor $T^{\mu\nu}$ - will carry a much smaller error, $O(a^6) \approx O(10^{-12}\,\text{fm})$. Then, the choice of the lattice spacing considerably affects the reliability of the results produced by IP-Glasma.

Related to these errors on the gauge links are so-called lattice effects, which come from our use of a discrete space to approximate our continuous universe. These effects are related to the resolution of the saturation scale $Q_s$ in the transverse plane. Indeed, it is understood that if the saturation scale in relevant interaction areas strays away from a range set by the physical extent of the lattice, errors driven by our lattice's poor resolution outside of this $Q_s$ range will matter. This range is

$$\frac{1}{L} \leq Q_s \leq \frac{1}{a} \tag{A.8}$$

where $a$ is the lattice spacing defined previously, and $L$ is the linear extent of the lattice in the transverse plane. These resolution considerations are critical in 3+1D, where the JIMWLK evolution evolves the saturation scale across a wide rapidity range, leading to a fairly wide range of probed saturation scales for any given event. The parameters used in our simulations lead to

$$0.01\,\text{GeV} \leq Q_s \leq 3.5\,\text{GeV}. \tag{A.9}$$

To ensure that the values of $Q_s$ probed within our simulations remain well within this range, we had to limit the rapidity range of our longitudinal evolution to $|y| \leq 4.0$. Therefore, lattice effects must be carefully considered when determining an appropriate parameter set for IP-Glasma.

Finally, derivatives taken in our derivations of the equations of motion on the lattice introduce errors. As a numerical simulation, IP-Glasma approximates derivatives using different techniques that depend on the differentiated functions' properties. While the code employs all best practices, unstable functions, such as those describing the gauge fields from site to site at early times (i.e. following the color charge density sampling) can produce considerable errors that must be considered. These early-time errors, for example, are dealt with by utilizing minimal time steps at early time to avoid large temporal derivatives and improve stability.

# B

# DETAILS OF NUMERICAL SIMULATIONS

## B.1 CONVERTING SPATIAL ANISOTROPY INTO ANISOTROPIC FLOW

We have already discussed at length the direct dependence momentum anisotropies have on initial state (or geometric) anisotropies. We have explained how asymmetric interaction regions lead to uneven buildups of flow, which, in turn, generate flow imbalances in the QGP, culminating in detectable anisotropies in the distributions of particles which are generated in a given collision. While we have defined momentum anisotropy thoroughly, we have not yet discussed the spatial anisotropy $\varepsilon_n$. It is given by [139]

$$\varepsilon_n = \frac{d^2x\, r^n \epsilon(\vec{x}_\perp) e^{in\phi}}{d^2x\, r^n \epsilon(\vec{x}_\perp)}, \tag{B.1}$$

where $\epsilon$ is the energy density and $\phi$ is the azimuthal angle, the same angle used in anisotropic flow calculations. The energy density's role in this observable is a weighting function: more energetic parcels of the glasma have more weight in the final calculated value. Therefore, this calculation differs significantly from simply extracting the general shape of the overlap area (much like we did qualitatively in Chapter 2), determining that it is anisotropic and positing that this anisotropy will have some effect on the final state. The inclusion of the energy density as a weight function here takes into account that energy imbalances are what drive anisotropic flow at a fundamental level; the shape of the overlap region has a large impact *if* we assume that the energy anisotropies match the pure spatial anisotropies exhibited by the overlap region, which is generally the case.

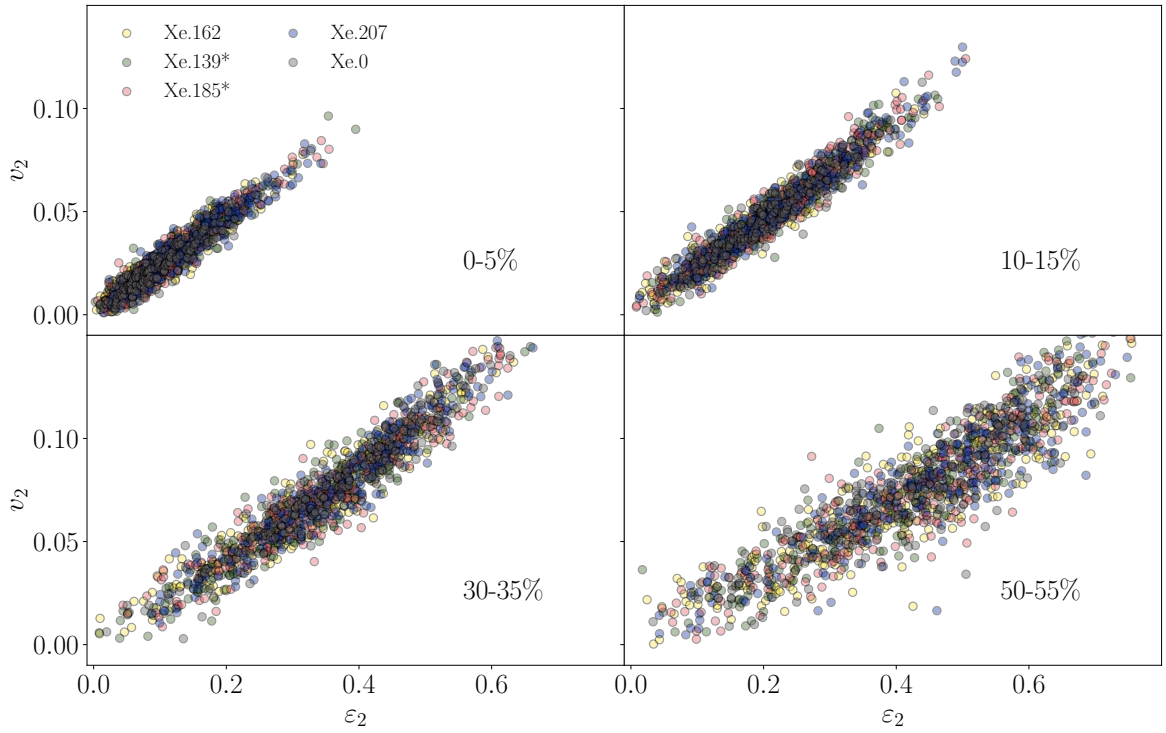


Figure 73: Event-by-event elliptic flow $v_2$ as a function of initial state ellipticity $\varepsilon_2$ for various narrow centrality slices in Xe+Xe collisions. All $^{129}$Xe parametrizations used are represented. All axes have the same scale to better demonstrate the correlation between these quantities.

Eq. (B.1)'s quantitative measure of initial state anisotropy can help us further cement the direct relationship between the shape of atomic nuclei and the momentum anisotropies presented by final-state particles. Figure 73 shows the $n = 2$ component of spatial anisotropy - the ellipticity - plotted against the event-by-event elliptic flow $v_2$. The four panels present four different narrow centrality slices. We find that, across all centrality slices, the correlation is robust and fairly consistent, with a slight dip in our most peripheral (50-55%) slice. In general, we write

$$v_n = \kappa_n \varepsilon_n$$

to showcase the linear dependency of the observable anisotropic flow on the spatial anisotropy of the initial state. We find $\kappa_2 \sim 0.23$ in our three most central slices, while our most peripheral slice yields $\kappa_2 = 0.18$. This smaller coefficient is explained as the

sum of multiple effects. Firstly, as is evident in Fig. 73, the distributions of both $v_2$ *and* $\varepsilon_2$ are much wider in peripheral events, weakening the correlation. Secondly, at a more interesting level for our stated goals of characterizing exotic nuclear matter, this dip in the coefficient is explained by the progressive breakdown of the applicability of our hydrodynamic framework in peripheral collisions. Indeed, the $\kappa_n$ coefficients are highly dependent on the parameters of the hydrodynamic evolution, such as the bulk and shear viscosities. This makes sense since, by definition, they measure how well initial state anisotropies are transferred into final state anisotropies via the hydrodynamic phase. Hydrodynamics therefore acts as a signal carrier, and both the shear and bulk viscosities play an important role in determining how much information from the initial state is encoded in the observed particle distributions. Therefore, as we move towards events where the hydrodynamic phase becomes less and less long-lived and applicable, we find that our events transform less and less initial state anisotropy into final state anisotropy.

Figure 73 simultaneously confirms that initial state ellipticity drives final-state elliptic flow and that the hydrodynamic evolution is critical to converting these geometric initial state properties into coherent final-state signals. One can (and should) wonder if and how this $\kappa_2$ coefficient changes when we move from 3D to 2D. Turning our attention to Fig. 74, we find the same striking correlation as before, with the New U and Def Au distributions overlapping considerably. Quantitatively, we find $\kappa_2^{\mathrm{U}} \sim 0.175$ and $\kappa_2^{\mathrm{Au}} \sim 0.185$. This slight difference in the correlation coefficients is mainly driven by the larger width of the $^{238}$U $\varepsilon_2$ distributions and by the slightly larger collision energy used for the $^{197}$Au events (193 GeV for $^{238}$U vs. 200 GeV for $^{197}$Au). This larger collision energy will inevitably lead to more energy being deposited in the transverse plane, leading to a longer hydrodynamic evolution *and* a more coherent signal of the initial state ellipticity in the final state. This difference in beam energy will also drive most of the differences between the $\kappa_2$ extracted from our 2D and 3D simulations; related to this, the fact that our proportionality constant $C$ (see Eq. (3.33)) is almost three times greater for our $^{129}$Xe runs as it was for our $^{238}$U and $^{197}$Au runs most certainly

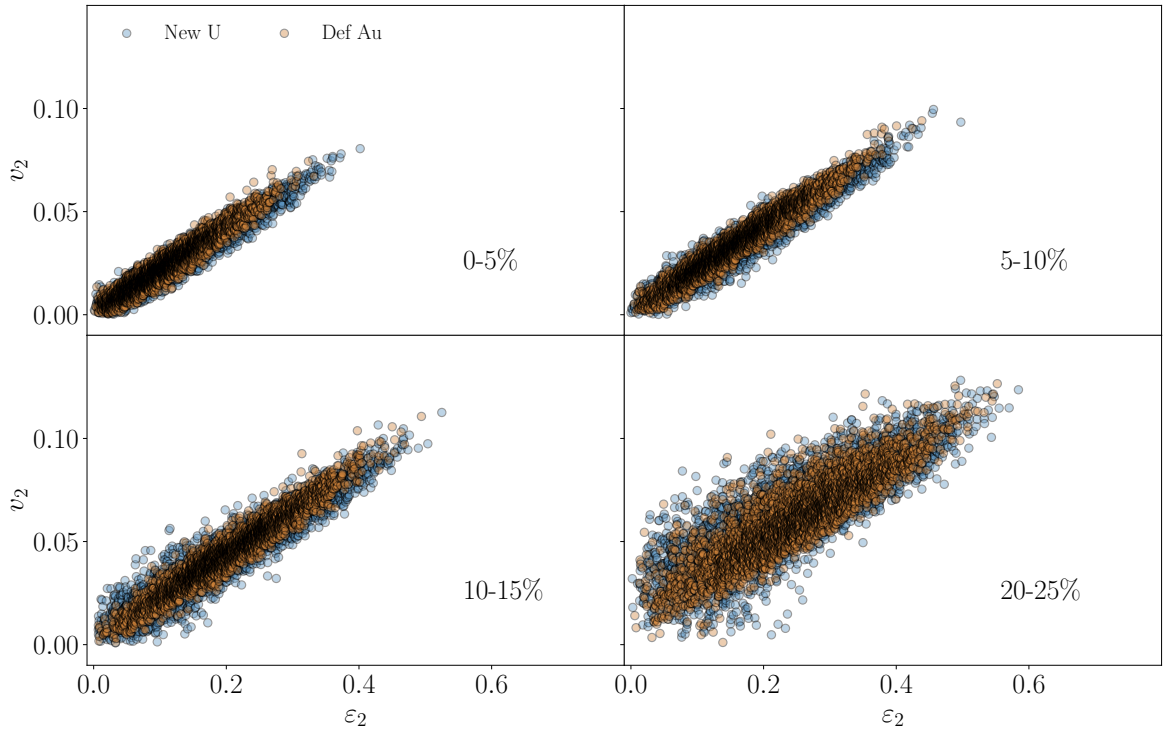


Figure 74: Event-by-event elliptic flow $v_2$ as a function of initial state ellipticity $\varepsilon_2$ for various narrow centrality slices in U+U and Au+Au collisions. Only two parametrizations of $^{238}$U and $^{197}$Au are represented. All axes have the same scale to better demonstrate the correlation between these quantities. Furthermore, the same scaling as Fig. 73 is preserved to enable more relevant comparisons between the figures.

plays a role, as it modifies how efficiently the saturation scale $Q_s$ is transformed into color charge fluctuations, which greatly affects the properties of the initial state and of its spatial anisotropy (because of our weighing by energy density $\epsilon$).

Even though we have found that triangular flow $v_3$ does not provide much discriminatory information for our nuclear shape extractions, it can be interesting to see how initial state triangularity is distributed against triangular flow. Figure 75 shows triangular flow plotted against triangularity for Xe+Xe collisions. We find a strong correlation between the spatial anisotropy and its corresponding anisotropic flow coefficient in central collisions. Interestingly, the distribution of triangularities in central events is fairly narrow. This is consistent with our underestimation of this observable across the centrality spectrum and energy spectrum: because triangular flow is driven by fluctu-

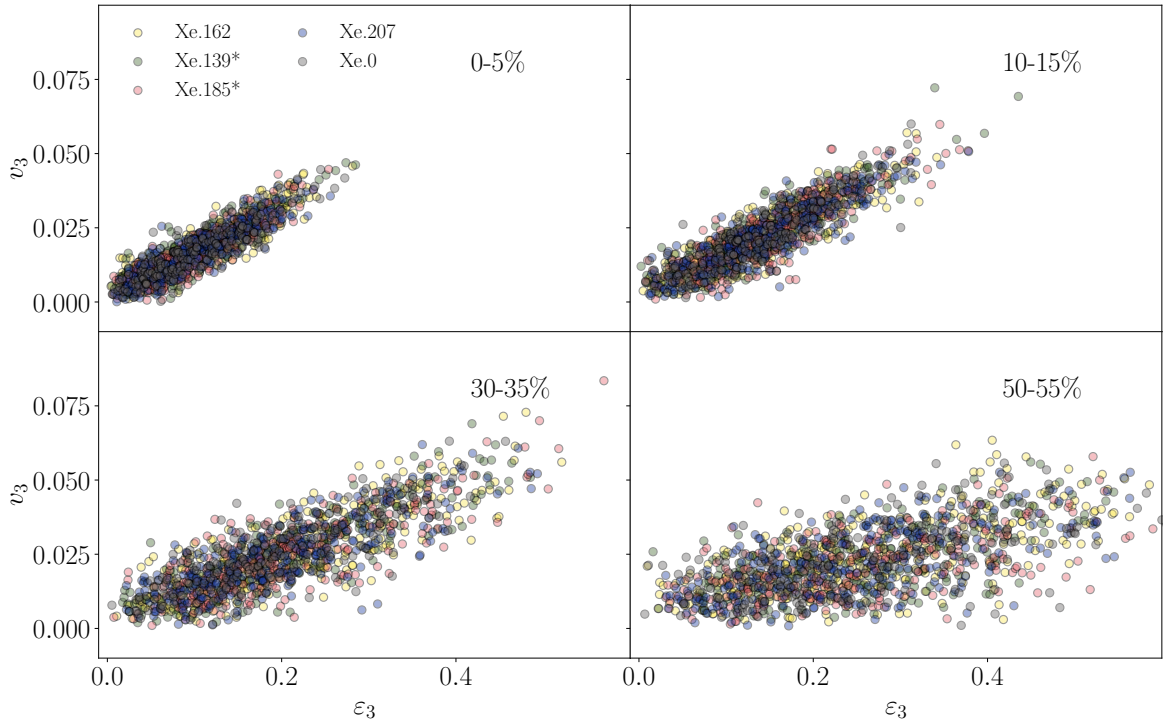


Figure 75: Event-by-event triangular flow $v_3$ as a function of initial state triangularity $\varepsilon_3$ for various narrow centrality slices in U+U and Au+Au collisions. All $^{129}$Xe parametrizations used are represented. All axes have the same scale to better demonstrate the correlation between these quantities.

ations, having too narrow of a triangularity distribution entails that we underestimate fluctuations in triangularity. As mentioned previously, this could be mended by the inclusion of sub-nucleonic degrees of freedom in the initial state. These quark hot spots would create more fluctuations in the energy density distribution $\epsilon(\vec{x}_\perp)$, widening our distribution and generating more triangular flow. In the more peripheral bins, our triangularity distribution widens and, consequently, we generate much more triangular flow. Referring back to Fig. 63, we see that our curves match the experimental curves better as we move to more peripheral collisions, consistent with what we observe in Fig. 75. Finally, $\kappa_3$ decreases much faster than $\kappa_2$ across the same centrality spectrum, going from $\kappa_3 \sim 0.145$ for 0-5% and 10-15% to $\kappa_3 \sim 0.1$ and 0.06 for 30-35% and 50-55% respectively. This captures both the fluctuation-driven nature of this observable *and* the role of the hydrodynamic evolution in allowing these signals to form: the faint

nature of the triangularity as an initial state signal requires more time to form in the hydrodynamics phase, meaning that it becomes less coherent quicker as we move to more peripheral collisions.

## B.2 LONGITUDINAL CORRELATIONS IN THE INITIAL STATE

When analyzing the longitudinal dependency of anisotropic flow in Chapter 7, we determined that our model did not seem to incorporate enough sources of decorrelations, leading to an overestimate of the anisotropic flow at large absolute rapidities. We shared avenues for improvement, ranging from including mini-jets in the evolution to including explicit rotational decorrelations before the hydrodynamic evolution. These missing components make it hard to determine whether or not the JIMWLK evolution introduces sufficient decorrelations into our model.

The JIMWLK evolution induces explicit decorrelations by including the noise terms $\zeta_i^a$ described in Eq. (6.11). These noise terms are random variables which serve as corrections to the color charges sourcing the classical gluon fields; they represent the stochastic (or random) nature of gluon emission and absorption, ensuring that the different color charge components are sufficiently decorrelated within a slice and from slice to slice. Looking at Eq. (6.10), we also find that the exponentials on both sides of $V(\vec{x}_\perp, Y)$ contain factors of $\sqrt{\mathrm{d}y}$, the longitudinal extent of our slices. This rapidity step factor is intrinsically related to the correlators $\zeta$ [122], and, actually, the scale of the stochastic term in Eq. (6.10) is proportional to $\sqrt{\mathrm{d}y}$. Therefore, choosing the extent of each rapidity slice in our simulations is no trivial matter, as it can directly affect correlations between slices. The JIMWLK evolutions assume a small enough rapidity step d$y$ to allow for expansions of the stochastic terms up to second order. However, each longitudinal slice is the equivalent of one 2D simulation; choosing a small longitudinal step may be safe, but it inevitably leads to rapidly increasing computational costs which complicate the types of large-scale analyses we are interested in.

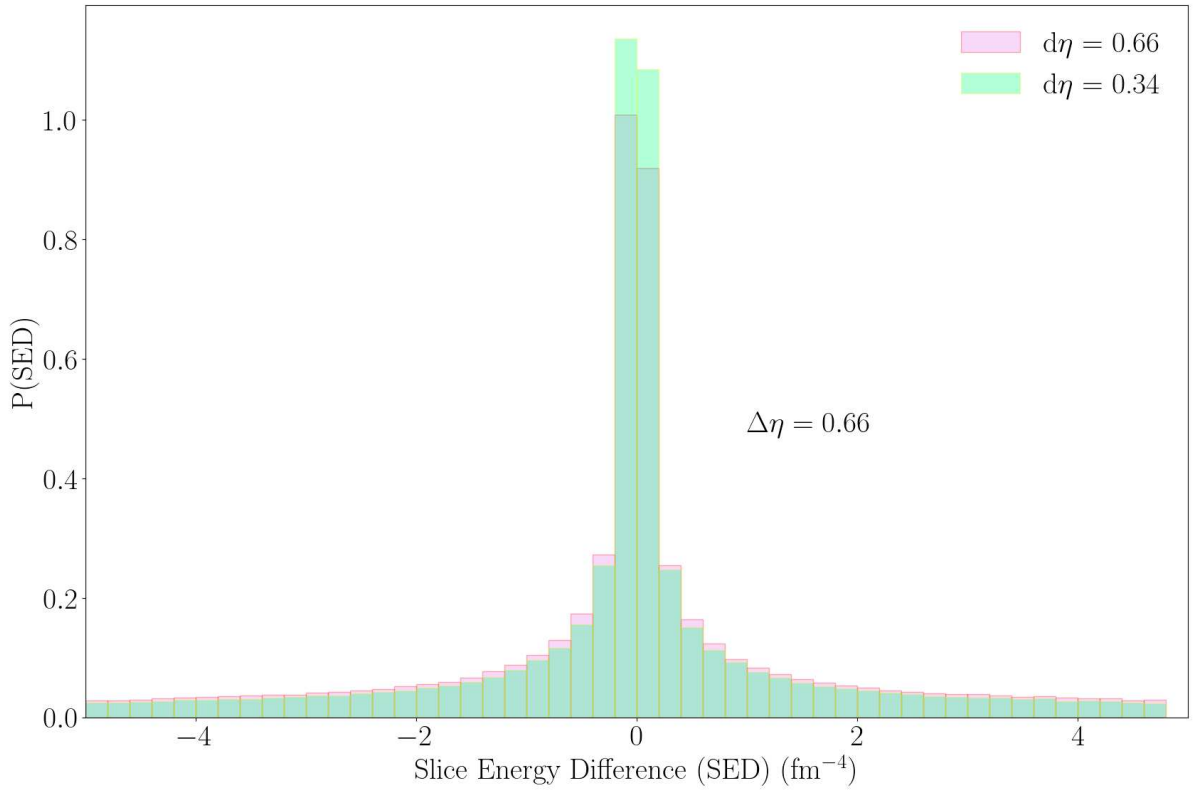


Figure 76: Distribution of the cell-to-cell difference in energy density between slices separated by $\Delta\eta = 0.66$, which is one longitudinal step using $d\eta = 0.66$ and two steps using $d\eta = 0.33$.

At the onset of our $^{129}$Xe runs, we decided to conduct a quantitative test comparing slice-to-slice correlations in the initial state energy density configurations of fixed-seed events (i.e. events which collide the exact same nuclei) stemming from a 'fine' $d\eta = 0.33$ and a 'coarse' $d\eta = 0.66$ implementation of our longitudinal steps. Our thought process was that if both distributions of cell-to-cell differences were similar from one setting to the other, the coarser implementation would be appropriate for our needs.

Figure 76 shows the distribution of differences in energy density for slices separated by $\Delta\eta = 0.66$, constituting a single and a double step for our finer and coarser configurations respectively. The differences are taken on a cell-to-cell basis: the energy density of the cell at $(x, y, \eta_0)$ is subtracted from that of the cell at $(x, y, \eta_1)$, providing an idea of how slice-to-slice differences are distributed. As is evident from Fig. 76, no meaningful difference exists between the two IP-Glasma configurations; if anything, the smaller $\eta$

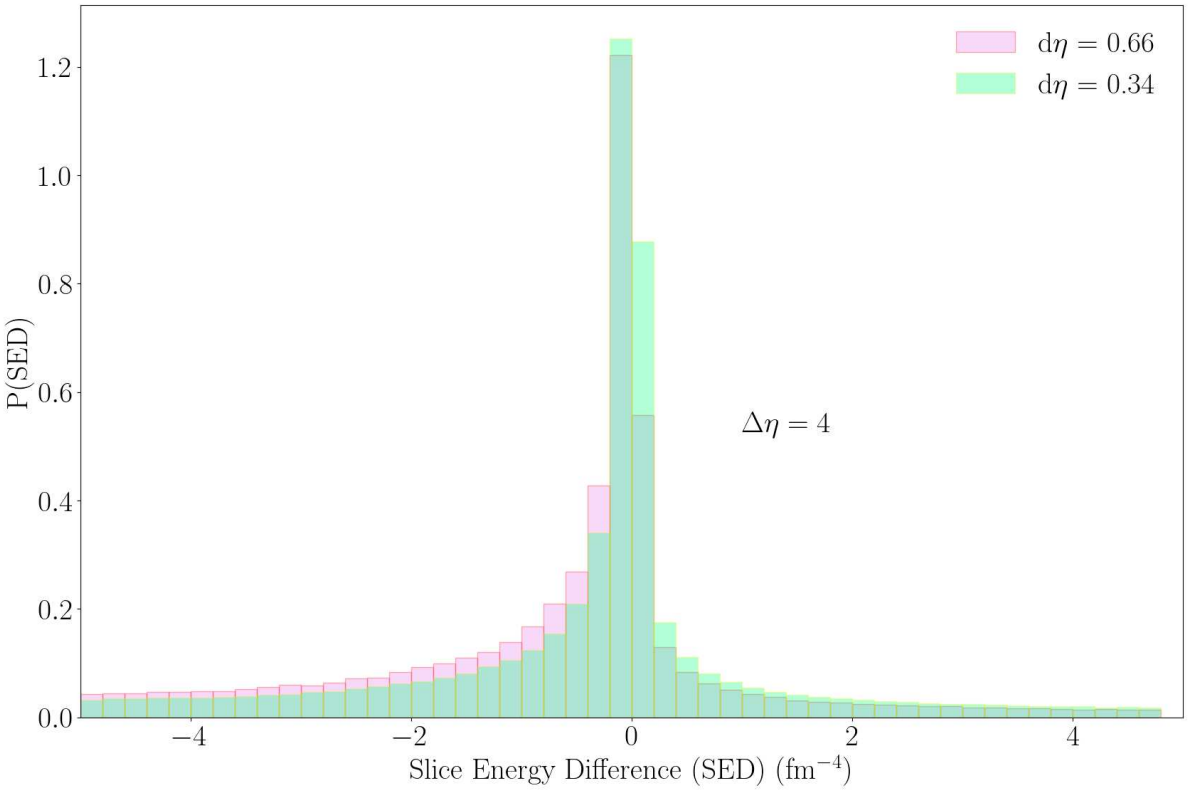


Figure 77: Distribution of the cell-to-cell difference in energy density between slices separated by $\Delta\eta = 4$, which is six longitudinal steps using $d\eta = 0.66$ and twelve steps using $d\eta = 0.33$.

steps seem to provide slightly larger correlations given the larger peak in the probability density around 0. We analyzed differences stemming from larger $\eta$ gaps to ensure that we were not overlooking larger-scale effects. Figure 77 shows the distribution of differences for both configurations stemming from slices separated by a large $\eta$ gap, namely $\Delta\eta = 4$. Once again, both distributions are remarkably similar given the analysis we conducted: once again, the smaller $\eta$ step seems to provide slightly less decorrelations given the the relationship between the two probability densities around 0. The negative skew of these distributions is because we are subtracting slices at mid-rapidity from slices at large $\eta$, which naturally have less energy density than those at mid-rapidity given the nature of the JIMWLK evolution.

Based on Figs. 76 and 77, we decided to use a coarser ($d\eta = 0.66$) longitudinal configuration for IP-Glasma, which greatly improved our computational efficiency on an event-by-event basis.

# BIBLIOGRAPHY


[1] Nicolas Fortier, Sangyong Jeon, and Charles Gale. *Comparisons and Predictions for Collisions of deformed $^{238}U$ nuclei at $\sqrt{s_{NN}}$ = 193 GeV*. 2024. arXiv: 2308.09816 [nucl-th].

[2] James Chadwick. "The existence of a neutron." In: *Proceedings of the Royal Society of London. Series A, Containing Papers of a Mathematical and Physical Character* 136.830 (1932), pp. 692–708. DOI: 10.1098/rspa.1932.0112. eprint: https://royalsocietypublishing.org/doi/pdf/10.1098/rspa.1932.0112. URL: https://royalsocietypublishing.org/doi/abs/10.1098/rspa.1932.0112.

[3] Arthur Eddington. "The Source of Stellar Energy." In: *Nature* 115.2890 (1925), pp. 419–420. ISSN: 1476-4687. DOI: 10.1038/115419c0. URL: https://doi.org/10.1038/115419c0.

[4] Hideki Yukawa. "On the Interaction of Elementary Particles I." In: *Proceeding of the Physico-Mathematical Society of Japan* 17 (1935), pp. 48–57. DOI: 10.1143/PTPS.1.1.

[5] Sidney Drell, Donald Levy, and Tung-Mow Yan. "Theory of Deep-Inelastic Lepton-Nucleon Scattering and Lepton-Pair Annihilation Processes. I." In: *Physical Review* 187 (5 1969), pp. 2159–2171. DOI: 10.1103/PhysRev.187.2159. URL: https://link.aps.org/doi/10.1103/PhysRev.187.2159.

[6] Murray Gell-Mann. "Symmetries of Baryons and Mesons." In: *Physical Review* 125 (3 1962), pp. 1067–1084. DOI: 10.1103/PhysRev.125.1067. URL: https://link.aps.org/doi/10.1103/PhysRev.125.1067.

[7] V. Khachatryan et al. "Measurement of the inclusive 3-jet production differential cross section in proton–proton collisions at 7 TeV and determination of the strong coupling constant in the TeV range." In: *The European Physical Journal C* 75.5 (May 2015). ISSN: 1434-6052. DOI: 10.1140/epjc/s10052-015-3376-y. URL: http://dx.doi.org/10.1140/epjc/s10052-015-3376-y.

[8] Claudia Ratti and Rene Bellwied. *The Deconfinement Transition of QCD: Theory Meets Experiment*. Vol. 981. Lecture Notes in Physics. June 2021. ISBN: 978-3-030-67234-8, 978-3-030-67235-5. DOI: 10.1007/978-3-030-67235-5.

[9] Jana N. Guenther. *Overview of the QCD phase diagram – Recent progress from the lattice*. 2021. arXiv: 2010.15503 [hep-lat]. URL: https://arxiv.org/abs/2010.15503.

[10] The DOE/NSF Nuclear Science Advisory Committee. *The Frontiers of Nuclear Science, A Long Range Plan*. 2008. arXiv: 0809.3137 [nucl-ex]. URL: https://arxiv.org/abs/0809.3137.

[11] Tanmoy Bhattacharya et al. "QCD Phase Transition with Chiral Quarks and Physical Quark Masses." In: *Physical Review Letters* 113 (2014), p. 082001.

[12] S. Chatrchyan et al. "Centrality dependence of dihadron correlations and azimuthal anisotropy harmonics in PbPb collisions at $\sqrt{s_{NN}}$ = 2.76 TeV." In: *The European Physical Journal C* 72.5 (May 2012). ISSN: 1434-6052. DOI: 10.1140/epjc/s10052-012-2012-3. URL: http://dx.doi.org/10.1140/epjc/s10052-012-2012-3.

[13] J. C. Collins and M. J. Perry. "Superdense Matter: Neutrons or Asymptotically Free Quarks?" In: *Physical Review Letters* 34 (21 1975), pp. 1353–1356. DOI: 10.1103/PhysRevLett.34.1353. URL: https://link.aps.org/doi/10.1103/PhysRevLett.34.1353.

[14] Wit Busza, Krishna Rajagopal, and Wilke van der Schee. "Heavy Ion Collisions: The Big Picture and the Big Questions." In: *Annual Review of Nuclear and Particle Science* 68.1 (2018), pp. 339–376. ISSN: 1545-4134. DOI: 10.1146/annurev-nucl-101917-020852. URL: http://dx.doi.org/10.1146/annurev-nucl-101917-020852.

[15] S. Hilaire and M. Girod. "The AMEDEE Nuclear Structure Database." In: *AIP Conference Proceedings* 1012.1 (May 2008), pp. 359–361. ISSN: 0094-243X. DOI: 10.1063/1.2939329. eprint: https://pubs.aip.org/aip/acp/article-pdf/1012/1/359/11892923/359_1_online.pdf. URL: https://doi.org/10.1063/1.2939329.

[16] Jia Liu, Chun Shen, and Ulrich Heinz. "Pre-equilibrium evolution effects on heavy-ion collision observables." In: *Physical Review C* 91 (6 2015), p. 064906. DOI: 10.1103/PhysRevC.91.064906. URL: https://link.aps.org/doi/10.1103/PhysRevC.91.064906.

[17] Scott McDonald, Sangyong Jeon, and Charles Gale. *The 3+1D initialization and evolution of the Glasma*. 2023. arXiv: 2306.04896 [hep-ph].

[18] Bjorn Schenke, Sangyong Jeon, and Charles Gale. "(3+1)D hydrodynamic simulation of relativistic heavy-ion collisions." In: *Physical Review C* 82.1 (2010). ISSN: 1089-490X. DOI: 10.1103/physrevc.82.014903. URL: http://dx.doi.org/10.1103/PhysRevC.82.014903.

[19] Sangwook Ryu, Jean-Fran çois Paquet, Chun Shen, Gabriel Denicol, Björn Schenke, Sangyong Jeon, and Charles Gale. "Effects of bulk viscosity and hadronic rescattering in heavy ion collisions at energies available at the BNL Relativistic Heavy Ion Collider and at the CERN Large Hadron Collider." In: *Physical Review C* 97 (3 2018), p. 034910. DOI: 10.1103/PhysRevC.97.034910. URL: https://link.aps.org/doi/10.1103/PhysRevC.97.034910.

[20] Paul Romatschke. "New Developments in Relativistic Viscous Hydrodynamics." In: *International Journal of Modern Physics E* 19.01 (2010), pp. 1–53. DOI: 10.1142/S0218301310014613. eprint: https://doi.org/10.1142/S0218301310014613. URL: https://doi.org/10.1142/S0218301310014613.

[21] J. Weil et al. "Particle production and equilibrium properties within a new hadron transport approach for heavy-ion collisions." In: *Physical Review C* 94 (2016), p. 054905.

[22] K. S. Egiyan et al. "Measurement of Two- and Three-Nucleon Short-Range Correlation Probabilities in Nuclei." In: *Physical Review Letters* 96 (8 2006), p. 082501. DOI: 10.1103/PhysRevLett.96.082501. URL: https://link.aps.org/doi/10.1103/PhysRevLett.96.082501.

[23] R. Shneor et al. "Investigation of Proton-Proton Short-Range Correlations via the $^{12}$C$(e, e'pp)$ Reaction." In: *Physical Review Letters* 99 (7 2007), p. 072501. DOI: 10.1103/PhysRevLett.99.072501. URL: https://link.aps.org/doi/10.1103/PhysRevLett.99.072501.

[24] R. Schiavilla, R. B. Wiringa, Steven C. Pieper, and J. Carlson. "Tensor Forces and the Ground-State Structure of Nuclei." In: *Physical Review Letters* 98 (13 2007), p. 132501. DOI: 10.1103/PhysRevLett.98.132501. URL: https://link.aps.org/doi/10.1103/PhysRevLett.98.132501.

[25] H De Vries, C W De Jager, and C De Vries. "Nuclear charge-density-distribution parameters from elastic electron scattering." In: *At. Data Nucl. Data Tables; (United States)* 36.1 (May 1987). DOI: 10.1016/0092-640X(87)90013-1.

[26] Lu-Meng Liu, Chun-Jian Zhang, Jun Xu, Jiangyong Jia, and Guang-Xiong Peng. "Free spectator nucleons in ultracentral relativistic heavy-ion collisions as a probe of neutron skin." In: *Physical Review C* 106.3 (2022). DOI: 10.1103/physrevc.106.034913. URL: https://doi.org/10.1103%2Fphysrevc.106.034913.

[27] Giuliano Giacalone, Govert Nijs, and Wilke van der Schee. *Determination of the neutron skin of $^{208}$Pb from ultrarelativistic nuclear collisions*. 2023. arXiv: 2305.00015 [nucl-th].

[28] Hannu Paukkunen. "Neutron skin and centrality classification in high-energy heavy-ion collisions at the LHC." In: *Physics Letters B* 745 (May 2015), 73–78. ISSN: 0370-2693. DOI: 10.1016/j.physletb.2015.04.037. URL: http://dx.doi.org/10.1016/j.physletb.2015.04.037.

[29] Luigi Coraggio, Saori Pastore, and Carlo Barbieri. "Editorial: The Future of Nuclear Structure: Challenges and Opportunities in the Microscopic Description of Nuclei." In: *Frontiers in Physics* 8 (2021). ISSN: 2296-424X. DOI: 10.3389/fphy.2020.626976. URL: https://www.frontiersin.org/articles/10.3389/fphy.2020.626976.

[30] Giuliano Giacalone. *A matter of shape: seeing the deformation of atomic nuclei at high-energy colliders*. 2021. arXiv: 2101.00168 [nucl-th]. URL: https://arxiv.org/abs/2101.00168.

[31] Giuliano Giacalone. "Observing the Deformation of Nuclei with Relativistic Nuclear Collisions." In: *Physical Review Letters* 124.20 (May 2020). ISSN: 1079-7114. DOI: 10.1103/physrevlett.124.202301. URL: http://dx.doi.org/10.1103/PhysRevLett.124.202301.

[32] Takashi Nakatsukasa, Kenichi Matsuyanagi, Masayuki Matsuo, and Kazuhiro Yabana. "Time-dependent density-functional description of nuclear dynamics." In: *Reviews of Modern Physics* 88.4 (Nov. 2016). ISSN: 1539-0756. DOI: 10.1103/revmodphys.88.045004. URL: http://dx.doi.org/10.1103/RevModPhys.88.045004.

[33] P. Ring and P. Schuck. *The Nuclear Many-Body Problem*. Physics and astronomy online library. Springer, 2004. ISBN: 9783540212065. URL: https://books.google.ca/books?id=PTynSM-nMA8C.

[34] A. Bohr and B.R. Mottelson. *Nuclear Structure: Volume Ii (nuclear Deformations)*. Nuclear Structure. Basic Books, 1969. ISBN: 9780805310160. URL: https://books.google.ca/books?id=dRhRAAAAMAAJ.

[35] Krishna Kumar. "Intrinsic Quadrupole Moments and Shapes of Nuclear Ground States and Excited States." In: *Physical Review Letters* 28 (4 1972), pp. 249–253. DOI: 10.1103/PhysRevLett.28.249. URL: https://link.aps.org/doi/10.1103/PhysRevLett.28.249.

[36] Wouter Ryssens, Giuliano Giacalone, Björn Schenke, and Chun Shen. "Evidence of Hexadecapole Deformation in Uranium-238 at the Relativistic Heavy Ion Collider." In: *Physical Review Letters* 130.21 (2023). DOI: 10.1103/physrevlett.130.212302. URL: https://doi.org/10.1103%2Fphysrevlett.130.212302.

[37] A. Poves, F. Nowacki, and Y. Alhassid. "Limits on assigning a shape to a nucleus." In: *Physical Review C* 101.5 (May 2020). ISSN: 2469-9993. DOI: 10.1103/physrevc.101.054307. URL: http://dx.doi.org/10.1103/PhysRevC.101.054307.

[38] Vittorio Somà. "From the liquid drop model to lattice QCD: A brief history of nuclear interactions." In: *The European Physical Journal Plus* 133.10 (Oct. 2018). ISSN: 2190-5444. DOI: 10.1140/epjp/i2018-12244-2. URL: http://dx.doi.org/10.1140/epjp/i2018-12244-2.

[39] Hilaire, S. and Girod, M. "Large-scale mean-field calculations from proton to neutron drip lines using the D1S Gogny force." In: *European Physics Journal A* 33.2 (2007), pp. 237–241. DOI: 10.1140/epja/i2007-10450-2. URL: https://doi.org/10.1140/epja/i2007-10450-2.

[40] E Grosse et al. "Collective Rotation of 238U at High Spins." In: *Physica Scripta* 24.1B (1981), p. 337. DOI: 10.1088/0031-8949/24/1B/033. URL: https://dx.doi.org/10.1088/0031-8949/24/1B/033.

[41] B. Pritychenko, M. Birch, B. Singh, and M. Horoi. "Tables of E2 transition probabilities from the first $2^+$ states in even–even nuclei." In: *Atomic Data and Nuclear Data Tables* 107 (Jan. 2016), 1–139. ISSN: 0092-640X. DOI: 10.1016/j.adt.2015.10.001. URL: http://dx.doi.org/10.1016/j.adt.2015.10.001.

[42] R.W. Hasse and W.D. Myers. *Geometrical Relationships of Macroscopic Nuclear Physics*. Computational Mechanics Publication. Springer-Verlag, 1988. ISBN: 9783540175100. URL: https://books.google.ca/books?id=esvvAAAAMAAJ.

[43] C. Loizides, J. Nagle, and P. Steinberg. "Improved version of the PHOBOS Glauber Monte Carlo." In: *SoftwareX* 1–2 (Sept. 2015), 13–18. ISSN: 2352-7110. DOI: 10.1016/j.softx.2015.05.001. URL: http://dx.doi.org/10.1016/j.softx.2015.05.001.

[44] Jean-Yves Ollitrault. "Anisotropy as a signature of transverse collective flow." In: *Physical Review D* 46 (1992), pp. 229–245.

[45] Michael L. Miller, Klaus Reygers, Stephen J. Sanders, and Peter Steinberg. "Glauber Modeling in High-Energy Nuclear Collisions." In: *Annual Review of Nuclear and Particle Science* 57.1 (Nov. 2007), 205–243. ISSN: 1545-4134. DOI: 10.1146/annurev.nucl.57.090506.123020. URL: http://dx.doi.org/10.1146/annurev.nucl.57.090506.123020.

[46] J. Scott Moreland, Jonah E. Bernhard, and Steffen A. Bass. "Alternative ansatz to wounded nucleon and binary collision scaling in high-energy nuclear collisions." In: *Physical Review C* 92.1 (July 2015). ISSN: 1089-490X. DOI: 10.1103/physrevc.92.011901. URL: http://dx.doi.org/10.1103/PhysRevC.92.011901.

[47] Charles Gale, Sangyong Jeon, Björn Schenke, Prithwish Tribedy, and Raju Venugopalan. "Event-by-event anisotropic flow in heavy-ion collisions from combined Yang-Mills and viscous fluid dynamics." In: *Physical Review Letters*

110.1 (2013), p. 012302. DOI: 10.1103/PhysRevLett.110.012302. arXiv: 1209.6330 [nucl-th].

[48] Scott McDonald, Chun Shen, Francois Fillion-Gourdeau, Sangyong Jeon, and Charles Gale. "Hydrodynamic predictions for Pb+Pb collisions at 5.02 TeV." In: *Physical Review C* 95.6 (2017). DOI: 10.1103/physrevc.95.064913. URL: https://doi.org/10.1103%2Fphysrevc.95.064913.

[49] Franç ois Gelis. "Initial state and thermalization in the Color Glass Condensate framework." In: *International Journal of Modern Physics E* 24.10 (2015), p. 1530008. DOI: 10.1142/s0218301315300088. URL: https://doi.org/10.1142%2Fs0218301315300088.

[50] Francois Gelis, Edmond Iancu, Jamal Jalilian-Marian, and Raju Venugopalan. "The Color Glass Condensate." In: *Annual Review of Nuclear and Particle Science* 60.1 (2010), pp. 463–489. ISSN: 1545-4134. DOI: 10.1146/annurev.nucl.010909.083629. URL: http://dx.doi.org/10.1146/annurev.nucl.010909.083629.

[51] Larry McLerran. *The Quark Gluon Plasma and The Color Glass Condensate: 4 Lectures*. 2003. arXiv: hep-ph/0311028 [hep-ph]. URL: https://arxiv.org/abs/hep-ph/0311028.

[52] A. H. Mueller. *Small-x Physics, High Parton Densities and Parton Saturation in QCD*. 1999. arXiv: hep-ph/9911289 [hep-ph]. URL: https://arxiv.org/abs/hep-ph/9911289.

[53] Larry McLerran and Raju Venugopalan. "Computing quark and gluon distribution functions for very large nuclei." In: *Physical Review D* 49.5 (1994), pp. 2233–2241. ISSN: 0556-2821. DOI: 10.1103/physrevd.49.2233. URL: http://dx.doi.org/10.1103/PhysRevD.49.2233.

[54] Edmond Iancu, Andrei Leonidov, and Larry McLerran. "Nonlinear gluon evolution in the color glass condensate: I." In: *Nuclear Physics A* 692.3–4 (Sept.

2001), 583–645. ISSN: 0375-9474. DOI: 10.1016/s0375-9474(01)00642-x. URL: http://dx.doi.org/10.1016/S0375-9474(01)00642-X.

[55] Edmond Iancu, Andrei Leonidov, and Larry McLerran. "The Colour Glass Condensate: An Introduction." In: *QCD Perspectives on Hot and Dense Matter* (2002), pp. 73–145. DOI: 10.1007/978-94-010-0267-7_3. URL: http://dx.doi.org/10.1007/978-94-010-0267-7_3.

[56] A M Cooper-Sarkar. *PDF Fits at HERA*. 2011. arXiv: 1112.2107.

[57] V. Khachatryan et al. "Transverse-Momentum and Pseudorapidity Distributions of Charged Hadrons in $pp$ Collisions at $\sqrt{s} = 7$ TeV." In: *Physical Review Letters* 105 (2 2010), p. 022002. DOI: 10.1103/PhysRevLett.105.022002. URL: https://link.aps.org/doi/10.1103/PhysRevLett.105.022002.

[58] J.L. Albacete and C. Marquet. "Gluon saturation and initial conditions for relativistic heavy ion collisions." In: *Progress in Particle and Nuclear Physics* 76 (May 2014), 1–42. ISSN: 0146-6410. DOI: 10.1016/j.ppnp.2014.01.004. URL: http://dx.doi.org/10.1016/j.ppnp.2014.01.004.

[59] Edmond Iancu and Raju Venugopalan. "The Color Glass Condensate and high energy scattering in QCD." In: *Quark-Gluon Plasma 3* (2004), pp. 249–363. DOI: 10.1142/9789812795533_0005. URL: http://dx.doi.org/10.1142/9789812795533_0005.

[60] Henri Kowalski and Derek Teaney. "Impact parameter dipole saturation model." In: *Physical Review D* 68.11 (2003). ISSN: 1089-4918. DOI: 10.1103/physrevd.68.114005. URL: http://dx.doi.org/10.1103/PhysRevD.68.114005.

[61] Amir H. Rezaeian, Marat Siddikov, Merijn Van de Klundert, and Raju Venugopalan. "Analysis of combined HERA data in the impact-parameter dependent saturation model." In: *Physical Review D* 87 (3 2013), p. 034002. DOI: 10.1103/PhysRevD.87.034002. URL: https://link.aps.org/doi/10.1103/PhysRevD.87.034002.

[62] Alfred H. Mueller. "Small x Behavior and Parton Saturation: A QCD Model." In: *Nuclear Physics B* 335 (1990), pp. 115–137. DOI: 10.1016/0550-3213(90)90173-B.

[63] L. Frankfurt, A. Radyushkin, and M. Strikman. "Interaction of a small-size wave packet with a hadron target." In: *Physical Review D* 55.1 (Jan. 1997), 98–104. ISSN: 1089-4918. DOI: 10.1103/physrevd.55.98. URL: http://dx.doi.org/10.1103/PhysRevD.55.98.

[64] Guido Altarelli and G. Parisi. "Asymptotic Freedom in Parton Language." In: *Nuclear Physics B* 126 (1977), pp. 298–318. DOI: 10.1016/0550-3213(77)90384-4.

[65] Yuri L. Dokshitzer. "Calculation of the Structure Functions for Deep Inelastic Scattering and $e^+$-$e^-$ Annihilation by Perturbation Theory in Quantum Chromodynamics." In: *Soviet Physics JETP* 46 (1977), pp. 641–653.

[66] Francois Gelis. *DGLAP equations solver*. URL: http://www-cs-faculty.stanford.edu/~uno/abcde.html. (Accessed 05.01.2020).

[67] Sangyong Jeon. "Color Glass Condensate in Schwinger–Keldysh QCD." In: *Annals of Physics* 340.1 (Jan. 2014), 119–170. ISSN: 0003-4916. DOI: 10.1016/j.aop.2013.09.019. URL: http://dx.doi.org/10.1016/j.aop.2013.09.019.

[68] F Gelis. "Probing colored glass via photoproduction II: diffraction." In: *Nuclear Physics A* 707.1–2 (Aug. 2002), 175–192. ISSN: 0375-9474. DOI: 10.1016/s0375-9474(02)00752-2. URL: http://dx.doi.org/10.1016/S0375-9474(02)00752-2.

[69] T. Lappi. "Wilson line correlator in the MV model: relating the glasma to deep inelastic scattering." In: *The European Physical Journal C* 55.2 (2008), pp. 285–292. ISSN: 1434-6052. DOI: 10.1140/epjc/s10052-008-0588-4. URL: http://dx.doi.org/10.1140/epjc/s10052-008-0588-4.

[70] Alex Kovner, Larry McLerran, and Heribert Weigert. "Gluon production from non-Abelian Weizsäcker-Williams fields in nucleus-nucleus collisions." In: *Physical Review D* 52 (11 1995), pp. 6231–6237. DOI: 10.1103/PhysRevD.52.6231. URL: https://link.aps.org/doi/10.1103/PhysRevD.52.6231.

[71] M. Gyulassy and Larry D. McLerran. "Yang-Mills radiation in ultrarelativistic nuclear collisions." In: *Physical Review C* 56 (1997), pp. 2219–2228. DOI: 10.1103/PhysRevC.56.2219. arXiv: nucl-th/9704034.

[72] Adrian Dumitru and Larry D. McLerran. "How protons shatter colored glass." In: *Nuclear Physics A* 700 (2002), pp. 492–508. DOI: 10.1016/S0375-9474(01)01301-X. arXiv: hep-ph/0105268.

[73] T. Lappi. "Production of gluons in the classical field model for heavy ion collisions." In: *Physical Review C* 67.5 (2003). ISSN: 1089-490X. DOI: 10.1103/physrevc.67.054903. URL: http://dx.doi.org/10.1103/PhysRevC.67.054903.

[74] M. Cautun. *Photon production in the Color Glass Condensate formalism*. MSc. Thesis, McGill University. 2009.

[75] Paul Romatschke and Raju Venugopalan. "The unstable glasma." In: *Physical Review D* 74.4 (2006). ISSN: 1550-2368. DOI: 10.1103/physrevd.74.045011. URL: http://dx.doi.org/10.1103/PhysRevD.74.045011.

[76] Paul Romatschke and Ulrike Romatschke. "Viscosity Information from Relativistic Nuclear Collisions: How Perfect is the Fluid Observed at RHIC?" In: *Physical Review Letters* 99.17 (Oct. 2007). ISSN: 1079-7114. DOI: 10.1103/physrevlett.99.172301. URL: http://dx.doi.org/10.1103/PhysRevLett.99.172301.

[77] Matthew R. Heffernan, Charles Gale, Sangyong Jeon, and Jean-François Paquet. *Bayesian quantification of strongly-interacting matter with color glass condensate initial conditions*. 2023. arXiv: 2302.09478 [nucl-th].

[78] Peter F. Kolb and Ulrich W. Heinz. "Hydrodynamic description of ultrarelativistic heavy ion collisions." In: *Quark Gluon Plasma 3* (May 2003). Ed. by Rudolph C. Hwa and Xin-Nian Wang, pp. 634–714. arXiv: nucl-th/0305084.

[79] Sangyong Jeon and Ulrich Heinz. "Introduction to hydrodynamics." In: *International Journal of Modern Physics E* 24.10 (2015), p. 1530010. ISSN: 1793-6608. DOI: 10.1142/s0218301315300106. URL: http://dx.doi.org/10.1142/S0218301315300106.

[80] W. Israel and J.M. Stewart. "Transient relativistic thermodynamics and kinetic theory." In: *Annals of Physics* 118.2 (1979), pp. 341–372. ISSN: 0003-4916. DOI: https://doi.org/10.1016/0003-4916(79)90130-1. URL: https://www.sciencedirect.com/science/article/pii/0003491679901301.

[81] Derek Teaney. "Effect of shear viscosity on spectra, elliptic flow, and Hanbury Brown–Twiss radii." In: *Physical Review C* 68.3 (Sept. 2003). ISSN: 1089-490X. DOI: 10.1103/physrevc.68.034913. URL: http://dx.doi.org/10.1103/PhysRevC.68.034913.

[82] William A. Hiscock and Lee Lindblom. "Generic instabilities in first-order dissipative relativistic fluid theories." In: *Physical Review D* 31 (4 1985), pp. 725–733. DOI: 10.1103/PhysRevD.31.725. URL: https://link.aps.org/doi/10.1103/PhysRevD.31.725.

[83] Paul Romatschke and Ulrike Romatschke. *Relativistic Fluid Dynamics In and Out of Equilibrium – Ten Years of Progress in Theory and Numerical Simulations of Nuclear Collisions*. 2017. arXiv: 1712.05815 [nucl-th].

[84] Ingo Müller. "Zum Paradoxon der Wärmeleitungstheorie." In: *Zeitschrift fur Physik* 198.4 (Aug. 1967), pp. 329–344. DOI: 10.1007/BF01326412.

[85] G. S. Denicol, H. Niemi, E. Molnár, and D. H. Rischke. "Derivation of transient relativistic fluid dynamics from the Boltzmann equation." In: *Physical Review D* 85.11 (June 2012). ISSN: 1550-2368. DOI: 10.1103/physrevd.85.114047. URL: http://dx.doi.org/10.1103/PhysRevD.85.114047.

[86] Alina Czajka and Sangyong Jeon. "Kubo formulas for the shear and bulk viscosity relaxation times and the scalar field theory shear calculation." In: *Physical Review C* 95.6 (June 2017). ISSN: 2469-9993. DOI: 10.1103/physrevc.95.064906. URL: http://dx.doi.org/10.1103/PhysRevC.95.064906.

[87] Matthew R. Heffernan, Charles Gale, Sangyong Jeon, and Jean-François Paquet. *Early-times Yang-Mills dynamics and the characterization of strongly interacting matter with statistical learning*. 2023. arXiv: 2306.09619 [nucl-th].

[88] A. Bazavov, P. Petreczky, and J.H. Weber. "Equation of state in 2+1 flavor QCD at high temperatures." In: *Physical Review D* 97.1 (2018). DOI: 10.1103/physrevd.97.014510. URL: https://doi.org/10.1103%2Fphysrevd.97.014510.

[89] D. Everett et al. "Multisystem Bayesian constraints on the transport coefficients of QCD matter." In: *Physical Review C* 103.5 (May 2021). ISSN: 2469-9993. DOI: 10.1103/physrevc.103.054904. URL: http://dx.doi.org/10.1103/PhysRevC.103.054904.

[90] Pasi Huovinen and Péter Petreczky. "QCD equation of state and hadron resonance gas." In: *Nuclear Physics A* 837.1–2 (June 2010), 26–53. ISSN: 0375-9474. DOI: 10.1016/j.nuclphysa.2010.02.015. URL: http://dx.doi.org/10.1016/j.nuclphysa.2010.02.015.

[91] Fred Cooper and Graham Frye. "Single-particle distribution in the hydrodynamic and statistical thermodynamic models of multiparticle production." In: *Physical Review D* 10 (1 1974), pp. 186–189. DOI: 10.1103/PhysRevD.10.186. URL: https://link.aps.org/doi/10.1103/PhysRevD.10.186.

[92] Harold Grad. "On the kinetic theory of rarefied gases." In: *Communications on Pure and Applied Mathematics* 2.4 (1949), pp. 331–407. DOI: https://doi.org/10.1002/cpa.3160020403. URL: https://onlinelibrary.wiley.com/doi/abs/10.1002/cpa.3160020403.

[93] Mike McNelis, Derek Everett, and Ulrich Heinz. *Particlization in fluid dynamical simulations of heavy-ion collisions: The iS3D module*. 2020. arXiv: 1912.08271 [nucl-th].

[94] Björn Schenke, Chun Shen, and Prithwish Tribedy. "Running the gamut of high energy nuclear collisions." In: *Physical Review C* 102.4 (2020). DOI: 10.1103/physrevc.102.044905. URL: https://doi.org/10.1103%2Fphysrevc.102.044905.

[95] Chun Shen, Zhi Qiu, Huichao Song, Jonah Bernhard, Steffen Bass, and Ulrich Heinz. *The iEBE-VISHNU code package for relativistic heavy-ion collisions*. 2015. arXiv: 1409.8164 [nucl-th].

[96] Gabriel S. Denicol, Charles Gale, Sangyong Jeon, Akihiko Monnai, Björn Schenke, and Chun Shen. "Net-baryon diffusion in fluid-dynamic simulations of relativistic heavy-ion collisions." In: *Physical Review C* 98.3 (Sept. 2018). ISSN: 2469-9993. DOI: 10.1103/physrevc.98.034916. URL: http://dx.doi.org/10.1103/PhysRevC.98.034916.

[97] Chun Shen. *iSS*. https://github.com/chunshen1987/iSS/releases. 2022.

[98] Giuliano Giacalone, Fernando G. Gardim, Jacquelyn Noronha-Hostler, and Jean-Yves Ollitrault. "Skewness of mean transverse momentum fluctuations in heavy-ion collisions." In: *Physical Review C* 103.2 (2021). DOI: 10.1103/physrevc.103.024910. URL: https://doi.org/10.1103%2Fphysrevc.103.024910.

[99] PAUL SORENSEN. "Elliptic Flow: a study of space-momentum correlations in relativistic nuclear collisions." In: *Quark-Gluon Plasma 4*. WORLD SCIENTIFIC, Feb. 2010, pp. 323–374. ISBN: 9789814293297. DOI: 10.1142/9789814293297_0006. URL: http://dx.doi.org/10.1142/9789814293297_0006.

[100] Nicolas Borghini, Phuong Mai Dinh, and Jean-Yves Ollitrault. "New method for measuring azimuthal distributions in nucleus-nucleus collisions." In: *Physical Review C* 63.5 (2001). DOI: 10.1103/physrevc.63.054906. URL: https://doi.org/10.1103%2Fphysrevc.63.054906.

[101] Ante Bilandzic, Raimond Snellings, and Sergei Voloshin. "Flow analysis with cumulants: Direct calculations." In: *Physical Review C* 83.4 (2011). DOI: 10.1103/physrevc.83.044913. URL: https://doi.org/10.1103%2Fphysrevc.83.044913.

[102] S. Voloshin and Y. Zhang. "Flow study in relativistic nuclear collisions by Fourier expansion of azimuthal particle distributions." In: *Zeitschrift fur Physik C Particles and Fields* 70.4 (May 1996), pp. 665–671. ISSN: 1431-5858. DOI: 10.1007/s002880050141. URL: http://dx.doi.org/10.1007/s002880050141.

[103] Piotr Bożek. "Transverse-momentum–flow correlations in relativistic heavy-ion collisions." In: *Physical Review C* 93.4 (2016). DOI: 10.1103/physrevc.93.044908. URL: https://doi.org/10.1103%2Fphysrevc.93.044908.

[104] D. L. Hendrie, B. G. Harvey, J. R. Meriwether, J. Mahoney, J.-C. Faivre, and D. G. Kovar. "Multipole Deformation of $^{238}$U." In: *Physical Review Letters* 30 (12 1973), pp. 571–574. DOI: 10.1103/PhysRevLett.30.571. URL: https://link.aps.org/doi/10.1103/PhysRevLett.30.571.

[105] L. Adamczyk, J.K. Adkins, G. Agakishiev, M.M. Aggarwal, Z. Ahammed, I. Alekseev, J. Alford, A. Aparin, D. Arkhipkin, E.C. Aschenauer, et al. "Azimuthal Anisotropy in U+U and Au+Au Collisions at RHIC." In: *Physical Review Letters* 115.22 (2015). ISSN: 1079-7114. DOI: 10.1103/physrevlett.115.222301. URL: http://dx.doi.org/10.1103/PhysRevLett.115.222301.

[106] Giuliano Giacalone. "Constraining the quadrupole deformation of atomic nuclei with relativistic nuclear collisions." In: *Physical Review C* 102 (2 2020),

p. 024901. DOI: 10.1103/PhysRevC.102.024901. URL: https://link.aps.org/doi/10.1103/PhysRevC.102.024901.

[107] Bjorn Schenke, Prithwish Tribedy, and Raju Venugopalan. "Initial-state geometry and fluctuations in Au + Au, Cu + Au, and U + U collisions at energies available at the BNL Relativistic Heavy Ion Collider." In: *Physical Review C* 89 (6 2014), p. 064908. DOI: 10.1103/PhysRevC.89.064908. URL: https://link.aps.org/doi/10.1103/PhysRevC.89.064908.

[108] P. Moller, J.R. Nix, W.D. Myers, and W.J. Swiatecki. "Nuclear Ground-State Masses and Deformations." In: *Atomic Data and Nuclear Data Tables* 59.2 (1995), pp. 185–381. ISSN: 0092-640X. DOI: https://doi.org/10.1006/adnd.1995.1002. URL: https://www.sciencedirect.com/science/article/pii/S0092640X85710029.

[109] P. Möller, A.J. Sierk, T. Ichikawa, and H. Sagawa. "Nuclear ground-state masses and deformations: FRDM(2012)." In: *Atomic Data and Nuclear Data Tables* 109-110 (May 2016), pp. 1–204. ISSN: 0092-640X. DOI: 10.1016/j.adt.2015.10.002. URL: http://dx.doi.org/10.1016/j.adt.2015.10.002.

[110] J. Adam, L. Adamczyk, et al. "Azimuthal Harmonics in Small and Large Collision Systems at RHIC Top Energies." In: *Physical Review Letters* 122.17 (2019). DOI: 10.1103/physrevlett.122.172301. URL: https://doi.org/10.1103%2Fphysrevlett.122.172301.

[111] M.S. Abdallah, B.E. Aboona, J. Adam, et al. "Pion, kaon, and (anti)proton production in U+U collisions at 193 GeV measured with the STAR detector." In: *Physical Review C* 107.2 (2023). DOI: 10.1103/physrevc.107.024901. URL: https://doi.org/10.1103%2Fphysrevc.107.024901.

[112] S. S. Adler, S. Afanasiev, C. Aidala, N. N. Ajitanand, et al. "Identified charged particle spectra and yields in Au+Au Collisions at $\sqrt{s_{NN}}$ = 200 GeV." In: *Physical Review C* 69.3 (Mar. 2004). ISSN: 1089-490X. DOI: 10.1103/physrevc.69.034909. URL: http://dx.doi.org/10.1103/PhysRevC.69.034909.

[113] Scott Pratt, Evan Sangaline, Paul Sorensen, and Hui Wang. "Constraining the Equation of State of Superhadronic Matter from Heavy-Ion Collisions." In: *Physical Review Letters* 114.20 (2015). DOI: 10.1103/physrevlett.114.202301. URL: https://doi.org/10.1103%2Fphysrevlett.114.202301.

[114] B. I. Abelev, M. M. Aggarwal, Z. Ahammed, B. D. Anderson, et al. "Systematic Measurements of Identified Particle Spectra in pp, d+Au and Au+Au Collisions from STAR." In: *Physical Review C* 79.3 (2009). DOI: 10.1103/physrevc.79.034909. URL: https://doi.org/10.1103%2Fphysrevc.79.034909.

[115] Arjun Kumar and Tobias Toll. "Investigating the structure of gluon fluctuations in the proton with incoherent diffraction at HERA." In: *The European Physical Journal C* 82.9 (2022). DOI: 10.1140/epjc/s10052-022-10774-3. URL: https://doi.org/10.1140%2Fepjc%2Fs10052-022-10774-3.

[116] A. Adare et al. "Measurements of Higher Order Flow Harmonics in Au+Au collisions at 200 GeV." In: *Physical Review Letters* 107.25 (2011). DOI: 10.1103/physrevlett.107.252301. URL: https://doi.org/10.1103%2Fphysrevlett.107.252301.

[117] J. Adams et al. "Azimuthal anisotropy in Au+Au collisions at 200 GeV." In: *Physical Review C* 72.1 (2005). DOI: 10.1103/physrevc.72.014904. URL: https://doi.org/10.1103%2Fphysrevc.72.014904.

[118] STAR Collaboration. *Imaging Shapes of Atomic Nuclei in High-Energy Nuclear Collisions*. 2024. arXiv: 2401.06625 [nucl-ex].

[119] Jiangyong Jia. "Probing triaxial deformation of atomic nuclei in high-energy heavy ion collisions." In: *Physical Review C* 105.4 (2022). DOI: 10.1103/physrevc.105.044905. URL: https://doi.org/10.1103%2Fphysrevc.105.044905.

[120] Jiangyong Jia. "Shape of atomic nuclei in heavy ion collisions." In: *Physical Review C* 105.1 (2022), p. 014905.

[121] Jamal Jalilian-Marian, Alex Kovner, Larry McLerran, and Heribert Weigert. "Intrinsic glue distribution at very smallx." In: *Physical Review D* 55.9 (1997), pp. 5414–5428. ISSN: 1089-4918. DOI: 10.1103/physrevd.55.5414. URL: http://dx.doi.org/10.1103/PhysRevD.55.5414.

[122] T. Lappi and H. Mäntysaari. "On the running coupling in the JIMWLK equation." In: *The European Physical Journal C* 73.2 (Feb. 2013). ISSN: 1434-6052. DOI: 10.1140/epjc/s10052-013-2307-z. URL: http://dx.doi.org/10.1140/epjc/s10052-013-2307-z.

[123] François Gelis, Tuomas Lappi, and Raju Venugopalan. "High energy factorization in nucleus-nucleus collisions. I." In: *Physical Review D* 78.5 (Sept. 2008). ISSN: 1550-2368. DOI: 10.1103/physrevd.78.054019. URL: http://dx.doi.org/10.1103/PhysRevD.78.054019.

[124] C.Y. Wong. *Introduction to High-energy Heavy-ion Collisions*. Introduction to High-energy Heavy-ion Collisions. World Scientific, 1994. ISBN: 9789810202637. URL: https://books.google.ca/books?id=Fnxvrdj2NOQC.

[125] Sören Schlichting and Björn Schenke. "The shape of the proton at high energies." In: *Physics Letters B* 739 (Dec. 2014), 313–319. ISSN: 0370-2693. DOI: 10.1016/j.physletb.2014.10.068. URL: http://dx.doi.org/10.1016/j.physletb.2014.10.068.

[126] Kari Rummukainen and Heribert Weigert. "Universal features of JIMWLK and BK evolution at small x." In: *Nuclear Physics A* 739.1–2 (July 2004), 183–226. ISSN: 0375-9474. DOI: 10.1016/j.nuclphysa.2004.03.219. URL: http://dx.doi.org/10.1016/j.nuclphysa.2004.03.219.

[127] S. Acharya et al. "Centrality and pseudorapidity dependence of the charged-particle multiplicity density in Xe-Xe collisions at $\sqrt{s_N N}$ = 5.44TeV." In: *Physics Letters B* 790 (Mar. 2019), pp. 35–48. ISSN: 0370-2693. DOI: 10.1016/j.physletb.2018.12.048. URL: http://dx.doi.org/10.1016/j.physletb.2018.12.048.

[128] V. Khachatryan et al. "Evidence for transverse-momentum- and pseudorapidity-dependent event-plane fluctuations in PbPb and pPb collisions." In: *Physical Review C* 92.3 (Sept. 2015). ISSN: 1089-490X. DOI: 10.1103/physrevc.92.034911. URL: http://dx.doi.org/10.1103/PhysRevC.92.034911.

[129] Benjamin Bally, Michael Bender, Giuliano Giacalone, and Vittorio Somà. "Evidence of the Triaxial Structure of $^{129}$Xe at the Large Hadron Collider." In: *Physical Review Letters* 128.8 (2022), p. 082301.

[130] Shujun Zhao, Hao jie Xu, You Zhou, Yu-Xin Liu, and Huichao Song. *Exploring the Nuclear Shape Phase Transition in Ultra-Relativistic $^{129}$Xe+$^{129}$Xe Collisions at the LHC*. 2024. arXiv: 2403.07441 [nucl-th]. URL: https://arxiv.org/abs/2403.07441.

[131] S. Acharya et al. "Production of pions, kaons, (anti-)protons and $\phi$ mesons in Xe-Xe collisions at $\sqrt{s_{\mathrm{NN}}}$=5.44 TeV." In: *The European Physical Journal C* 81.7 (July 2021). ISSN: 1434-6052. DOI: 10.1140/epjc/s10052-021-09304-4. URL: http://dx.doi.org/10.1140/epjc/s10052-021-09304-4.

[132] S. Acharya et al. "Transverse momentum spectra and nuclear modification factors of charged particles in Xe–Xe collisions at $\sqrt{s_{NN}}$ = 5.44 TeV." In: *Physics Letters B* 788 (Jan. 2019), 166–179. ISSN: 0370-2693. DOI: 10.1016/j.physletb.2018.10.052. URL: http://dx.doi.org/10.1016/j.physletb.2018.10.052.

[133] S. Acharya et al. "Anisotropic flow in Xe-Xe collisions at $\sqrt{s_{NN}}$ = 5.44 TeV." In: *Physics Letters B* 784 (Sept. 2018), 82–95. ISSN: 0370-2693. DOI: 10.1016/j.physletb.2018.06.059. URL: http://dx.doi.org/10.1016/j.physletb.2018.06.059.

[134] S. Acharya et al. "Pseudorapidity dependence of anisotropic flow and its decorrelations using long-range multiparticle correlations in Pb–Pb and Xe–Xe collisions." In: *Physics Letters B* 850 (Mar. 2024), p. 138477. ISSN: 0370-2693.

DOI: 10.1016/j.physletb.2024.138477. URL: http://dx.doi.org/10.1016/j.physletb.2024.138477.

[135] Piotr Bożek, Wojciech Broniowski, and João Moreira. "Torqued fireballs in relativistic heavy-ion collisions." In: *Physical Review C* 83.3 (Mar. 2011). ISSN: 1089-490X. DOI: 10.1103/physrevc.83.034911. URL: http://dx.doi.org/10.1103/PhysRevC.83.034911.

[136] G. Aad et al. "Longitudinal Flow Decorrelations in Xe+Xe Collisions at $\sqrt{s_{NN}}$ = 5.44 TeV with the ATLAS Detector." In: *Physical Review Letters* 126.12 (Mar. 2021). ISSN: 1079-7114. DOI: 10.1103/physrevlett.126.122301. URL: http://dx.doi.org/10.1103/PhysRevLett.126.122301.

[137] S. Acharya et al. "Skewness and kurtosis of mean transverse momentum fluctuations at the LHC energies." In: *Physics Letters B* 850 (Mar. 2024), p. 138541. ISSN: 0370-2693. DOI: 10.1016/j.physletb.2024.138541. URL: http://dx.doi.org/10.1016/j.physletb.2024.138541.

[138] G. Aad et al. "Correlations between flow and transverse momentum in Xe+Xe and Pb+Pb collisions at the LHC with the ATLAS detector: A probe of the heavy-ion initial state and nuclear deformation." In: *Physical Review C* 107.5 (May 2023). ISSN: 2469-9993. DOI: 10.1103/physrevc.107.054910. URL: http://dx.doi.org/10.1103/PhysRevC.107.054910.

[139] Derek Teaney and Li Yan. "Triangularity and dipole asymmetry in relativistic heavy ion collisions." In: *Physical Review C* 83.6 (June 2011). ISSN: 1089-490X. DOI: 10.1103/physrevc.83.064904. URL: http://dx.doi.org/10.1103/PhysRevC.83.064904.

[140] J.J. Sakurai and J. Napolitano. *Modern Quantum Mechanics*. Addison-Wesley, 2011.

[141] L.D. Landau and E.M. Lifshitz. *Fluid Mechanics*. v. 6. Elsevier Science, 2013.

[142] J. I. Kapusta and Charles Gale. *Finite-temperature field theory: Principles and applications*. Cambridge University Press, 2011.

[143] Sangyong Jeon. *Personal communications*. 2022.

[144] Michael E Peskin and Daniel V Schroeder. *An introduction to quantum field theory*. Includes exercises. Boulder, CO: Westview, 1995.

[145] Aleksey Cherman, Thomas D. Cohen, and Paul M. Hohler. "A sticky business: the status of the conjectured viscosity/entropy density bound." In: *Journal of High Energy Physics* 2008.02 (2008), p. 026.

[146] Charles Gale, Sangyong Jeon, Bjorn Schenke, Prithwish Tribedy, and Raju Venugopalan. "Initial state fluctuations and higher harmonic flow in heavy-ion collisions." In: *Nuclear Physics A* 904-905 (2013), pp. 409c–412c. ISSN: 0375-9474. DOI: 10.1016/j.nuclphysa.2013.02.037. URL: http://dx.doi.org/10.1016/j.nuclphysa.2013.02.037.

[147] WORLD SCIENTIFIC, 1997, pp. 21–49. ISBN: 9789814261036. DOI: 10.1142/9789814261036_0002. URL: http://dx.doi.org/10.1142/9789814261036_0002.

[148] F. Antinori and U.A. Wiedemann. "Heavy-ion collisions—Selected topics." In: *Proceedings of the International School of Physics Enrico Fermi* 178 (2011). Ed. by A. Bracco and E. Nappi, pp. 229–277. DOI: 10.3254/978-1-60750-974-5-229.

[149] A Chaudhuri. "A Short Course on Relativistic Heavy Ion Collisions." In: (2014). DOI: 10.1088/978-0-750-31060-4. URL: http://dx.doi.org/10.1088/978-0-750-31060-4.

[150] S. Ryu, J.-F. Paquet, C. Shen, G.-S. Denicol, B. Schenke, S. Jeon, and C. Gale. "Importance of the Bulk Viscosity of QCD in Ultrarelativistic Heavy-Ion Collisions." In: *Physical Review Letters* 115.13 (2015). ISSN: 1079-7114. DOI: 10.1103/physrevlett.115.132301. URL: http://dx.doi.org/10.1103/PhysRevLett.115.132301.